

THERMODYNAMICS AND CHARGED DEFECTS IN NUCLEAR ALLOYS AND
SEMICONDUCTOR MATERIALS FROM FIRST-PRINCIPLES CALCULATIONS

By

MICHELE L. FULLARTON

A DISSERTATION PRESENTED TO THE GRADUATE SCHOOL
OF THE UNIVERSITY OF FLORIDA IN PARTIAL FULFILLMENT
OF THE REQUIREMENTS FOR THE DEGREE OF
DOCTOR OF PHILOSOPHY

UNIVERSITY OF FLORIDA

2020

© 2020 Michele L. Fullarton

To my parents and grandparents

ACKNOWLEDGMENTS

First and foremost, I would like to thank Prof. Simon Phillpot for the opportunity he gave me to join his group and pursue a Ph.D. in my area of interest. In addition to his guidance with research and studies, I could not have asked for a more patient and understanding advisor during these roller-coaster years of graduate school.

I would also like to acknowledge the members of my doctoral committee, Prof. Richard Hennig, Prof. Yong Yang, and Prof. Youping Chen from the Department of Mechanical and Aerospace Engineering. I would like to extend my thanks to Prof. Susan Sinnot and Dr. Aleksandr Chernatynskiy for their help and advice on my earlier research projects, and Prof. Kevin Jones for his insight into semiconductor materials.

One of the highlights of my graduate studies has been my work on nuclear materials which would not have been possible without the support of Dr. Yongfeng Zhang and the supervision of Dr. Larry Aagesen during my internship at Idaho National Laboratory (INL). I would also like to thank the other members of the Fuels Modeling and Simulation Department at INL for their time and advice.

My thanks to the Phillpot, Sinnot and Hennig group members past and present for their friendship. To Jessi and Lindsay for being dear friends and people I can depend on. To Lauren for being the best, despite the distance. And to Simon M. without whom I would have never have pursued a Ph.D. Lastly, my deepest gratitude is extended to my parents, Andrew and Gwlenys, grandparents, David and Eunice, Wally and Mable, and granduncle John, who always encouraged my studies and believed the best in me. To them, I will be forever grateful for their sacrifices which got me here today.

TABLE OF CONTENTS

	<u>page</u>
ACKNOWLEDGMENTS	4
LIST OF TABLES	7
LIST OF FIGURES	10
ABSTRACT	15
CHAPTER	
1 INTRODUCTION	17
1.1 Tellurium Doped Gallium Arsenide	17
1.2 Thermodynamics of the Zirconium-Hydride System	20
2 COMPUTATIONAL METHODS	24
2.1 Charged Defect Calculations	24
2.1.1 Formation Energies	25
2.1.2 Chemical Potential and Gibbs Free Energy	25
2.1.3 FNV Correction for Formation Energies	28
2.1.4 Charge State Transition Levels	30
2.2 Calculation of Thermodynamic Properties	31
2.2.1 The Ising Model	32
2.2.2 Cluster Expansion Formalism	35
2.2.2.1 Effective cluster interaction	35
2.2.2.2 Structure selection	37
2.2.3 Statistical Mechanical Techniques	39
2.2.4 Phonon Contributions	40
3 TELLURIUM DOPED GALLIUM ARSENIDE	44
3.1 Configuration of Structures	44
3.2 Simulation Parameters	45
3.3 Chemical Potentials and Bulk Properties	49
3.4 Workflow for Simulations	50
3.5 Charged Intrinsic Point Defects in GaAs	52
3.5.1 Vacancies	55
3.5.2 Interstitials	58
3.6 Charged Extrinsic Point Defects in Te Doped GaAs	59
3.7 Charged Defect Complexes in Te Doped GaAs	61
3.7.1 Double Defect Complexes	61
3.7.2 Triple Defect Complexes	72
3.8 Discussion of Defect Formation in Te Doped GaAs	76
3.9 Correction Energies	81

3.10	Conclusions	86
4	THERMODYNAMIC PROPERTIES OF ZIRCONIUM HYDRIDE	90
4.1	Configuration of Structures	90
4.2	Simulation Parameters	93
4.3	Bulk Zr-H Phase Properties	95
4.4	Cluster Expansion	96
4.4.1	HCP Lattice Model	99
4.4.2	FCT ($c/a > 1$) Lattice Model and Addition of Octrahedral Interstitial Sites	104
4.4.3	FCC (Fluorite) Lattice Model and Effects of Changing Strain Limitations on CE	106
4.4.4	FCT ($c/a < 1$) Lattice Model Results	111
4.4.5	Zero Temperature Energetics Summary	112
4.5	Monte Carlo Simulations and Total Energy Surfaces	114
4.6	Phonon Calculations	123
4.7	Free Energy Surfaces	129
4.8	Conclusions	137
5	SUMMARY AND CONCLUSION	140
5.1	Tellurium Doped Gallium Arsenide	140
5.2	Zirconium Hydride	143
APPENDIX		
A	TE DOPED GAAS SUPPLEMENTAL DATA	146
B	ZR-H SUPPLEMENTAL DATA	150
REFERENCES		166
BIOGRAPHICAL SKETCH		176

LIST OF TABLES

Table	page
1-1 Band gap energy and type, electron mobility, thermal conductivity and dielectric constant at room temperature for Si and GaAs.	18
2-1 Upper and lower bounds on chemical potential of atomic species in a binary compound	28
3-1 Calculated lattice parameter, a (Å), heat of formation, ΔH (eV), and band gap energy, E_g (eV), for zinc-blende GaAs.	47
3-2 Calculated chemical potentials and internal energies of bulk Ga, As, Te and GaAs. . .	50
3-3 Intrinsic vacancy formation energies (E_{form}) in eV for GaAs.	56
3-4 Ga Interstitial formation energies (E_{form}) in eV for a charge neutral system.	59
3-5 As Interstitial formation energies (E_{form}) in eV for a charge neutral system.	59
3-6 Intrinsic interstitial formation energies (E_{form}) in eV for GaAs with charges (q) ranging from -3 to +3.	60
3-7 Extrinsic point defect formation (E_{form}), in eV, for Te doped GaAs with charges (q) ranging from -3 to +3.	61
3-8 $V_{Ga}+Te_{As}$ formation energies (E_{form}) in eV for Te doped GaAs with charges (q) ranging from -3 to +3.	63
3-9 $V_{Ga}+Te_{Int[Te-X]}$ formation energies (E_{form}) in eV for Te doped GaAs with charges (q) ranging from -3 to +3.	64
3-10 $Te_{As}+Ga_{Tetra[Ga-As]}$ formation energies (E_{form}) in eV for Te doped GaAs with charges (q) ranging from -3 to +3.	67
3-11 $Te_{As}+As_{Tetra[As-As]}$ formation energies (E_{form}) in eV for Te doped GaAs with charges (q) ranging from -3 to +3.	68
3-12 $Te_{As}+Te_{Tetra[Te-Ga]}$ formation energies (E_{form}) in eV for Te doped GaAs with charges (q) ranging from -3 to +3.	69
3-13 $V_{As}+Te_{Ga}$ formation energies (E_{form}) in eV for Te doped GaAs with charges (q) ranging from -3 to +3.	70
3-14 Two Te_{As} formation energies (E_{form}) in eV for Te doped GaAs with charges (q) ranging from -3 to +3.	71
3-15 $V_{Ga}+2Te_{As}$ formation energies (E_{form}) in eV for Te doped GaAs with charges (q) ranging from -3 to +3.	73

3-16	$2V_{Ga}+Te_{As}$ formation energies (E_{form}) in eV for Te doped GaAs with charges (q) ranging from -3 to +3.	74
3-17	Formation energies (E_{form}) in eV for $V_{Ga}+2Te_{Int[Te-Ga]}$ in Te doped GaAs with charges (q) ranging from -3 to +3.	74
3-18	Formation energies (E_{form}) in eV for $V_{Ga}+Te_{As}+Te_{Int[Te-Ga]}$ in Te doped GaAs with charges (q) ranging from -3 to +3.	75
3-19	Summary of formation energies (E_{form}) and charge states for the most favorable defects in Te-doped GaAs.	77
3-20	Transition levels ($\epsilon(q_a/q_b)$) in eV for five most likely defects in Te doped GaAs defects.	78
3-21	Defect concentrations for the Fermi level at the VBM and CBM.	79
4-1	Phase names, structures and space groups of Zr and Zr-H phases	91
4-2	Calculated lattice parameters (\AA) and formation energies (eV/atom) for Zr-H phases compared to values reported by literature.	97
4-3	Ground state structure space groups, lattice parameters (\AA) of the primitive cell and formation energies (eV/atom) from the hcp lattice model fitted CE.	100
4-4	Ground state structure space groups, lattice parameters (\AA) of the primitive cell and formation energies (eV/atom) from the fct ($c/a>1$) lattice model fitted CE.	107
4-5	Ground state structure space groups, lattice parameters (\AA) of the primitive cell and formation energies (eV/atom) from the fcc lattice model fitted CE with strain limited to 10%.	109
4-6	Ground state structure space groups, lattice parameters (\AA) of the primitive cell and formation energies (eV/atom) from the fcc lattice model fitted CE with strain limited to 4%.	110
4-7	Ground state structure space groups, lattice parameters (\AA) of the primitive cell and formation energies (eV/atom) from the fct ($c/a<1$) lattice model fitted CE.	113
4-8	Degree of fitted polynomial variables and error values for phonon energies of Zr-H structures.	127
A-1	Defect formation energies (E_{form}) in eV for Te doped GaAs defects.	147
A-2	Correction energies (E_{corr}) in eV for Te doped GaAs defects.	148
A-3	Transition levels ($\epsilon(q_a/q_b)$) in eV for Te doped GaAs defects.	149
B-1	Characteristics of calculated cluster expansions.	150
B-2	Cluster and ECI information for hcp-lattice model.	160

B-3	Cluster and ECI information for fct ($c/a > 1$) tetrahedral interstitials only-lattice model.	160
B-4	Cluster and ECI information for fct ($c/a > 1$) tetrahedral and octrahedral interstitials lattice model.	161
B-5	Cluster and ECI information for fcc-lattice model limited to 10% strain.	162
B-6	Cluster and ECI information for fcc-lattice model limited to 4% strain.	164
B-7	Cluster and ECI information for fct ($c/a < 1$) lattice model.	165

LIST OF FIGURES

<u>Figure</u>	<u>page</u>
1-1 Semiconductor energy band diagrams.	19
1-2 Electronic configuration of valence shells for Ga, As and Te atoms.	19
1-3 Area of high hydride concentration in high burnup ZIRLO™ cladding.	21
1-4 Comparison by Okamoto et al. [1] of Zirconium-Hydrogen phase diagrams published in Zuzek et al. [2], Dupin et al. [3] and Setoyama et al. [4]	22
2-1 Workflow for calculating thermodynamic properties from first principles calculations.	33
3-1 Atomic structures of GaAs, Ga, As and Te.	45
3-2 Interstitial positions in the GaAs structure.	46
3-3 Convergence tests for GaAs structure.	49
3-4 Comparison of time and memory cost for $1 \times 1 \times 1$, $2 \times 2 \times 2$ and $3 \times 3 \times 3$ sized GaAs simulation cells with similar k-point densities.	49
3-5 Workflow for Te-doped GaAs simulations.	52
3-6 Initial and aligned potentials averaged on the xy plane for a V_{Ga}^{-3} defect in a $3 \times 3 \times 3$ GaAs supercell calculated by <i>sxdefectalign</i>	54
3-7 Potentials for a V_{Ga}^{-3} defect in a $3 \times 3 \times 3$ GaAs supercell calculated by Freysoldt et al. [5].	55
3-8 Effect of supercell size on formation energy of unrelaxed V_{Ga}^{-3} with and without correction term.	56
3-9 Calculated formation energies (E_{form}), as a function of the Fermi level (μ_e) for V_{Ga} and V_{As}	57
3-10 Calculated formation energies (E_{form}), as a function of the Fermi level (μ_e), for intrinsic vacancies under Ga-rich, stoichiometric and As-rich growth conditions.	57
3-11 Calculated potentials averaged on the xy plane for the V_{Ga}^{-3} defect in a $2 \times 2 \times 2$ GaAs supercell with relaxed ions.	58
3-12 Calculated formation energies (E_{form}), as a function of the Fermi level (μ_e), for intrinsic interstitials and their initial and relaxed structures.	60
3-13 Calculated formation energies (E_{form}), as a function of the Fermi level (μ_e), for extrinsic Te substitutions.	62
3-14 Calculated formation energies (E_{form}), as a function of the Fermi level (μ_e), for extrinsic Te interstitials and their initial and relaxed structures.	62

3-15	Calculated formation energies (E_{form}), as a function of the Fermi level (μ_e), for $V_{Ga}+Te_{As}$ and the initial and relaxed structure of the closest cluster configuration. .	63
3-16	Initial and final structures of $V_{Ga}+Te_{Int[Te-X]}$ with distances between the defects of 2.5 Å 2.8 Å and 4.7 Å.	65
3-17	Initial and final structures of $V_{Ga}+Te_{Int[Te-X]}$ with distances between the defects of 4.9 Å 6.1 Å and 6.3 Å.	65
3-18	Calculated formation energies (E_{form}), as a function of the Fermi level (μ_e), for $V_{Ga}+Te_{Int[Te-X]}$	66
3-19	Calculated formation energies (E_{form}), as a function of the Fermi level (μ_e), for $Te_{As}+Ga_{Tetra[Ga-As]}$ and the initial and relaxed structure of the closest cluster configuration. .	67
3-20	Calculated formation energies (E_{form}), as a function of the Fermi level (μ_e), for $Te_{As}+As_{Tetra[As-As]}$ and the initial and relaxed structure of the closest cluster configuration. .	68
3-21	Calculated formation energies (E_{form}), as a function of the Fermi level (μ_e), for $Te_{As}+Te_{Tetra[Te-Ga]}$ and the initial and relaxed structure of the closest cluster configuration.	69
3-22	Calculated formation energies (E_{form}), as a function of the Fermi level (μ_e), for $V_{As}+Te_{Ga}$ and the initial and relaxed structure of the closest cluster configuration. .	70
3-23	Calculated formation energies (E_{form}), as a function of the Fermi level (μ_e), for two Te_{As} and the initial and relaxed structure of the closest cluster configuration. .	71
3-24	Calculated formation energies (E_{form}), as a function of the Fermi level (μ_e), for $V_{Ga}+2Te_{As}$	73
3-25	Calculated formation energies (E_{form}), as a function of the Fermi level (μ_e), for $2V_{Ga}+Te_{As}$	74
3-26	Calculated formation energies (E_{form}), as a function of the Fermi level (μ_e), for $V_{Ga}+2Te_{Int[Te-Ga]}$	75
3-27	Calculated formation energies (E_{form}), as a function of the Fermi level (μ_e), for $V_{Ga}+Te_{As}+Te_{Int[Te-Ga]}$	76
3-28	Correction energies (E_{corr}) for intrinsic vacancies as a function of defect charge (q). .	81
3-29	Correction energies (E_{corr}) for extrinsic defects as a function of defect charge (q). .	82
3-30	Correction energies (E_{corr}) for $V_{Ga}+Te_{As}$ as a function of charge (q).	83
3-31	Correction energies (E_{corr}) for $V_{Ga}+Te_{Int}$ as a function of charge (q).	83
3-32	Correction energies (E_{corr}) for Te_{As} +interstitials as a function of charge (q).	84
3-33	Correction energies (E_{corr}) for $V_{As}+Te_{Ga}$ as a function of charge (q).	85

3-34	Correction energies (E_{corr}) for two Te_{As} as a function of charge (q).	85
3-35	Calculated correction energies for triple defect complexes in Te doped GaAs as a function of defect charge (q).	86
3-36	Calculated correction energies for $Te_{As}+Te_{Int[Te-Ga]}+V_{Ga}$ in Te doped GaAs as a function of defect charge (q).	87
4-1	Interstitial sites in hcp α -Zr.	91
4-2	H interstitial configurations for γ -ZrH, δ -ZrH _{1.5} and ϵ -ZrH ₂	92
4-3	Three of the seven proposed structures for ζ -Zr ₂ H by Zhao et al.[6].	93
4-4	Convergence tests for α -Zr structure.	94
4-5	Convergence tests for γ -ZrH structure.	95
4-6	Convergence tests for δ -ZrH ₂ structure.	95
4-7	Convergence tests for ϵ -ZrH ₂ structure.	96
4-8	Example of lattice model input for the hcp unit cell and the end members (hcp-Zr and hcp-ZrH ₂) generated by MAPS.	98
4-9	Predicted, and fitted formation energies (eV/H site), referenced to hcp-Zr and hcp-ZrH ₂ , from the hcp-lattice model fitted CE.	101
4-10	Formation energies calculated with VASP and ECIs of the hcp-lattice model fitted CE.	102
4-11	Residuals of the fit and fitted vs calculated formation energies of the hcp-lattice model fitted CE.	103
4-12	Resulting ground states from the hcp-Zr lattice model fitted CE.	104
4-13	Lattice model inputs for the fct (c/a>1) unit cells.	105
4-14	Convex hulls generated by CEs of the fct (c/a>1) lattice models.	106
4-15	Resulting ground states from the fct (c/a>1) lattice model with tetrahedral interstitial sites only fitted CE.	107
4-16	Conventional and primitive unit cells for fcc ZrH ₂	108
4-17	Resulting ground states from the fcc lattice model with strain limited to 10%.	109
4-18	Resulting ground states from the fcc lattice model with strain limited to 4%.	110
4-19	Convex hulls generated by CEs of the fcc (fluorite) lattice models with tetrahedral interstitial sites.	111

4-20	Lattice model for the fct ($c/a < 1$) CE.	112
4-21	Resulting ground states from the fct ($c/a < 1$) lattice model.	113
4-22	Convex hull generated by CE of the fct ($c/a < 1$) lattice model.	114
4-23	Convex hulls generated by all the CEs.	115
4-24	Example of chemical potential in relation to ground state references from the MAPS code.	116
4-25	Results from MC simulations of the hcp-lattice model.	117
4-26	Results from MC simulations of the fct ($c/a > 1$)-lattice model.	118
4-27	Results from MC simulations of the fcc-lattice model.	120
4-28	Results from MC simulations of the fcc-lattice model.	121
4-29	Results from MC simulations of the fct ($c/a < 1$)-lattice model.	122
4-30	Free energy surfaces as a function of concentration for $T = 300$ K.	123
4-31	Phase diagram calculated by the PHB code.	124
4-32	Calculated phonon free energies for ϵ -ZrH ₂ (eV).	125
4-33	Phonon free energy surface for the hcp lattice model ground states.	126
4-34	Phonon free energy surface for the fct ($c/a > 1$) lattice model ground states.	128
4-35	Phonon free energy surface for the fcc (fluorite) lattice model ground states.	130
4-36	Phonon free energy surface for the fct ($c/a < 1$) lattice model ground states.	131
4-37	Total free energies for α -Zr.	132
4-38	Total free energies for γ -ZrH.	133
4-39	Total free energies for δ -ZrH _x	134
4-40	Total free energies for ϵ -ZrH ₂	135
4-41	Temperature sequence of G-X curves for Zr-H system.	136
4-42	Example of common tangent construction for the G-X curves at 300K.	137
4-43	Zirconium-Hydride phase diagram published by Simnad et al.[7].	138
4-44	Zirconium-Hydride phase diagram published by Zhong et al.[8].	139

B-1	Predicted, and fitted formation energies (eV/H site), referenced to fct (c/a>1)-Zr and fct (c/a>1)-ZrH ₂ , from the fct (c/a>1) tetrahedral interstitials only lattice model fitted CE.	151
B-2	Formation energies calculated with VASP and ECI of the fct (c/a>1) tetrahedral interstitials only lattice model CE.	152
B-3	Residuals of the fit and fitted vs calculated formation energies of the fct (c/a>1) tetrahedral interstitials only lattice model CE.	153
B-4	Predicted, and fitted formation energies (eV/H site), referenced to fcc-Zr and fcc-ZrH ₂ , from the fcc-lattice model fitted CE limited to 4% strain.	154
B-5	Formation energies calculated with VASP and ECI of the fcc-lattice model fitted CE limited to 4% strain.	155
B-6	Residuals of the fit and fitted vs calculated formation energies of the fcc-lattice model fitted CE limited to 4% strain.	156
B-7	Predicted, and fitted formation energies (eV/H site), referenced to fct (c/a<1)-Zr and fct (c/a<1)-ZrH ₂ , from the fct (c/a<1)-lattice model fitted CE.	157
B-8	Formation energies calculated with VASP and ECI of the fct (c/a<1)-lattice model CE.	158
B-9	Residuals of the fit and fitted vs calculated formation energies of the fct (c/a<1)-lattice model CE.	159

Abstract of Dissertation Presented to the Graduate School
of the University of Florida in Partial Fulfillment of the
Requirements for the Degree of Doctor of Philosophy

THERMODYNAMICS AND CHARGED DEFECTS IN NUCLEAR ALLOYS AND
SEMICONDUCTOR MATERIALS FROM FIRST-PRINCIPLES CALCULATIONS

By

Michele L. Fullarton

May 2020

Chair: Simon R. Phillpot

Major: Materials Science and Engineering

Density Functional Theory (DFT) calculations are used to investigate electrical deactivation after heat treatment in Tellurium (Te) doped Gallium Arsenide (GaAs) semiconductors, an effect that has been observed experimentally. DFT's predictive capabilities are explored in the generation of the phase diagram and free energy functionals of the Zirconium-Hydride (Zr-H) system. In addition to providing insights into the Zr-H phase diagram, the temperature dependence of the free energies of the various phases are important inputs into mesoscale models of Zr-based clad.

GaAs is a III-V direct band gap semiconductor that, when doped with Te, becomes *n*-type. Previously a decrease in electrical activation has been observed in the semiconductor after annealing. In this work, charged defect formation energies have been calculated using DFT. Additionally, the energy correction term compensating for the electrostatic interactions between the defects and their periodic images has been studied and a systematic approach to similar studies is recommended. The formation of Ga vacancies with charge -3, Te substitution with As atoms with charge +1 and combinations of the two defects are found to be the most energetically favorable. This work shows that the formation of the Ga vacancy and Te-substitutional defect complexes are the most likely cause for electrical deactivation in Te-doped GaAs.

Zr-alloys for nuclear fuel cladding are known to precipitate hydride phases during operation. These precipitates can cause several issues including increased stresses due to

lattice mismatches between the precipitate and the alloy and hydrogen embrittlement leading to cracking and failure of the cladding. In order to predict the materials properties of the cladding, the hydride phases must be accurately simulated. The thermodynamic stability of phases in the Zr-H system was evaluated using DFT. Cluster expansion techniques were employed to assess the stability of each phase over a range of concentrations at zero temperature. Phonon contributions were calculated and combined with results of statistical mechanical techniques calculating finite-temperature energetics to create free energy surfaces for the ground states as a function of temperature and concentration. These free energy surfaces can be employed by mesoscale modeling techniques to more accurately calculate microstructure and material properties of the cladding.

CHAPTER 1 INTRODUCTION

With the advancement of computing power in the last 100 years, it has become commonplace for industry and academia to employ computational models for the prediction of materials properties and to further understand physical processes. Models are used to predict properties which can be difficult or dangerous to physically measure and, in some cases, modeling can be faster and cheaper than experiments. However, it must be kept in mind that modeling may not be as accurate as experimental approaches, due to issues such as imperfectly described systems or the theory underlying the model being unable to accurately describe the physics of the system. In this work density functional theory (DFT) is used to explore two systems, for different purposes, to promote understanding of processes within those systems.

DFT is a quantum mechanical approach used to explore the electronic structure of many-body systems. It can predict structural, mechanical, thermodynamic, transport, electronic, optical, magnetic and chemical properties of materials. It can aid experimental work in the analysis of a material's behavior at an atomic level, or drive materials design. DFT also serves as a foundation on which experiment and other computational methods can build on.

In this work, DFT is used to predict structural properties, including crystal structures and defect structures, electronic properties, such as band gaps, and thermodynamic properties, like formation energies of materials and phase stability. Specifically, DFT is used to evaluate the formation energies of the Tellurium doped Gallium Arsenide charged defect system and to calculate thermodynamic properties of the Zirconium-Hydride system, and to generate Gibbs free energy surfaces which can be used to fit free energy functionals for use with mesoscale modeling techniques and generate phase diagrams.

1.1 Tellurium Doped Gallium Arsenide

Gallium Arsenide (GaAs) is a III-V compound semiconductor. It has applications in infrared light-emitting diodes (IR LED), field-effect transistors (FETs), integrated circuits (ICs),

Table 1-1. Band gap energy and type, electron mobility, thermal conductivity and dielectric constant at room temperature for Si and GaAs.

Property	Unit	Si	GaAs
Band gap energy [9]	eV	1.11	1.44
Band gap type [9]	-	Indirect	Direct
Electron mobility [9]	$cm^2 V^{-1}s^{-1}$	1900	9000
Hole mobility [9]	$cm^2 V^{-1}s^{-1}$	500	500
Thermal conductivity [9]	$mW cm^{-1} \cdot K^{-1}$	1240	560
Static Dielectric constant	-	11.9 [9]	12.85 [10]

solar cells and laser diodes. It has high electron mobility, a 1.44 eV direct band gap, low noise, and a wide operating temperature range. Properties of GaAs are compared to Silicon (Si) in Table 1-1. High electron mobility means GaAs can function at GHz frequencies, enabling use in high voltage power ICs. A direct band gap implies the semiconductor can emit light with high efficiency through radiative recombination. The width of the band gap also contributes to high thermal stability and resistance to radiation damage. The largest disadvantage of GaAs is that Gallium (Ga) is rare and does not occur in elemental form, but has to be extracted from minerals, causing a high cost of production.

Semiconductors are commonly doped in order to control electrical properties. Doping is the introduction of an impurity during the production of the material, creating an extrinsic semiconductor. An intrinsic semiconductor at thermal equilibrium will have an equal number of charge carriers, electrons (n) and holes (p). The introduction of an impurity will change carrier concentration from:

$$n = p = n_i \quad (1-1)$$

where n_i is the intrinsic concentration of electrons in the material, to:

$$n_0 \cdot p_0 = n_i^2 \quad (1-2)$$

where n_0 and p_0 are the concentrations of electrons and holes, respectively, in the doped material. Due to the increase in carrier concentration, the conductivity of the semiconductor

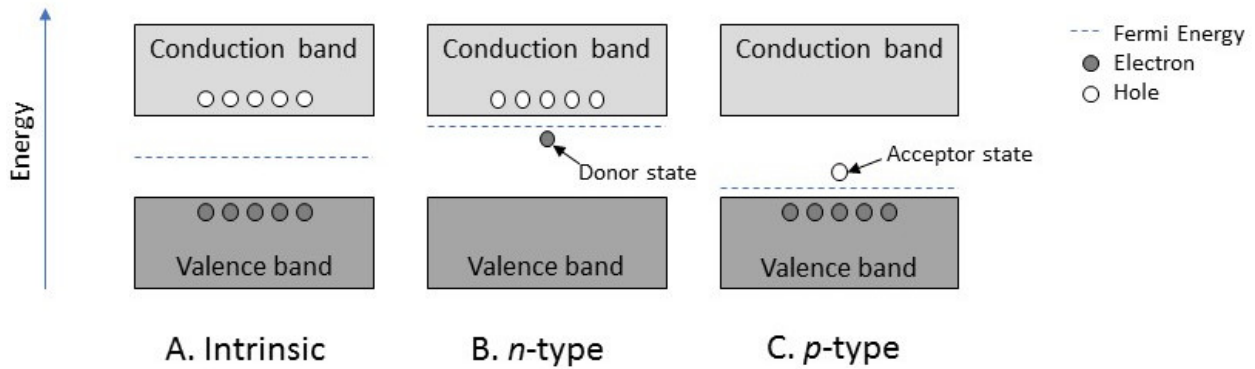


Figure 1-1. Semiconductor energy band diagrams. A) Intrinsic, B) *n*-type and C) *p*-type.

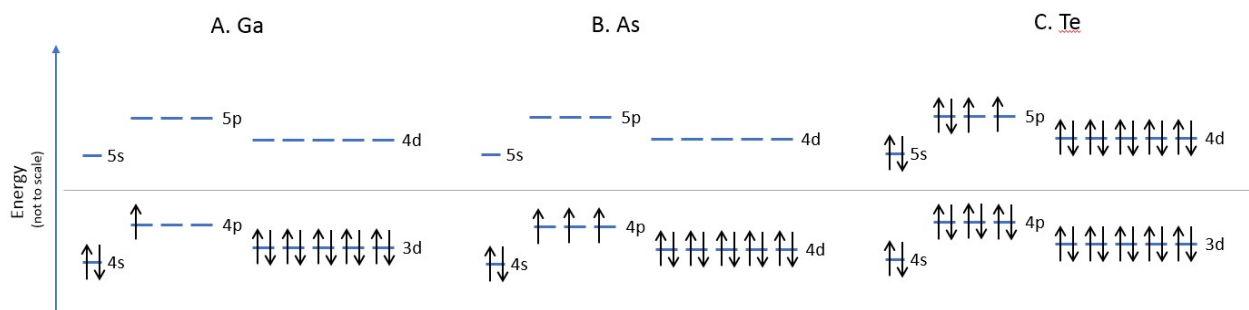


Figure 1-2. Electronic configuration of valence shells for Ga, As and Te atoms.

increases, and energy states within the band gap are allowed. In *n*-type semiconductors these are known as donor states, and in *p*-type as acceptor states, see Figure 1-1. Dopants that donate an electron create states near the conduction band, shifting the Fermi energy from the midpoint between the valence band and conduction band in an intrinsic semiconductor, at 0 K, closer to the conduction band. Dopants that accept electrons create states near the valence band, shifting the Fermi energy towards the valence band. Gallium (Ga) is a group III atoms, with 31 electrons in total and three in the $4s^2 4p^1$ subshells, Figure 1-2. Arsenic (As) is a group V atom with 33 electrons in total and five valence electrons in the $4s^2 4p^3$ subshells. In the intrinsic case, Ga shares its three valence electrons with the five from As, averaging to four bonds per atom. Tellurium (Te) is a group VI atom with 52 electrons. It has 6 valence electrons which occupy the $5s^2 5p^4$ subshells with two electrons missing from the $5p$ shell.

When Tellurium (Te) is introduced as a dopant to GaAs it brings an excess of electrons, causing Te-doped GaAs to become an *n*-type semiconductor with a negative charge. The

excess electrons increase the carrier concentration, which increases the conductivity of the semiconductor. However, carrier concentration is limited by the formation of compensating defects which also decreases carrier mobility [11]. In *n*-doped GaAs, the carrier concentration is generally limited to the mid- 10^{18} cm^{-3} range [12]. Te-doped GaAs has also been observed to undergo electrical deactivation after heat treatment [13]. Activation is the process of applying a heat treatment to a doped semiconductor in order to obtain desired electronic properties. The thermal energy creates vacancies in the material which facilitate the movement of the dopant species to substitutional positions [13]. However, in Te-doped GaAs the concentration of electrons decreases after heat treatment.

The mechanism behind electrical deactivation in Te-doped GaAs is generally thought to be the formation of Ga vacancy and Te substitution on As pairs [12]. By understanding the mechanisms which cause compensation and electrical deactivation it may be possible to suppress the concentration of the compensating defects, thus increasing the carrier concentration and conductivity without loss of mobility. This requires the intrinsic and extrinsic defects in the semiconductor material to be identified at an atomic scale. In this work, charged defects in Te-doped GaAs have been studied in a systematic manner with DFT to identify these mechanisms. In addition, a workflow for simulating charged defects in materials with DFT has been developed.

1.2 Thermodynamics of the Zirconium-Hydride System

Zirconium (Zr) alloys are commonly used in light water nuclear reactors (LWR) as fuel cladding as they have a low thermal neutron capture cross-section and act as a moderator [7]. Within a LWR, the fuel clad acts as a barrier between the fuel and coolant water and prevents fission product release into the reactor vessel. Zr-alloy in contact with water oxidizes and produces Hydrogen (H_2) gas which is then absorbed by the clad. Once the solubility limit of H is reached, the Zr changes structure on an atomic scale to a Zirconium-hydride (Zr-H) phase. The addition of H to an alloy degrades its strength, ductility, hardness, impact resistance and fracture toughness. In Zr-alloys it creates hydride precipitates, see Figure 1-3, which can cause

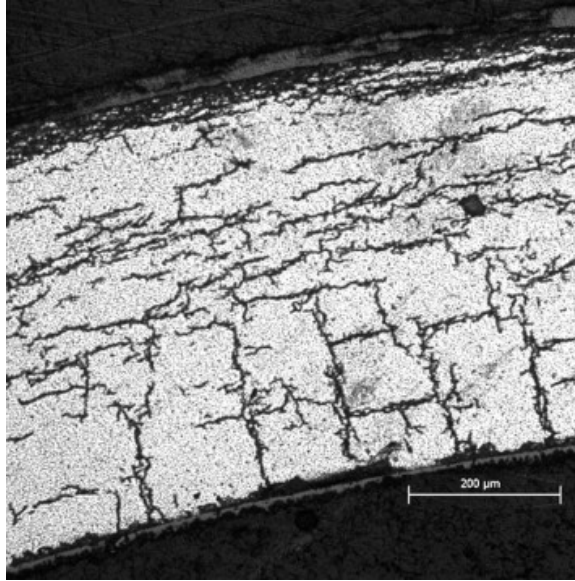


Figure 1-3. Area of high hydride concentration in high-burnup ZIRLO™ cladding. [Used with permission from Billone et al.[14]]

the clad to crack and fail. From a safety standpoint, preventing cracking or rupture is a priority in the alloy design and must be considered in predicting the operational lifespan of fuel and mechanical properties of the clad during and after use.

The performance of nuclear materials is frequently simulated on atomistic and engineering scales. However, connecting these two scales is challenging. In recent years phase field simulations have emerged as a mesoscale methodology with has the potential to bridge this gap [15]. To calculate material performance accurately with phase field methods, the models must be provided with data including the thermodynamic properties of the material from experiments and/or atomistic simulations. The Zr-H system has been studied extensively in the past by experimental techniques; however, disagreement about the phase diagram and stability of the different phases still exist. Figure 1-4 is a comparison of Zr-H phase diagrams compiled by Okamoto et al. [1] which shows an example of the uncertainty in the stability of the δ and ϵ -Zr-H phases. The phase diagram by Zuzek et al. [2] shows a region of the δ -phase from approximately 1.5 to 2 weight percent (wt.%) H, a small, two phase δ - ϵ region, and a ϵ -phase region above 2 wt.% H. Dupin et al.s' [3] phase diagram also shows the δ -phase from 1.5 to 2 wt.% H, but does not have a two-phase region and only shows the ϵ -phase as stable from 2

wt.% H above 300 K. Setoyama et al. [4] shows the δ -phase to be stable from approximately 1.6 wt.% H above 300 K, and no ϵ -phase.

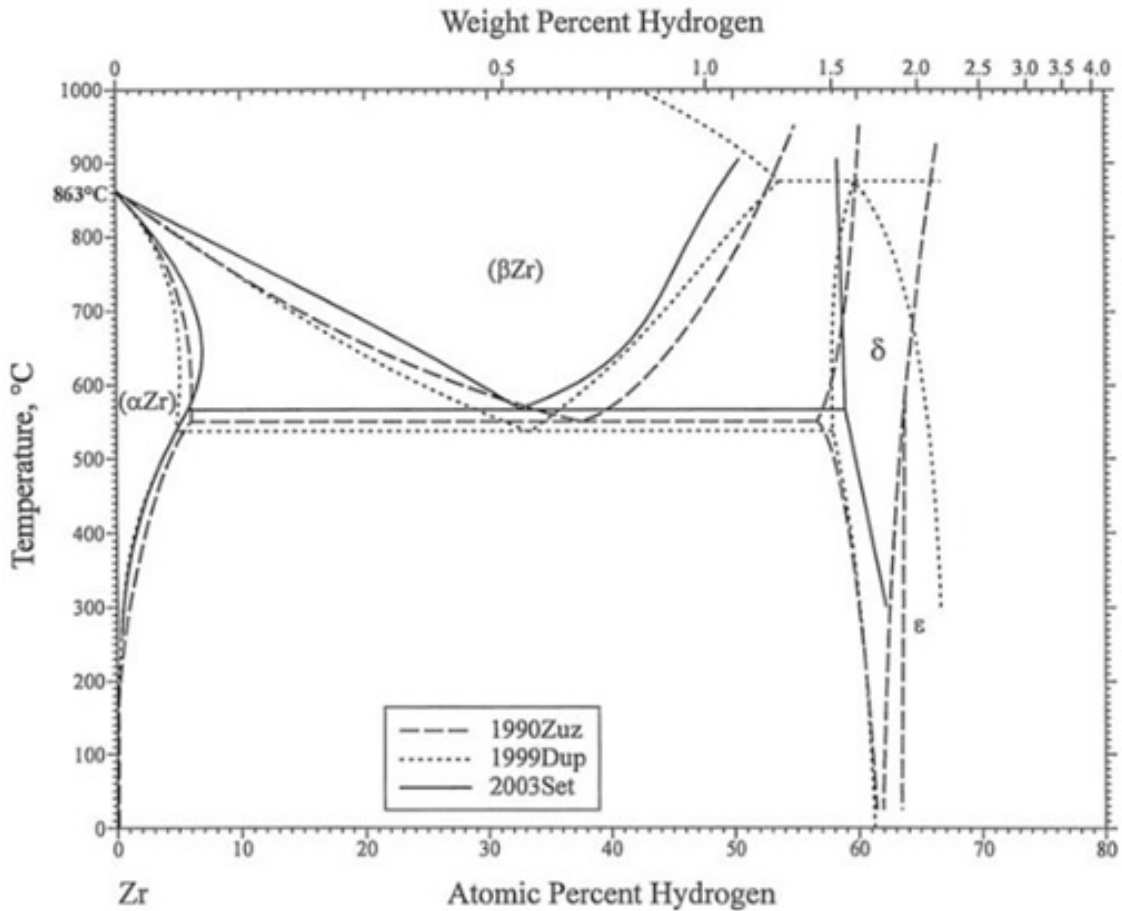


Figure 1-4. Comparison by Okamoto et al. [1] of Zirconium-Hydrogen phase diagrams published in Zuzek et al. [2], Dupin et al. [3] and Setoyama et al. [4]. [Used with permission from Okamoto et al. [1]].

Understanding and accurately modeling this region of the Zr-H phase diagram is of critical importance as the most commonly observed experimental phase is δ -ZrH_{1.667}. H also thermally diffuses towards lower temperature regions, causing a higher concentration towards the outer rim of the cladding [7, 16]. It is expected that a range of Zr-H concentrations within 1.5 to 2 wt.% H will be observed. Additionally, the phase diagrams in Figure 1-4 do not contain the metastable γ -ZrH phase or the more recently observed ζ -Zr₂H [6]. DFT will be used to predict the atomic structure of Zr and Zr-H over a range of temperatures and compositions, which will

be used to fit a free energy functionals that can be utilized by mesoscale models to predict the behavior of nuclear fuel cladding.

CHAPTER 2 COMPUTATIONAL METHODS

Density functional theory (DFT) is a quantum mechanical approach used to explore the electronic structure of many-body systems. In quantum mechanics, the many-body wavefunction, Ψ , contains all possible information for every configuration of electrons and nuclei in a system and the many-body Schrödinger wave-equation predicts the behaviour the system in terms of the wavefunction. DFT calculates an approximate solution to the Schrödinger equation using the Hohenburg-Kohn theorems [17] and solving the Kohn-Sham equations [18]. The *Vienna Ab initio Simulation Package* (VASP) [19–21] is the program used herein for DFT calculations.

In Section 2.1, the approach by which DFT is used to evaluate the formation energies of charged defect systems is described. Section 2.2 explores how DFT can be expanded upon to calculate thermodynamic properties, generate phase diagrams and feed into mesoscale modeling techniques.

2.1 Charged Defect Calculations

Calculating defect formation energies with DFT is achieved by simulating a perfect supercell, a supercell with the defect, and calculating the chemical potentials, μ_i , of each of the atomic species, i . In a charge neutral calculation, VASP will apply a homogeneous background charge if the number of electrons in the cell is inconsistent with the number derived from the valence of the atoms, so that the overall charge remains neutral. However, it is possible to directly set the number of electrons in the system and therefore change the charge of the system. With this method, also known as a supercell approach, it is possible to calculate charged defect formation energies, outlined in Section 2.1.1. However, one issue with the supercell approach is the interaction of charged defects with their periodic images, which includes overlapping wavefunctions, elastic interactions and electrostatic interactions. Section 2.1.3 outlines the Freysoldt, Neugebauer and Van de Walle (FNV) methodology [22] for calculating a correction term to remove the electrostatic interactions.

2.1.1 Formation Energies

The formation energy of a defect X in a charge state q is calculated as follows [22, 23]:

$$E_{form}[X^q] = E_{tot}[X^q] - E_{tot}[bulk^0] - \sum_i n_i \mu_i + qE_F + E_{corr} \quad (2-1)$$

Where $E_{tot}[X^q]$ is the total internal energy of the supercell with the defect from VASP, and $E_{tot}[bulk^0]$ is the total internal energy of the equivalent perfect supercell with a neutral charge. n_i is the number of atoms of species i added ($n_i > 0$) or subtracted ($n_i < 0$) in the defect cell and μ_i is the chemical potential (see Section 2.1.2) of the atomic species. E_F is the Fermi energy with respect to the the vacuum of the perfect charge neutral structure. It is equal to $E_F = E_{VBM} + \mu_e$; μ_e is the Fermi level, with respect to the valance band maximum (VBM), and is also known as the electron chemical potential. E_{VBM} is the energy of the VBM with respect to the vacuum. μ_e is bound by the energy of the band gap ($0 \leq \mu_e \leq E_g$) and will be varied so that each charge state will have a range of calculated defect formation energies. E_{corr} is the correction term to account for the periodicity inherent in DFT calculations calculated by the FNV method (Section 2.1.3).

2.1.2 Chemical Potential and Gibbs Free Energy

From Equation 2-1, the formation energy of a charged defect in a compound is a function of the electron chemical potentials of the atomic species (μ_i), which varies according to the physical growth conditions of the compound. The chemical potential of a substance (μ) can be defined as the chemical energy inherent in one mole of the substance [24]:

$$\mu = \frac{U_C}{N} \quad (2-2)$$

Where U_C is the chemical energy and N is the number of moles of a substance. The internal energy of a system comprises of its thermal (U_T), mechanical (U_M) and chemical (U_C) energies. Combining the first and second laws of thermodynamics the internal energy is

expressed as a function of entropy (S), volume (V) and number of moles of the substance [24]:

$$U = U_T + U_M + U_C = TS - PV + \mu N \quad (2-3)$$

Where T is the temperature, and P is the pressure.

The Gibbs free energy function is defined as:

$$G \equiv U + PV - TS \quad (2-4)$$

By rearranging and combining Equations 2-3 and 2-4 the relation between the chemical potential and Gibbs free energy can be expressed as:

$$\mu = \frac{G}{N} \quad (2-5)$$

Using the relation in Equation 2-5, it is a simple process to calculate the chemical potential of an atomic species using VASP. In a unary system, after relaxing a supercell VASP outputs a total internal energy of the ground state of the supercell. As VASP simulations are run with a constant temperature, $T = 0 \text{ K}$, and pressure, $P = 0 \text{ Pa}$, the TS and PV terms in Equation 2-3 and 2-4 become zero. The Gibbs free energy, G , becomes equal to the internal energy, U , so the chemical potential of an atomic species is the energy divided by the number of moles of substance. In the unary case, as there is only one species of atom, the energy outputted by VASP is divided by the total number of atoms in the supercell to find the bulk chemical potential of the species ($\mu_{i(bulk)}$).

Extending Equation 2-5 to systems with i -components, the Gibbs free energy becomes [25]:

$$G = U = \mu N = \mu_1 N_1 + \mu_2 N_2 + \mu_3 N_3 + \dots + \mu_i N_i \quad (2-6)$$

Where μ_i is the chemical potential of the atomic species i , N_i is the number of moles of that component and $N = N_1 + N_2 + \dots + N_i$. If the mole fraction of each atomic species is $x_i = \frac{N_i}{N}$ and $x_1 + x_2 + \dots + x_i = 1$, the internal energy of an i -component system in terms of the chemical

potentials for each atomic species becomes [25] :

$$G = \mu_1x_1 + \mu_2x_2 + \cdots + \mu_ix_i \quad (2-7)$$

This is commonly referred to as the molar Gibbs free energy, Gibbs free energy or just the Gibbs energy of a system [24]; however, in this work the notation of $E_{AB(bulk)}$ will be used. In literature it is also commonly notated as μ_{AB} [22, 23, 26–30]. Similar to the chemical potential of an atomic species, $\mu_{i(bulk)}$, to calculate the Gibbs energy of a compound, using VASP the total internal energy of the compound is divided by the total number of formula units in the simulated cell.

Experimentally, chemical potentials are controlled by growth conditions and can be considered as variables. In an excess of atom A , a precipitate of bulk A may form and the chemical potential of A cannot exceed the chemical potential of the bulk; $\mu_A \leq \mu_{A(bulk)}$. Similarly, the same bounds can be applied to any other atomic species in a compound, e.g. $\mu_B \leq \mu_{B(bulk)}$ [23]. These are the upper bounds on the chemical potentials. The chemical potentials of any impurity atoms in the system are also treated in this same manner. Additionally, the internal energy of the compound is proportional to it's heat of formation plus the maximum chemical potentials of it's constituents [31]:

$$E_{AB(bulk)} = \mu_{A(bulk)} + \mu_{B(bulk)} + \Delta H(AB) \quad (2-8)$$

Where $\Delta H < 0$ for a stable compound. With the upper bounds and Equation 2-8, the lower bounds can be defined as:

$$\mu_A \geq \mu_{A(bulk)} + \Delta H(AB) \quad (2-9)$$

$$\mu_B \geq \mu_{B(bulk)} + \Delta H(AB) \quad (2-10)$$

Table 2-1 shows how the upper and lower bounds of a binary AB compound can be calculated for either A-rich or B-rich growth conditions. In the case of GaAs, at the As-rich limit

$\mu_{As} = \mu_{As(bulk)}$ and $\mu_{Ga} = \mu_{Ga(bulk)} + \Delta H(GaAs)$. For the Ga-rich limit $\mu_{Ga} = \mu_{Ga(bulk)}$

and $\mu_{As} = \mu_{As(bulk)} - \Delta H(GaAs)$. However, in this work μ_{Ga} and μ_{As} will be equal to the midpoint of their respective range of chemical potentials so that the growth conditions are for the stoichiometric case. The chemical potential for Te will be treated as $\mu_{Te} = \mu_{Te(bulk)}$.

Table 2-1. Upper and lower bounds on chemical potential of atomic species in a binary compound

Environment	μ_A	μ_B
A-rich	$\mu_{A(bulk)}$	$\mu_{B(bulk)} + \Delta H(AB)$
B-rich	$\mu_{A(bulk)} + \Delta H(AB)$	$\mu_{B(bulk)}$

2.1.3 FNV Correction for Formation Energies

The Freysoldt, Neugebauer and Van de Walle (FNV) method [5] for calculating the correction term is based on the electrostatic potentials generated by DFT calculations. The following discussion of their method follows closely to their published material [5, 32] and can be reduced to two general steps taken after calculating the charge neutral defect:

1. Introduction of a charge, q , to a defect state, ψ_d , by adding or subtracting electrons. Electrons screen the introduced charge, changing the electrostatic potential.
2. Impose an artificial periodicity and remove divergence of the potential with a compensating background.

In step one, the unscreened charge density from the introduced charge is:

$$q_d(\mathbf{r}) = q|\psi_d(\mathbf{r})|^2 \quad (2-11)$$

Where \mathbf{r} is the distance from the localized charge. The defect-induced potential is the difference between the electrostatic potential, V^{els} , calculated by VASP of charged defect and that of the perfect bulk reference structure:

$$V = V^{els}(charged\ defect) - V^{els}(reference) \quad (2-12)$$

Potential, V , can also be described in terms of a short-range and long-range term:

$$V = V^{lr} + V^{sr} \quad (2-13)$$

The long-range potential, V^{lr} , assuming that microscopic screening effects, also known as local field effects, can be ignored as they generally 'average out' [5], is given by:

$$V^{lr}(\mathbf{r}) = \int d^3\mathbf{r}' \frac{q^{model}(\mathbf{r}')}{\epsilon|\mathbf{r} - \mathbf{r}'|} \quad (2-14)$$

where q^{model} is a Gaussian model of charge density with a width of one Bohr (0.53 Å), Equation 2-15. Use of this model assumes that the defect effects are strongly localized.

$$q^{model} = q_d(\mathbf{r}) = qxN_\gamma e^{-r/\gamma} + q(1-x)N_\beta e^{-r^2/\beta^2} \quad (2-15)$$

Where N_γ and N_β are normalization constants.

With a large enough supercell size and appropriate choice of q^{model} , the V^{sr} term will decay to zero within the supercell and remain the same for all the periodic defects. The short-range interaction energy between the defect and the background charge, $n = -q/\Omega$, is written as:

$$\int d^3\mathbf{r} nV^{sr}(\mathbf{r}) = -q \left[\frac{1}{\Omega} \int d^3\mathbf{r} V^{sr}(\mathbf{r}) \right] \quad (2-16)$$

where Ω is the unit cell volume.

A Fourier transform is applied to the long-range potential and background potential, Equation 2-17, so that the long-range interaction energy can be estimated from the screened Madelung energy of point charges [33]. The long-range interaction energy for spherical charge densities in reciprocal space becomes Equation 2-18.

$$\tilde{V}^{lr}(\mathbf{G} \neq 0) = \frac{4\pi q^{model}(\mathbf{G})}{\epsilon|\mathbf{G}|^2} \quad \text{and} \quad \tilde{V}^{lr}(\mathbf{0}) = 0 \quad (2-17)$$

$$E^{lat}[q^{model}] = \frac{2\pi}{\epsilon\Omega} \sum_{\mathbf{G} \neq 0}^{|G| \leq G_{cut}} \frac{\{q^{model}(|\mathbf{G}|)\}^2}{|\mathbf{G}|^2} - \frac{1}{\pi\epsilon} \int_0^{G_{cut}} dg \{q^{model}(g)\}^2 \quad (2-18)$$

Where ϵ is the dielectric constant of the material and \mathbf{G} runs over the reciprocal lattice vectors. In Equation 2-18 the first term is the energy of the periodic array and the second term is the unscreened electrostatic energy of q^{model} interacting with itself.

The formation energy is now modified to:

$$E_{form}[X^q] = E_{form}[X^0] + \Delta E^{iso}(q) + E^{lat}[q^{model}] - q\Delta \quad (2-19)$$

where $E_{form}[X^0]$ is the formation of energy of the charge neutral defect and $\Delta E^{iso}(q)$ is the difference between the formation energy of a charged defect and $\Delta E^{iso}(q)$. Δ is the alignment term from the short-range potential:

$$V^{sr} = \tilde{V}^{els}(charged\ defect) - \tilde{V}^{els}(neutral) - \tilde{V}^{lr} + \Delta V \quad (2-20)$$

ΔV is the alignment constant, which is set by the user so that V^{sr} decays to zero between the periodic images of the defect.

Up to this point the reference state has been the charge neutral defect. Freysoldt et al. [5, 32] states that the reference can be changed to the perfect neutral bulk material due to a neutral defect having no long-range Coulomb potential. Hence the formation energy of a charged defect becomes:

$$E_{form}[X^q] = E_{tot}[X^q] - E_{tot}[bulk^0] - E^{lat}[q^{model}] + q\Delta V - \sum_i n_i \mu_i + qE_F \quad (2-21)$$

which is analogous to Equation 2-1, with $E^{lat}[q^{model}] + q\Delta V$ being the correction term.

Freysoldt et al. [5] developed the *sxdefectalign* code, which employs the scheme outlined above, to calculate the correction term. As electrostatic potentials are generated when undertaking DFT calculations, no additional first principles calculations are required to determine the correction term. *sxdefectalign* can calculate the correction from the potential files of the charged defect supercell, the perfect bulk supercell, and the dielectric constant with minimal input from the user. It makes the method of calculating charged defect formation energies more robust and simplifies the analysis.

2.1.4 Charge State Transition Levels

The addition of a charge carrier, for example, a dopant, creates new levels either near the edges of the band gap or within the gap. The charge state, q_1 , of a defect in an equilibrated

configuration can be changed by processes such as optical excitation or the application of an electric field. Electrons potentially added or removed to/from the valence band to one of the new levels created by the dopant or the conduction band, and the material transitions to a new charge state, q_2 . The levels calculated by DFT methods are not directly comparable to experimental results, and so the total energies of the defect configurations before and after transition are calculated instead. This is known as the thermodynamic transition level, $\epsilon(q_1/q_2)$, and is calculated using the following [22]:

$$\epsilon(q_1/q_2) = \frac{E_{form}(X^{q_1}; \mu_e = 0) - E_{form}(X^{q_2}; \mu_e = 0)}{q_2 - q_1} \quad (2-22)$$

Where $E_{form}(X^{q_i}; \mu_e = 0)$ is the formation energy of defect X in charge state q_i and the Fermi level μ_e at the valence band maximum.

From this equation, if the Fermi level is below $\epsilon(q_1/q_2)$ the charge state q_1 will be stable, and if above q_2 will be stable. The position of $\epsilon(q_1/q_2)$ also indicates if a defect is a shallow or deep level defect. Shallow defect levels occur near the valence band maximum or conduction band minimum and are more likely to be thermally ionized at room temperature, that is, the energy difference with the valence band or conduction band is within a few k_bT , approximately 0.025 to 0.1 eV. Deep level defects occur near the middle of the band gap and are not likely to be thermally ionized at room temperature, i.e. the energy required to move electrons from the valence band, or to the conduction band, is much larger than k_bT .

2.2 Calculation of Thermodynamic Properties

It is well established that the properties of the materials of a system at 0 K can be calculated from first principles techniques. However, simulating a system at finite temperatures with first principles techniques is challenging. Currently, thermal density functional theory [34] is an emerging area of study under active development, but other methods can be used in the meantime. In this work, the finite temperature energetics of the system is calculated by expanding upon DFT calculations using simpler models such as Monte Carlo (MC) techniques and the finite displacement method (FDM).

When studying thermodynamic stability, the Helmholtz free energy, F , is reasonably easy to calculate and will be explored in this work. F consists of configurational, electronic and vibrational contributions which can be calculated separately. The method employed to calculate the configurational thermodynamic properties is outlined by van de Walle [35] and consists of three generalized steps:

1. The partition function of the system is reduced to a coarse-grained lattice model which describes the possible configurational disorder of the system (The Ising model).
2. The energy of the system is parameterized with a simpler model to limit the number of terms to be calculated by the coarse-grain partition function (Cluster Expansion).
3. The system is thermally equilibrated to obtain properties from statistical mechanical techniques (Monte Carlo simulations).

These steps will be further described in Section 2.2.1-2.2.3, including descriptions of the algorithms implemented in the ATAT package [36, 37], specifically the MAPS [35] and EMC2 codes [38].

To calculate the vibrational thermodynamics, the ground states from the cluster expansion (CE) will be used in conjunction with the FDM to calculate the phonon thermal properties. A description of the methodology as implemented by the *Phonopy* package [39] is outlined in Section 2.2.4. The electronic contribution is generally assumed to be small and will not be calculated as part of this work.

Once configurational and vibrational free energies have been calculated a free energy functional can be fit for use in mesoscale modeling techniques. Figure 2-1 shows a simplified workflow describing the steps required to generate the thermodynamic properties and at which stages DFT, or other *ab-initio* methods, are used to generate data.

2.2.1 The Ising Model

To overcome the complexity of a large system or temperatures above 0 K, the description of the system is simplified to an Ising model, which is frequently used for the calculation of phase diagrams [40]. The partition function of a system is mapped onto the partition function

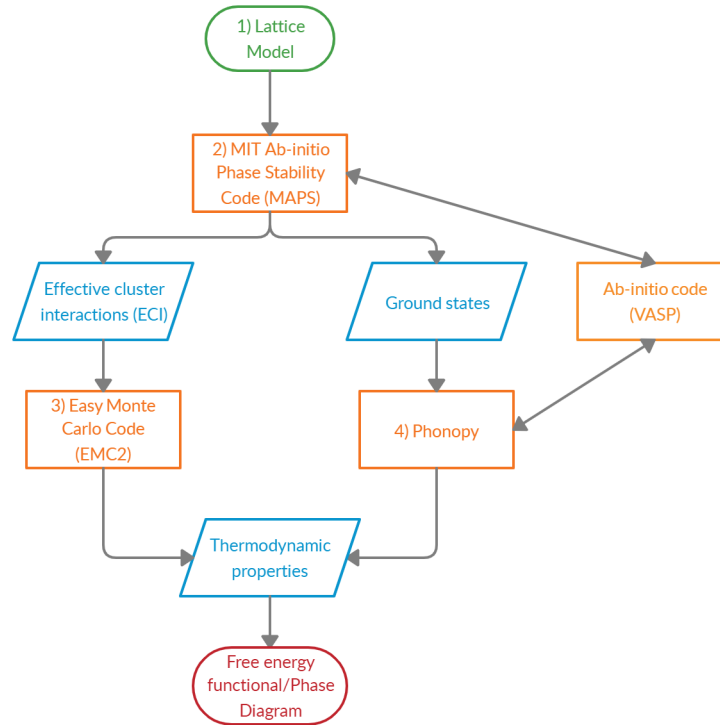


Figure 2-1. Workflow for calculating thermodynamic properties from first principles calculations. Initial input is in the green bubble, packages used to calculate data are in orange rectangles, outputted data are in blue rhomboids and the final results are indicated by the red bubble. 1) through 3) are the steps outlined to calculate the configurational thermodynamic properties and 4) is the step to calculate vibrational properties. Double headed arrows indicate that data from a package is parsed into an *ab-initio* code, which then calculates the needed property, and then is parsed back into the origin package.

of an Ising lattice and atom interactions are described through effective cluster interaction (ECI) parameters.

Originally the Ising Hamiltonian was derived as a model of ferromagnetism in statistical mechanics in which the magnetic dipole moments of atoms are represented with spins of either +1 or -1. Generalizing the Ising model for a case with an arbitrary number and type of interactions, each site in a parent lattice is represented by i , and the spin of the site as σ_i . The vector σ contains the spin variables for each lattice site and is known as the *configuration*.

Assuming the external magnetic field is zero the energy of a configuration is given by [40]:

$$H(\sigma) = \sum_{\alpha} J_{\alpha} \sigma_{\alpha} \quad (2-23)$$

Equation 2-23 is the Ising Hamiltonian, where α are a group of sites, or *clusters*, and σ_{α} is the product of all the spins in the α -cluster. J_{α} is the effective interaction parameter for cluster α .

To calculate thermodynamic properties of an alloy, the spin variable σ_i now represents the occupation of a site. That is if lattice site i is occupied by atomic species A then $\sigma_i = +1$. If occupied by species B then $\sigma_i = -1$. In the ternary case, the spin variable can take the values of +1, 0 or -1. The summation in Equation 2-23 is over all possible clusters in the lattice. If a set of appropriate effective interactions, J_{α} , are known, the energy of stable structures as a function of composition can be obtained.

A full derivation of the Ising model for alloys from the free energy partition function was published by Ceder [40]. The key points of this derivation is that at 0 K each atom occupies a site on an Ising lattice. The Ising lattice is not necessarily a Bravais lattice, but instead is a set of possible lattice positions. Only substitutional processes can change the spin configuration at non-zero temperatures. In an alloy, each configuration, σ , is subdivided into microstates, which are partitioned into groups with the same configuration. The sum over of all the microstates projects onto the same configuration on the Ising lattice with the connectivity between atoms being taken into account rather than the exact spatial coordinates.

In practice, the Ising Hamiltonian is further truncated. It has been shown that including only first and second nearest-neighbor interactions produces reasonably accurate phase diagrams for the fcc and bcc lattices [41, 42]. Section 2.2.2 covers the cluster expansion (CE) method employed by the MAPS code[36] to limit the number of terms.

2.2.2 Cluster Expansion Formalism

The CE formalism utilizes the generalization of the Ising Hamiltonian in Equation 2-23.

The parameterization of the energy (per atom) is as follows:

$$E(\sigma) = \sum_{\alpha} m_{\alpha} J_{\alpha} \left\langle \prod_{i \in \beta} \sigma_i \right\rangle \quad (2-24)$$

Where the sum is taken over all clusters α that are not equivalent by symmetry. The average is taken over all clusters β that are equivalent to α by symmetry. J_{α} becomes the effective cluster interaction (ECI) coefficient and m_{α} is the multiplicity of the clusters that are equivalent by symmetry to α .

The unknown parameters in the ECI are determined utilizing the structure inversion method (SIM)[43], which fits the ECI to the energies of a number of configurations calculated through first-principles methods. An initial CE consisting of all point clusters and all nearest-neighbor pairs is constructed from density functional theory (DFT) calculations, to which the initial ECI are fitted.

The greatest advantage to the CE formalism is that it converges quickly, generally requiring approximately 10-20 ECIs, which corresponds to approximately 30-50 first principles calculations of ordered structures. However, prior to automation in the ATAT program[36], CE was largely a non-systematic trial and error process relying on researcher knowledge of the system and intuition. van de Walle[35] proposed that this subjectivity could be overcome by selectively choosing which clusters should be included in the CE and which configurations should be used to calculate the unknown ECI. Sections 2.2.2.1 and 2.2.2.2 describe the algorithms implemented in MAPS[36] to make these selections.

2.2.2.1 Effective cluster interaction

To determine the CE exactly would require an infinite number of ECIs. In practice, the CE is approximated with a series truncated to a finite number of terms. With the energies of a finite number of structures known, the number of ECI terms retained must maintain a balance between too few terms, resulting in imprecisely predicted energies, and too many, causing

overfitting. When overfitted, the CE may include clusters which actually have no physical significance in the engineered material. This may also cause the CE to incorrectly predict the energies of new structures.

Deciding if a cluster is a candidate to be included in the fit is achieved by assessing the accuracy of the new fit. Mean squared error is not considered as a measure of the accuracy of the CE as an ECI, J_β , not included in the fit might be attributed to an ECI, J_α , which was included in the fit. As in the case of when the product of all spins in the lattice sites of cluster α ($\langle \prod_{i \in \alpha} \sigma_i \rangle$) are correlated with the product of all spins in the lattice sites of cluster β ($\langle \prod_{i \in \beta} \sigma_i \rangle$). Instead, the measure of the predictive power of a CE is evaluated with the cross-validation score[44]:

$$(CV)^2 = n^{-1} \sum_{i=1}^n (E_i - \hat{E}_{(i)})^2 \quad (2-25)$$

where n is the number of structures included in the fit, the energy of the structure i calculated by first principles is E_i and the predicted value of the energy of structure i , from a least-squares fit to the $(n - 1)$ other structures, is $\hat{E}_{(i)}$. A small CV score, on the order of 0.025 eV or smaller, is recommend for a well fitted CE by van de Walle et al. [45]

The CV score will decrease as the number of parameters fitted increases until a minimum is reached. This is due to an increased number of degrees of freedom in the CE accounting for energy variations. It has been shown that at this minimum the number of terms included in the CE are optimal[46]. As more terms are added the CV will begin increasing, indicating that the predictive power of the CE is deteriorating due to increased noise in the ECI.

Additionally, the CV is restricted to 'physically meaningful' CEs, limiting the chance that a sub-optimal ECI rising from statistical noise gives a smaller CV than the optimal ECI. By 'physically meaningful' van de Walle[35] applied the following restrictions for including a cluster:

- All sub-clusters of the cluster must have already been included, which allows for a description of the interactions between two smaller clusters

- A cluster with m -points can only be included if all clusters of m -points and a smaller diameter have already been included, this accounts for larger clusters describing weaker electrostatic interactions

To satisfy these restrictions the algorithm employed by MAPS[35] considers the clusters of pairs, triplets, quadruplets, etc, in increasing number of atoms and size.

Finally, as the aim of this work is generating the thermodynamic properties of a system, it is of primary importance that the CE predicts the correct ground states. Section 2.2.2.2 describes how the code handles structure selection. However, if the selection process fails and CE cannot correctly predict the ground states they can be given an artificial 'weight'. The weighted CE requires the calculation of the CV to be altered. van de Walle et al. [35] have described the weighted CV score and the process behind its implementation. They do not recommend the use of this algorithm unless absolutely needed as it can result in widely varying energy predictions by the CE, and so it is mentioned here only for completeness.

2.2.2.2 Structure selection

To optimize structure selection, structures with the smallest error and computation time should be added to the fit first. However, as the CV score uses the energy of a new structure to be added to the fit, this optimal selection method is not possible with the MAPS framework. Instead, van de Walle proposes a method to estimate the energy of the structure to be added to the fit.

The CE is fit with a least-squares method which consists of the bias and variance components. To reduce the prediction error, both components should be minimized; however, this is not possible for the bias as it requires knowledge of the candidate structure and so van de Walle has focused on reducing the variance instead.

The covariance matrix of a least-squares estimation is

$$V = (X^T X)^{-1} e^2 \quad (2-26)$$

Where X are the matrices $\langle \prod_{j \in \alpha} \sigma_j \rangle$ for the structures and e^2 is the mean squared error of the fit. Using this, the predicted energy for structure i is

$$\hat{E}_i = \sum_{\alpha} X_{i\alpha} J_{\alpha}^* \equiv X_{i.} J^* \quad (2-27)$$

given that \hat{E}_i is a linear function of the ECI. J_{α}^* is the vector of ECI multiplied by the respective multiplicities. The variance of a linear function of a vector J^* with the covariance matrix V becomes

$$\text{Var}[\hat{E}_i] = X_{i.} V X_{i.}^T \quad (2-28)$$

Which is the variance of the predicted energy of one structure. This is averaged over all structures, including those not yet in the fit, to obtain the predictive power of the CE. This is done by assuming that the correlations, $X_{i.}$, of every possible structure are distributed isotropically in a sphere. The expected variance of a structure is randomly chosen and given by the trace of the covariance matrix

$$\text{tr}[e^2 (X^T X)^{-1}] \quad (2-29)$$

which is used to estimate the expected variance of the energies predicted by the CE.

Since the least squares fit minimizes the error of the fit ($e^2 \rightarrow 0$), the MAPS algorithm finds new structures that maximize the difference between the trace of the existing $(X^T X)^{-1}$ and the trace of the new structure to be added $(X^T X + X_{i.}^T X_{i.})^{-1}$. The full derivation of this method can be found in [35].

Summarized, the algorithm scans the structures in increasing total number of atoms and computes the variance reduction if it is added to the fit. The structure with the maximum variance reduction will then be added to the fit. If a new ground state is predicted, the calculation of its energy via first principles will be prioritized over finding the maximum variance reduction to maintain the true ground state predictions.

Once an adequate CE has been fitted using these processes statistical mechanical techniques are applied to the model to obtain thermodynamic properties. The ATAT code[37]

includes the EMC2 tool[38] which utilizes the thermodynamic integration method to assess finite temperature properties. A description of the methodology is included in Section 2.2.3.

2.2.3 Statistical Mechanical Techniques

The partition function of the system contains all essential information about that system, and can be directly connected to its thermodynamic properties. Monte Carlo (MC) methods are frequently used to calculate these properties. The course-grain partition function evaluated by the CE can now be expressed as:

$$Z = \sum_{\sigma} e^{-\beta E(\sigma)} \quad (2-30)$$

Where $\beta = 1/(k_B T)$, k_B is the Boltzmann constant, T is the temperature in K, and $E(\sigma)$ is the energy (per atom) of the alloy with configuration σ (Equation 2-24)[47]. The thermodynamic quantities of free energy, internal energy and entropy are directly connected to the partition function through the relations:

$$F = -k_B T \ln Z \quad (2-31)$$

$$U = -T^2 \frac{\partial(F/T)}{\partial T} \quad (2-32)$$

$$S = -\left(\frac{\partial F}{\partial T}\right)_{V,N} \quad (2-33)$$

Where F is the Helmholtz free energy of the system, U is the internal energy and S is the entropy. The volume, V , and number of atoms, N , are kept fixed [48].

MC simulations are used to obtain thermodynamic information of an alloy through sampling the semi-grand-canonical ensemble. In this ensemble the number of atoms, N , remains fixed while the concentration is allowed to change as a chemical potential and temperature are imposed on the system externally [38]. The Helmholtz free energy is related to the thermodynamic potential, ϕ , by:

$$\phi = F - \mu x \quad (2-34)$$

where, in a binary A-B alloy, x is the concentration of element A, $(1 - x)$ is the concentration of element B, μ_A is the chemical potential of A, μ_B the chemical potential of B, and μ is the chemical potential difference, $\mu_A - \mu_B$.

The thermodynamic potential (per atom) for the ensemble in terms of β and μ becomes:

$$\phi(\beta, \mu) = -\frac{1}{\beta N} \ln \left(\sum_i \exp(-\beta N(E_i - \mu x_i)) \right) \quad (2-35)$$

where E_i is the internal energy (per atom) and x_i is the concentration the of state of interest, i . The potential, ϕ , expressed as a total differential is:

$$d(\beta\phi) = (E - \mu x)d\beta - \beta x d\mu \quad (2-36)$$

Where E and x now refer to the average internal energy (per atom) and concentration of the system.

Values for E and x can now be calculated for any β and μ through thermodynamic integration:

$$\beta_1\phi(\beta_1, \mu_1) = \beta_0\phi(\beta_0, \mu_0) + \int_{(\beta_0, \mu_0)}^{(\beta_1, \mu_1)} (E - \mu x, -\beta x)d(\beta, \mu) \quad (2-37)$$

Where the path between (β_0, μ_0) and (β_1, μ_1) must be continuous and maintain the same phase (no phase transition). With the EMC2 tool [38], if the user does not set an initial value for ϕ the package calculates the low temperature expansion (LTE)[49] approximation for the initial point, $\phi(\beta_0, \mu_0)$, of ordered structures.

In order to automate the MC calculations, the EMC2 algorithm employs various criteria to establish if a simulation has been successful and accurate. These include assessing when the system has reached thermodynamic equilibrium, appropriate averaging time, detection of phase transitions and phase boundary tracing. A full description of the algorithms can be found in van de Walle et al. [38].

2.2.4 Phonon Contributions

Up until this point the thermodynamic properties calculated only include configurational disorder. However, the affects of lattice vibrations must also be taken into account when

assessing the stability of phases. The vibrational portion of the free energy can be determined from forces calculated via the Hellmann-Feynman theorem. The first-principles finite displacement method (FDM) [50, 51], employed by the *Phonopy* package [39], is used to calculate the force constants and phonon thermal properties.

With the FMD method, an atom in a supercell, denoted as the κ -th atom in the l -th unit cell, is displaced a small distance, $\mathbf{u}(l\kappa)$, from its equilibrium lattice position, $\mathbf{r}(l\kappa)$, which induces forces acting on all other atoms in the system. The potential energy of the crystal, Φ , can be assumed to be an analytic function of $\mathbf{u}(l\kappa)$ and when expanded has the form:

$$\Phi = \Phi_0 + \sum_{l\kappa} \sum_{\alpha} \Phi_{\alpha} \mathbf{u}_{\alpha} + \frac{1}{2} \sum_{l'\kappa'} \sum_{\alpha\beta} \Phi_{\alpha\beta} \mathbf{u}_{\alpha} \mathbf{u}_{\beta} + \frac{1}{3!} \sum_{l''\kappa''} \sum_{\alpha\beta\gamma} \Phi_{\alpha\beta\gamma} \mathbf{u}_{\alpha} \mathbf{u}_{\beta} \mathbf{u}_{\gamma} + \dots \quad (2-38)$$

where α, β and γ are the Cartesian indices, and $\Phi_0, \Phi_{\alpha}, \Phi_{\alpha\beta}$ and $\Phi_{\alpha\beta\gamma}$ are the zeroth, first, second and third order force constants, respectively. The second-order force constants are solved with harmonic approximation, with the force, F_{α} , given by:

$$F_{\alpha}(l\kappa) = -\frac{\partial\Phi}{\partial u_{\alpha}(l\kappa)} \quad (2-39)$$

and the second-order force constant, $\Phi_{\alpha\beta}(l\kappa, l'\kappa')$, by:

$$\Phi_{\alpha\beta}(l\kappa, l'\kappa') = \frac{\partial^2\Phi}{\partial u_{\alpha}(l\kappa)\partial u_{\beta}(l'\kappa')} = -\frac{\partial F_{\beta}(l'\kappa')}{\partial u_{\alpha}(l\kappa)} \quad (2-40)$$

Third-order and higher terms are determined with perturbation theory.

A force vector, \mathbf{F} , cumulative force constant matrix, \mathbf{P} , and displacement vector, \mathbf{U} , are populated by *Phonopy*, which automatically generates a number of structures with different atomic displacements, according to user specified inputs, and then calculates the forces with the user's choice of first-principles code at a constant volume. Additionally, symmetry operations of the crystal's spacegroup are applied to further improve the accuracy of the force calculations, which is outlined in more detail in References [50, 52].

A dynamical matrix, $D(\mathbf{q})$, describing the properties of atoms in harmonic approximation in the crystal can now be given by:

$$D_{\kappa\kappa'}^{\alpha\beta}(\mathbf{q}) = \frac{1}{\sqrt{m_{\kappa}m_{\kappa'}}} \sum_{l'} \Phi_{\alpha\beta}(l\kappa, l'\kappa') e^{i\mathbf{q}\cdot[\mathbf{r}(l'\kappa') - \mathbf{r}(l\kappa)]} \quad (2-41)$$

where m is the atomic mass of atom κ , and \mathbf{q} is the wave vector. Phonon eigenfrequencies are determined by solving the eigenvalue problem:

$$D(\mathbf{q})\mathbf{e}_{qj} = \omega_{qj}^2 \mathbf{e}_{qj} \quad (2-42)$$

where ω_{qj}^2 gives the phonon frequencies, \mathbf{e}_{qj} the polarization vector of the phonon mode, and with $\{\mathbf{q}j\}$ labeling the set. From the phonon frequencies, the harmonic energies of the phonon system are calculated using Bose-Einstein statistics and including the zero-point energy as:

$$E_{vib} = \sum_{qj} \hbar\omega_{qj} \left[\frac{1}{2} + \frac{1}{e^{\hbar\omega_{qj}/k_B T} - 1} \right] \quad (2-43)$$

where \hbar is the reduced Planck constant. The vibrational contributions to the Helmholtz free energy, F_{vib} , constant volume heat capacity, C_V , and entropy, S_{vib} , can be calculated as functions of temperature using the thermodynamic relations in Equations 2-31, 2-32 and 2-33 [53]:

$$F_{vib} = \frac{1}{2} \sum_{qj} \hbar\omega_{qj} + k_B T \sum_{qj} \ln \left[1 - e^{(-\hbar\omega_{qj}/k_B T)} \right] \quad (2-44)$$

$$C_V = \sum_{qj} C_{qj} = \sum_{qj} k_B \left(\frac{\hbar\omega_{qj}}{k_B T} \right)^2 \frac{e^{(\hbar\omega_{qj}/k_B T)}}{\left[e^{(\hbar\omega_{qj}/k_B T)} - 1 \right]^2} \quad (2-45)$$

$$S_{vib} = \frac{1}{2T} \sum_{qj} \hbar\omega_{qj} \coth \left[\hbar\omega_{qj}/k_B T \right] - k_B \sum_{qj} \ln \left[2 \sinh(\hbar\omega_{qj}/k_B T) \right] \quad (2-46)$$

Harmonic approximation does not accurately describe volume dependant effects, such as thermal expansion and heat capacity, or anharmonic effects. The description of volume dependant effects can be improved by quasi-harmonic approximation, which is beyond the scope of this work. Hydrogen vibrations can be very anharmonic and isotropic [54] and may effect the ground state properties in a hydride system. Studies comparing anharmonic, or

relativistic, simulations with non-relativistic simulations found that in cubic 4d transition metal dihydrides the addition of the quantum effects did not lead to any improvement in the bulk modulus or cohesive energy [54]. Although the Zirconium-Hydrogen system does include a cubic ground state, it also has a hexagonal and two tetragonal ground states. As the above equations are calculated with Bose-Einstein statistics, quantum effects have been accounted for in this work.

CHAPTER 3 TELLURIUM DOPED GALLIUM ARSENIDE

In semiconductors, doping is the addition of impurities which allows electrical properties to be controlled. The addition of a group VI element to a III-V compound creates an n-type semiconductor, which is a semiconductor with an excess of electrons. The process of doping semiconductors creates damage in its atomic lattice, which is repaired by heat treatment. Heat treatment also, generally, electrically activates the dopants, making the excess or dearth of electrons available for conduction. However, work by Kennon et al. [55] on supersaturated Tellurium (Te) -doped Indium Gallium Arsenide (InGaAs) found electrical activation decreased after annealing. Kennon et al. proposed that this deactivation was caused by either Te-Te clustering or Te- point defect reactions.

Although only focusing on Te doped GaAs, the work in this chapter is intended as a prelude to a study of defect energetics in InGaAs to increase understanding of the mechanisms behind the observed electrical deactivation. The structure of GaAs is the same as InGaAs; InGaAs is a ternary alloy of InAs and GaAs. Previously, experimental work by Gebauer et al. [12] found three types of defects contribute to charge carrier compensation in Te doped GaAs; Ga vacancies (V_{Ga}), Te substitution on As sites (Te donors, Te_{As}) and Ga vacancy-donor complexes ($V_{Ga}-Te_{As}$).

In addition to quantifying the defect energetics of the system, this work will explore the correction term for defect formation energy calculations computed via the Freysoldt, Neugebauer and Van de Walle (FNV) method [5]. As the FNV method was developed for point defects, the suitability of the method when applied to defect complexes will be assessed in comparison to infinitely spaced defects and trends are identified.

3.1 Configuration of Structures

GaAs is a compound semiconductor with a zinc-blende structure [10], see Figure 3-1A, space group $F\bar{4}3m$. Gallium (Ga) has an orthorhombic structure with the space group $Cmce$, Figure 3-1B. The most common Arsenic (As) allotrope is α -As, with a double layered

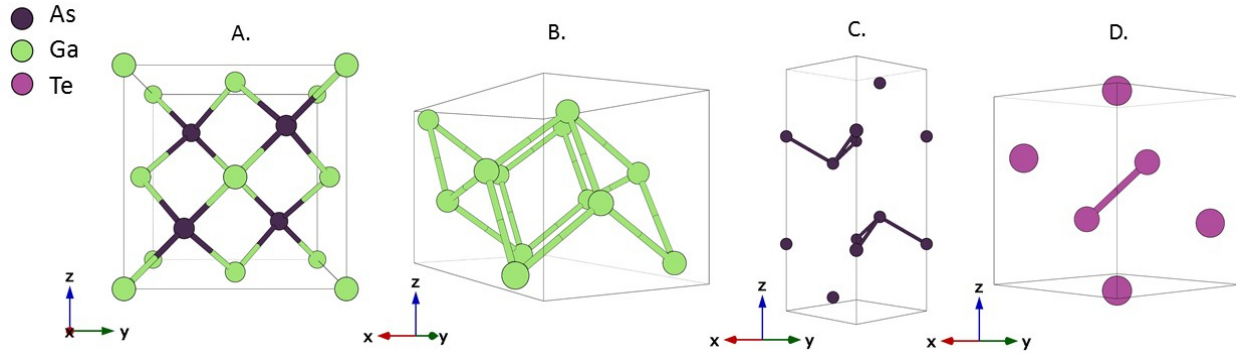


Figure 3-1. Atomic structures of GaAs, Ga, As and Te. A) GaAs (zinc-blende $F\bar{4}3m$), B) Ga (orthorhombic $Cmce$), C) As (rhombohedral $R\bar{3}m$) and D) Te (trigonal $P3_121$). Ga atoms represented by green spheres, As atoms by dark purple and Te atoms by light purple.

rhombohedral structure, spacegroup $R\bar{3}m$, Figure 3-1C. The Te crystal structure is trigonal, spacegroup $P3_121$, Figure 3-1D.

Malouin et al. [56] suggested the GaAs structure has nine possible interstitial sites, two tetrahedral sites ($Tetra_{[Int-As]}$ and $Tetra_{[Int-Ga]}$), one hexagonal, a site on a bond center, two split interstitial dumbbells in the $\langle 110 \rangle$ direction ($110\text{-split}_{[Int-As]}$ and $110\text{-split}_{[Int-Ga]}$), two split interstitial dumbbells in the $\langle 100 \rangle$ direction ($100\text{-split}_{[Int-As]}$ and $100\text{-split}_{[Int-Ga]}$) and a split interstitial dumbbell in the $\langle 111 \rangle$ direction ($111\text{-split}_{[Int-As]}$). Malouin et al. simulated the insertion of Ga self interstitials in these configurations and found $Tetra_{[Ga-Ga]}$ to be the most stable configuration, followed by $Tetra_{[Ga-As]}$. $110\text{-split}_{[Ga-As]}$ was the next most favorable in a negative or charge neutral system but relaxed to $111\text{-split}_{[Ga-As]}$ in a charge positive system. Malouin et al. reported that these defect structures and the $100\text{-split}_{[Ga-Ga]}$, the least favorable interstitial position, are metastable states. Additionally, they found that the hexagonal, bond center and $110\text{-split}_{[Ga-Ga]}$ relaxed into $Tetra_{[Ga-Ga]}$. Finally, $100\text{-split}_{[Ga-As]}$ was found to be highly unstable. All configurations except the hexagonal, bond center and 111-split are shown in Figure 3-2.

3.2 Simulation Parameters

Total energies of the GaAs, Ga, As and Te structures were calculated by density functional theory (DFT) using the Vienna Ab initio Simulation Package (VASP) [19, 20, 57, 58].

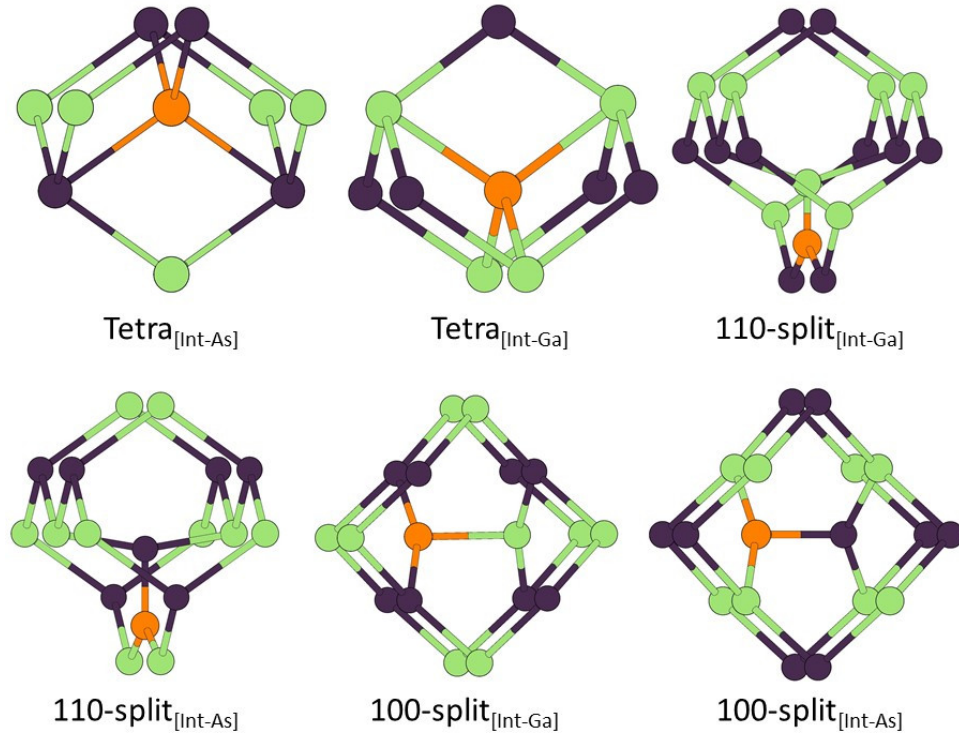


Figure 3-2. Interstitial positions in the GaAs structure. Ga atoms represented by green spheres, As atoms by dark purple and interstitial sites by orange.

Geometries of the conventional unit cells, Figure 3.1, were relaxed at a constant pressure $P = 0$ Pa, and temperature $T = 0$ K, with no symmetry constraints using projector augmented wave (PAW) pseudopotentials [21, 59] and the Local Density Approximation (LDA) [60] exchange correlation. The pseudopotentials treated As $4s^2p^3$, Ga $4s^2p^1$ and Te $5s^2p^4$ electrons as valence. Pseudopotentials which treat the d -electrons as valence are also available; however, the d states are calculated too high (particularly for Ga), placing them closer to the valence band maximum (VBM), which, in turn, repels the p states higher [61]. This pushes the VBM higher and decreases the band gap, as can be seen in the work by Schultz et al. [30] comparing pseudopotentials with and without d -electrons, Table 3-1. In addition to decreasing the band gap, including the d -shell electrons increases the computational expense of simulations. For these reasons, in this work d -electrons have been treated as core electrons.

LDA is commonly used in first-principles calculations of zinc-blende semiconductors [67] as it is able to calculate bulk properties, charge densities and formation energies with a high

Table 3-1. Calculated lattice parameter, a (Å), heat of formation, ΔH (eV), and band gap energy, E_g (eV), for zinc-blende GaAs. Exchange correlation specifies if the 3d electrons are treated as core electrons (Core), valence (Val) or is not listed in reference (NL).

Reference	Year	Exchange correlation	Basis set	a (Å)	ΔH (eV)	E_g (eV)
Experimental	1982/2020	-	-	5.6533 [10]	0.74 [9]	1.52 [62]
This work	2020	LDA-Core	PW*	5.610	0.645	0.95
Jana [63]	2018	LDA-NL	PW	5.627	-	0.50
		GGA-NL	PW	5.763	-	0.15
		SCAN-NL	PW	5.664	-	0.80
Mejia-Rodriguez [64]	2018	SCAN-Val	PW	5.659	-	0.77
Yang [65]	2016	LDA-NL	PW	-	-	0.30
		GGA-NL	PW	-	-	0.53
		SCAN-NL	PW	-	-	0.45
		HSE-NL	PW	-	-	1.41
Komsa [66]	2009	LDA-Val	PW	5.605	-	0.53
Schick [28]	2002	LDA-Val	PW	-	-	0.80
Schultz [30]	2009	LDA-Core	DZP**	5.628	0.636	0.47
		LDA-Val	DZP	5.599	0.740	0.83
		GGA-Core	DZP	5.767	0.694	0.13
		GGA-Val	DZP	5.739	0.787	0.45
Malouin [56]	2007	LDA-Val	DZP	5.60	0.737	0.82

* PW: Plane wave.

** DZP: Double- ζ polarized.

degree of accuracy [61]. The generalized gradient approximation (GGA) does not have any advantages or improvements over LDA in calculations of bulk properties and formation energies [68, 69]. Work by Jana et al. [63] and Schultz et al. [30] shows this is true for the GaAs compound, as the lattice parameter (a) and heat of formation (ΔH) calculated by LDA is a better match to the experimental results than GGA, Table 3-1. However, it is well known that both the LDA and GGA exchange correlation underestimate the band gap. This is seen in all computational examples in Table 3-1. In the case of LDA, generally the calculated upper valence bands agree well with experimental work and the conduction bands are underestimated [67]. This underestimation leads to smaller band gaps than experimental values. Attempts to overcome this include methods such as the use of meta-GGA functionals, such as the Strongly

constrained and appropriately normed semi-local density functional (SCAN) [70], and hybrid functionals, such as the Heyd–Scuseria–Ernzerhof (HSE) functional [71]. The SCAN functional is reported by Jana et al. [63], Meijia-Rodriguez et al. [64] and Yang et al. [65] to also underestimate the band gap. The HSE functional calculated a band gap similar to experimental values; however it was deemed to be prohibitively expensive for this work. As the focus of this work is on defect energetics LDA is considered to be an appropriate exchange correlation, as also used in previous literature focused on charged defect formation in GaAs [5, 28, 56, 66].

Convergence tests for ENCUT, KPOINT and cell size for the neutral GaAs structure were preformed. In Figures 3-3 A. and B. a single conventional unit cell with 8 atoms, 4 Ga and 4 As, was used to establish that an energy cut off of 500 eV and $8 \times 8 \times 8$ Monkhorst-Pack k-point grid gives a precision better than 1 meV per atom. 500 eV is a conservative choice for the energy cutoff, but was chosen to maintain the precision as the difference between 400 eV and 450 eV was greater than 1 meV. Figure 3-3C. compares the simulation of the 8 atom conventional unit cell to a 64 atom supercell with a k-point grid of $4 \times 4 \times 4$ and a 216 atom supercell with a k-point grid of $2 \times 2 \times 2$. Note, in C. the scale is significantly decreased in comparison to A. and B. The k-point density was decreased with the increase in cell size in an effort to maintain a similar k-point density across the simulations.

The energy difference between the 64 atom and 216 atom supercell was less than 1 meV. A further test to assess the time and memory required for each supercell was conducted, see Figure 1-3. The 216 atom supercell simulation took approximately 1.7 times longer than the 64 atom supercell and the memory required was more than double. Given these calculations are for the perfect bulk structure and cost is expected to increase with defect structures, the small amount of additional precision gained with the $3 \times 3 \times 3$ supercell was not deemed worth the computational cost and the $2 \times 2 \times 2$ supercell with a $4 \times 4 \times 4$ k-point grid was used going forward in this work.

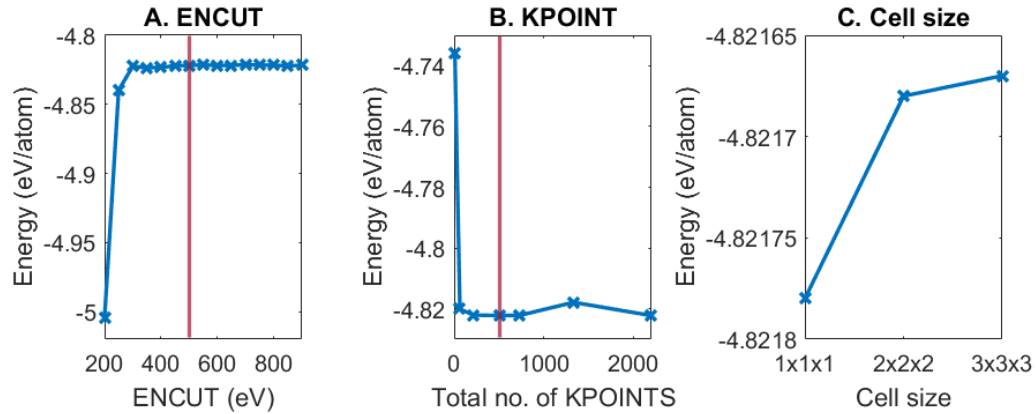


Figure 3-3. Convergence tests for GaAs structure. A) ENCUT convergence for a $1 \times 1 \times 1$ cell: Red line indicates at 500 eV precision became better than 1 meV per atom. B) KPOINT convergence for a $1 \times 1 \times 1$ cell: Red line indicates number of k-points at which precision became better than 1 meV per atom. This resulted in a k-point grid of $8 \times 8 \times 8$. C) Cell size convergence: Shows the energy difference between a $2 \times 2 \times 2$ and $3 \times 3 \times 3$ cell to be smaller than 0.01 meV per atom.

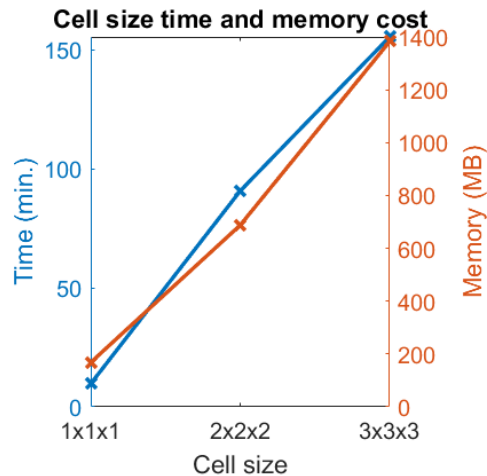


Figure 3-4. Comparison of time and memory cost for $1 \times 1 \times 1$, $2 \times 2 \times 2$ and $3 \times 3 \times 3$ sized GaAs simulation cells with similar k-point densities. Time (min.) is indicated by the blue line and memory (MB) by the orange.

3.3 Chemical Potentials and Bulk Properties

Chemical potentials and energies of the bulk materials were calculated as VASPs' outputted total energy per formula unit for the atomic species or compound. The midpoint value between the maximum and minimum chemical potentials for Ga and As were chosen as the values for (μ_i) as GaAs can be grown in either Ga-rich or As-rich environments, see

Table 3-2. Calculated chemical potentials and internal energies of bulk Ga, As, Te and GaAs. Chemical potentials in the bulk, $\mu_{(bulk)}$, for Ga, As and Te are in eV per atom and energy per pair of bulk GaAs, $E_{GaAs(bulk)}$ is in eV per formula unit.

System	Energy (eV per atom or formula unit)
μ_{Ga}	-3.93
μ_{As}	-5.71
$\mu_{Te(bulk)}$	-3.80
$E_{GaAs(bulk)}$	-9.64

Table 3-2. By choosing the midpoint, the calculations are for stoichiometric conditions in the case of GaAs. If the growth conditions are known μ_i can be easily calculated as outlined in Section 2.1.2. The heat of formation, ΔH , was calculated as 0.645 eV using Equation 2-8 ($\Delta H = -E_{GaAs(bulk)} + \mu_{Ga(bulk)} + \mu_{As(bulk)}$).

Table 3-1 compares the calculated lattice parameter, a , and ΔH to experimental and DFT values. This work uses the plane wave-LDA exchange correlation with d -electrons as core electrons to ensure the widest possible band gap and similar values to experiment for the lattice parameter and heat of formation with minimal computational expense. Despite this, the calculated band gap is 0.953 eV, approximately 0.6 eV smaller than the experimental band gap. The wider band gap in this work in comparison to the other DFT values in Table 3-1 stems from the different basis sets used and the treatment of the d -electrons as either core or valence, as discussed in Section 3.2.

3.4 Workflow for Simulations

In this work, defect formation energies are calculated with Equation 2-1, also shown below. Each structure is simulated with charges (q) ranging from -3 to +3. Chemical potentials (μ_i) are listed in Table 3-2. The Fermi energy (E_F) is set as the VBM (E_{VBM}) relative to the vacuum of the perfect GaAs structure, calculated as 3.99 eV, plus the Fermi level with respect to the E_{VBM} , $E_F = E_{VBM} + \mu_e$. μ_e is bound by the energy of the band gap ($0 \leq \mu_e \leq E_g$); as a result, each charge state has a range of calculated defect formation energies, similar to Figure 3-3. As discussed in Section 3.2, LDA calculations underestimate the band gap energy, and so the experimental band gap is used as a guide for the value of E_g . The

experimental band gap energy is 1.52 eV at 0 K and 1.43 eV at 300 K [62], thus in this work E_g is set at 1.5 eV in an effort to show defect behaviors over the full band gap.

$$E_{form}[X^q] = E_{tot}[X^q] - E_{tot}[bulk^0] - \sum_i n_i \mu_i + qE_F + E_{corr} \quad (2-1)$$

Calculations for this work were carried out in a systematic approach. Initially, intrinsic point defects in GaAs were simulated to compare to the literature. The results for the Ga vacancy, As vacancy, Ga interstitial and As interstitial are in Section 3.5. Extrinsic point defects, two Te interstitials and Te substituted on As or Ga sites, are investigated in Section 3.6. Double defect complexes comprising of mixed intrinsic and extrinsic defects and double extrinsic defects were considered next. From the four intrinsic and four extrinsic point defects there is a total of 32 different combinations possible (2×4^2), not including double intrinsic defects. In addition, each structure is simulated 7 times for differing charge states, leading to 224 simulations to be carried out if all combinations were to be explored. The most energetically favorable defects were combined to create double defects and a sample of less favorable defects combined with the most favorable defects is also investigated to generally characterize the behaviour for the 32 combinations. These results are reported in Section 3.7.1. Once double defect complexes were studied, complexes with negative formation energies and one positive formation energy complex had an additional defect added to understand the system with triple defect complexes, Section 3.7.2.

This approach is illustrated in Figure 3-5, with intrinsic and extrinsic point defects colored according to their defect formation energy: negative (green), low but positive (orange), or high and positive (red). Double defects are colored light blue and triple defects are colored dark blue. Lines from one defect to another show which defects combine to create a complex, e.g., the green line from the V_{Ga} box to the Te_{As} and $Te_{Int[Te-X]}$ boxes then continue on to create the $V_{Ga}-Te_{As}$, $V_{Ga}-Te_{Int[Te-Ga]}$ and $V_{Ga}-Te_{Int[Te-As]}$ double defect complexes.

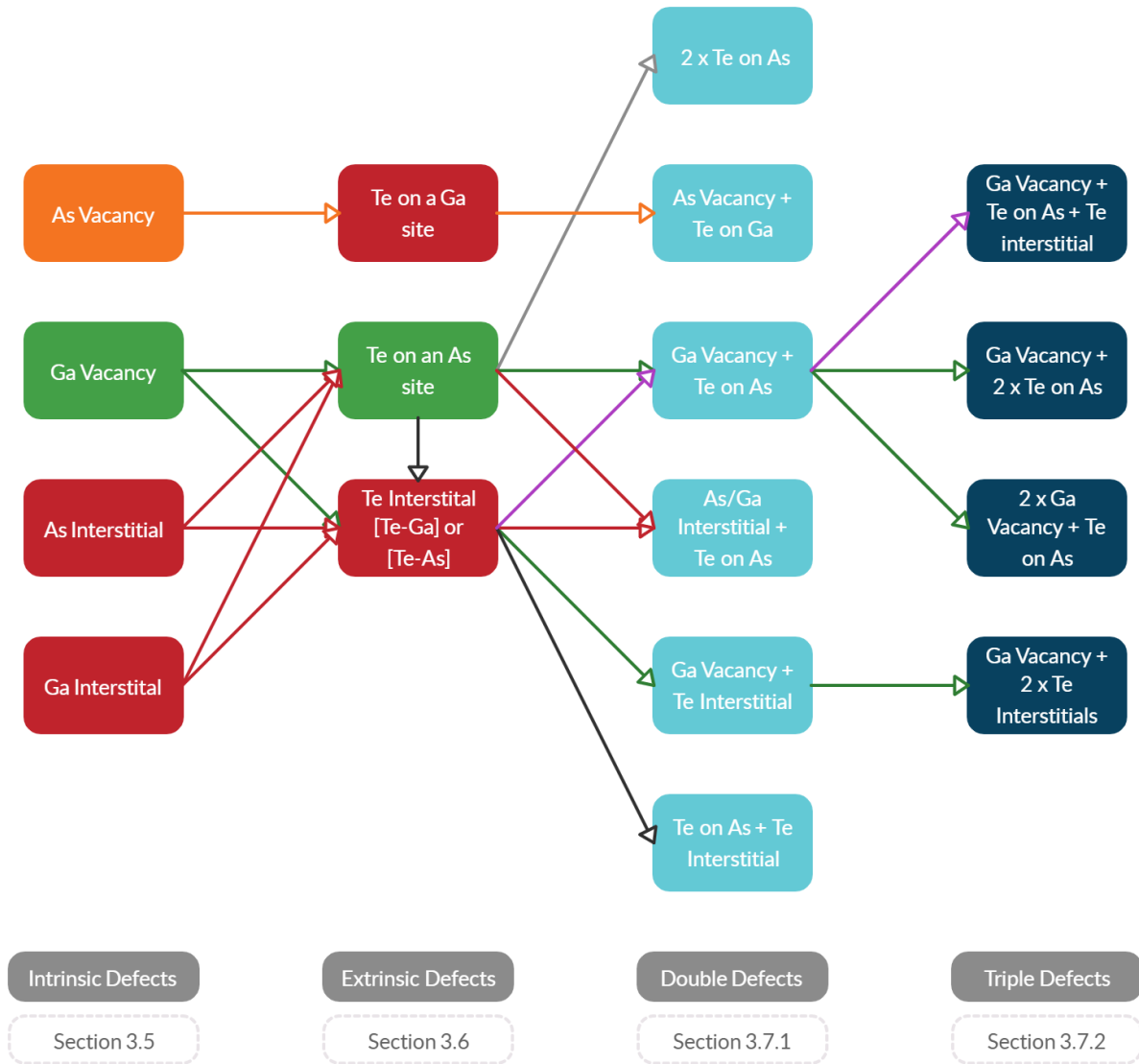


Figure 3-5. Workflow for Te-doped GaAs simulations. Intrinsic and extrinsic defects are listed in the left two columns with colors indicating if they are favorable (green), potentially favorable (orange) or unfavorable (red). Double defects are indicated by light blue boxes and triple by dark blue. Colored lines between boxes show which defects combine to create double or triple defect complexes.

3.5 Charged Intrinsic Point Defects in GaAs

The values reported in all tables henceforth are the defect formation energies for $\mu_e = 0$. The lowest defect formation energies as a function of Fermi level, μ_e , are shown in figures accompanying tables and span a range from $0 \leq \mu_e \leq 1.5$, where 1.5 eV is the experimental band gap energy in eV.

The *sxdefectalign* code, created by Freysoldt et al. [5, 32] and outlined in Section 2.1.3, is used to calculate the energy corrections (E_{corr}) and is discussed in Section 3.9. Freysoldt et al. provides practical examples of the code including its application to the Ga vacancy in GaAs with a charge state of $q = -3$ (V_{Ga}^{-3}) which is used here as a benchmark. The following steps were taken in simulating the benchmark:

1. A static self-consistent (SC) calculation is performed on a perfect $3 \times 3 \times 3$ GaAs supercell, generating a file with the local potential.
2. A Ga atom is removed from the supercell, three electrons are added, creating a charge of $q = -3$, and a static SC calculation is performed, generating a file with the local potential.
3. *sxdefectalign* uses the local potential files to calculate the the short-range, V^{sr} , and long-range potentials, V^{lr} (initial potentials in Figure 3-6).
4. Alignment constant C is set to the V^{sr} plateau height and *sxdefectalign* is used to calculate the aligned V^{sr} , V^{lr} (aligned potentials in Figure 3-6), and the energy correction term (E_{corr}).

The potentials in Figure 3-6 are averaged over the xy plane as a function of z , and include the V^{sr} , V^{lr} and defect induced potential (from DFT). The defect induced potential should show a parabolic shape similar to V^{lr} between the defect and its periodic image, in this case between at $z = 0$ and $z = 31.21$ bohr (1 bohr = 0.53 Å). The V^{sr} must show a plateau between the defects to indicate the short-range and long-range effects have been separated in order to use the *sxdefectalign* code. The alignment constant (C) is indicated on the plot of the initial potentials. The potentials have been correctly aligned when the V^{sr} plateau is at 0 eV and the DFT potential overlaps V^{lr} , as shown.

Figure 3-6 shows that the criteria of a plateau in the V^{sr} existing, upon alignment being at $V = 0$ eV, and the defect induced potential overlapping the V^{lr} was met. This work has resulted in a similar potential shape as published by Freysoldt et al., Figure 3-7, for the same system. There is a some slight difference in the figures stemming from small differences in the GaAs lattice parameter; however the same shapes and trends are observed. Larger differences such as the defect induced potential and V^{sr} having lower potential values at $z = 0$ and

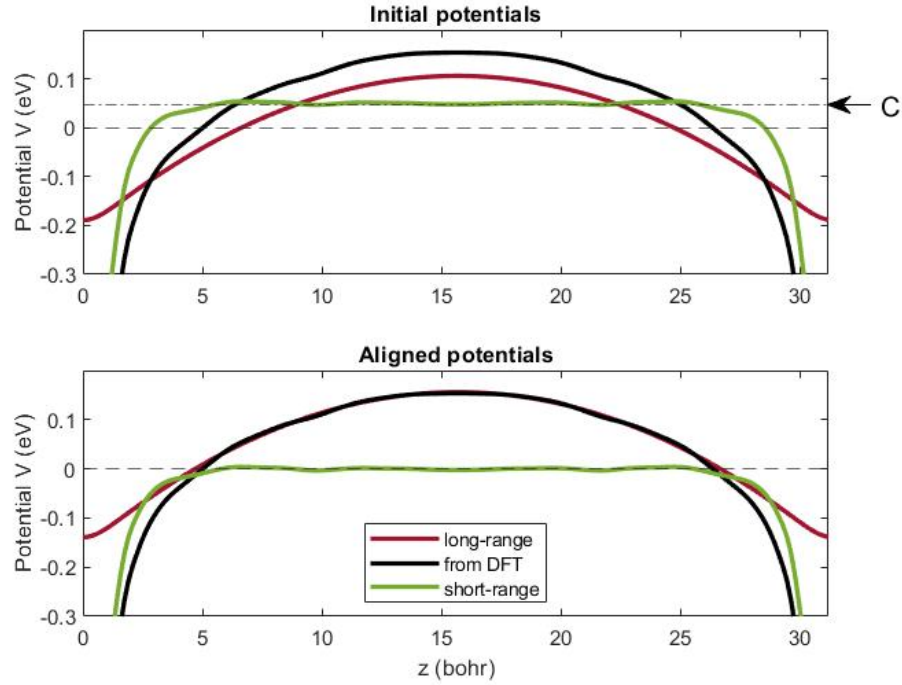


Figure 3-6. Initial and aligned potentials averaged on the xy plane for a V_{Ga}^{-3} defect in a $3 \times 3 \times 3$ GaAs supercell calculated by *sxdefectalign*. The defect is located at $z = 0$ bohr, and a periodic image at $z = 31.21$ bohr. Alignment constant C is indicated on the initial potentials.

the periodic image are most likely due to Freysoldt et al. using a different code for DFT calculations, the SPHInX code [72], and slight differences in simulation parameters. Freysoldt et al. calculated the defect formation energy for V_{Ga}^{-3} with the Fermi energy at the VBM to be 5.8 eV, with an E_{corr} of 1 eV [5]. This work found the E_{corr} to be 1.01 eV, resulting in a formation energy of 5.65 eV, 0.15 eV smaller than Freysoldt's calculations.

To assess the precision of the FNV method on removing effects of defects interacting with their periodic images, the same steps outlined above were performed on V_{Ga}^{-3} defects in supercell of sizes ranging from $2 \times 2 \times 2$ to $4 \times 4 \times 4$. From Figure 3-8, the formation energy ranges from 3.69 eV to 4.74 eV for the uncorrected calculation, and from 5.25 eV to 5.65 eV for the corrected calculation. The spread for the uncorrected energies is 1.05 eV and 0.4 eV for the corrected energies. This result is similar to results from Freysoldt et al. [5], who found a spread of 0.8 eV for uncorrected formation energies and 0.2 eV for corrected energies.

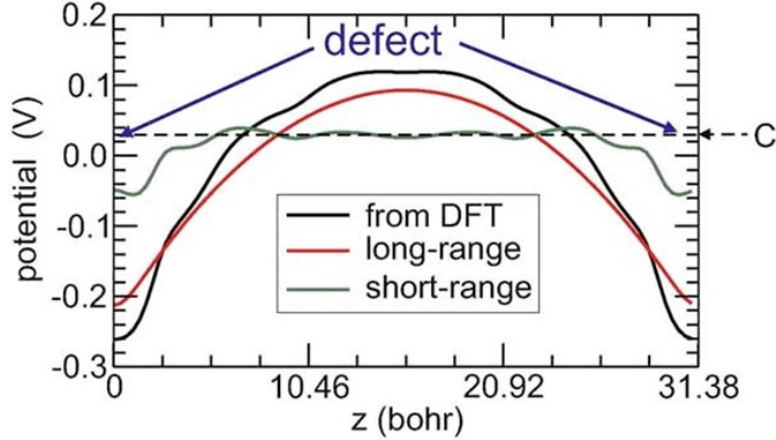


Figure 3-7. Potentials for a V_{Ga}^{-3} defect in a $3 \times 3 \times 3$ GaAs supercell calculated by Freysoldt et al. [5]. The defect is located at $z = 0$ bohr, and a periodic image at $z = 31.21$ bohr. [Used with permission from Freysoldt et al.[5]]

Since the results of Freysoldt et al. were reasonably well reproduced in this work, E_{corr} will be calculated with *sxdefectalign* in the remainder of this work. Additionally, as the range of values for the corrected energies varied by 0.4 eV, it is assumed that the accuracy of formation energies calculated with the FNV method is approximately the same. Combined with the maximum thermal energy that can be applied to the system before melting at approximately 1500 K, approximately 0.13 eV, any formation energy of 0.6 eV or lower will be considered as reasonably low and potentially become favorable when heat is applied to the system.

3.5.1 Vacancies

The formation energies and calculated correction energies for Ga and As vacancies (V_{Ga} and V_{As}) are reported in Tables 3-3 and A-2. By rearranging Equation 2-1 it is possible to create plots of the formation energy (E_{form}) as a function of the Fermi level (μ_e). For each charge state a linear formation energy function exists with the E_{form} from Table 3-3 as the intercept of the horizontal axis and the gradient equal to the charge, q . The lowest energy line at any μ_e is the most favorable charge state for that μ_e . Examples showing the formation energy functions for each charge state for the intrinsic vacancies are in Figure 3-9.

At $\mu_e = 0$ (Table 3-3), V_{Ga} has lower defect formation energies in the neutral and negative charge states, while V_{As} has lower formation energies in positive charge states.

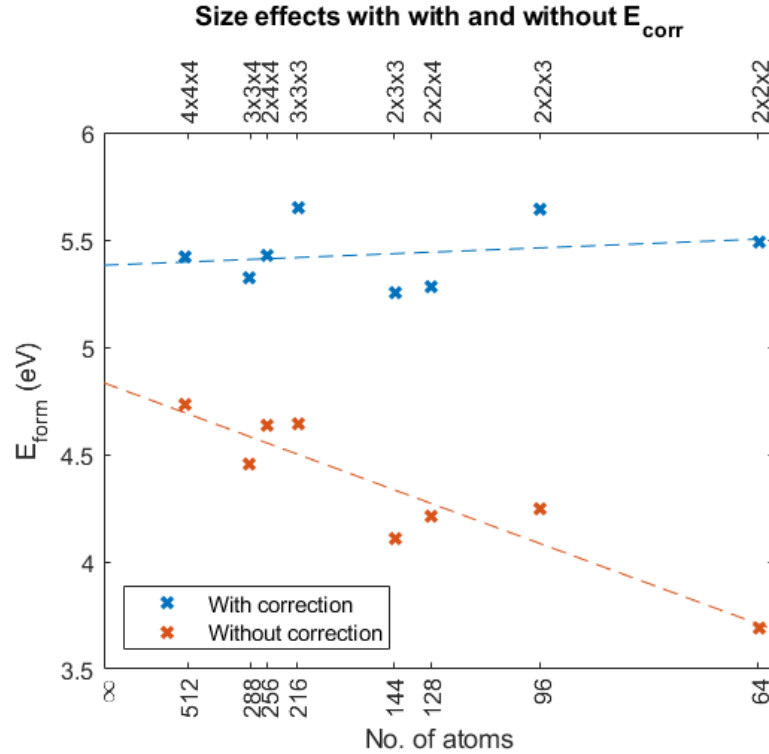


Figure 3-8. Effect of supercell size on formation energy of unrelaxed V_{Ga}^{-3} with and without correction term. Blue indicates the formation energy with the correction term applied and orange without. Dashed lines indicate linear polynomial fit to each data set.

However, overall V_{Ga} has lower formation energies than V_{As} , as illustrated in Figure 3-10 center, with the two plots in Figure 3-9 superimposed for stoichiometric conditions. The image to the left shows how adjusting the chemical potentials for a Ga-rich environment shifts the V_{Ga} formation energies up, in blue, and the V_{As} formation energies down, in orange. The image to the right shows the As-rich environment, with V_{Ga} shifting down and V_{As} shifting up. In the stoichiometric case, the V_{Ga} line is lower than the V_{As} line, except for $\mu_e < 0.025$.

Table 3-3. Intrinsic vacancy formation energies (E_{form}) in eV for GaAs. Charges (q) range from -3 to +3. Lowest formation energy for each defect indicated in bold print.

Defect	Charge (q)						
	-3	-2	-1	0	+1	+2	+3
V_{Ga}	3.842	3.175	2.856	2.884	3.244	3.949	5.002
V_{As}	5.275	4.237	3.526	3.070	2.810	3.214	3.451

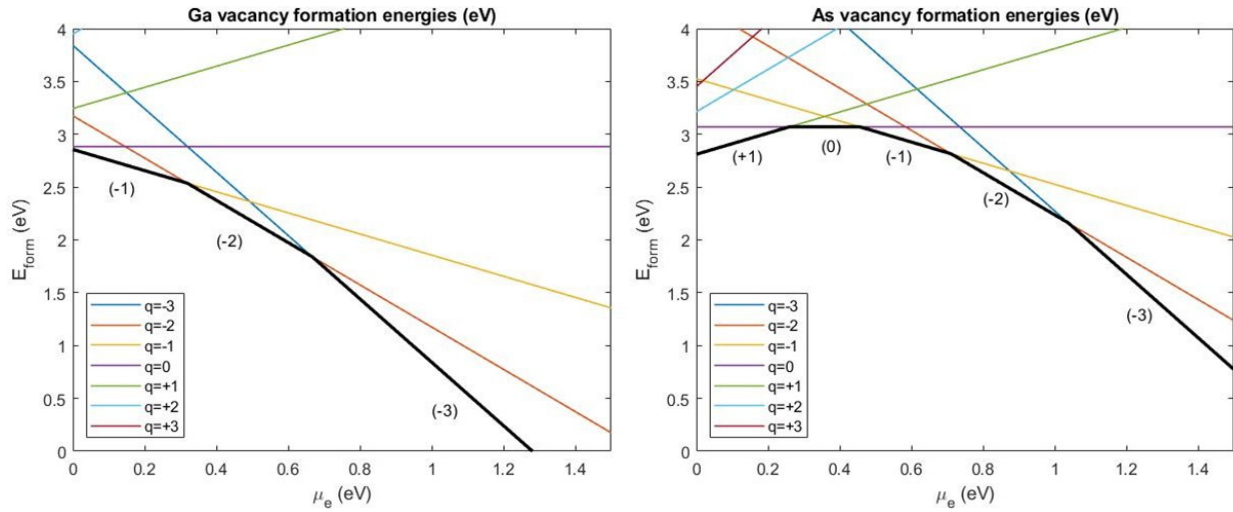


Figure 3-9. Calculated formation energies (E_{form}), as a function of the Fermi level (μ_e) for V_{Ga} and V_{As} . Black lines indicate the most favorable charge states for given μ_e .

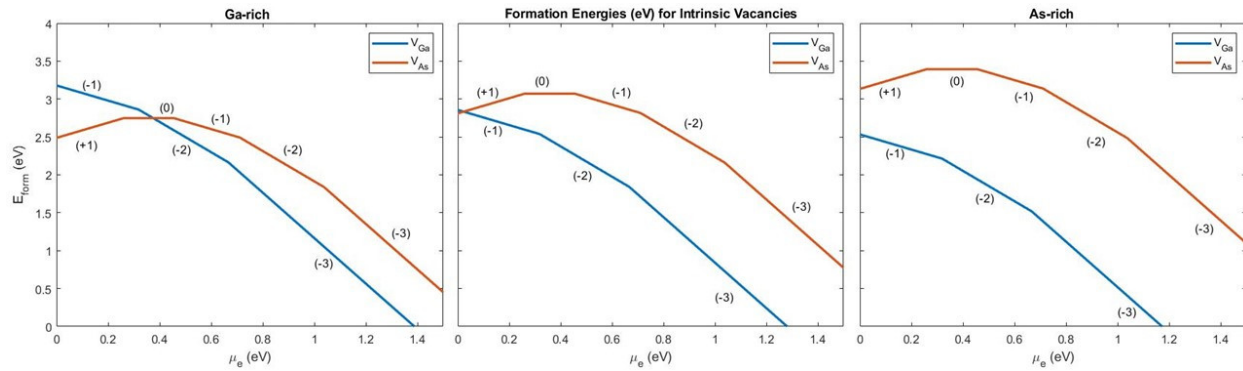


Figure 3-10. Calculated formation energies (E_{form}), as a function of the Fermi level (μ_e), for intrinsic vacancies under Ga-rich, stoichiometric and As-rich growth conditions. V_{Ga} is in blue and V_{As} in orange. Ga-rich growth conditions are on the left, stoichiometric in the middle and As-rich on the right.

Approaching $\mu_e = 1.5$, the V_{Ga} formation energy becomes negative, indicating that as the Fermi level approaches the conduction band minimum (CBM) these vacancies will form with a charge $q = -3$. This is in agreement with Gebauer et al. [73] who found that formation of V_{Ga}^{-3} is favorable.

Figure 3-11 is an example of the potentials calculated for V_{Ga}^{-3} . This differs from Figures 3-6 and 3-7, with more oscillations in the defect induced potential (from DFT) and the V^{sr} due to the ion positions having been relaxed. However, there is a clearly defined

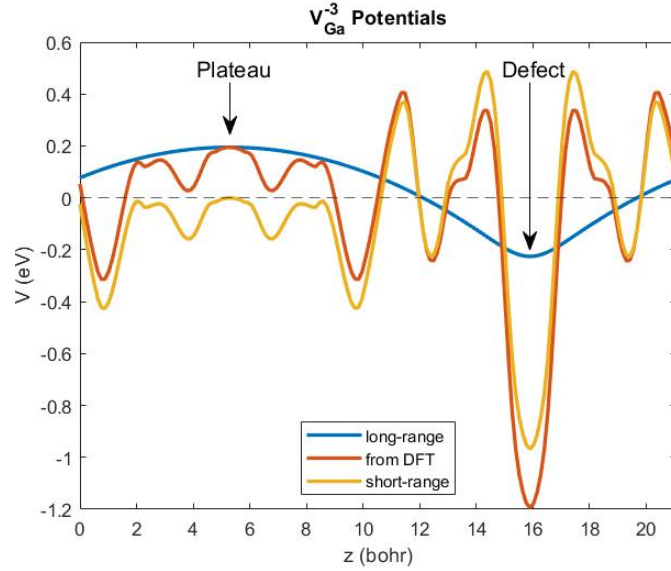


Figure 3-11. Calculated potentials averaged on the xy plane for the V_{Ga}^{-3} defect in a $2 \times 2 \times 2$ GaAs supercell with relaxed ions. The defect is located at $z = 15.9$ bohr.

plateau which, when aligned, results in the induced potential following the trend of V^{lr} , thus meeting the criteria outlined in Section 3.5.

3.5.2 Interstitials

Ga interstitials (Ga_I) on the sites listed in Section 3.1 were simulated with a neutral charge to compare to the results from Malouin et al. [56], see Table 3-4. The $111\text{-split}_{[Ga-Ga]}$ interstitial was not simulated as Malouin only found this structure upon relaxation of the $110\text{-split}_{[Ga-As]}$ interstitial with a positive charge. Additionally, the hexagonal and bond center interstitials were not simulated as Malouin found they relaxed to the $Tetra_{[Ga-Ga]}$ structure. As the values reported by Malouin are generally larger than the results of this work due to their use of a double- ζ polarized basis set (DZP) and a different energy correction scheme, they are not directly comparable. However the same trend in stability was observed with the $Tetra_{[Ga-Ga]}$ interstitial defect having the lowest formation energy. In this work the $110\text{-split}_{[Ga-Ga]}$ relaxed into a $Tetra_{[Ga-As]}$ interstitial.

Similarly, the formation energies for the As interstitial (As_I) in the same defect sites were calculated to find the configuration with the lowest formation energy, see Table 3-5. It was

Table 3-4. Ga Interstitial formation energies (E_{form}) in eV for a charge neutral system. Lowest formation energy for each defect indicated in bold print.

Interstitial defect	This work	Malouin et al. [56]
Tetra _[Ga-As]	3.448	3.73
Tetra _[Ga-Ga]	3.124	3.42
110-split _[Ga-As]	4.641	4.24
110-split _[Ga-Ga]	relaxed to Tetra _[Ga-As]	relaxed to Tetra _[Ga-Ga]
100-split _[Ga-As]	not simulated	does not converge
100-split _[Ga-Ga]	4.902	4.92

Table 3-5. As Interstitial formation energies (E_{form}) in eV for a charge neutral system. Lowest formation energy for each defect indicated in bold print.

Interstitial defect	This work
Tetra _[As-As]	5.307
Tetra _[As-Ga]	5.040
110-split _[As-As]	4.239
110-split _[As-Ga]	4.690
100-split _[As-As]	4.684
100-split _[As-Ga]	not simulated

found that an As interstitial in a split-dumbbell in the $\langle 110 \rangle$ direction is the most favorable position; however the Ga Tetra_[Ga-Ga] interstitial formation energy is overall lower.

The formation energies for the Ga_{Tetra[Ga-Ga]} and As_{110-split[As-As]} interstitial sites as a function of charge are reported in Table 3-6. Ga_{Tetra[Ga-Ga]}, is more favorable than As_{110-split[As-As]} over all charge states with lower formation energies (blue line), see Figure 3-12. Ga_{Tetra[Ga-Ga]} has the lowest formation energy at $\mu_e = 0$ with the charge $q = +1$. The most favorable As_{110-split[As-As]} also has its lowest formation energy for $q = +1$.

Overall, for intrinsic point defects in GaAs, this work found the V_{Ga}^{-3} defect has the lowest defect formation energy and will form as the Fermi level approaches the CBM. This is in agreement with experimental work by Gebauer et al.[12]. This work was also able to largely replicate the work of Freysoldt et al.[5] and employ the FNV method to calculate the correction term to remove electrostatic interactions between periodic images.

3.6 Charged Extrinsic Point Defects in Te Doped GaAs

Extrinsic Te point defects in GaAs were also simulated with charges ranging from -3 to +3. Te interstitials bonded to Ga and As (Te_{Int[Te-Ga]} and Te_{Int[Te-As]}) were simulated along

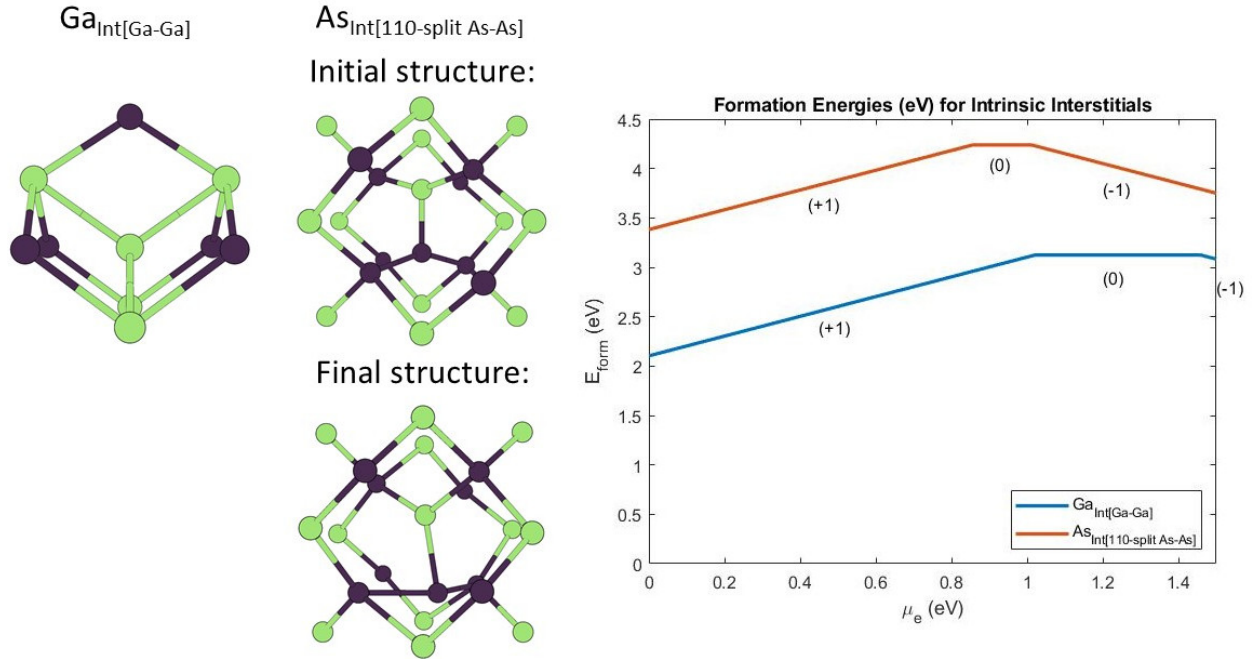


Figure 3-12. Calculated formation energies (E_{form}), as a function of the Fermi level (μ_e), for intrinsic interstitials and their initial and relaxed structures. $\text{Ga}_{Tetra}[\text{Ga}-\text{Ga}]$ is in blue and $\text{As}_{110-split}[\text{As}-\text{As}]$ in orange.

Table 3-6. Intrinsic interstitial formation energies (E_{form}) in eV for GaAs with charges (q) ranging from -3 to +3. Lowest formation energy for each defect indicated in bold print.

Defect	Charge (q)						
	-3	-2	-1	0	+1	+2	+3
$\text{Ga}_{Tetra}[\text{Ga}-\text{Ga}]$	8.426	6.364	4.583	3.124	2.104	2.497	3.218
$\text{As}_{110-split}[\text{As}-\text{As}]$	8.765	6.821	5.250	4.239	3.382	3.854	3.998

with Te atoms substituted on Ga and As sites (Te_{Ga} and Te_{As}). Table 3-7 shows the results of these calculations. The lowest neutral defect formation energy at $\mu_e = 0$ is for Te_{As} , followed by Te_{Ga} , $\text{Te}_{\text{Int}[\text{Te}-\text{As}]}$ and the highest formation energy is $\text{Te}_{\text{Int}[\text{Te}-\text{Ga}]}$. In Figure 3-13, Te_{As} has negative formation energies for $\mu_e < 0.3$, showing charge state $q = +1$ as very favorable. Figure 3-14 shows that $\text{Te}_{\text{Int}[\text{Te}-\text{Ga}]}$ has a lower formation energy than $\text{Te}_{\text{Int}[\text{Te}-\text{As}]}$ for all values of μ_e , but does not approach favorable negative formation energies. The structures show $\text{Te}_{\text{Int}[\text{Te}-\text{Ga}]}$ remains in its initial position; however, upon relaxation the $\text{Te}_{\text{Int}[\text{Te}-\text{As}]}$

interstitial leaves the tetrahedral position and bonds with a neighboring Ga atom in a dumbbell configuration.

This work has also shown agreement with Gebauer et al. [12] in that the Te_{As}^{+1} has negative formation energies, indicating its formation is favorable. The final type of defect found by Gebauer et al. is Ga vacancy-donor complex, $V_{Ga}-\text{Te}_{As}$, which is explored in Section 3.7.1.

3.7 Charged Defect Complexes in Te Doped GaAs

Freysoldt et al.'s *sxdefectalign* code [5, 32] was created to systematically calculate the energy corrections needed to compensate for interactions between periodic images of a charged point defects. In the case of defect complexes, if the anisotropy in the charge distribution isn't large it should be possible to use its average in the direction of the defect's alignment to calculate the correction energy. This will be further studied in this section by calculating the corrections for a series of double and triple defects in Te doped GaAs with charges ranging from -3 to +3, and for a few select complexes varying the distance between the defects. The formation energies of the double and triple defects are compared to the formation energies of the point defects that combine to create the complex as if they were infinitely spaced. Referred to in this work as 'infinite' distance defects, these formation energies are calculated by adding the minimum formation energies of each point defect in the complex at the specified μ_e .

3.7.1 Double Defect Complexes

Defect complexes are studied in this section starting with double defect complexes containing at least one of the point defects predicted to form, V_{Ga} or Te_{As} . The formation

Table 3-7. Extrinsic point defect formation (E_{form}), in eV, for Te doped GaAs with charges (q) ranging from -3 to +3. Lowest formation energy for each defect indicated in bold print.

Defect	Charge (q)						
	-3	-2	-1	0	+1	+2	+3
Te_{Ga}	7.278	5.294	4.552	3.232	2.318	2.419	3.033
Te_{As}	6.039	4.008	2.246	0.789	-0.265	0.165	0.957
$\text{Te}_{Int[Te-Ga]}$	10.799	8.873	7.434	6.360	5.621	5.242	5.242
$\text{Te}_{Int[Te-As]}$	9.253	7.271	5.576	4.255	3.960	4.246	4.915

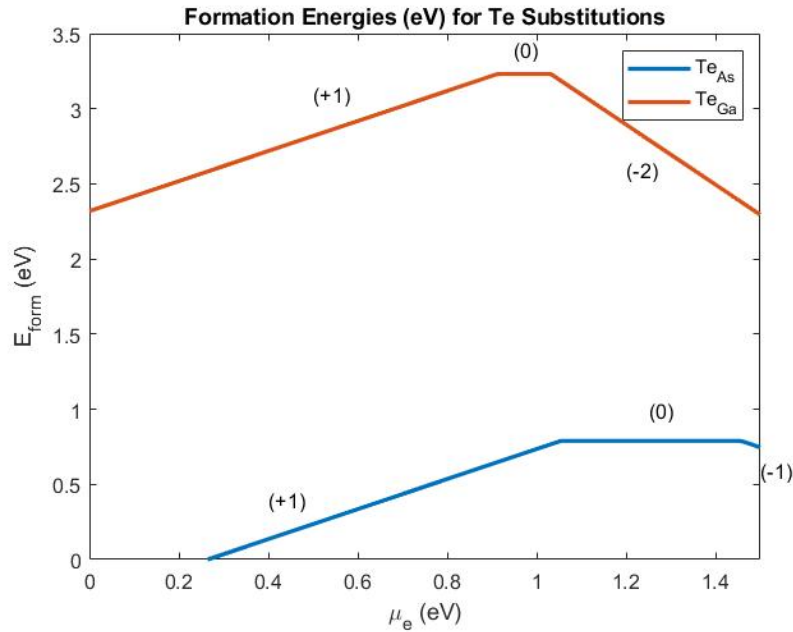


Figure 3-13. Calculated formation energies (E_{form}), as a function of the Fermi level (μ_e), for extrinsic Te substitutions. Te_{As} energies are blue and Te_{Ga} are orange.

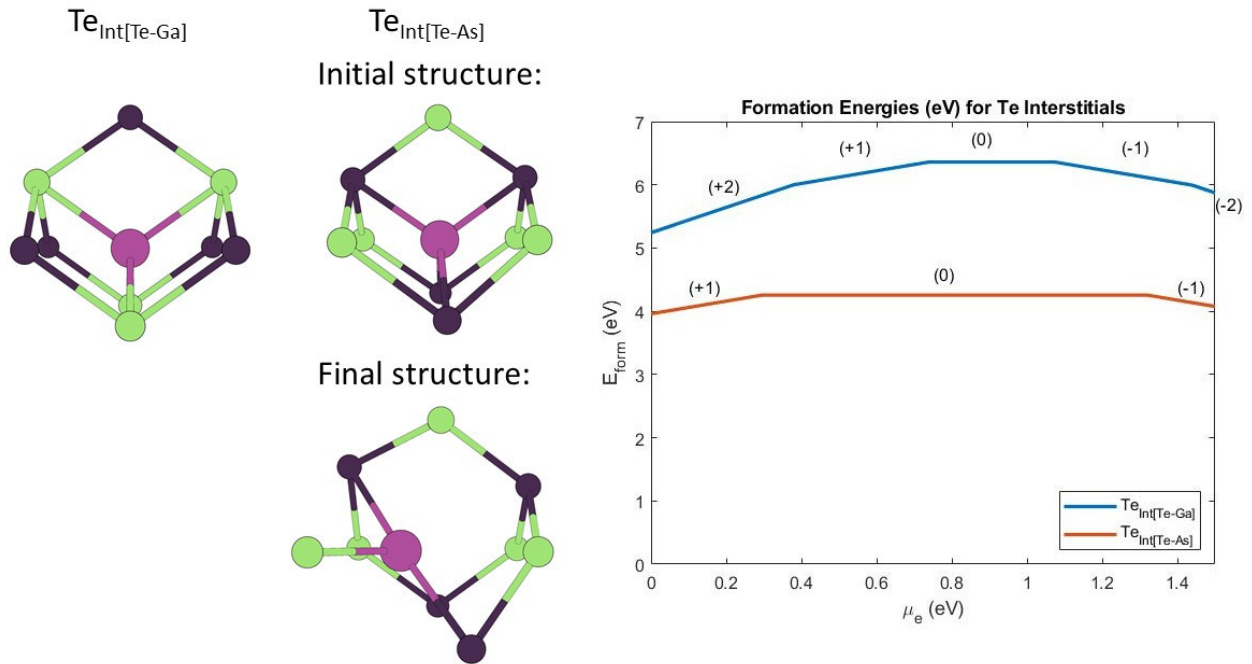


Figure 3-14. Calculated formation energies (E_{form}), as a function of the Fermi level (μ_e), for extrinsic Te interstitials and their initial and relaxed structures. $Te_{Int[Te-Ga]}$ is in blue and $Te_{Int[Te-As]}$ in orange.

energy of V_{As}^{-3} is reasonably low, 0.75 eV (Figure 3-10 center), that the defect may form under

Table 3-8. $V_{Ga}+Te_{As}$ formation energies (E_{form}) in eV for Te doped GaAs with charges (q) ranging from -3 to +3. Lowest formation energy for each defect indicated in bold print.

Distance	Charge (q)						
	-3	-2	-1	0	+1	+2	+3
2.5 Å	4.113	2.348	1.879	1.768	1.992	2.597	3.534
4.7 Å	4.700	2.929	2.422	2.283	2.475	3.023	3.914
6.1 Å	4.839	3.049	2.537	2.371	2.543	3.074	3.960
7.3 Å	4.796	3.044	2.584	2.454	2.621	3.228	4.181

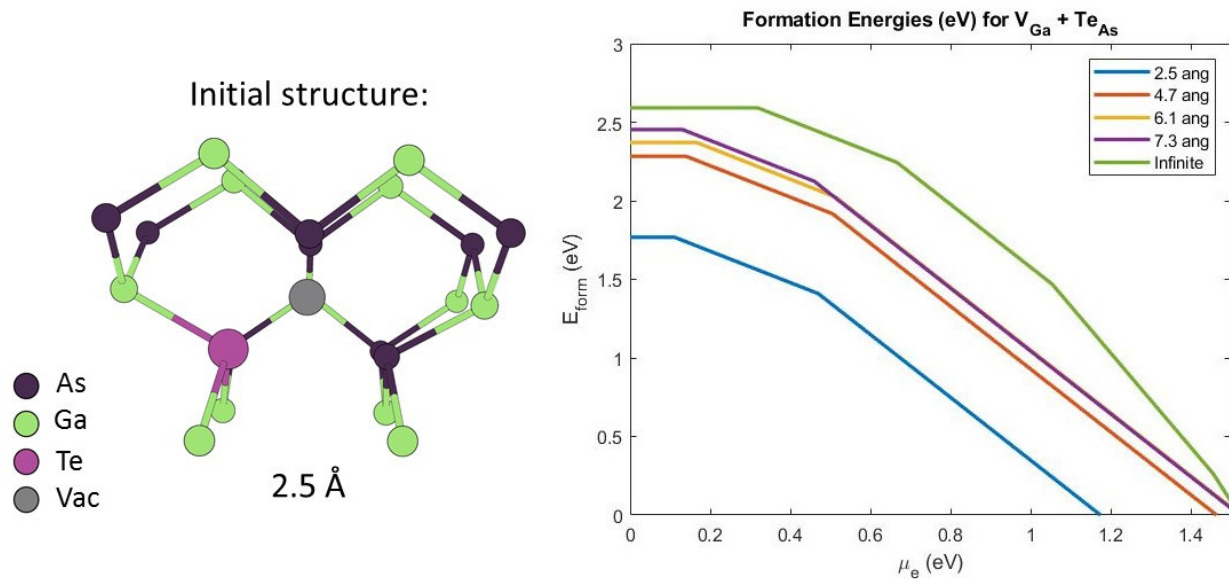


Figure 3-15. Calculated formation energies (E_{form}), as a function of the Fermi level (μ_e), for $V_{Ga}+Te_{As}$ and the initial and relaxed structure of the closest cluster configuration. Blue is for the defect complex with a distance of 2.5 Å between sites, 4.7 Å is orange, 6.1 Å is yellow, 7.3 Å is purple and green is at an infinite distance.

dopant implantation or post-heat treatment. Thus, V_{As} is simulated with a less favorable defect, Te_{Ga} , to characterize the behaviour of a defect which is expected to be unlikely to form. Finally the double- Te_{As} complex is simulated.

A Ga vacancy and a Te substituted with an As atom ($V_{Ga}+Te_{As}$) is simulated with the defects in first to forth nearest neighbor positions. Table 3-8 shows that when the defects are closer their formation is more favorable, with the first nearest neighbor position (2.5 Å, blue) having the lowest formation energies, most likely due to the opposite charges on the

Table 3-9. $V_{Ga}+Te_{Int[Te-X]}$ formation energies (E_{form}) in eV for Te doped GaAs with charges (q) ranging from -3 to +3. Te interstitial is in the tetrahedral position bonded to either As (Te-As) or Ga (Te-Ga) atoms. Lowest formation energy for each defect indicated in bold print.

Bond	Distance	Charge (q)						
		-3	-2	-1	0	+1	+2	+3
Te-Ga	2.5 Å	7.244	5.289	3.726	2.882	2.611	2.443	3.058
Te-As	2.8 Å	6.736	5.358	4.123	3.166	2.318	2.417	3.028
Te-Ga	4.7 Å	7.037	5.109	4.207	2.844	1.850	1.927	2.465
Te-As	4.9 Å	7.137	6.462	6.461	6.348	6.590	7.141	7.824
Te-Ga	6.1 Å	7.923	6.740	5.750	5.571	5.753	6.235	4.062
Te-As	6.3 Å	7.535	6.865	6.104	5.945	6.144	6.666	7.505

constituent defects attracting each other. The 2.5 Å structure is shown in Figure 3-15 and the plot shows that the formation energy of this structure becomes negative as μ_e approaches the CBM, indicating that it's likely to form with a charge $q = -2$. As the distance between the defects increases, their formation energies increase, approaching the infinite distance complex (green).

The Ga vacancy and Te interstitial ($V_{Ga}+Te_{Int[Te-X]}$) defect complex is simulated with the Te interstitial in the tetrahedral position bonded to either Ga or As atoms, and with the vacancy and interstitial in first to eighth nearest neighbor positions. Table 3-9 shows that when the defects are closer they have lower formation energies, with the third nearest neighbor position (4.7 Å) having the lowest at $q = +2$. However, there is significant relaxation of the structures from their initial configurations in almost all cases.

The initial and final structures for each distance are shown in Figures 3-16 and 3-17. The 2.5 Å, 4.7 Å and 6.1 Å structures initially have the interstitial Te bonded with Ga atoms, while the 2.8 Å, 4.9 Å and 6.3 Å structures are initially bonded to As atoms. In most cases, the Te atom moves to a final position closer to the Ga vacancy; however for the 4.7 Å structure (the third nearest neighbor) the Te substitutes onto an As site and pushes the As atom into the Ga vacancy site forming the $Te_{As}+As_{Ga}$ defect complex. Because of these relaxations, this defect complex cannot be used to observe any trends in formation energies in relation to the distance between the defects.

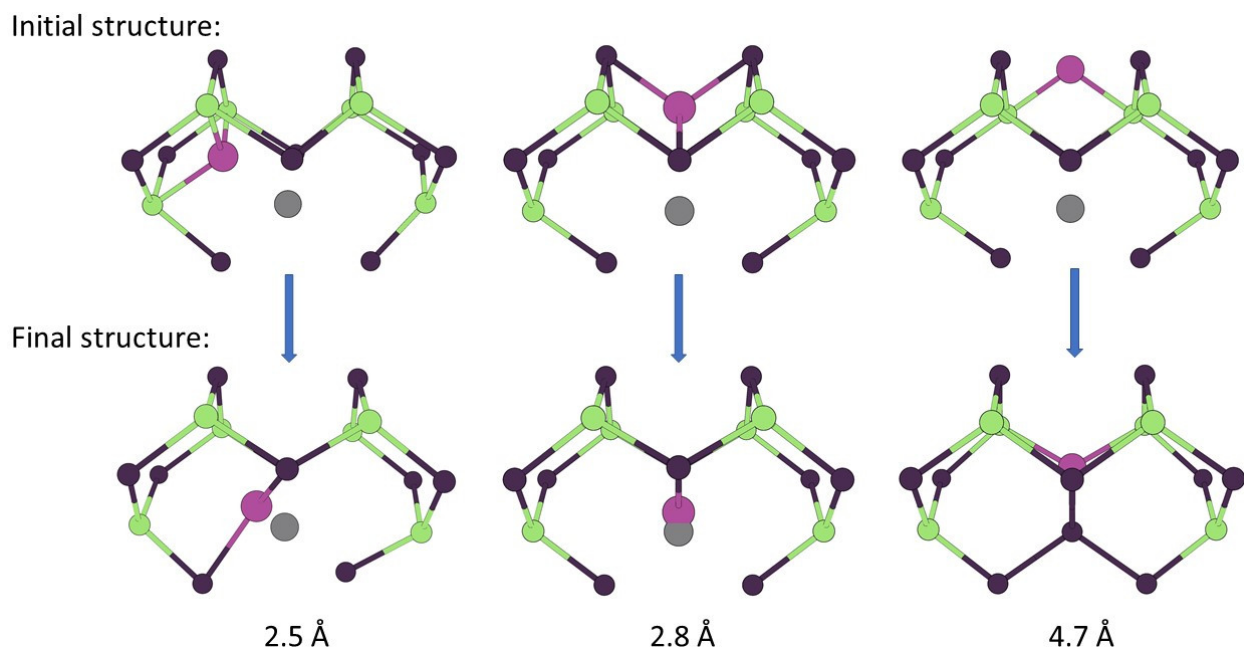


Figure 3-16. Initial and final structures of $V_{Ga} + Te_{Int[Te-X]}$ with distances between the defects of 2.5 Å 2.8 Å and 4.7 Å. In the 2.5 Å complex the Te interstitial is initially bonded to Ga atoms, in the 2.8 Å to As atoms and in 4.7 Å to Ga atoms.

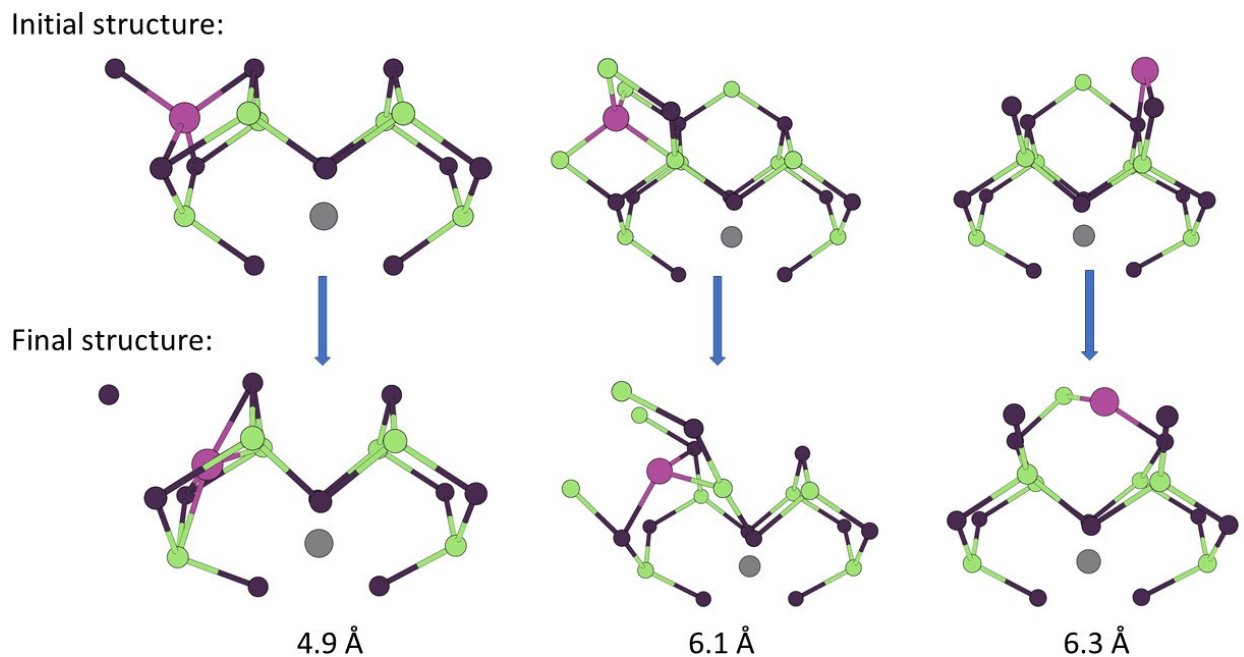


Figure 3-17. Initial and final structures of $V_{Ga} + Te_{Int[Te-X]}$ with distances between the defects of 4.9 Å 6.1 Å and 6.3 Å. In the 4.9 Å complex the Te interstitial is initially bonded to As atoms, in the 6.1 Å to Ga atoms and in 6.3 Å to As atoms.

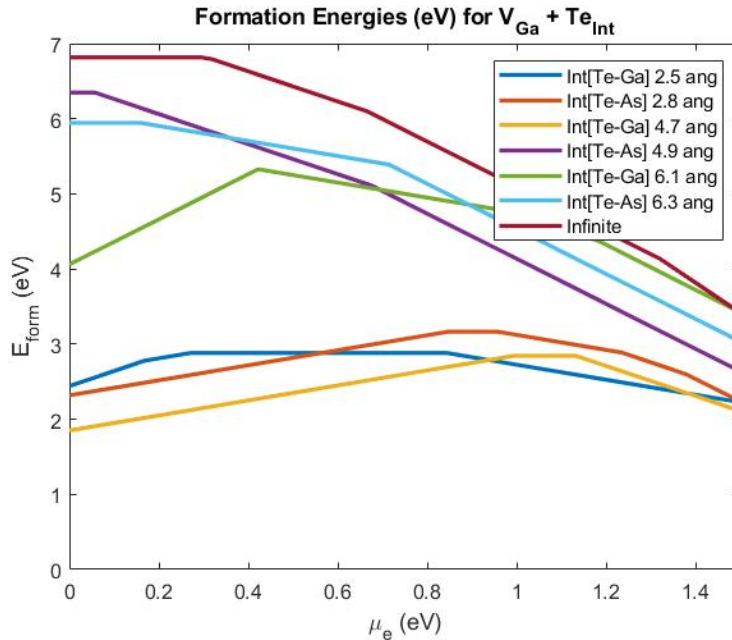


Figure 3-18. Calculated formation energies (E_{form}), as a function of the Fermi level (μ_e), for $V_{Ga} + Te_{Int[Te-X]}$. Blue is for the defect complex with a distance of 2.5 Å between the atoms, 2.8 Å is orange, 4.7 Å is yellow, 4.9 Å is purple, 6.1 Å is green, 6.3 Å is sky blue and at an infinite distance is magenta. Bonding environment for the Te interstitial is noted.

In Figure 3-18 the 4.7 Å structure has the lowest formation energy of all structures at $\mu_e = 0$ and a charge $q = +1$. There is no discernible difference between interstitials bonded to Ga or As atoms; however, the first three nearest neighbor complexes and last three are separated. This is due to the final structures of the three nearest neighbors relaxing to either fill the vacancy or having the Te atom move to a position less than 1 Å from the vacancy site. All formation energies are positive and larger than 1.9 eV or larger, suggesting these complexes are unlikely to form.

A Te substituted on an As site and a Ga interstitial bonded to As atoms ($Te_{As} + Ga_{Tetra[As-Ga]}$) is simulated in first to fourth nearest neighbor positions. Table 3-10 and Figure 3-19 show that the defect formation energies have similar trends and are generally high, indicating the defect complex is unlikely to form. It can also be seen that as the distance between the defects increases the formation energy converges on the infinite distance complex. For all distances the structure didn't differ from the initial structure upon relaxation.

Table 3-10. $\text{Te}_{\text{As}} + \text{Ga}_{\text{Tetra}[\text{Ga}-\text{As}]}$ formation energies (E_{form}) in eV for Te doped GaAs with charges (q) ranging from -3 to +3. Ga interstitial on a tetrahedral site bonded to As atoms. Lowest formation energy for each defect indicated in bold print.

Distance	Charge (q)						
	-3	-2	-1	0	+1	+2	+3
2.4 Å	9.821	7.789	6.000	4.449	3.201	2.316	2.597
4.6 Å	9.727	7.956	6.043	4.410	3.087	2.143	2.363
6.1 Å	9.951	7.839	5.979	4.395	3.124	2.235	2.438
7.2 Å	10.064	7.904	5.990	4.356	3.030	2.084	2.278

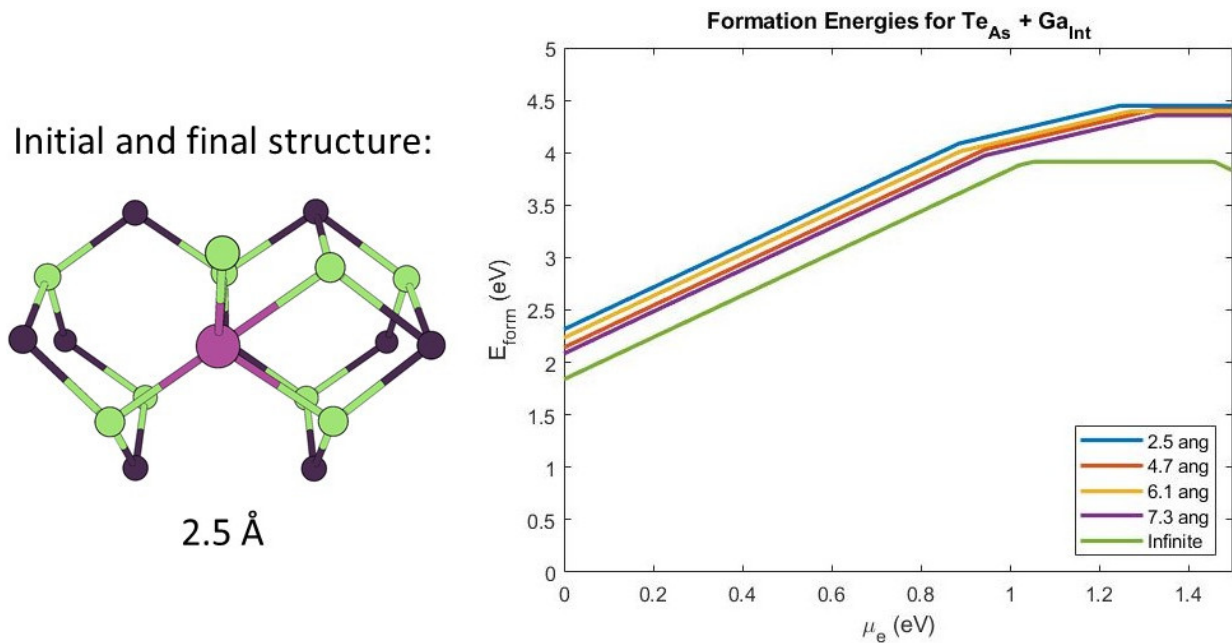


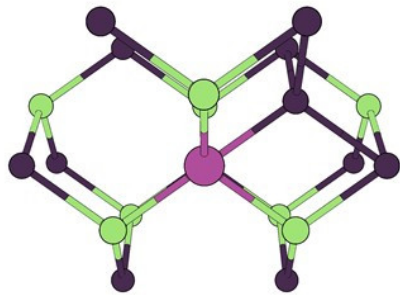
Figure 3-19. Calculated formation energies (E_{form}), as a function of the Fermi level (μ_e), for $\text{Te}_{\text{As}} + \text{Ga}_{\text{Tetra}[\text{Ga}-\text{As}]}$ and the initial and relaxed structure of the closest cluster configuration. Blue is for the defect complex with a distance of 2.5 Å between sites, 4.7 Å is orange, 6.1 Å is yellow, 7.3 Å is purple and green is at an infinite distance.

A Te substituted with an As atom and an As interstitial bonded to As atoms ($\text{Te}_{\text{As}} + \text{As}_{\text{Tetra}[\text{As}-\text{As}]}$) is simulated with the defects in nearest neighbor positions, see Figure 3-20. The As atom relaxed to a position where it bonds with a neighboring Ga atom. Table 3-11 and Figure 3-20 show that the defect formation energies are high and the formation of this complex is unfavorable at any distance as the infinite complex has similar formation energies.

Table 3-11. $\text{Te}_{\text{As}} + \text{As}_{\text{Tetra}[\text{As}-\text{As}]}$ formation energies (E_{form}) in eV for Te doped GaAs with charges (q) ranging from -3 to +3. As interstitial on a tetrahedral site bonded to As atoms. Lowest formation energy for each defect indicated in bold print.

Charge (q)						
-3	-2	-1	0	+1	+2	+3
9.925	7.978	6.314	5.014	3.985	3.196	3.744

Initial structure:



Final structure:

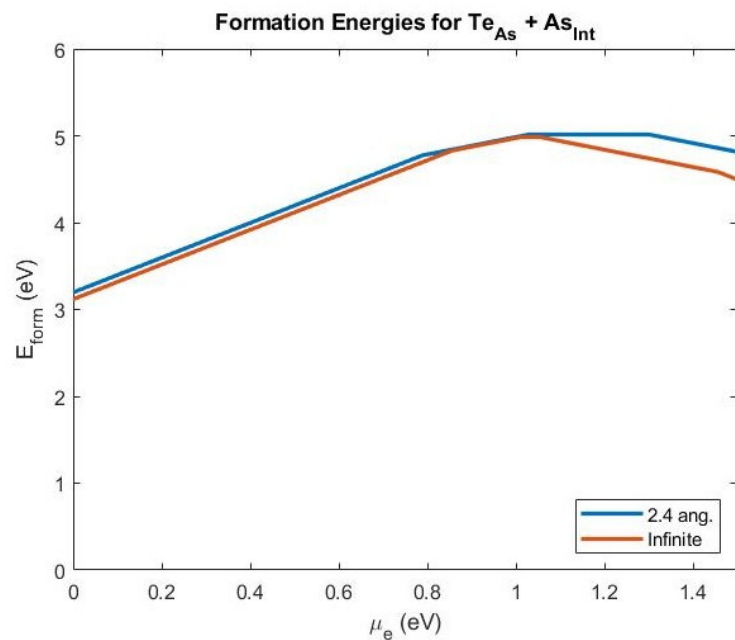
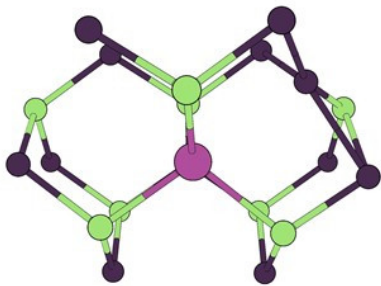


Figure 3-20. Calculated formation energies (E_{form}), as a function of the Fermi level (μ_e), for $\text{Te}_{\text{As}} + \text{As}_{\text{Tetra}[\text{As}-\text{As}]}$ and the initial and relaxed structure of the closest cluster configuration. Blue is for the defect complex with a distance of 2.4 Å between sites and orange is at an infinite distance.

A Te substituted on an As site and a Te interstitial bonded to Ga atoms

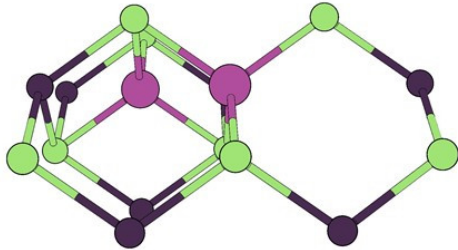
($\text{Te}_{\text{As}} + \text{Te}_{\text{Tetra}[\text{Te}-\text{Ga}]}$) is simulated with the defects in nearest neighbor positions, see Figure 3-21. The Te interstitial relaxes to a position where it can form a dumbbell with the substituted Te atom. Table 3-12 and Figure 3-21 show that the defect formation energies are high and formation of this complex is unfavorable at any distance as the infinite complex has similar formation energies.

An As vacancy and a Te substituted on a Ga site ($\text{V}_{\text{As}} + \text{Te}_{\text{Ga}}$) is simulated with the defects in first to fourth nearest neighbor positions. Table 3-13 shows that when the defects

Table 3-12. $\text{Te}_{\text{As}} + \text{Te}_{\text{Tetra}[\text{Te}-\text{Ga}]}$ formation energies (E_{form}) in eV for Te doped GaAs with charges (q) ranging from -3 to +3. Te interstitial on a tetrahedral site bonded to Ga atoms. Lowest formation energy for each defect indicated in bold print.

Charge (q)						
-3	-2	-1	0	+1	+2	+3
9.821	7.859	6.247	4.881	3.848	3.947	4.458

Initial structure:



Final structure:

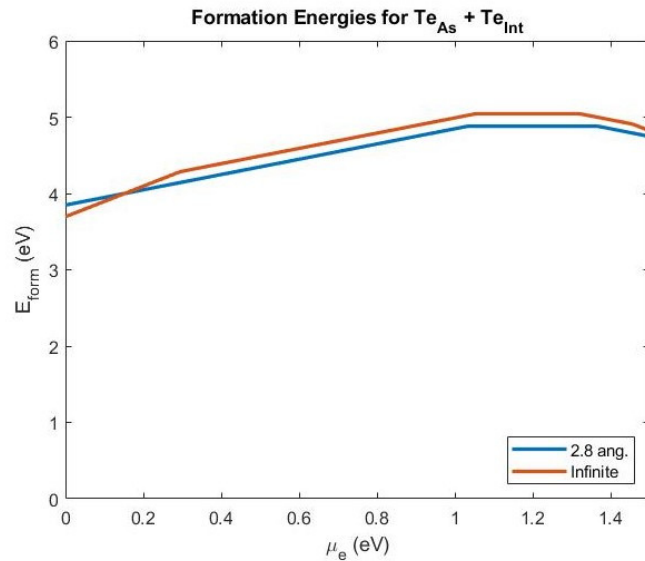
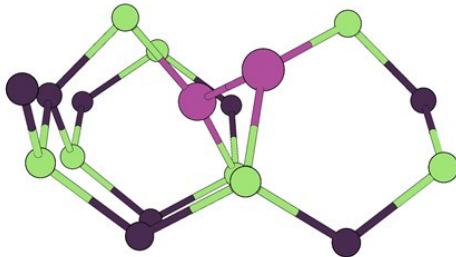


Figure 3-21. Calculated formation energies (E_{form}), as a function of the Fermi level (μ_e), for $\text{Te}_{\text{As}} + \text{Te}_{\text{Tetra}[\text{Te}-\text{Ga}]}$ and the initial and relaxed structure of the closest cluster configuration. The blue line is for the defect complex with an initial distance of 2.8 Å between sites and orange is at an infinite distance.

are in first nearest neighbor positions, 2.5 Å, the formation energy is lowest. The initial and final structures for the complexes with 2.5 Å and 6.1 Å between the defects are shown in Figure 3-22. In the 2.5 Å structure the Te atom moves into the As vacancy site, leaving a Ga vacancy. This means that the defect has relaxed into a Ga vacancy and Te substitution on an As site ($V_{\text{Ga}} + \text{Te}_{\text{As}}$), as in Figure 3-15. The plot shows that the formation energy of the 2.5 Å structure matches Figure 3-15. The defect in third nearest neighbor position, 6.1 Å, relaxed into $V_{\text{Ga}} + \text{Ga}_{\text{As}} + \text{Te}_{\text{Ga}}$. As this structure was not simulated it cannot be compared. It is unlikely to form due to high formation energies across the band gap. All other distances remain in the same configuration as their initial structure, have high defect formation energies

Table 3-13. $V_{As}+Te_{Ga}$ formation energies (E_{form}) in eV for Te doped GaAs with charges (q) ranging from -3 to +3. Lowest formation energy for each defect indicated in bold print.

Distance	Charge (q)						
	-3	-2	-1	0	+1	+2	+3
2.5 Å	4.001	2.182	1.812	1.764	2.104	2.851	3.908
4.7 Å	7.673	6.527	5.841	5.441	5.246	5.316	5.437
6.1 Å	6.845	6.244	5.355	4.765	4.849	4.432	4.970
7.3 Å	7.701	6.530	5.837	5.441	5.237	5.265	5.425

Initial structure:

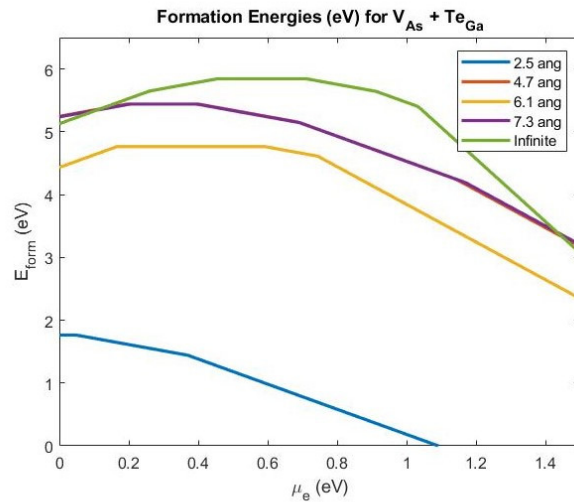
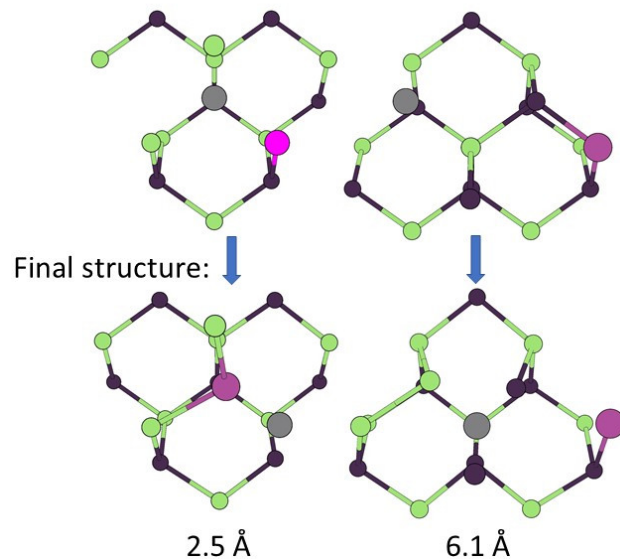


Figure 3-22. Calculated formation energies (E_{form}), as a function of the Fermi level (μ_e), for $V_{As}+Te_{Ga}$ and the initial and relaxed structure of the closest cluster configuration. Blue is for the defect complex with a distance of 2.5 Å between sites, 4.7 Å is orange, 6.1 Å is yellow, 7.3 Å is purple and green is at an infinite distance.

and are also unlikely to form. As the second and fourth nearest neighbor defects have almost matching plots, no trend as the distance between defects increases can be observed. Despite the lack of trend, they are close in magnitude to the infinite case, so it is assumed that the formation energy of this defect complex will be high regardless of the distance between the defects.

A complex consisting of two Te substitutions with As atoms ($2Te_{As}$) is simulated with Te atoms occupying first to fourth nearest neighbour positions. Table 3-14 shows that for each

Table 3-14. Two Te_{As} formation energies (E_{form}) in eV for Te doped GaAs with charges (q) ranging from -3 to +3. Lowest formation energy for each defect indicated in bold print.

Distance	Charge (q)						
	-3	-2	-1	0	1	2	3
4.7 Å	7.260	5.174	3.354	1.808	0.572	-0.268	0.371
5.6 Å	7.208	5.133	3.311	1.773	0.544	-0.291	0.340
6.8 Å	7.184	5.090	3.274	1.730	0.492	-0.348	0.312
7.9 Å	7.173	5.097	3.273	1.740	0.517	-0.314	0.327

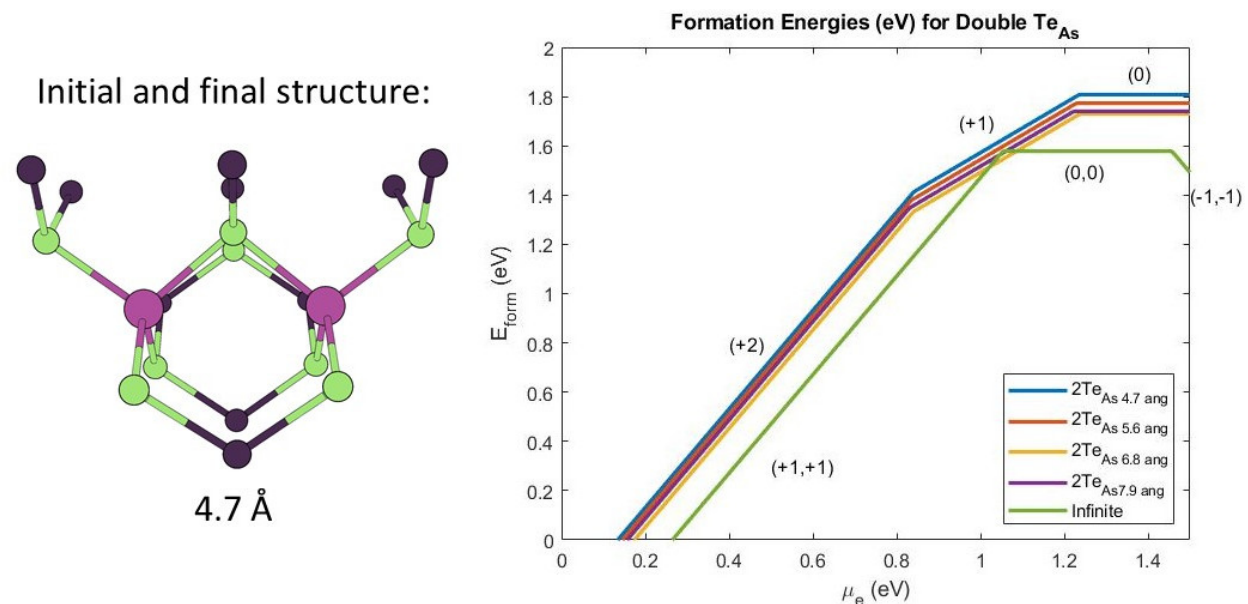


Figure 3-23. Calculated formation energies (E_{form}), as a function of the Fermi level (μ_e), for two Te_{As} and the initial and relaxed structure of the closest cluster configuration. Blue is for the defect complex with a distance of 4.7 Å between sites, 5.6 Å is orange, 6.8 Å is yellow, 7.9 Å is purple and green is at an infinite distance.

configuration the defect formation energies vary less than 0.1 eV. This same trend is also seen in Figure 3-23 with tightly packed minimum formation energy lines. Defect formation energies are expected to be highest for defects in the first nearest neighbor positions due to the positive charges of each Te ion repelling the other. However, at all distances the formation energies become negative as μ_e approaches the VBM ($\mu_e = 0$), indicating that 2Te_{As} is favorable when the systems' overall charge is $q = +2$. The lowest defect formation energy is when the defects are in the third nearest neighbor position, 6.1 Å and $q = +2$. As the distance increases between the two defects the formation energies approach that of the infinite distance defect.

From the double defect complexes simulated only $V_{Ga}+Te_{As}$ and $2Te_{As}$ defects have negative formation energies when the system has a charge $q = -2$ and $q = +2$, respectively. $[V_{Ga}+Te_{As}]^{-2}$ is in agreement with the work by Gebauer et al. [12], who observed neutral charged $V_{Ga}+Te_{As}$ complexes on the surface of their material and theorized that the defect can exist in the bulk with a $q = -2$. Additionally, this work found that the $[2Te_{As}]^{+2}$ defect complex is also a potential defect in the material. However, as $2Te_{As}$ is more favorable with larger distances between the defects, the $V_{Ga}+Te_{As}$ is expected to have a higher concentration.

3.7.2 Triple Defect Complexes

Building on Sections 3.5, 3.6 and 3.7.1, V_{Ga} , Te_{As} , $V_{Ga}-Te_{As}$ and $2Te_{As}$ are the only defects with negative formation energies. In this section, the $V_{Ga}-Te_{As}$ and $2Te_{As}$ are expanded to a triple defects by adding these point defects. A $Te_{Int[Te-Ga]}$ was also added to the $V_{Ga}-Te_{As}$, and a complex with a V_{Ga} and two $Te_{Int[Te-Ga]}$ is simulated to check that the addition of high formation energy defects also results in high formation energy defect complexes.

A Ga vacancy and two Te substitutions on As sites ($V_{Ga}+2Te_{As}$) is simulated with the defects clustered in the smallest possible radius, see Figure 3-24. In Table 3-15 the lowest defect formation energy is for the charge neutral system, with $E_{form} = 0.698$ eV, however in Figure 3-24, the formation energy becomes negative for the system with a charge $q = -1$ as the Fermi level (μ_e) approaches the CBM. If the charges for the lowest energy individual defects, V_{Ga}^{-3} and Te_{As}^{+1} , are added in the same ratio as the triple defect complex the resulting charge, $q = -1$, is in agreement with the simulated lowest energy of the complex. The defects at an infinite distance have higher defect formation energies (greater than 0.8 eV) and are unlikely to form.

Two Ga vacancies and a Te substituted on an As site ($2V_{Ga}+Te_{As}$) were simulated with the defect cluster in smallest possible radius. Table 3-16 shows that the defect formation energies calculated are large and positive (greater than 7 eV), which is also seen in the closest

Table 3-15. $V_{Ga}+2Te_{As}$ formation energies (E_{form}) in eV for Te doped GaAs with charges (q) ranging from -3 to +3. Lowest formation energy for each defect indicated in bold print.

			Charge (q)			
-3	-2	-1	0	+1	+2	+3
4.311	2.398	0.871	0.698	0.904	1.451	2.343

Initial and final structure:

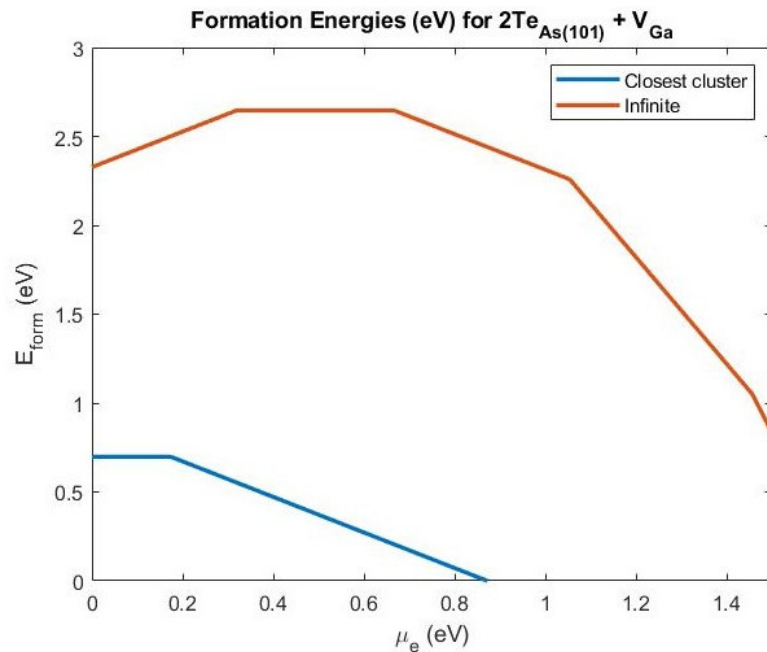
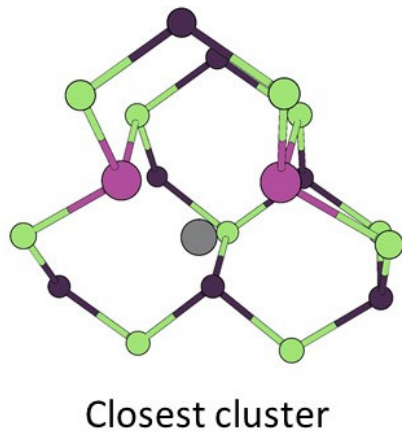


Figure 3-24. Calculated formation energies (E_{form}), as a function of the Fermi level (μ_e), for $V_{Ga}+2Te_{As}$. The blue line is for the defect complex with the closest distance between sites (pictured) and orange is for the defects at an infinite distance.

cluster calculations in Figure 3-25, indicating the defect is unfavorable. However, when the defects are at an infinite distance, the formation energy becomes negative as μ_e approaches the CBM for the system with a charge $q = -7$. This highlights an issue with the addition of point defect formation energies to find the formation energies of a complex at infinite distance; a charge state of $q = -7$ is not physical. The charges of the lowest energy individual defects add to $q = -5$. To create a charge state of $q = -7$, electrons would have to be stripped from other atoms, which is very unlikely. So, despite the infinite-spaced cluster having a near negative formation energy, this state is not physical and overall the complex is not expected to form.

Table 3-16. $2V_{Ga}+Te_{As}$ formation energies (E_{form}) in eV for Te doped GaAs with charges (q) ranging from -3 to +3. Lowest formation energy for each defect indicated in bold print.

Charge (q)						
-3	-2	-1	0	+1	+2	+3
8.454	7.857	7.339	7.643	7.990	8.122	9.046

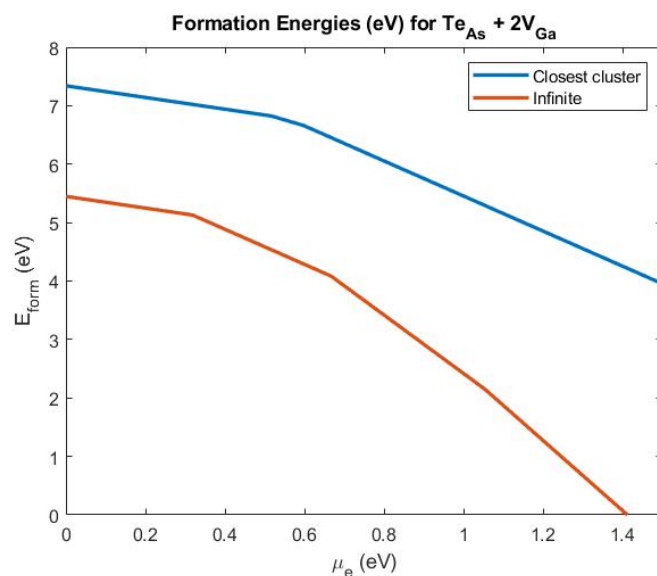


Figure 3-25. Calculated formation energies (E_{form}), as a function of the Fermi level (μ_e), for $2V_{Ga}+Te_{As}$. The blue line is for the defect complex with the closest distance between sites and orange is for the defects at an infinite distance.

A Ga vacancy and two Te interstitials bonded to Ga atoms ($V_{Ga}+2Te_{Int[Te-Ga]}$) was simulated with the defects clustered in the smallest possible radius. Table 3-17 shows that the defect formation energy is large and positive for all charges investigated, as expected from combining two high formation energy defects, Te_{Int} , with V_{Ga} . In Figure 3-26, formation energies remain positive regardless of distance between defects and the complex is unfavorable.

Table 3-17. Formation energies (E_{form}) in eV for $V_{Ga}+2Te_{Int[Te-Ga]}$ in Te doped GaAs with charges (q) ranging from -3 to +3. Te interstitials sit on tetrahedral sites bonded to Ga atoms. Lowest formation energy for each defect indicated in bold print.

Charge (q)						
-3	-2	-1	0	+1	+2	+3
9.680	7.658	6.027	5.427	4.569	4.539	4.871

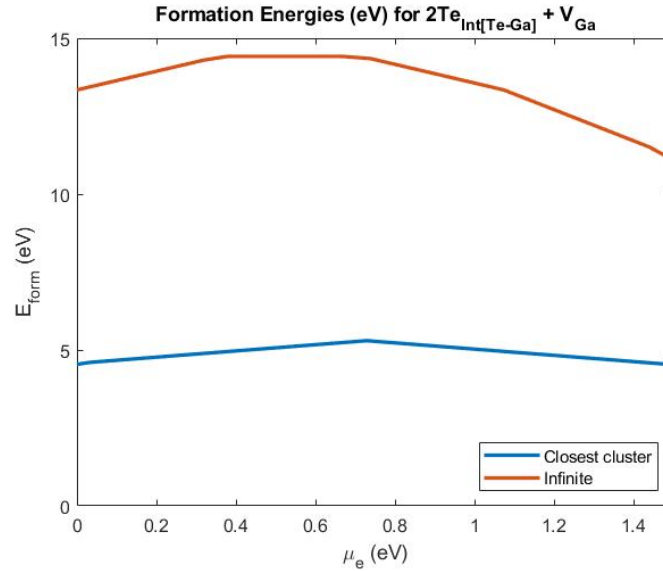


Figure 3-26. Calculated formation energies (E_{form}), as a function of the Fermi level (μ_e), for $V_{Ga}+2Te_{Int[Te-Ga]}$. The blue line is for the defect complex with the closest distance between sites and orange is for the defects at an infinite distance.

A Ga vacancy, Te substituted on an As site and a Te interstitial bonded to a Ga atoms ($V_{Ga}+Te_{As}+Te_{Int[Te-Ga]}$) is simulated with the Te atoms in first to third nearest neighbor positions. Table 3-18 shows that the Te atoms in the third nearest neighbor position, 5.9 Å, with a system charge of $q = +2$ have the lowest defect formation energy (1.83 eV) for μ_e at the VBM. Figure 3-27 shows that this defect complex will always have a positive formation energy, regardless of distance, and is not favorable.

Of the double and triple defect complexes simulated, the $V_{Ga}+Te_{As}$, $2Te_{As}$ and $V_{Ga}+2Te_{As}$ complexes were found to have negative formation energies and are expected to form in GaAs. $V_{Ga}+Te_{As}$ has a negative formation energy with a charge $q = -2$ over the

Table 3-18. Formation energies (E_{form}) in eV for $V_{Ga}+Te_{As}+Te_{Int[Te-Ga]}$ in Te doped GaAs with charges (q) ranging from -3 to +3. Lowest formation energy for each defect indicated in bold print.

Distance	Charge (q)						
	-3	-2	-1	0	+1	+2	+3
2.6 Å	6.569	5.854	4.235	2.998	2.656	2.346	2.968
4.4 Å	7.746	5.697	3.971	2.648	2.124	2.095	2.804
5.9 Å	7.185	5.504	4.493	3.363	2.706	1.825	2.277

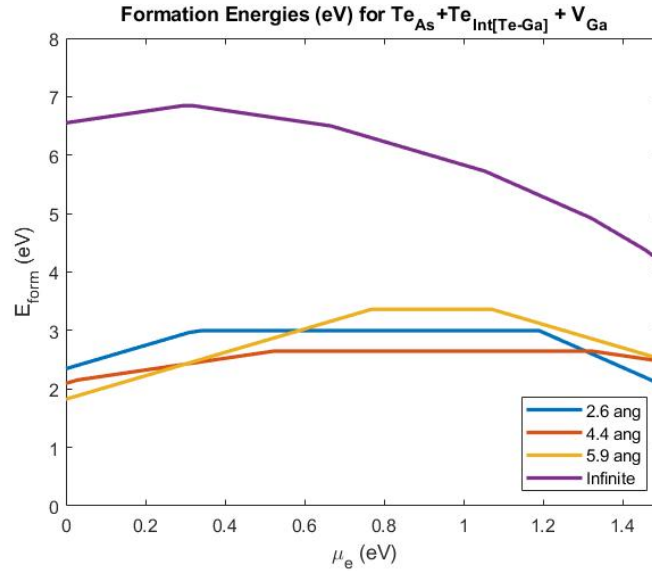


Figure 3-27. Calculated formation energies (E_{form}), as a function of the Fermi level (μ_e), for $V_{Ga} + Te_{As} + Te_{Int[Te-Ga]}$. Blue is for the defect complex with a distance of 2.6 Å between Te atoms, 4.4 Å is orange, 5.9 Å is yellow and at an infinite distance is purple.

whole system when it is in nearest neighbor configuration and the Fermi level is near the CBM. $2Te_{As}$ has a negative defect formation energy with a charge $q = +2$ over the system when the defects are spaced further apart from each other and the Fermi level is near the VBM. $V_{Ga} + 2Te_{As}$ also has a negative defect formation energy with a charge $q = -1$ over the system when the defects are in the closest cluster formation and the Fermi level is near the CBM.

3.8 Discussion of Defect Formation in Te Doped GaAs

The defect formation energies for intrinsic and extrinsic point defects, double defect complexes and triple defect complexes in Te-doped GaAs have been investigated in a systematic manner in Sections 3.5, 3.6, 3.7.1 and 3.7.2. A summary of the lowest formation energies and charge states for the most likely defects, V_{Ga} , Te_{As} , $V_{Ga} + Te_{As}$, $2Te_{As}$ and $V_{Ga} + 2Te_{As}$, is given in Table 3-19. To illustrate Fermi level (μ_e) shift with an excess or dearth of electrons the formation energies for the $\mu_e = VBM$ (dearth) and $\mu_e = CBM$ (excess) are given. However, although the experimental band gap (1.5 eV) was used to generate the formation energy vs. Fermi level plots and calculate the formation energies at $\mu_e = 1.5$ eV,

Table 3-19. Summary of formation energies (E_{form}) and charge states for the most favorable defects in Te-doped GaAs. Lowest formation energy and charge state for each defect is reported for the Fermi level (μ_e) at the VBM and CBM.

Defect	$\mu_e = VBM$		$\mu_e = CBM$	
	Charge (q)	E_{form} (eV)	Charge (q)	E_{form} (eV)
V_{Ga}	-1	2.90	-3	-0.64
Te_{As}	+1	-0.27	-1	1.50
$V_{Ga}+Te_{As}$	0	1.77	-2	-0.64
$2Te_{As}$	+2	-0.34	0	1.74
$V_{Ga}+2Te_{As}$	0	0.70	-1	-0.62

the band gap calculated with the LDA exchange correlation was 0.95 eV. It is not clear at this point in time how the levels should be transformed to approximate the experimental band gap. As such, the formation energies or charge states of defects at the CBM are expected to change, potentially becoming more positive in both cases.

As the results have not been transformed to reflect the experimental band gap, conclusions about defect st abilities as μ_e approaches the CBM can only be taken as indications of what is expected to occur in the physical system. Te is a donor atom and doping GaAs with Te is expected to add electrons to donor levels just below the conduction band (CB), shifting the Fermi level towards the CB. It is assumed that the formation energies calculated with μ_e approaching the CBM are expected to reflect the physical system.

Overall, the defects with the lowest formation energies are V_{Ga} with a charge of -3, and $V_{Ga}+Te_{As}$ with a system charge of -2, and formation energies of -0.64 eV. Negative charges indicates there are excess electrons, which shift the Fermi energy closer to the CBM. Since the formation energies are negative, these defect complex is expected to form with a high concentration. The next lowest formation energy is for $V_{Ga}+2Te_{As}$, charge -1 with the Fermi level near the CBM. $2Te_{As}$, with a +2 charge on the system, is next with a formation energy of -0.34 eV with the Fermi level near the VBM. The positive charge indicates the presence of a hole in the band levels just above the valence band, shifting the Fermi energy closer to the VBM. The last negative formation energy is for Te_{As} , which is -0.27 eV for a charge of +1 and

Table 3-20. Transition levels ($\epsilon(q_a/q_b)$) in eV for five most likely defects in Te doped GaAs defects.

Defect	Charge (q)					
	(+3/+2)	(+2/+1)	(+1/0)	(0/-1)	(-1/-2)	(-2/-3)
V_{Ga}	-	-	-	-0.03	0.32	0.67
Te_{As}	-	-	1.05	1.46	-	-
$V_{Ga} + Te_{As}$	-	-	-	0.11	0.47	-
$2Te_{As}$	-	0.84	1.24	1.54	-	-
$V_{Ga} + 2Te_{As}$	-	-	-	0.17	1.53	-

the Fermi level near the VBM. The small difference between these formation energies may be within the uncertainty from the DFT calculations or the correction energy terms.

A more robust method for examining the stability of the defects relative to each other than directly comparing formation energies is to calculate the transition levels, see Equation 2-22. The transition levels for the five favorable defects are reported in Table 3-20. Any transition levels that fall outside of the band gap have been removed, however the full data is reported in Table A-3 in Appendix A.

According to Freysoldt et al. [22], shallow defects occur within a few $k_B T$ of the VB or CB, and deep defects occur near the middle of the band gap. Due to the uncertainty in the transformation of the computed band gap to the experimental band gap, only shallow donor transitions can be attested from Table 3-20. These include $\epsilon(0/ - 1)$ for the V_{Ga} defect, at μ_e -0.03 eV, $\epsilon(0/ - 1)$ for the $V_{Ga} + Te_{As}$ defect, at μ_e 0.11 eV, and possibly $\epsilon(0/ - 1)$ for the $V_{Ga} + 2Te_{As}$ defect, at μ_e 0.17 eV. Additionally, if the Fermi level in the material is below $\epsilon(q_a/q_b)$, then charge states with q_a are more stable, and if it is above then charge states with q_b are more stable. From this statement, if the Fermi level approaches the VB, V_{Ga}^0 , $[V_{Ga} + Te_{As}]^0$ and $[V_{Ga} + 2Te_{As}]^0$ are expected to be stable defects. As the Fermi level approaches the experimental band gap (CB), V_{Ga}^{-3} , Te_{As}^{-1} , $[V_{Ga} + Te_{As}]^{-2}$, $[2Te_{As}]^{-1}$ and $[V_{Ga} + 2Te_{As}]^{-2}$ are expected to be more stable.

From Table 3-19 and the equation for defect concentration in the dilute limit, Equation 3-1, if the temperature is held constant a general understanding of the defect concentrations with respect to the Fermi level shift can be made. Equation 3-1 is used to approximate the

Table 3-21. Defect concentrations for the Fermi level at the VBM and CBM. c_i^0 is the density of lattice sites available to the defect in cm^{-3} , and c_D is the defect concentration at $T=800$ K in cm^{-3} .

Defect	c_i^0 ($\times 10^{22}$ cm^{-3})	c_D (cm^{-3})	
		VBM	CBM
V_{Ga}	2.22	11910	$> 2 \times 10^{20}$
Te_{As}	2.22	$> 2 \times 10^{20}$	7.87×10^{12}
$V_{Ga} + Te_{As}$	2.22	1.6×10^{11}	$> 2 \times 10^{20}$
$2Te_{As}$	1.11	$> 2 \times 10^{20}$	1.21×10^{11}
$V_{Ga} + 2Te_{As}$	1.11	4.31×10^{17}	$> 2 \times 10^{20}$

dilute limit defect concentrations in equilibrium (c_D) with respect to the temperature of the system [74–77]. It can be used up to the melting temperature of the material, after which the concentration would exhibit non-Arrhenius behavior[22, 78]. c_i^0 is the density of the lattice sites available to the defect/s, E_{form} is the defect energy of formation from DFT, k_b is the Boltzmann constant (8.617×10^{-5} eV/K) and T is the temperature (in K). By holding the temperature constant and calculating the concentrations for the defect formation energies with the Fermi level at the VBM and CBM, the effect of the Fermi level shift on the defect concentration trends can be observed.

$$c_D = c_i^0 \exp[-E_{form}/k_b T] \quad (3-1)$$

The density of the lattice sites available to the defects, c_i^0 , is calculated as the total number of lattice sites the defect can occupy in a unit cell divided by the volume of the unit cell. For example, the total number of atomic sites in a unit cell of GaAs is eight, four Ga and four As. The total density of sites, not including interstitials, is $8/(5.65 \times 10^{-8} \text{ cm})^3 = 4.44 \times 10^{22} \text{ cm}^{-3}$. As there are only four Ga sites, the numerator becomes 4 when calculating c_i^0 for V_{Ga} . Similarly, Te can only substitute with the four As atoms, there can only be a maximum of four $V_{Ga} + Te_{As}$ defects in a unit cell, two $2Te_{As}$ or two $V_{Ga} + 2Te_{As}$. The c_i^0 and defect concentrations for these defects are reported in Table 3-21 for $T = 800$ K, which is the approximate temperature Kennon et al.[55] grew their material.

From Table 3-21, the concentration of V_{Ga} , $V_{Ga}+Te_{As}$ and $V_{Ga}+2Te_{As}$ defects increases as the Fermi level shifts towards the CBM. Conversely, the concentration of Te_{As} and $2Te_{As}$ decreases. Note, the calculated c_D for V_{Ga} , $V_{Ga}+Te_{As}$ and $V_{Ga}+2Te_{As}$ at the CBM would exceed the total density of sites ($4.44 \times 10^{22} \text{ cm}^{-3}$), which is physically impossible. Similarly, Te_{As} and $2Te_{As}$ would exceed the total density of sites at the VBM. This is due to the assumption that formation energy is independent of concentration. This work also does not take into consideration the law of mass action. As such, values in Table 3-21 are approximations made for general trend observations. After growth of the doped semiconductor the number of Te, Ga and As atoms in the material remain fixed. Since the concentration of single and double Te_{As} defects decreases and the concentration of $V_{Ga}+Te_{As}$ and $V_{Ga}+2Te_{As}$ complexes increases as the Fermi level shifts to toward the CBM it is concluded that Te_{As} are combining with V_{Ga} to form complexes. This is possibly the source of the electrical deactivation observed by Kennon et al. as the favorable charge states of $V_{Ga}+Te_{As}$ and $V_{Ga}+2Te_{As}$ are $q = -2$ as the Fermi level approaches the CB, decreasing the number Te_{As}^{-1} and $[2Te_{As}]^{-1}$ defects in the system and in addition to decreasing the number of electrons available, and thus decreasing the activation of the semiconductor. This supports the work by Kennon et al., who theorized that Te-point defect reactions are the likely cause of the observed electrical deactivation.

In addition to the defect energetics, it was observed that the 'infinite' distance defect formation energies, which were calculated by adding the minimum formation energies of each point defect in the complex, can be used in conjunction with the nearest neighbor complex formation energy to establish boundaries on the defect formation energies. Generally, when the defect complexes didn't relax to another structure, the defect formation energies converged on the infinite case as the distance between the defects increased. However, care must be taken with the infinite distance defect, as unrealistic charge states can be calculated as in $Te_{As}+2V_{Ga}$. This method allows for the trends in the formation energies of a complex to

be estimated from the charged point defects before the charge states of the complex are calculated.

3.9 Correction Energies

All correction energies (E_{corr}), calculated with the *sxdefectalign* code, are reported in the Appendix A, Table A-2. Figures 3-28 to 3-36 show the correction energies as a function of defect charge (q). To observe patterns, the data points are fitted to quadratic functions, indicated on each figure as the corresponding color lines.

Intrinsic defect correction energies are plotted in Figure 3-28. The correction energies for both types of defects, vacancies and interstitials, follow the same trend with the vertex of the vacancies between the neutral charge and $q = +1$, and for interstitials between the neutral charge and $q = -1$. In the systems with more As atoms than Ga atoms the correction energies are larger.

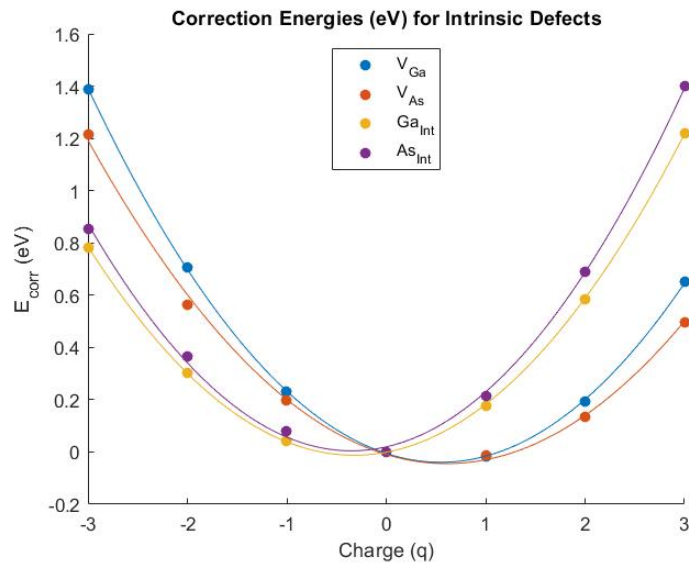


Figure 3-28. Correction energies (E_{corr}) for intrinsic vacancies as a function of defect charge (q). V_{Ga} correction energies are blue, V_{As} are orange, $Ga_{Int[Ga-Ga]}$ are yellow and $As_{Int[110-split\ As-As]}$ are purple.

The correction energies for extrinsic defects are plotted in Figure 3-29. Similar trends are observed for all defects with the formation energy vertexes between the neutral charge

and $q = -1$. Generally, the formation energies are higher for extrinsic interstitials than substitutions.

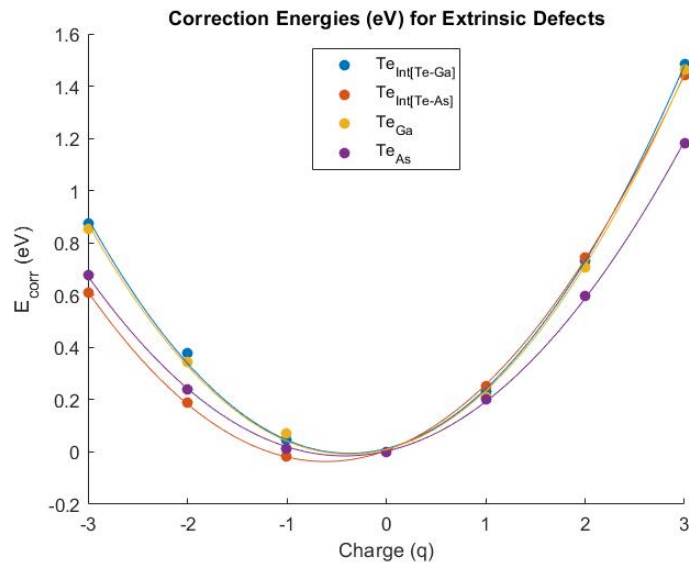


Figure 3-29. Correction energies (E_{corr}) for extrinsic defects as a function of defect charge (q). $Te_{Int[Te-Ga]}$ is in blue, $Te_{Int[Te-As]}$ is in orange, Te_{Ga} is in yellow, and Te_{As} in purple.

The calculated correction energies for $V_{Ga}+Te_{As}$ are plotted in Figure 3-30. Additionally, the corrections for the constituent defects, V_{Ga} and Te_{As} , are also plotted. As the distances between the defects changes there is a small spread of the energy correction terms, approximately 0.2 eV. Overall, the behaviour of the energy corrections for the complex are closer to that of V_{Ga} , but fall between the corrections for V_{Ga} and Te_{As} .

The calculated correction energies for all $V_{Ga}+Te_{Int}$ defects are plotted in Figure 3-31, however, as there was significant differences in the relaxed structures no conclusions about trends of these correction energies can be made.

The calculated correction energies for $Te_{As}+$ various interstitials are plotted in Figure 3-32. Similar to $V_{Ga}+Te_{As}$, as the distances between the defects changes the energy correction terms show a spread of approximately 0.2 eV. No trend can be observed in regards to the interstitial atomic species.

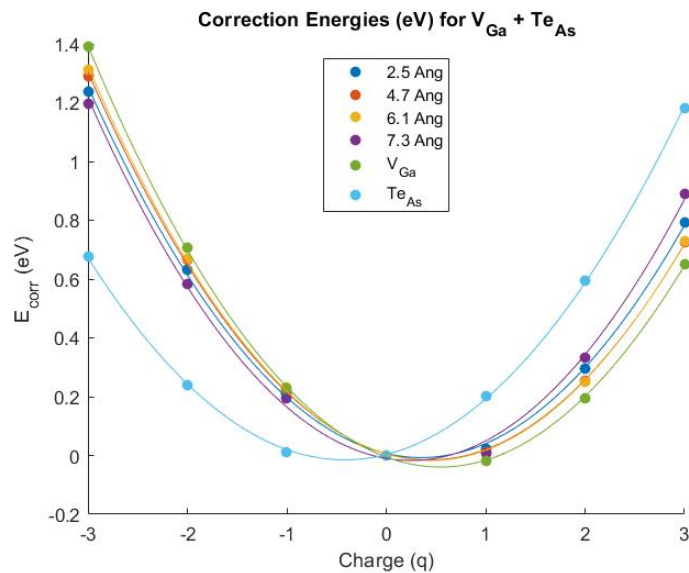


Figure 3-30. Correction energies (E_{corr}) for $V_{Ga}+Te_{As}$ as a function of charge (q). Blue is for the defect complex with a distance of 2.5 Å between sites, 4.7 Å is orange, 6.1 Å is yellow, and 7.3 Å is purple. E_{corr} for V_{Ga} is in green and Te_{As} is in cyan.

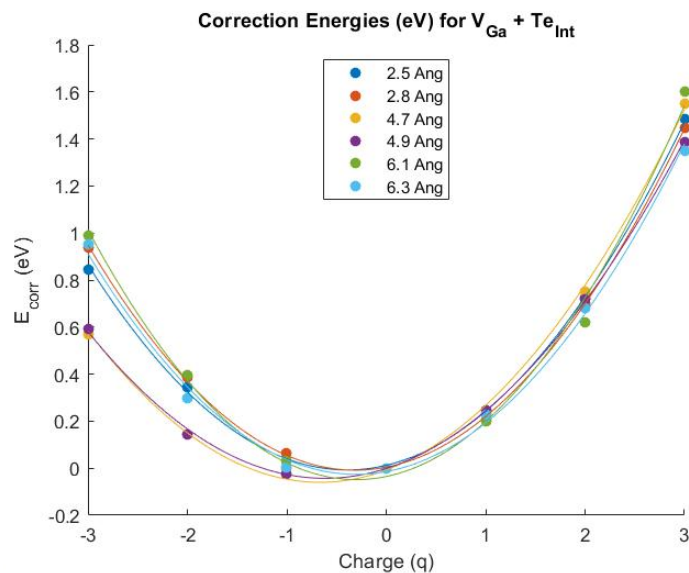


Figure 3-31. Correction energies (E_{corr}) for $V_{Ga}+Te_{Int}$ as a function of charge (q). Blue is for the defect complex with a distance of 2.5 Å between sites, 2.8 Å is orange, 4.7 Å is yellow, 4.9 Å is purple, 6.1 Å is green, and 6.3 Å is cyan.

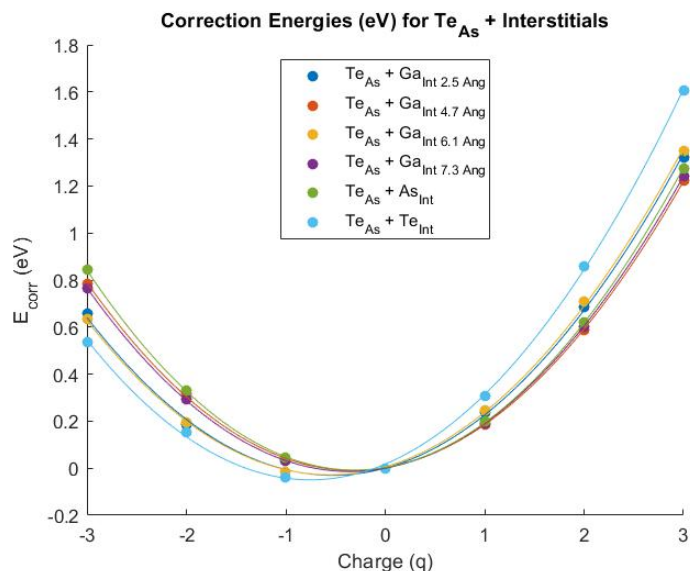


Figure 3-32. Correction energies (E_{corr}) for Te_{As} +interstitials as a function of charge (q). $\text{Ga}_{Tetra[Ga-As]}$ interstitials range in distance to the Te_{As} atom, where 2.5 Å is in blue, 4.7 Å is orange, 6.1 Å is yellow, and 7.3 Å is purple. The $\text{As}_{Tetra[As-As]}$ is green and the $\text{Te}_{Tetra[Te-Ga]}$ is cyan.

The calculated correction energies for $\text{V}_{As}+\text{Te}_{Ga}$ are plotted in Figure 3-33. As with $\text{V}_{Ga}+\text{Te}_{Int}$, as the relaxed structures had significant differences to the initial structures no conclusions about these energy corrections can be made.

The calculated correction energies for two Te_{As} are plotted in Figure 3-34. Additionally, the corrections for the single Te_{As} is plotted. The correction energies do not show a spread as the distance between the defects changes, but instead are near equal. Interestingly, the correction energy vertices of the double defects shift left to occur closer to the $q = -1$ charge state, with the correction energies lower than that of the single defect for charge negative states and higher for charge positive states.

All triple defect complex correction energies are plotted in Figures 3-35 and 3-36. Figure 3-36 also shows the corrections for the constituent defects, Te_{As} , $\text{Te}_{Int[Te-Ga]}$ and V_{Ga} . The correction energies for $\text{Te}_{As}+\text{Te}_{Int[Te-Ga]}+\text{V}_{Ga}$ show the same spread of approximately 0.2 eV for the defects with different distances between them. Unlike $\text{V}_{Ga}+\text{Te}_{As}$, the correction

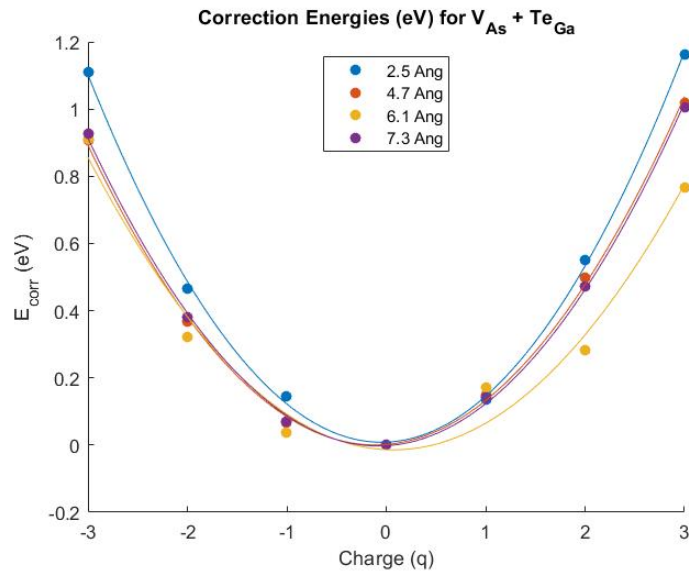


Figure 3-33. Correction energies (E_{corr}) for $V_{As} + Te_{Ga}$ as a function of charge (q). Blue is for the defect complex with a distance of 2.5 Å between sites, 4.7 Å is orange, 6.1 Å is yellow and 7.3 Å is purple.

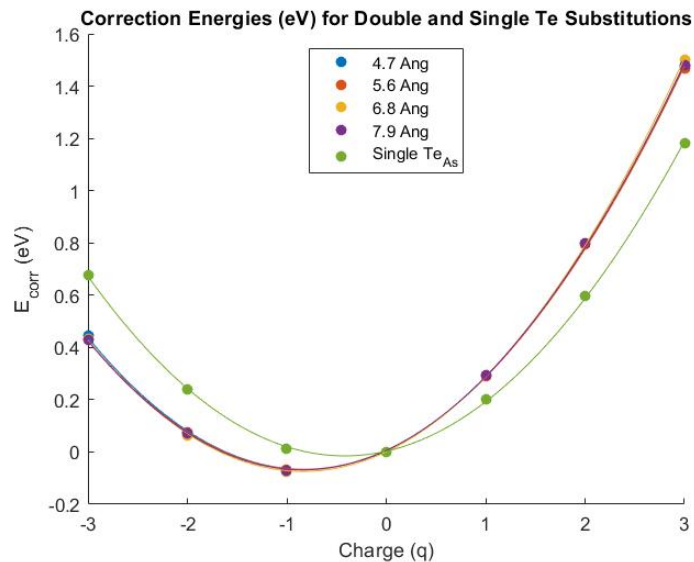


Figure 3-34. Correction energies (E_{corr}) for two Te_{As} as a function of charge (q). Blue is for the defect complex with a distance of 4.7 Å between sites, 5.6 Å is orange, 6.8 Å is yellow and 7.9 Å is purple. The single Te_{As} defect is green.

energies for $e_{As} + Te_{Int[Te-Ga]} + V_{Ga}$ do not fall between the correction energies of the individual constituent defects.

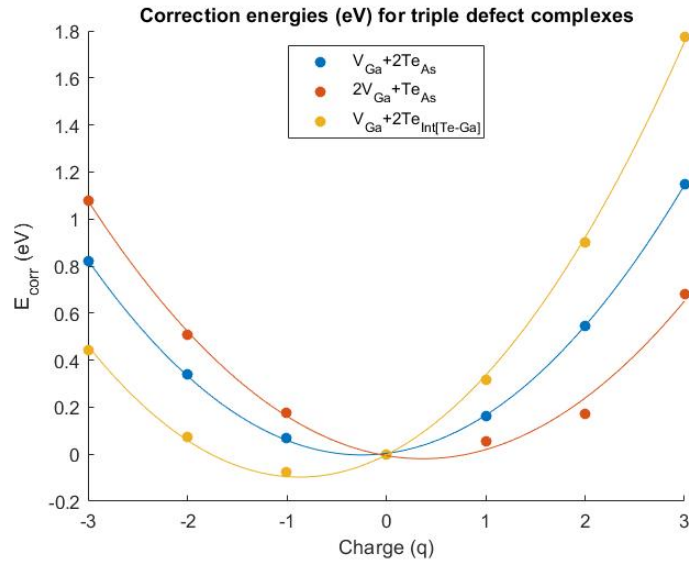


Figure 3-35. Calculated correction energies for triple defect complexes in Te doped GaAs as a function of defect charge (q). $V_{Ga} + 2Te_{As}$ is indicated by blue, $2V_{Ga} + Te_{As}$ by orange and $V_{Ga} + 2Te_{Int[Te-Ga]}$ by yellow. Data points are fit to quadratic functions to generate the lines.

In summary, the only trend observe in the correction energy terms is that regardless of the distance between distances, the calculated correction energies will be very similar for each charge state. The correction energies will either be near equal, as in $V_{As} + Te_{Ga}$ or $2Te_{As}$, or have a spread less than or equal to 0.2 eV, such as $V_{Ga} + Te_{As}$, $V_{Ga} + Te_{Int}$, $Te_{As} + Int_X$ or $Te_{As} + Te_{Int[Te-Ga]} + V_{Ga}$.

3.10 Conclusions

The charged defect energetics of Te-doped GaAs are relevant to developing an understanding of the mechanisms behind electrical deactivation. The Ga vacancy with a charge $q = -3$ (V_{Ga}^{-3}), the Te substitution on As with a charge $q = +1$ (Te_{As}^{+1}), the Ga vacancy-donor complex ($V_{Ga} + Te_{As}$) with a charge $q = -2$ over the system, the double Te substitution on As ($2Te_{As}$) with a charge $q = +2$ over the system, and the Ga-vacancy-double donor complex ($V_{Ga} + 2Te_{As}$) with a charge $q = -1$ over the system found to have negative formation energies

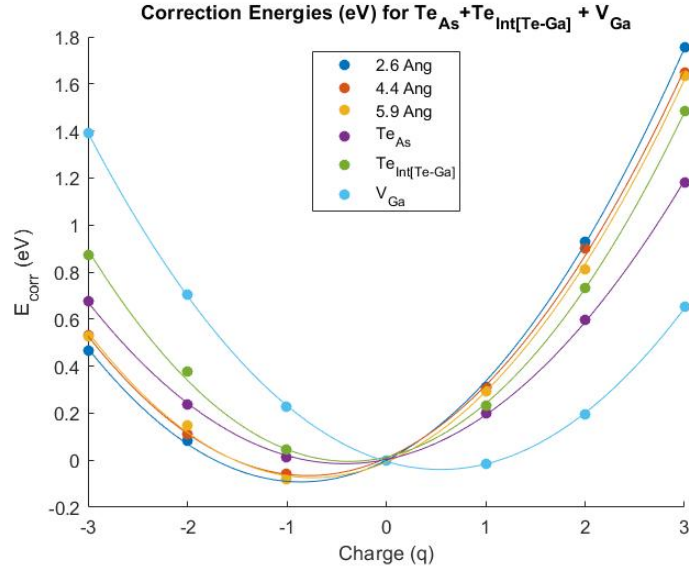


Figure 3-36. Calculated correction energies for $\text{Te}_{\text{As}} + \text{Te}_{\text{Int}[\text{Te-Ga}]} + \text{V}_{\text{Ga}}$ in Te doped GaAs as a function of defect charge (q). Blue is for the defect complex with a distance of 2.5 Å between sites, 4.4 Å is orange, and 5.9 Å is yellow. Te_{As} is purple, $\text{Te}_{\text{Int}[\text{Te-Ga}]}$ is green and V_{Ga} is cyan.

indicating they are likely to form. These results agree with experimental work by Gebauer et al. [12] who observed the $\text{V}_{\text{Ga}}^{-3}$, $\text{Te}_{\text{As}}^{+1}$ and $\text{V}_{\text{Ga}} + \text{Te}_{\text{As}}$ defects in Te-doped GaAs experimentally.

The charged defect formation energies as a function of the Fermi level were also explored. Te is a n -type dopant, or a donor impurity, which will donate electrons to states just below the CB, raising the Fermi level from the midpoint between the VBM and CBM to a level closer to the CB. Hence, Te-doped GaAs is expected to defects with favorable charge transition levels as the μ_e approaches the CB. As the Fermi level approaches the CB, the $\text{V}_{\text{Ga}}^{-3}$, $\text{Te}_{\text{As}}^{-1}$, $[\text{V}_{\text{Ga}} + \text{Te}_{\text{As}}]^{-2}$, $[2\text{Te}_{\text{As}}]^{-1}$ and $[\text{V}_{\text{Ga}} + 2\text{Te}_{\text{As}}]^{-2}$ are expected to be more stable.

As the Fermi level approaches the CB, the concentrations of V_{Ga} , $\text{V}_{\text{Ga}} + \text{Te}_{\text{As}}$ and $\text{V}_{\text{Ga}} + 2\text{Te}_{\text{As}}$ are expected to increase. Conversely, the concentrations of Te_{As} and 2Te_{As} are expected to decrease. After growth of the doped semiconductor the number of Te, Ga and As atoms in the system will not change. With this and the defect concentrations as a function of μ_e in consideration, it was concluded that the Te_{As} and 2Te_{As} defects will form but will also

combine with V_{Ga} to form $V_{Ga}+Te_{As}$ or $V_{Ga}+2Te_{As}$ defect complexes as the μ_e approaches the CB.

In work by Kennon et al. [55], it was observed that during post-growth annealing of supersaturated Te-doped InGaAs electrical deactivation occurred. In that work it was postulated that the deactivation was likely caused by Te-Te clustering, which was not observed, or Te-point defect reactions. The work in this chapter has shown that Te-point defect reactions with V_{Ga} in GaAs are predicted to occur and their concentrations increase as the Fermi level approaches the CB. The more favorable charge states of $V_{Ga}+Te_{As}$ and $V_{Ga}+2Te_{As}$ is $q = -2$, in comparison to the most favorable charge state of V_{Ga} , $q = -3$. By forming the Te-vacancy defect complexes the overall charge of the system will become less negative, suggesting that in Te-doped GaAs their formation will lead to a decrease in electrical activation. Similar behaviour in Te-doped InAs and InGaAs is expected. This supports the conclusion of Kennon et al. that a group III vacancy-Te defect complex formation is the likely mechanism behind the observed electrical deactivation.

The number of defect complexes spaced at different distances to be simulated can also be minimized by calculating the 'infinite' distance defect formation energies from the addition of the point defect formation energies which form the complex. The formation energies for different spaced defects fall between that of the nearest neighbor complex and the infinite distance formation energies. From this it can be determined if the formation energies will increase or decrease in comparison to the nearest neighbor complex, and if the complex becomes more favorable as the distance between the defects increases. However, care must be taken to ensure the charge states of the infinite defect complex can physically exist.

Finally, the only trend observed from the calculation of energy correction terms was that for complexes with defects at varying distances the E_{corr} either varied ≤ 0.2 eV or had equal values across each charge state. Over all simulations there was no consistent relations between the types of defects, atomic species or constituent defects of complexes and their calculated E_{corr} . This means that the infinite defect formation energy calculated by adding the formation

energies of the constituent defects will not result in an accurate formation energy, and should only be considered as a trend line to assess if further simulations are needed.

CHAPTER 4 THERMODYNAMIC PROPERTIES OF ZIRCONIUM HYDRIDE

Zirconium (Zr) alloys are commonly used as fuel cladding in nuclear reactors. Cladding functions as a container for the fuel pellets which not only acts as an organizing structure but also prevents the pellets from being in contact with the coolant. As such, cladding must meet certain standards for mechanical properties. Zr-alloys are used due to their low thermal neutron capture cross-section and the ability to act as a moderator. In light water reactors, the Zr-alloys are in contact with the coolant water, which causes oxidation and hydrogen (H) absorption by the clad. The absorption of H creates Zr-hydride precipitates, which are detrimental to the mechanical properties of the clad. This reaction must be taken into account during alloy design to prevent clad cracking and failure. Use of mesoscale simulations is becoming standard in the design and prediction of nuclear fuel and clad performance under reactor operating conditions.

Mesoscale simulations rely on accurate thermodynamic data to make predictions of cladding behavior. The Zr-H system has been studied extensively in the past by both experimental and first-principles techniques. However, there remains uncertainty in the phase diagram as the H/Zr ratio approaches 2. This work aims to study the thermal stability of Zr-H phases from first-principles techniques, including finite temperature effects with phonon contributions, and to generate free energy surfaces as a function of temperature and concentration. These free energy surfaces are intended for use by mesoscale modeling techniques in addition to phase diagram generation.

4.1 Configuration of Structures

There are two allotropes of zirconium: the α -Zr phase, an hcp structure, and the high temperature β -Zr phase, a bcc structure. The β -Zr phase develops above 863°C, and since current light water reactors have a maximum cladding operating of temperature 650°C[79] the β -phase has not been included in this work. In a two atom hcp unit cell there are two octahedral interstitial sites and four tetrahedral interstitial sites, see Figure 4-1. Hydrogen

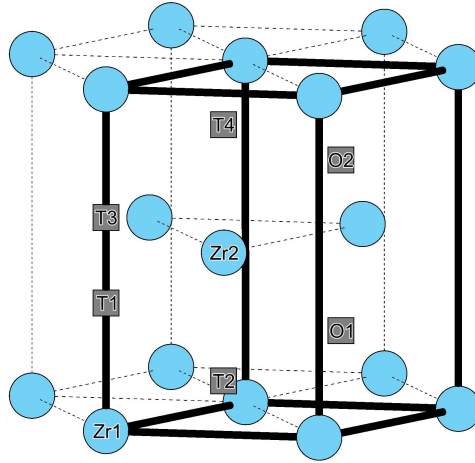


Figure 4-1. Interstitial sites in hcp α -Zr. Zr atoms are represented by blue spheres and interstitial sites by gray squares. Labels indicate either T or O for tetrahedral and octahedral sites, respectively. The primitive unit cell is outlined in bold.

Table 4-1. Phase names, structures and space groups of Zr and Zr-H phases

Phase	Structure	Space group
α -Zr	hcp	$P6_3/mmc$
β -Zr	bcc	$Im\bar{3}m$
ζ -Zr ₂ H	trigonal	$P3m1$
γ -ZrH _{1-1.5}	fct ($c/a > 1$) (fluorite-like)	$P4_2/mmc$
δ -ZrH _{1.3-1.7}	fcc (fluorite-like)	$Fm\bar{3}m$
ϵ -ZrH _{1.7-2}	fct ($c/a < 1$) (fluorite-like)	$I4/mmm$

has been observed experimentally to preferentially occupy tetrahedral interstitial sites in α -Zr [80–82].

Experimentally observed hydrides include ζ -Zr₂H, γ -ZrH_{*x*} with the composition range $1 < x < 1.5$, δ -ZrH_{*x*} with $1.3 < x < 1.7$, and ϵ -ZrH_{*x*}, with $1.7 < x < 2$. A list of each Zr and Zr-H phase structure and spacegroup can be found in Table 4-1. The δ and ϵ -hydrides are stable phases, while the γ -hydride is considered metastable, existing only at lower temperatures[2, 83]. ζ -Zr₂H was only recently observed, by Zhao et al. [6], who suggest it is also metastable. Similar to α -Zr, theory and experiment suggest that in all Zr-hydrides the H atoms preferentially sit in tetrahedral sites, as opposed to the octahedral sites [6, 80–82, 84–87].

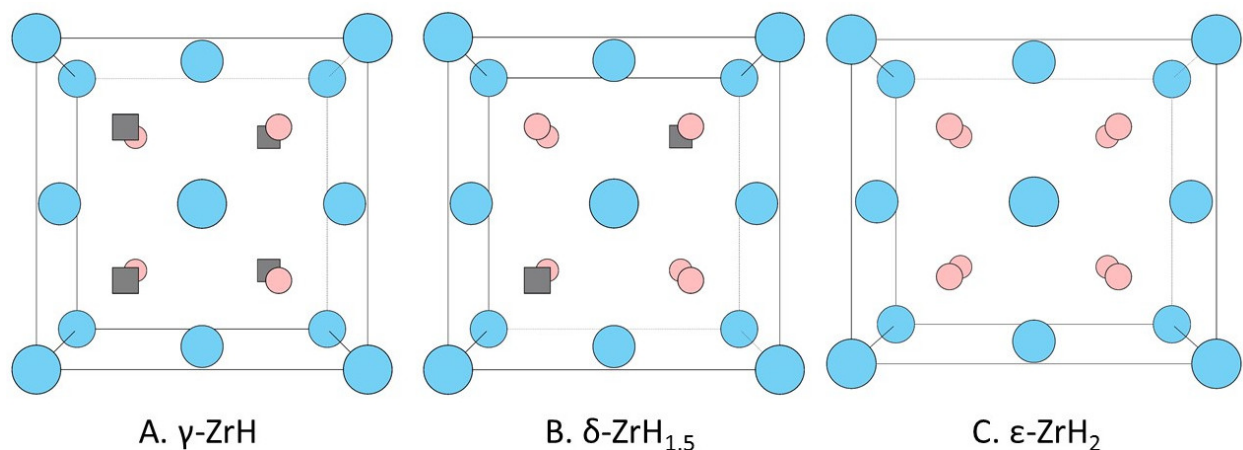


Figure 4-2. H interstitial configurations for γ -ZrH, δ -ZrH_{1.5} and ϵ -ZrH₂. Zr atoms represented by blue spheres, H by pink and empty tetrahedral sites by gray squares.

Domain et al. [84] considered various configurations of the H interstitials in γ -ZrH and found that the most stable structure had the H atoms occupy the tetrahedral sites on the $\{110\}$ plane and a c/a ratio of 1.1 (Figure 4-2A). The unit cell of δ -ZrH_{*x*} cannot accommodate the concentration $x = 1.67$, the most commonly observed phase experimentally [87], as it has 4 Zr atoms and 8 H tetrahedral interstitial positions. Larger supercells with approximately 100 atoms have been used previously to simulate $x = 1.67$ using Special Quasi-random Structure generation [88]; however, previously simulations of this size were considered too computationally expensive. Domain and others [84, 86, 87, 89, 90] commonly used δ -ZrH_{1.5} as an approximation for $x = 1.67$, with 6 tetrahedral interstitial H atoms and 2 empty tetrahedral sites in the $[111]$ direction (Figure 4-2B). ϵ -ZrH₂ is simulated with all tetrahedral interstitial sites filled by H (Figure 4-2C).

Zhao et al. [91] proposed a number of crystal structures for ζ -Zr₂H with various arrangements of H atoms in tetrahedral interstitial positions, of which the S2 structure had the lowest formation energy (see Figure 4-3). As ζ -Zr₂H is coherent with hcp α -Zr, a cluster expansion (CE) using ζ -Zr₂H as a lattice model wouldn't be distinguishable from that of the α -Zr lattice model and so has not been included in this work. If the ζ -Zr₂H structures are true ground states the CE generated by the hcp lattice model will indicate them as such.

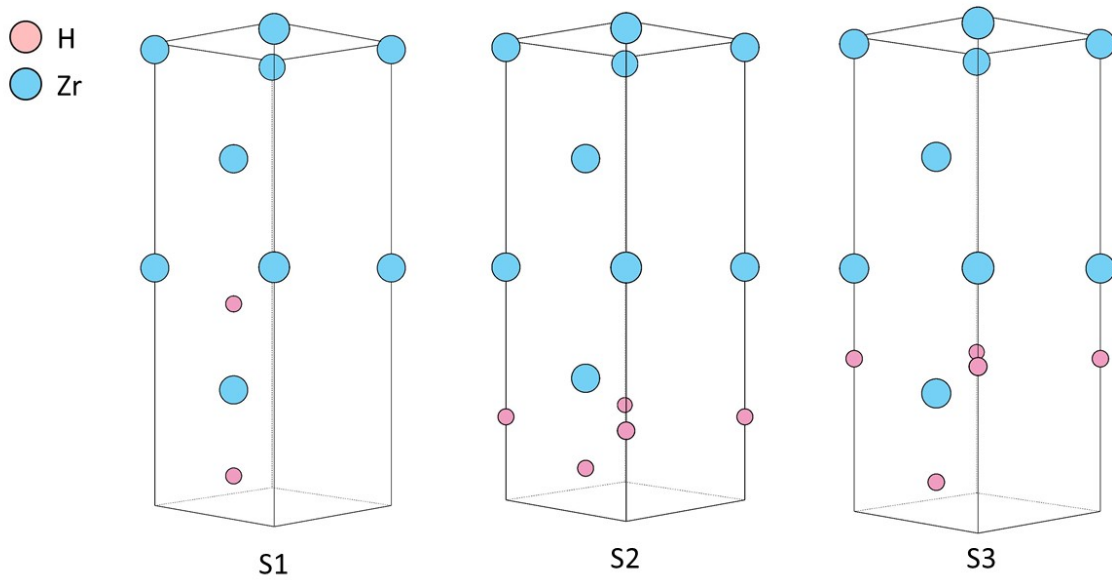


Figure 4-3. Three of the seven proposed structures for ζ -Zr₂H by Zhao et al.[6]. H atoms occupy different configurations of tetrahedral sites in two stacked α -Zr unit cells. The total energy calculated by Zhao with DFT for each structure are -41.576 eV, -41.710 eV and -41.479 eV, respectively. The structure with the lowest energy (most stable) is the S2 structure.

4.2 Simulation Parameters

Zero temperature energetics were calculated using density functional theory as implemented by VASP [19–21]. Total energies of α -Zr (hcp), and H₂ (gas) structures were calculated by carrying out geometry optimization on primitive cells with no symmetry constraints and at constant pressure. All VASP calculations used projector augmented wave (PAW) pseudopotentials [21, 59] with the GGA-PBE [92] exchange correlation supplied with the VASP package. GGA-PBE was chosen as previous work by Domain et al. [84] showed that the Local Density Approximation (LDA) [17] exchange correlation results in underestimated lattice parameters in the Zr-H system in addition to predicting H occupying octahedral interstitial sites in α -Zr, in conflict with experimental results[80–82]. GGA is better able to simulate the observed experimental parameters and correctly predicts that H occupies the tetrahedral sites. The GGA exchange correlation has been used as the standard for simulating Zr-H with *ab-initio*

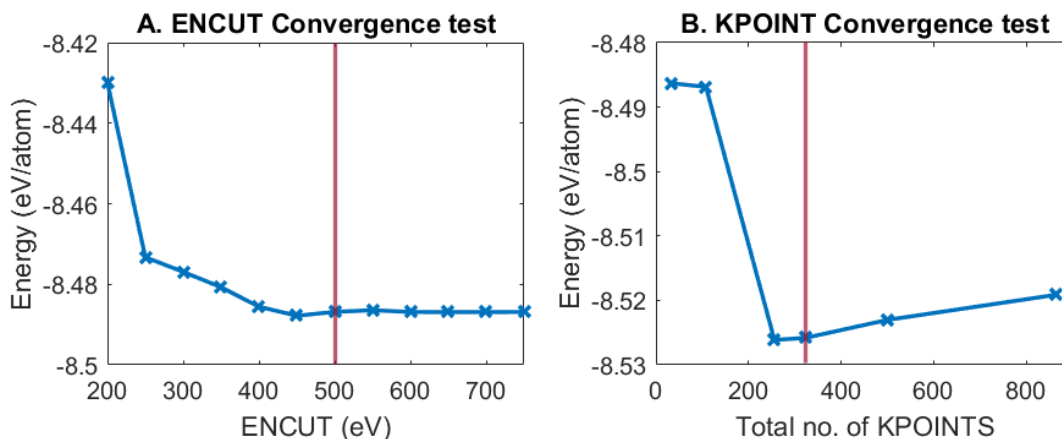


Figure 4-4. Convergence tests for α -Zr structure. A) ENCUT convergence: Red line indicates at 500 eV precision became better than 1 meV per atom. B) KPOINT convergence: Red line indicates number of k-points at which precision became better than 1 meV per atom. For α -Zr this occurred at with a $9 \times 9 \times 4$ (total of 324) k-point grid.

methods in recent years [89, 93–98]. In this work the pseudopotentials treated Zr $4s^2p^6d^25s^2$ and hydrogen $1s^1$ electrons as valence.

Convergence tests for each Zr-H structure were run (Figures 4-4 through 4-7) and an energy cutoff of 500 eV with a Methfessel-Paxton smearing width of 0.2 eV (recommended for metals [99]) was chosen for the initial bulk calculations as they resulted in a precision better than 1 meV per atom for all structures. The CEs used Methfessel-Paxton smearing to relax the geometry of each structure, followed by a static calculation with the tetrahedron method with Blöchl corrections to ensure accurate electronic density of states and total energy calculations. A Γ -centered k-point density of 6000 k-points per reciprocal atom (KPPRA) was chosen as most metals require a value of 5000-6000 KPPRA [45] to achieve an energy convergence of less than 1 meV. This KPPRA translates to k-point grids of $12 \times 12 \times 7$ for α -Zr and γ -ZrH, and $13 \times 13 \times 13$ for δ -ZrH₂ and ϵ -ZrH₂ primitive cells, all of which are much better than the minimum number of k-points required from the convergence tests. These optimized structures were used as the input geometries for the cluster expansion.

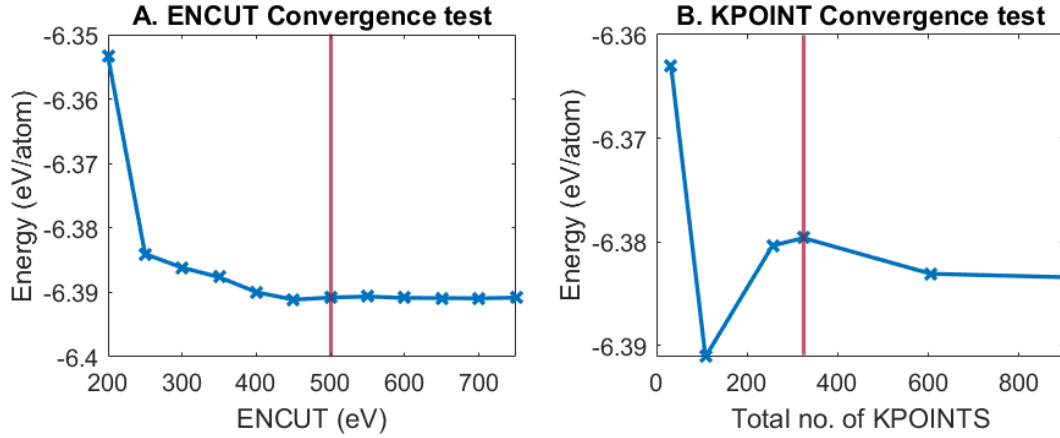


Figure 4-5. Convergence tests for γ -ZrH structure. A) ENCUT convergence: Red line indicates at 500 eV precision became better than 1 meV per atom. B) KPOINT convergence: Red line indicates number of k-points at which precision became better than 1 meV per atom. For γ -ZrH this occurred at with a $9 \times 9 \times 4$ (total of 324) k-point grid.

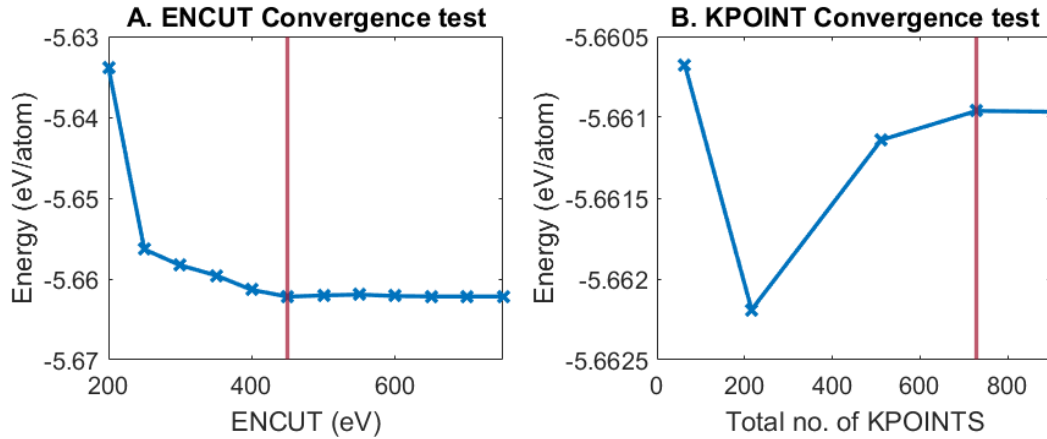


Figure 4-6. Convergence tests for δ -ZrH₂ structure. A) ENCUT convergence: Red line indicates at 450 eV precision became better than 1 meV per atom. B) KPOINT convergence: Red line indicates number of k-points at which precision became better than 1 meV per atom. For δ -ZrH₂ this occurred at with a $9 \times 9 \times 9$ (total of 729) k-point grid.

4.3 Bulk Zr-H Phase Properties

Table 4-2 shows that the calculated lattice parameters for all phases agree with the experimental values with less than 1% error. Energies of formation were calculated via the equation[87]:

$$\Delta E^f = \frac{1}{a+b} \left[E\{Zr_a H_b\} - aE\{\alpha Zr\} - b\frac{1}{2}E\{H_2\} \right] \quad (4-1)$$

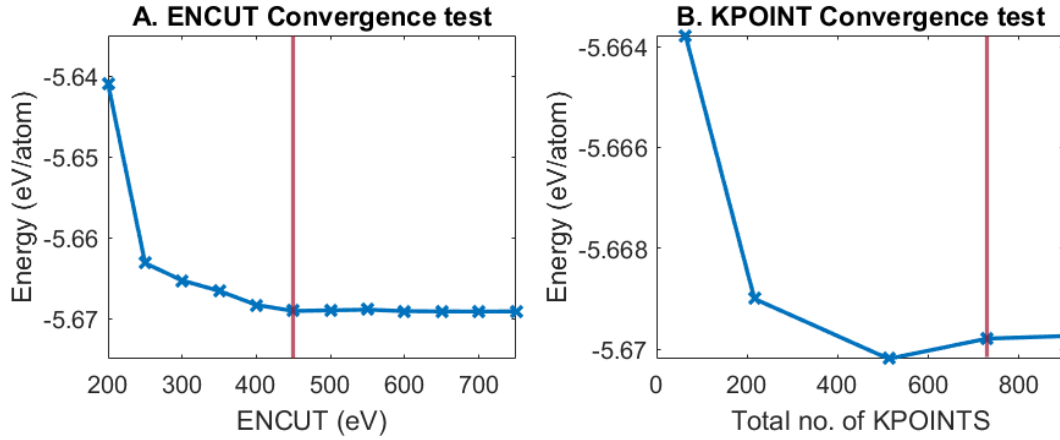


Figure 4-7. Convergence tests for ϵ -ZrH₂ structure. A) ENCUT convergence: Red line indicates at 450 eV precision became better than 1 meV per atom. B) KPOINT convergence: Red line indicates number of k-points at which precision became better than 1 meV per atom. For ϵ -ZrH₂ this occurred at with a $9 \times 9 \times 9$ (total of 729) k-point grid.

where $E\{Zr_aH_b\}$ is the total energy of the hydride as calculated by VASP, $E\{\alpha Zr\}$ is the energy per atom of α -Zr and $\frac{1}{2}E\{H_2\}$ is the energy of the H₂ molecule per atom. $E\{\alpha Zr\}$ was calculated as -8.520 eV/atom and $\frac{1}{2}E\{H_2\}$ as -3.365 eV/atom. The total number of atoms for each phase varies; hence to normalize the formation energies to eV/atom the number of Zr atoms are represented by 'a' and the number of H atoms by 'b'. The formation energies calculated in this work are all within the ranges of values reported by the literature for all phases. ϵ -ZrH₂ has the lowest formation energy of -0.588 eV/atom, followed by δ -ZrH₂ at -0.577 eV/atom, δ -ZrH_{1.5} at -0.515 eV/atom and finally γ -ZrH with the highest formation energy of -0.438 eV/atom. This trend of ϵ -ZrH₂ having the lowest formation energy, γ -ZrH having the highest and δ -ZrH_x between them is also observed in other computational work (Table 4-2).

4.4 Cluster Expansion

For the cluster expansion (CE), the MAPS code[36] uses the relaxed geometries from VASP as inputs for the lattice models to describe the configurational disorder of the phases. In the case of hydrides, the Zr sites remain filled by Zr atoms and the possible interstitial positions for the H atoms are notated in such a way that they can be either filled with an H

Table 4-2. Calculated lattice parameters (Å) and formation energies (eV/atom) for Zr-H phases compared to values reported by literature. Lattice parameters for γ , δ and ϵ -phases are reported for the structures converted to the fcc or fct structures similar to that in Figure 4-2. All calculations used the GGA-PBE exchange correlation.

Structure	Reference	a	c	c/a	ΔE^f
α -Zr	Experimental [2]	3.232	5.148	1.593	-
	This work	3.238	5.161	1.594	-
	Domain [84]	3.23	5.18	1.603	-
	Udagawa [86]	3.23	5.17	1.601	-
	Lumley [87]	3.22	5.20	1.615	-
	Olsson [89]	3.231	5.171	1.600	-
	Christensen [90]	3.237	5.183	1.609	-
	Experimental [2]	3.232	5.148	1.593	-
γ -ZrH	Experimental [2]	4.596	4.969	1.08	-
	This work	4.592	5.013	1.082	-0.438
	Domain [84]	4.58	5.04	1.104	-0.507
	Udagawa [86]	4.56	5.02	1.101	-0.489
	Lumley [87]	4.57	5.01	1.096	-0.44
	Olsson [89]	4.58	5.02	1.096	-0.392
	Christensen [90]	4.586	5.022	1.095	-0.417
δ -ZrH _{1.5}	This work	4.728	4.886	1.033	-0.515
	Domain [84]	4.79	-	1.0	-0.594
	Udagawa [86]	4.77	-	1.0	-0.566
	Lumley [87]	-	-	-	-
	Olsson [89]	4.77	4.80	1.006	-0.464
	Christensen [90]	-	-	-	-
δ -ZrH ₂	Experimental [2]	4.780	-	1.0	-
	This work	4.809	-	1.0	-0.577
	Domain [84]	4.82	-	1.0	-0.671
	Udagawa [86]	-	-	-	-
	Lumley* [87]	4.78	-	1.0	-0.53
	Olsson [89]	-	-	-	-
	Christensen [90]	4.821	-	1.0	-0.548
ϵ -ZrH ₂	Experimental [2]	4.969	4.596	0.925	-
	This work	4.998	4.422	0.885	-0.588
	Domain [84]	5.01	4.44	0.886	-0.678
	Udagawa [86]	4.99	4.41	0.884	-0.641
	Lumley [87]	5.00	4.42	0.884	-0.59
	Olsson [89]	5.01	4.42	0.882	-0.53
	Christensen [90]	5.002	4.458	0.891	-0.557

* Values cited are for the special quasi-random structure of δ -ZrH_{1.67}. Lattice parameters have been averaged.

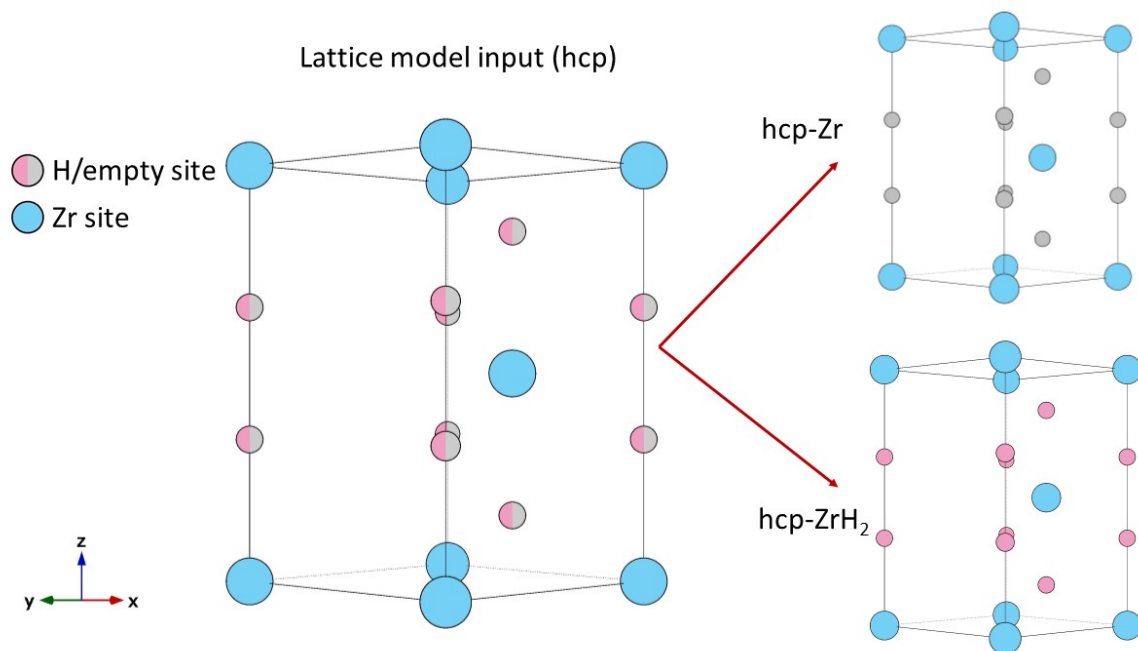


Figure 4-8. Example of lattice model input for the hcp unit cell and the end members (hcp-Zr and hcp-ZrH₂) generated by MAPS. Blue atoms indicate Zr atom sites, pink indicates H and grey indicates empty sites. The lattice model is inputted so that Zr atom sites will always be filled and the H/empty sites will be filled according to the H concentration and calculated clustering.

atom or left empty, according to the H concentration. MAPS then uses VASP to calculate the total energies of the end members for each structure inputted for the initial CE. The term 'end members' refers to the structures with all interstitial H positions filled or empty. An example of the end members for the hcp structure, hcp-Zr and hcp-ZrH₂, with H only filling tetrahedral interstitial sites, is illustrated in Figure 4-8. The VASP input parameters remain the same as outlined in Section 4.3.

The user guide for the MAPS code recommends three stopping criteria to ensure a well fit CE expansion[45]. The first is that the cross-validation score (CV, Equation 2-25) is less than 25 meV to ensure that the fitted CE is able to accurately predict new ground states. The second criteria is flagged by the code and indicated in the log file. That criteria is that "Among structures of known energy, true and predicted ground states agree", which should additionally result in a low CV-score, and "No other ground states of xx atoms/unit cell or less

exist”, which means that the fitted CE has not predicted any new ground states in structures containing xx number of sites. Finally, the last criteria is that the magnitude of the effective cluster interaction parameter (ECI, Section 2.2.2.1) decays as a function of the number of sites in a cluster and the maximum distance between any two atoms in the cluster, showing that the long range interactions are decreasing. MAPS also allows the user to disregard any structures with a lattice strain greater than a specified percentage from the fit. The user guide recommends on the fly removal of structures with strains greater than 10% to ensure no relaxation to other phases. In this work, 10% strain is used as a guide for removal in conjunction with monitoring predicted ground states for relaxation to other space groups. If the CE tends to relax to other space groups the strain is further limited.

4.4.1 HCP Lattice Model

The CE for the hcp ZrH_x lattice model was initially set to find ground states from $0 \leq x \leq 2$, and with hcp-Zr and hcp- ZrH_2 (Figure 4-8) as the end members and formation energy reference states. Once five ground states were found but the fit was no longer improving, the analysis of $1 < x \leq 2$ concentrations was stopped. The $1 < x \leq 2$ range was expected to have ground states with lower formation energies from the other lattice models. The fitting of the CE was continued in the range of $0 \leq x \leq 1$ to see if the ζ - Zr_2H could be predicted as a ground state. Once the stopping criteria were met, the initial five ground states remained the only ground states found by MAPS. Additionally, structures with a lattice strain greater than 10% were removed from the fit (24 structures in total) as it progressed.

The CE predicted a total of 43324 structures, Figure 4-9A, of which 181 were then calculated with VASP, Figure 4-9B. Comparisons between the formation energies from the fit and the first-principles calculations are shown in Figures 4-10A and 4-11B. The number of atoms in these structures range up to 24, and no other ground states were found for structures up to 30 atomic sites. The cross-validation score was 6.3 meV, much smaller than the recommended maximum value, and represents a very good fit. Figure 4-10B shows that the magnitude of the ECI mostly decays as a function of the number of sites in a cluster. The

Table 4-3. Ground state structures, lattice parameters (\AA) of the primitive cell and formation energies (eV/atom) from the hcp lattice model fitted CE. Formation energies are calculated with Equation 4-1 and with α -Zr phase and H_2 (gas) as reference. They include the formation energies calculated by VASP (DFT) and the energies fitted by the CE (MAPS). Space groups found with *pymatgen* with tolerance set to 0.1.

Structure	Space group	a	b	c	ΔE^f (DFT)	ΔE^f (MAPS)
α -Zr	$P6_3/mmc$	3.23	3.23	5.17	0.0	0.02
ZrH	$P\bar{3}m1$	3.26	3.26	5.66	-0.36	-0.35
Zr_2H_3 ($ZrH_{1.5}$)	$P\bar{3}m1$	3.28	3.28	11.66	-0.41	-0.41
Zr_3H_5 ($ZrH_{1.67}$)	$P\bar{3}m1$	3.28	3.28	17.68	-0.43	-0.43
ZrH ₂	$P6_3/mmc$	3.29	3.29	6.00	-0.45	-0.46

residuals of the fit are shown graphically in Figure 4-11A, and have a spread of less than 0.06 eV/H site.

The calculated ground states in Figure 4-9B are shown in Figure 4-12. They are α -Zr, ZrH, $\text{ZrH}_{1.5}$, $\text{ZrH}_{1.67}$ and ZrH₂. The space groups, lattice parameters and formation energies from VASP and the CE are reported in Table 4-3. The CE correctly found the α -Zr and ZrH₂ phases as hexagonal structures, however the other structures were identified as trigonal. From Figure 4-12 and the reported lattice parameters, the ZrH, $\text{ZrH}_{1.5}$ and $\text{ZrH}_{1.67}$ phases are observed to be coherent with the hcp phases.

The CE also found the three structures Zhao et al.[91] proposed for the ζ -Zr₂H ground state in Figure 4-3. As in Zhao et al., the S2 structure was found to have the lowest internal energy, -42.154 eV per simulation cell. The S1 structure has an energy of -42.023 eV and the S3 structure -41.922 eV, which also follow the trend shown by Zhao. When the formation energies of the ζ -structures are calculated with α -Zr and hcp-ZrH₂ replacing the reference states in Equation 4-1, their values are positive (0.018 eV/atom, 0.001 eV/atom and 0.030 eV/atom for S1, S2 and S3 respectively). Positive formation energies lie above the convex hull in Figure 4-9C, which uses the same reference states, and so the ζ -Zr₂H structure was not predicted as a ground state by MAPS.

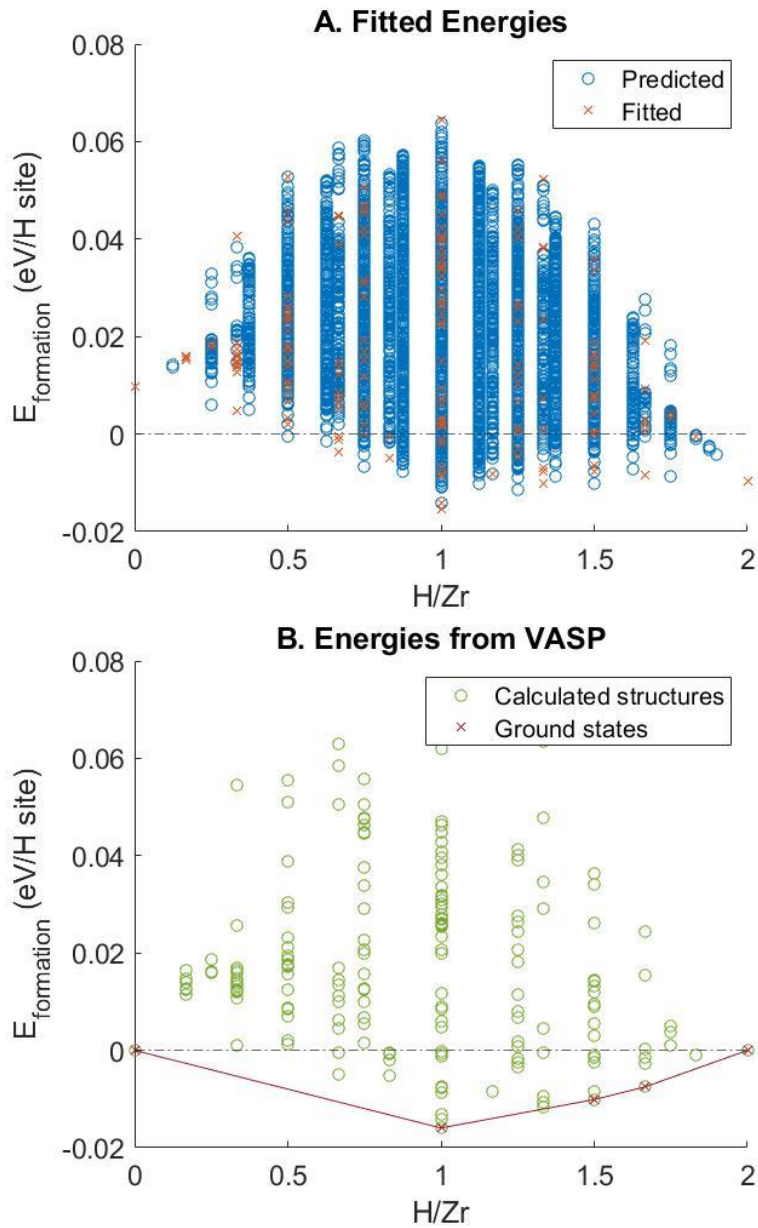


Figure 4-9. Predicted, and fitted formation energies (eV/H site), referenced to hcp-Zr and hcp-ZrH₂, from the hcp-lattice model fitted CE. A) Shows the energies predicted by the CE, blue circles, and energies fitted by the CE, orange crosses. B) Shows the formation energies calculated by VASP, green circles, and the final ground states, red crosses.

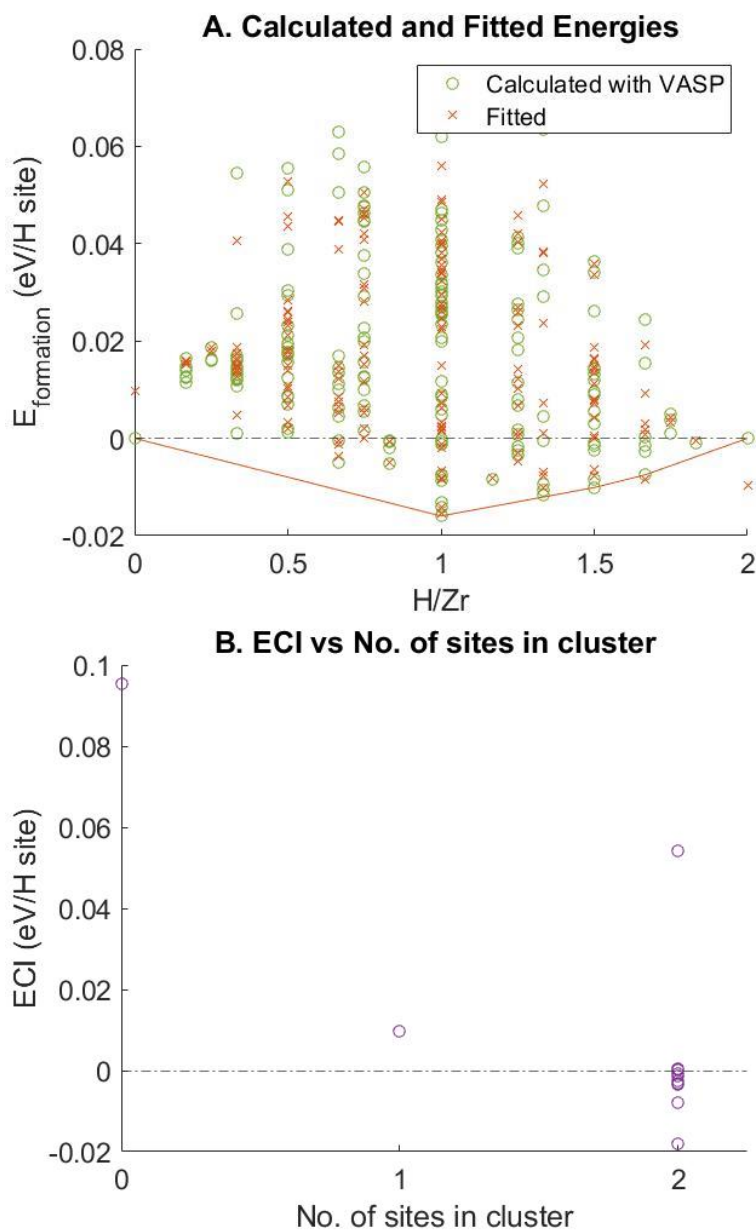


Figure 4-10. Formation energies calculated with VASP and residuals of the fit of the fcc-lattice model fitted CE. A) Compares the VASP formation energies, green circles, with the CE fitted energies, orange crosses. B) Shows the ECI generally decrease as the number of sites in the clusters increases.

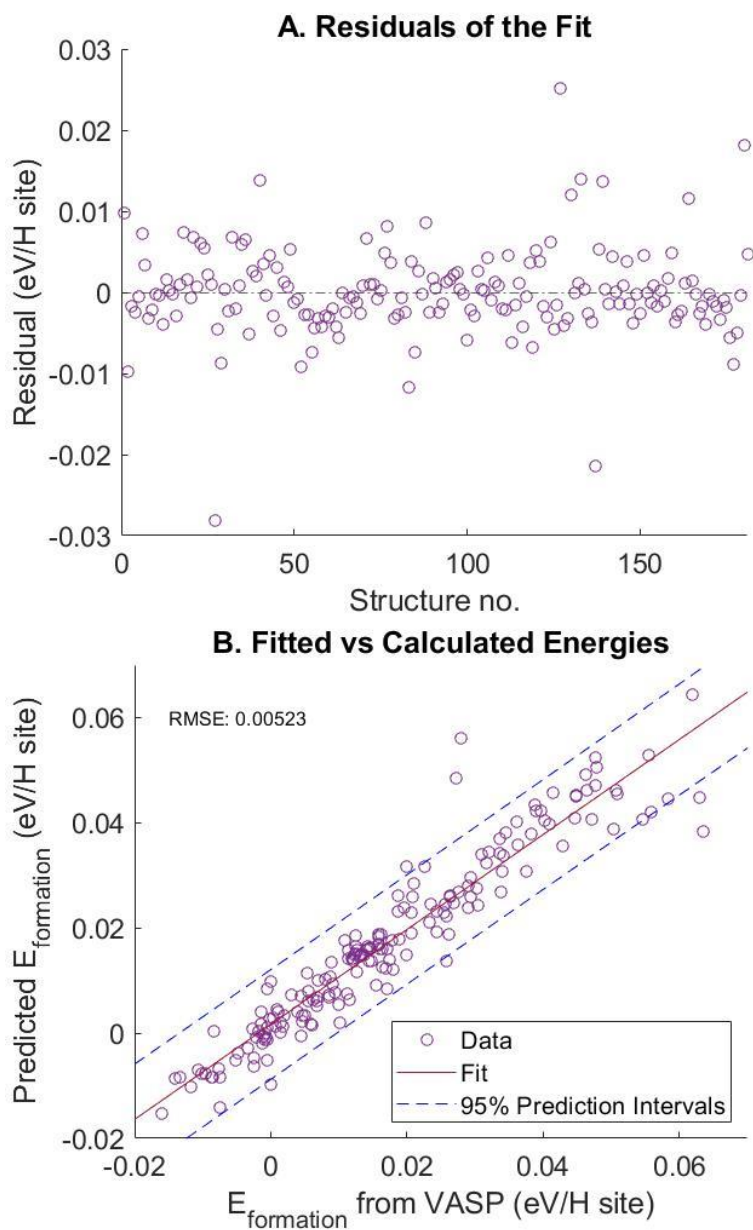


Figure 4-11. Residuals of the fit and fitted vs calculated formation energies of the hcp-lattice model fitted CE. A) Shows the spread of the residuals of the fit range over 0.06 eV/H site. B) Compares the fitted formation energies (eV/H sites) to the formation energies (eV/H site) calculated by VASP.

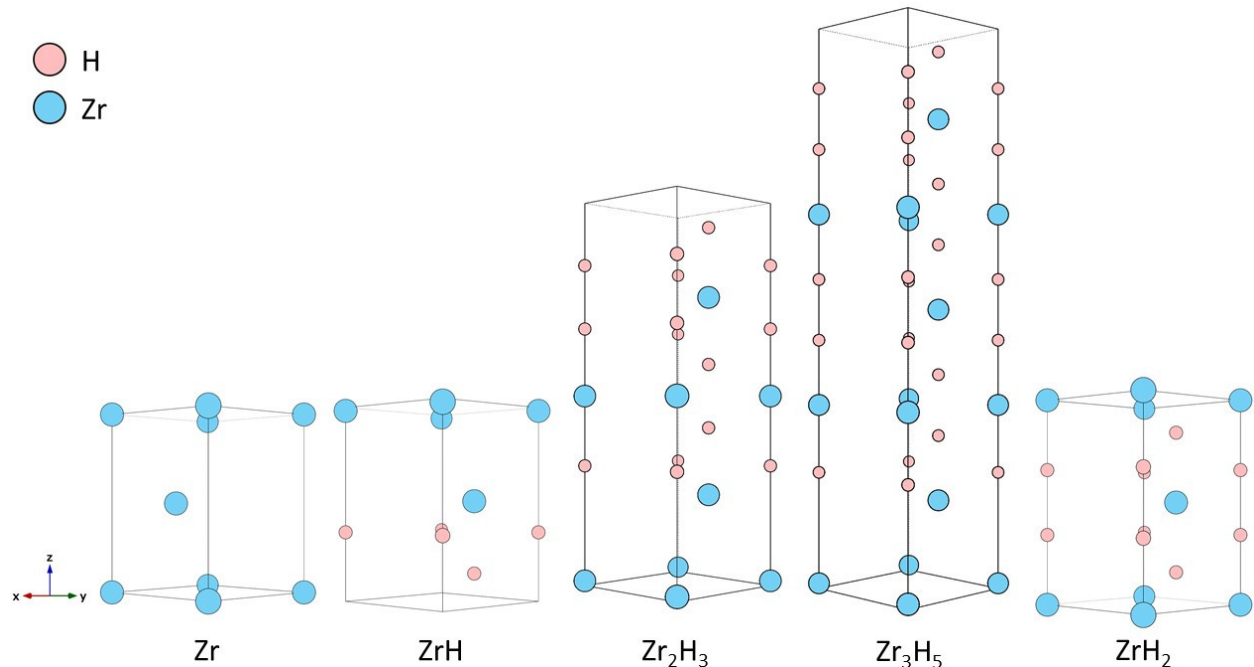


Figure 4-12. Resulting ground states from the hcp-Zr lattice model fitted CE. Blue indicates Zr atoms and pink indicate H atoms. The hcp-Zr structure (left) matches that of α -Zr.

4.4.2 FCT ($c/a > 1$) Lattice Model and Addition of Octrahedral Interstitial Sites

The fct ($c/a > 1$) ZrH_x lattice was used to test whether including octrahedral interstitial sites in a lattice model would result in different ground states being predicted. CEs were fit for three different interstitial site lattice models, one with only octrahedral sites, one with only tetrahedral sites and one with both, see Figure 4-13. Due to the total number of interstitial sites available in each lattice model, the concentration ranges were $0 \leq x \leq 1$ for the octrahedral model, $0 \leq x \leq 2$ for the tetrahedral model, and $0 \leq x \leq 3$ for the combined model. In all cases, structures with lattice strain greater than 10% were removed as the fits progressed. All were fitted until they had a CV-score less than 25 meV (octrahedral 15.3 meV, tetrahedral 17.2 meV, combined 23.3 eV). The octrahedral model and combined model were both stopped once it was determined that including octrahedral sites does not result in ground states with H atoms occupying octrahedral positions in the range of $0 \leq x \leq 2$.

Figure 4-14 shows the formation energies of the ground states predicted by the three fct ($c/a > 1$) lattice models. Formation energies were calculated using the total energy of each

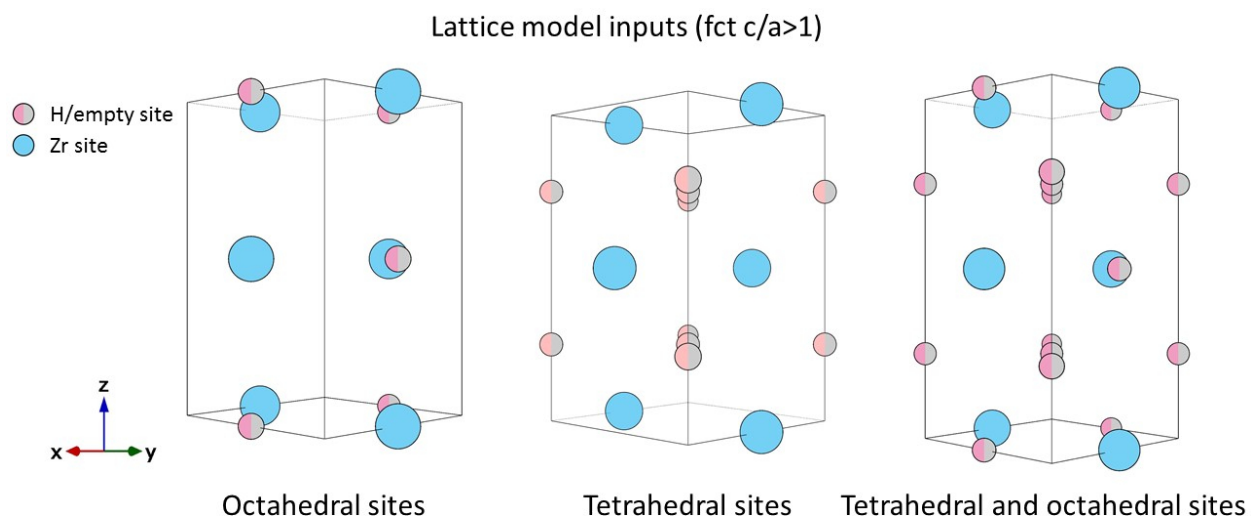


Figure 4-13. Lattice model inputs for the fct ($c/a > 1$) unit cells. Blue atoms indicate Zr atom sites, pink/gray sites indicate potential H or empty sites. Three different lattice models were tested; octrahedral interstitial sites, tetrahedral interstitial sites and a combination of both (from left to right).

structure from VASP calculations and Equation 4-1. The octrahedral only model convex hull is above the other two models, indicating that the model with only octrahedral interstitial sites does not produce true ground states. The combined model predicts the same ground states as the tetrahedral site only model (sits on the same points as the yellow line) up to $x = 2$, indicating that the low energy ground states only have H atoms occupying tetrahedral sites. As the $2 < x \leq 3$ concentration is beyond the scope of this work, using lattice models with only tetrahedral sites is acceptable, and preferable in terms of computational cost.

Continuing with the tetrahedral interstitial sites only model, the CE was fit until all stopping criteria were met, resulting in three ground states. A total of 13 structures with a lattice strain greater than 10% were removed from the fit. The final fit included 37 structures calculated by VASP and predicted no additional ground states with 30 or more atomic sites. Similar figures to Figure 4-9 and 4-10 with the ATAT results for the tetrahedral interstitial site only fct ($c/a > 1$) lattice model are in Appendix B. The calculated ground states are shown in Figure 4-15. They are Zr, γ -ZrH and ZrH₂. The space groups, lattice parameters and formation energies from VASP and the CE are reported in Table 4-4. The CE correctly found

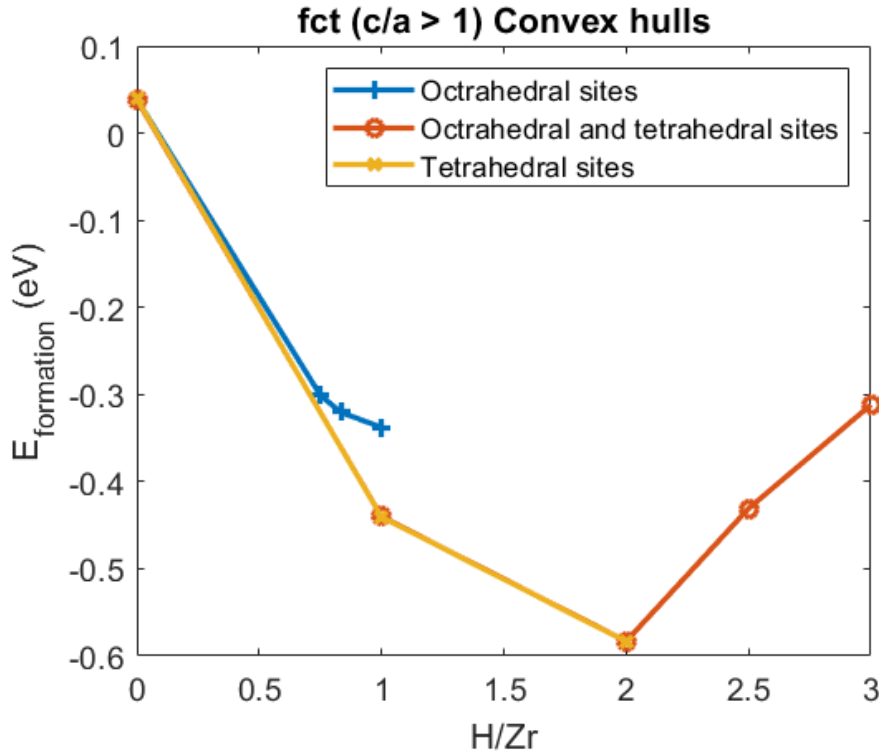


Figure 4-14. Convex hulls generated by CEs of the fct ($c/a > 1$) lattice models. Octrahedral interstitial sites only are in blue, octrahedral and tetrahedral interstitial sites are in orange, and tetrahedral interstitial sites only are in yellow. Formation energies are all calculated with α -Zr and H_2 (gas) as references.

the γ -ZrH structure with space group $P4_2/mmc$ and H interstitials occupying tetrahedral sites on the $\{110\}$ plane. However, the structure for the Zr relaxed to $Fm\bar{3}m$, the same space group as the δ -phase, and ZrH_2 relaxed to $I4/mmm$, the space group of the ϵ -phase. As the Zr formation energy is positive and larger than α -Zr, this structure is unlikely to form and can be discarded. If c/a for ZrH_2 is calculated the result is 1.57, which implies that this structure remains as fct ($c/a > 1$).

4.4.3 FCC (Fluorite) Lattice Model and Effects of Changing Strain Limitations on CE

The MAPS code allows for the lattice strain constraints to be specified in order to prevent relaxation into other phases. To explore if relaxation into either the γ or ϵ -phases could be prevented the fcc lattice model was tested with structures of high and low strain removed. The fcc lattice model (Figure 4-16) CE was set to search the range $0 \leq x \leq 2$ for ground states

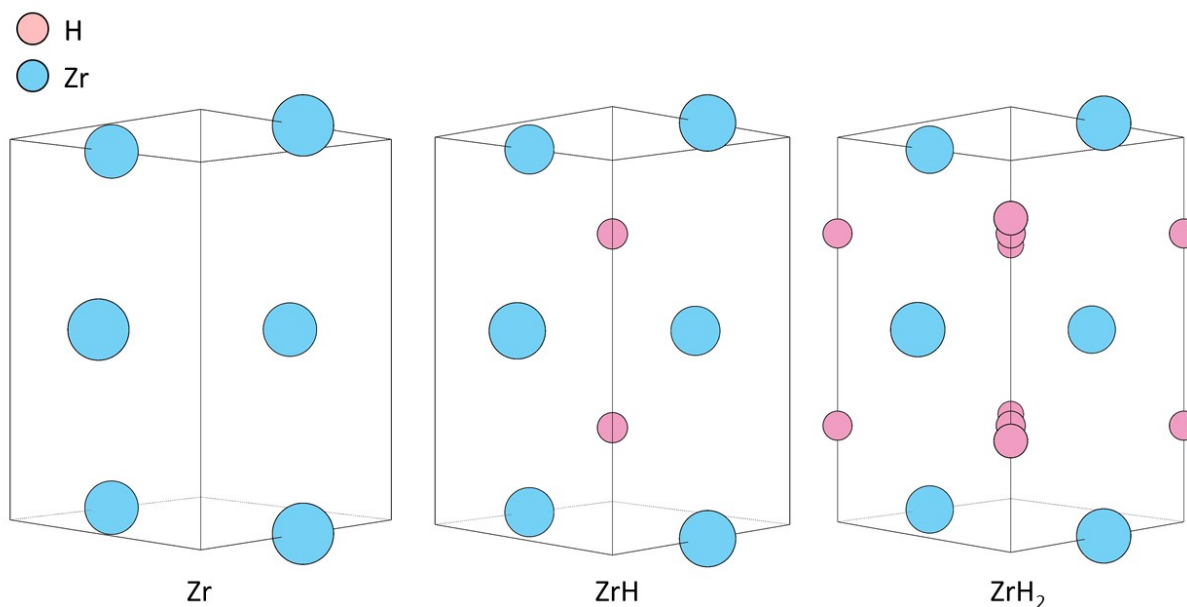


Figure 4-15. Resulting ground states from the fct ($c/a > 1$) lattice model with tetrahedral interstitial sites only fitted CE. Blue indicates Zr atoms and pink indicates H atoms. The ZrH structure (middle) matches that of γ -ZrH.

Table 4-4. Ground state structures, lattice parameters (\AA) of the primitive cell and formation energies (eV/atom) from the fct ($c/a > 1$) lattice model fitted CE. Formation energies are calculated with Equation 4-1 and with α -Zr phase and H_2 (gas) as reference. They include the formation energies calculated by VASP (DFT) and the energies fitted by the CE (MAPS). Space groups found with *pymatgen* with tolerance set to 0.1.

Structure	Space group	a	b	c	ΔE^f (DFT)	ΔE^f (MAPS)
Zr	$Fm\bar{3}m$	3.21	3.21	4.52	0.04	0.08
γ -ZrH	$P4_2/mmc$	3.24	3.24	5.00	-0.44	-0.42
ZrH ₂	$I4/mmm$	3.28	3.28	5.15	-0.58	-0.58

with structures of lattice strains greater than 10% and 4% being removed as the fit progressed. Once all stopping criteria had been met, the fcc lattice model with strain limited to 10% found four ground states, Zr, ZrH, ZrH_{1.88} and ZrH₂, see Figure 4-17 and Table 4-5. The fcc lattice model with strain limited to 4% also found four ground states, Zr, ZrH_{1.67}, ZrH_{1.86} and ZrH₂, Figure 4-18 and Table 4-6. The Zr and ZrH₂ structures from both strains are the same and are fcc structures, space group $Fm\bar{3}m$, similar to the δ -phase.

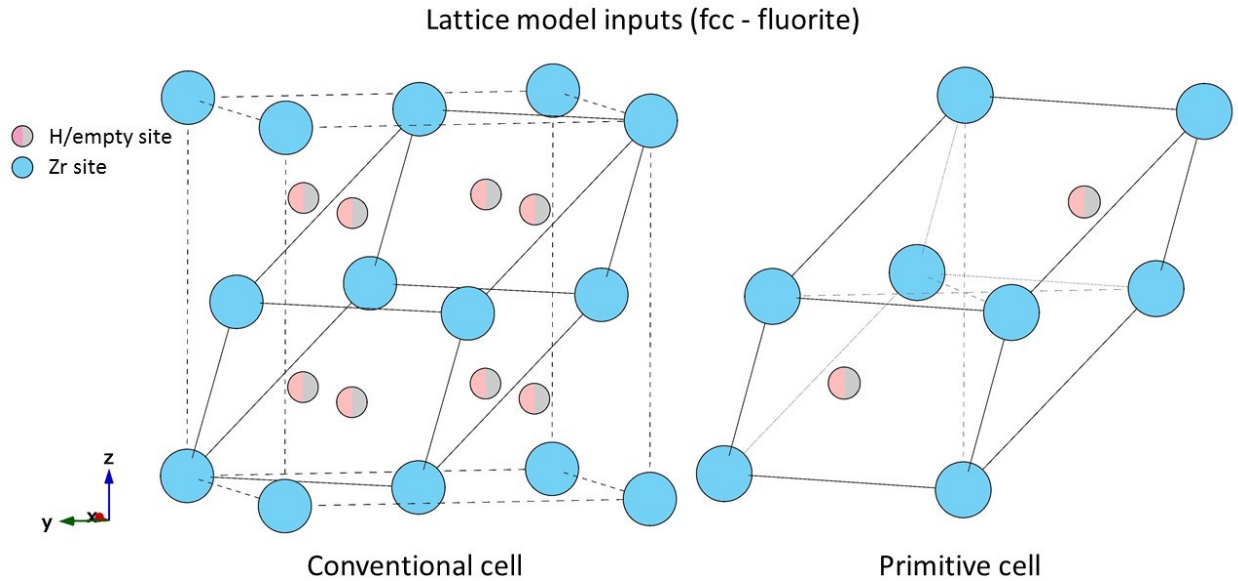


Figure 4-16. Conventional and primitive unit cells for fcc ZrH_2 . The primitive cell was used as the lattice model input for the CE. Blue atoms indicate Zr atom sites, pink/gray sites indicate potential H or empty sites.

The CE limited to 10% strain found ZrH with space group $P4_2/mmc$, similar to the γ - ZrH phase. The lattice parameters differed from γ - ZrH by 0.01-0.02 Å, which agrees with the structure relaxing to the γ -fct ($c/a > 1$) phase. $\text{ZrH}_{1.88}$ relaxed to the triclinic $P1$ structure; however, addition of a H atom to the structure to create Zr_8H_{16} , for the purposes of analyzing the space group with *pymatgen*, identifies the phase as $I4/mmm$ with $a = b = 3.53$ Å and $c = 4.42$ Å. This is similar to the ϵ -fct phase with the exception that $c/a > 1$. In summary, the CE limited to 10% strain found δ -phase like end members, Zr and ZrH_2 , the ZrH phase relaxed to a γ -like structure and $\text{ZrH}_{1.88}$ relaxed to an ϵ -like structure.

The CE limited to 4% strain found $\text{ZrH}_{1.67}$ with the space group $C2/m$. Addition of two H atoms to the structure to create Zr_6H_{12} does not change the the space group after analysis, and it remains as the monoclinic $C2/m$. Although the CE identified a $\text{ZrH}_{1.67}$ phase, which is most commonly observed H concentration, it did not find the fcc δ - $\text{ZrH}_{1.67}$ phase. $\text{ZrH}_{1.86}$ relaxed to the trigonal $R3$ structure. Addition of an H atom to the structure to create Zr_7H_{14} identifies the phase as $Fm\bar{3}m$ with $a = b = c = 4.80$ Å, which is the same structure as the δ -phase. In summary, the CE limited to 4% strain found three ground states with

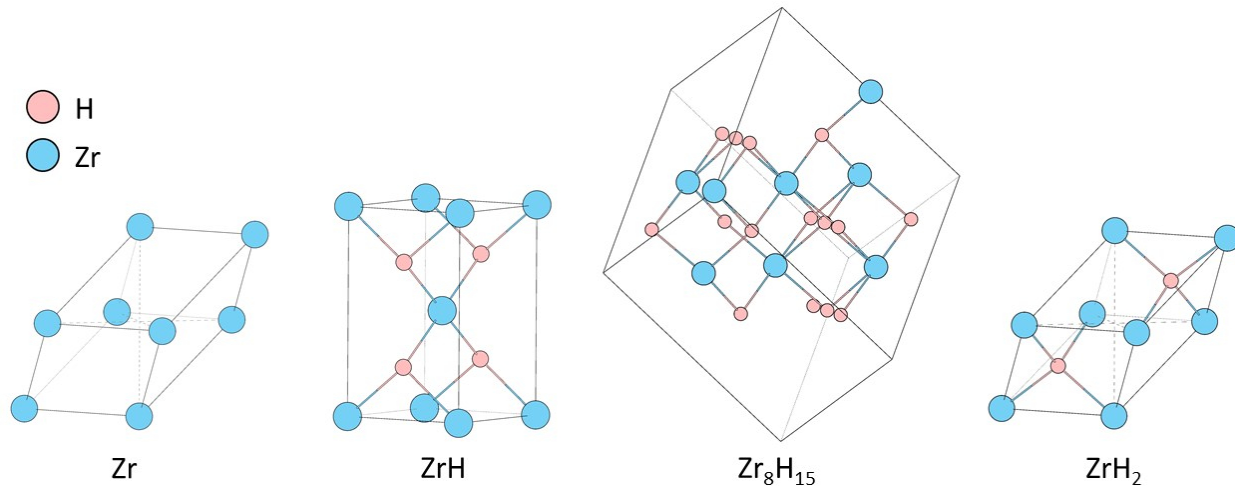


Figure 4-17. Resulting ground states from the fcc lattice model with strain limited to 10%. Blue indicates Zr atoms and pink indicates H atoms. The ZrH_2 structure (right) matches that of δZrH_2 .

Table 4-5. Ground state structures, lattice parameters (\AA) of the primitive cell and formation energies (eV/atom) from the fcc lattice model fitted CE ground states with strain limited to 10%. Formation energies are calculated with Equation 4-1 and with α -Zr phase and H_2 (gas) as reference. They include the formation energies calculated by VASP (DFT) and the energies fitted by the CE (MAPS). Space groups found with *pymatgen* with tolerance set to 0.1.

Structure	Space group	a	b	c	ΔE^f (DFT)	ΔE^f (MAPS)
Zr	$Fm\bar{3}m$	3.20	3.20	3.20	0.04	0.02
ZrH	$P4_2/mmc$	3.23	3.23	5.02	-0.44	-0.49
Zr_8H_{15} ($ZrH_{1.88}$)	$P1$	5.66	6.00	7.06	-0.57	-0.54
ZrH_2	$Fm\bar{3}m$	3.40	3.40	3.40	-0.58	-0.58

the fluorite-like fcc δ -structure, Zr, $ZrH_{1.86}$ and ZrH_2 , and the $ZrH_{1.67}$ phase relaxed to a monoclinic $C2/m$ structure.

The results of the CEs for the fcc lattice model with high and low strains show that setting a lower strain limitation, in this work 4%, can prevent predicted ground states from relaxing into the γ or ϵ -phases. It must be noted, however, that even with the strain limited to 4% the CE predicted a ground state with the $C2/m$ space group. Both the ZrH and $ZrH_{1.88}$ structures from the CE limited to 10% strain relaxed into γ and ϵ -phases, respectively. Figure 4-19 shows the formation energies from the DFT calculations for both strains. In general,

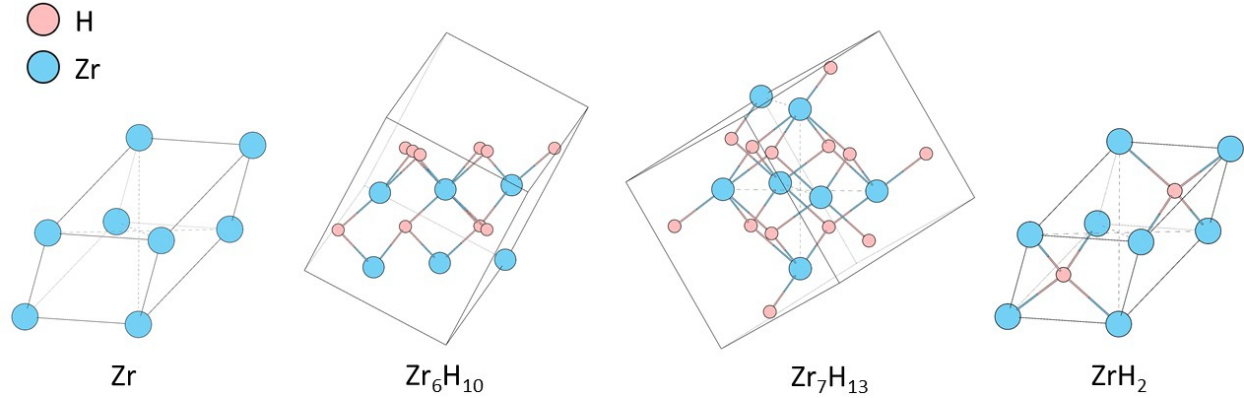


Figure 4-18. Resulting ground states from the fcc lattice model with strain limited to 4%. Blue indicates Zr atoms and pink indicates H atoms. The ZrH_2 structure (right) matches that of δZrH_2 .

Table 4-6. Ground state structures, lattice parameters (\AA) of the primitive cell and formation energies (eV/atom) from the fcc lattice model fitted CE ground states with strain limited to 4%. Formation energies are calculated with Equation 4-1 and with α -Zr phase and H_2 (gas) as reference. They include the formation energies calculated by VASP (DFT) and the energies fitted by the CE (MAPS). Space groups found with *pymatgen* with tolerance set to 0.1.

Structure	Space group	a	b	c	ΔE^f (DFT)	ΔE^f (MAPS)
Zr	$Fm\bar{3}m$	3.20	3.20	3.20	0.04	0.02
Zr_6H_{10} ($\text{ZrH}_{1.67}$)	$C2/m$	5.84	5.84	5.94	-0.54	-0.54
Zr_7H_{13} ($\text{ZrH}_{1.86}$)	$R3$	5.86	5.86	5.86	-0.56	-0.57
ZrH_2	$Fm\bar{3}m$	3.4	3.40	3.40	-0.58	-0.58

the convex hull from the CE limited to 10% strain is slightly more favorable, except for when $\text{H}/\text{Zr}=1.67$. However, due to the 10% strain CEs' inability to predict a fcc-phase between the end members, the 4% strain CE will be used in this work. It is assumed that if a CE limited to a higher strain is able to predict a ground state with the correct space group for an experimentally observed H concentration, then the CE is sufficient. If it is not able to meet this criteria then a CE with a lower constraint on the strain must be calculated.

The cluster expansion with lattice strains limited to less than 4% removed a total of 67 structures from the fit. 78 structures were included in the final fit. The CV score was 4 meV and the largest simulation cell predicted included 27 atoms. Similar figures to Figure 4-9 and 4-10 with the ATAT results for the 4% strain fcc lattice model are in Appendix B. However,

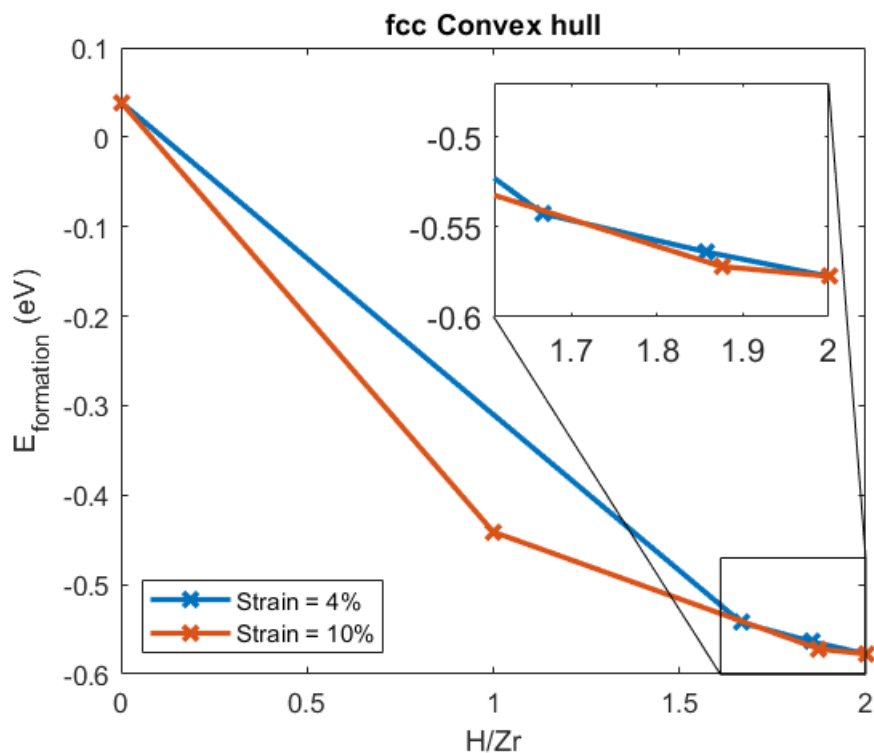


Figure 4-19. Convex hulls generated by CEs of the fcc (fluorite) lattice models with tetrahedral interstitial sites. Formation energies are all calculated with α -Zr and H_2 (gas) as references.

the CE predicted new ground states with 30 atoms or more in the cell which were not explored. According to the author of the ATAT code, Prof. A. van de Walle, if the criteria of predicting no new ground states is not met it will not prevent the finite temperature energetics from being calculated [100]. No long range order in the H sublattice of δ -ZrH_x has been observed experimentally, so there is the possibility that the CE would continue to predict ground states beyond cells with 30 atoms or more. This CE had been calculating for approximately 25,000 core hours, and had met all criteria other than predicting new ground states, when finite temperature calculations were attempted and found the CE sufficient, see Section 4.5.

4.4.4 FCT ($c/a < 1$) Lattice Model Results

The lattice model for the fct ($c/a < 1$) CE (Figure 4-20) searched the range $0 \leq x \leq 2$ for ground states. Structures with lattice strains greater than 12% were disregarded. A total of 154 structures were removed, resulting in 49 structures included in the final fit. The CV score

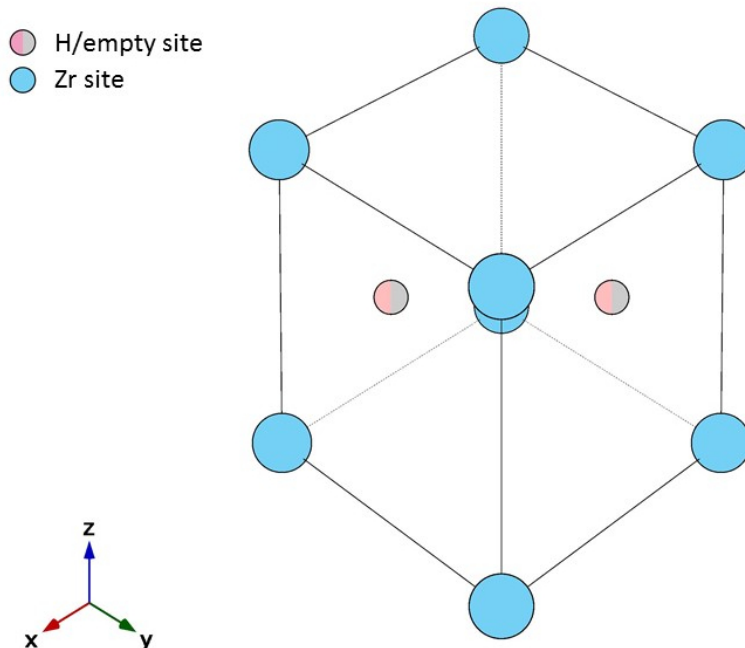


Figure 4-20. Lattice model for the fct ($c/a < 1$) CE. Blue atoms indicate Zr atom sites, pink/gray sites indicate potential H or empty sites.

was 9 meV and there were no new ground states predicted in cells containing up to 21 atomic sites. Similar figures to Figure 4-9 and 4-10 with the MAPS results for the fct ($c/a < 1$) lattice model are in Appendix B.

The CE predicted three ground states, shown in Figure 4-21. They include Zr, Zr_2H_3 and ϵ - ZrH_2 . The CE was able to correctly find the ϵ - ZrH_2 phase with the $I4/mmm$ space group. The Zr structure relaxed to $Fm\bar{3}m$, similar to the δ -phase, and $ZrH_{1.5}$ relaxed to $C2/M$. With the addition of two H atoms to the $ZrH_{1.5}$ structure, for analyzing the space group with *pymatgen*, the phase is identified as $I4/mmm$, with $a = b = 3.54 \text{ \AA}$ and $c = 4.27 \text{ \AA}$. This is an ϵ -fct phase with $c/a > 1$. Overall, the CE identified two ground states with the ϵ -phase structure and the Zr structure as a δ -like structure. The convex hull created from the ground states and Equation 4-1 is shown in Figure 4-22.

4.4.5 Zero Temperature Energetics Summary

In order to directly compare the convex hulls, the formation energies were calculated with respect to α -Zr and H_2 as in Equation 4-1. The results are shown in Figure 4-23. The final

Table 4-7. Ground state structures, lattice parameters (\AA) of the primitive cell and formation energies (eV/atom) from the fct ($c/a < 1$) lattice model fitted CE. Formation energies are calculated with Equation 4-1 and with α -Zr phase and H_2 (gas) as reference. They include the formation energies calculated by VASP (DFT) and the energies fitted by the CE (MAPS). Space groups found with *pymatgen* with tolerance set to 0.1.

Structure	Space group	a	b	c	ΔE^f (DFT)	ΔE^f (MAPS)
Zr	$Fm\bar{3}m$	3.20	3.20	3.20	0.04	0.04
Zr_2H_3 ($\text{ZrH}_{1.5}$)	$C2/M$	6.04	6.04	3.26	-0.52	-0.52
ϵ -ZrH ₂	$I4/mmm$	3.33	3.33	3.33	-0.59	-0.59

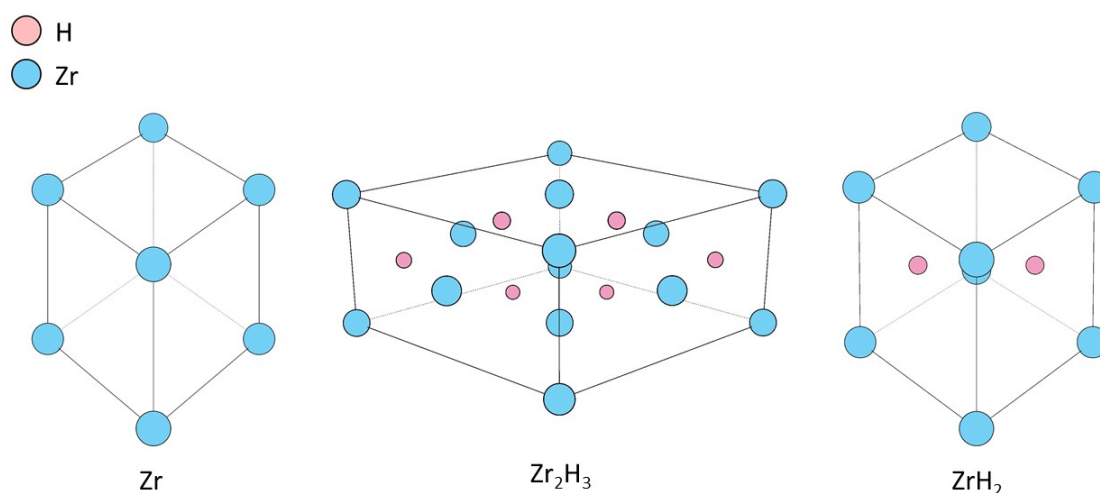


Figure 4-21. Resulting ground states from the fct ($c/a < 1$) lattice model. Blue indicates Zr atoms and pink indicates H atoms. The ZrH_2 structure (right) matches that of ϵ -ZrH₂.

Zr-H ground states over the range of $0 \leq x \leq 2$ are α -Zr, γ -ZrH, ϵ -ZrH_{1.5}, δ -ZrH_{1.67} and ϵ -ZrH₂ at 0K. All of these phases have been observed experimentally except for the ϵ -ZrH_{1.5}. The region around this concentration has been experimentally observed as a two-phase γ - δ region. The δ -phase is nearing the convex hull of the ϵ -phase in the $1.67 \leq x \leq 1.86$ range, and is estimated to be less than 10 meV higher than the ϵ -phase. This difference is very small and given that room temperature corresponds to approximately 25 meV, it suggests that either δ or ϵ -phases may form in this range and both are metastable [101]. It is also possible that one

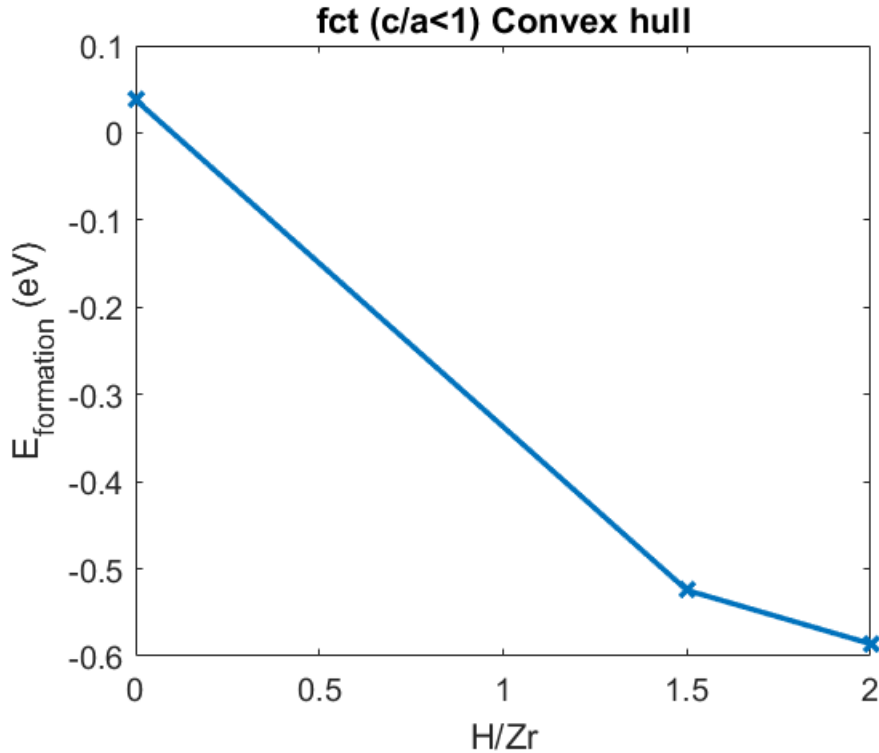


Figure 4-22. Convex hull generated by CE of the fct ($c/a < 1$) lattice model. Formation energies calculated with α -Zr and H_2 (gas) as references.

may become more stable than the other at higher temperatures, which will be explored through finite temperature effects in the following section.

4.5 Monte Carlo Simulations and Total Energy Surfaces

Monte Carlo methods were used to calculate the finite temperature energetics with respect to configurational disorder in the Zr-H system. Vibrational effects are discussed in Section 4.6. The EMC2 code [38] was developed alongside the MAPS code, as part of the ATAT package [36], to allow automation of this process. It requires the lattice models, ECI, cluster information and ground states outputted by the MAPS code. EMC2 then uses semi-grand canonical Monte-Carlo simulations (Section 2.2.3) to calculate each phase's free energy surface via thermodynamic integration. In practice, the user specifies which ground state to focus on, the range of temperatures and chemical potentials over which the stable free energy surfaces are to be calculated, a radius used to determine the smallest possible supercell that would fit a sphere of the given radius inside the supercell and the precision to which the

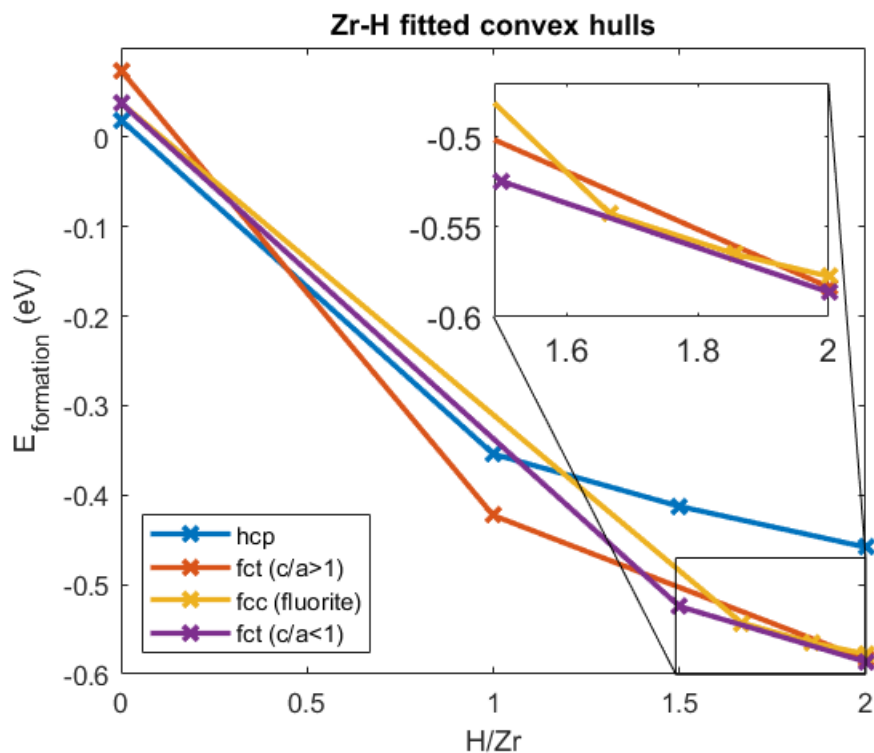


Figure 4-23. Convex hulls generated by all the CEs. Formation energies are all calculated with α -Zr and H_2 (gas) as references. The hcp-ZrH_{1.67} ground state was removed because it was above the hcp-convex hull when calculated with these reference energies, hence not a true ground state.

composition is calculated. Additionally, EMC2 normalizes the chemical potentials such that the absolute values are not required. For example, chemical potential $\mu = 3$, an integer, stabilizes a two-phase equilibrium between ground state 2 and 3, making the range of chemical potentials to explore ground state $x = 3$ be simplified to $(x - 0.5 = 2.5) \leq \mu \leq (x + 1.5 = 4.5)$, see Figure 4-24.

In this work the Monte Carlo simulations were run from 100 K to 1000 K in steps of 10 K, with each simulation cell containing a sphere of at least 50 \AA^3 . Chemical potentials changed in steps of 0.04 and the precision of the concentration was set to 0.001. The code was also set so that simulations were run for ground states of each lattice model from the CEs which didn't relax to a different space group to find the statistical averages of concentration and temperature at which each were stable. The code outputs the Gibbs free energy for each stable

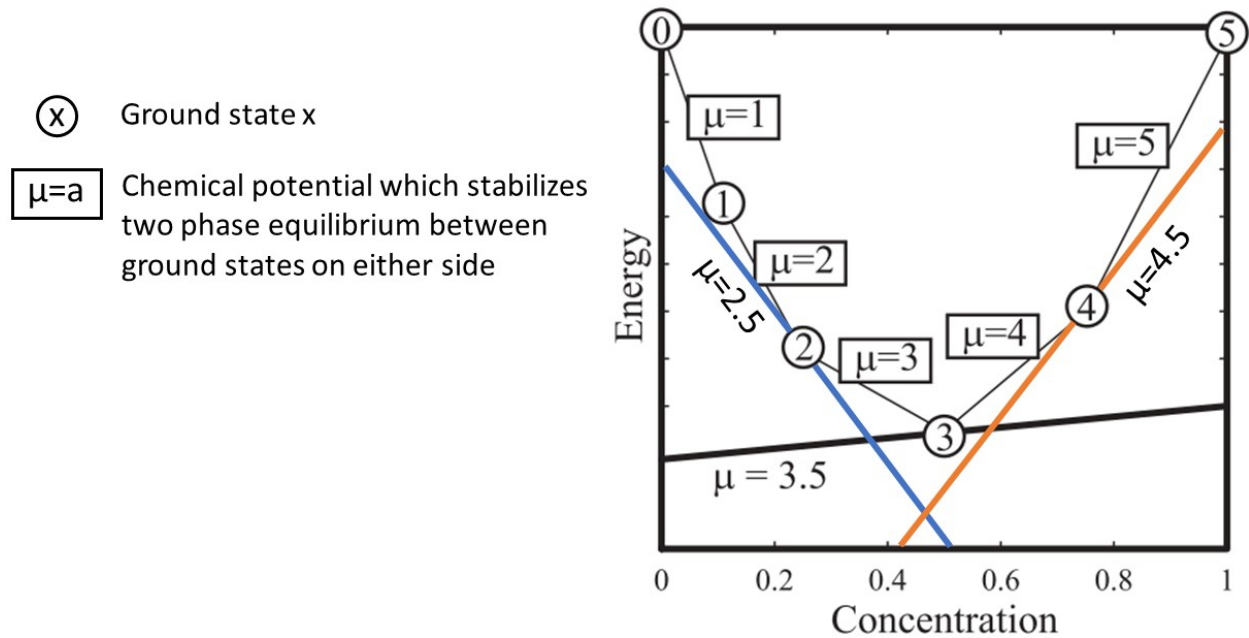


Figure 4-24. Example of chemical potential normalization in relation to ground state references from the MAPS code.[Adapted from van de Walle et al. [102] and used with permission.]

concentration and temperature with the end members for each lattice model as the references. For the purposes of comparison and further manipulation of the data, this work has converted the output from EMC2 to Gibbs free energy with respect to α -Zr and H_2 (gas).

Figure 4-25 shows the EMC2 results of the hcp lattice model. The α -Zr ground state ($H/Zr=0$ at $T=0$ K) shows a large region of stability with all Gibbs free energies below zero (-0.32 eV/atom to 0 eV/atom) for $0 \leq T \leq 1000$ K. The other ground states predicted by the CE relaxed to different space group structures and were not been simulated with the MC code. The α -Zr is stable in the range $0 < H/Zr < 0.7$.

The EMC2 results of the fct ($c/a > 1$) lattice model are shown in Figure 4-26. γ -ZrH was the only predicted ground state which didn't relax to a different space group, and was the only ground state to be simulated with the MC code. γ -ZrH free energy ranges from -0.37 eV to -0.48 eV for $0.8 \leq H/Zr \leq 1.3$. The γ -ZrH phase becomes unstable above 400 K, as seen by the absence of stable structures above 400 K at $H/Zr=1$, suggesting it is a low temperature metastable phase.

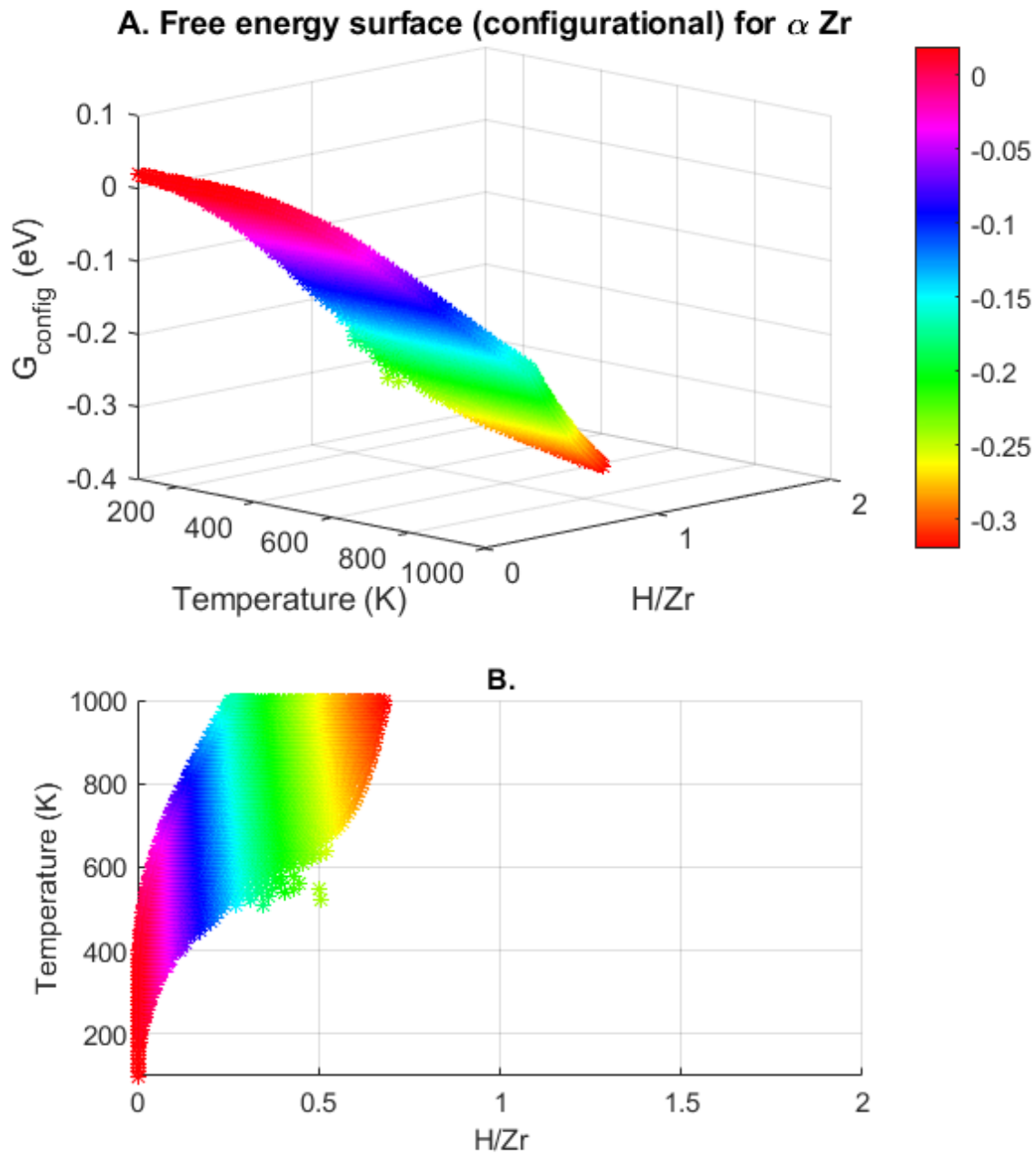


Figure 4-25. Results from MC simulations of the hcp-lattice model. Each point is a stable structure with statistical averages of concentration and temperature calculated by MC methods. A) The configurational Gibbs free energy (eV) of stable structures as a function of temperature (K) and concentration (H/Zr). B) Stable structures as a function of temperature and concentration.

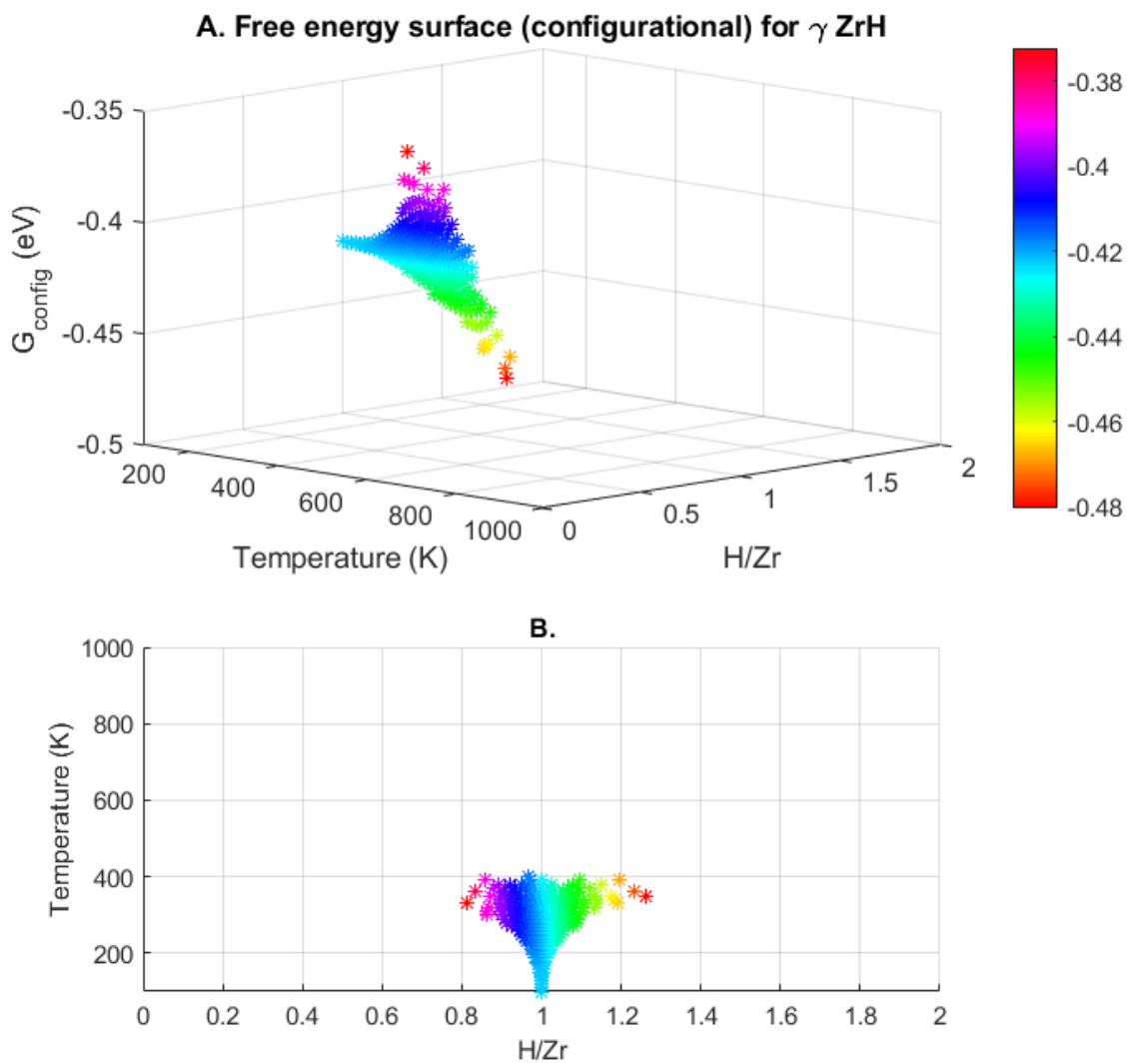


Figure 4-26. Results from MC simulations of the fct ($c/a > 1$)-lattice model. Each point is a stable structure with statistical averages of concentration and temperature calculated by MC methods. A) The configurational Gibbs free energy (eV) of stable structures as a function of temperature (K) and concentration (H/Zr). B) Stable structures as a function of temperature and concentration.

The initial results from the EMC2 calculations for the fcc lattice model are in Figure 4-27. The results show that the $\text{ZrH}_{1.67}$ ground state has unrealistically high Gibbs free energies and any differences in the energies of the other ground states are lost due to the scale. The unrealistically high values suggest that the state is not stabilized by the chemical potentials within the range $(x - 0.5) \leq \mu \leq (x + 1.5)$ and is disordered in the H sublattice. The MC calculations for the $\text{ZrH}_{1.67}$ structure were rerun as a disordered structure, which resulted in energies similar to fcc- $\text{ZrH}_{1.86}$, see Figure 4-28. The fcc model Gibbs free energies range from -0.52 eV to -0.58 eV for $1.47 \leq \text{H/Zr} \leq 1.97$.

Figure 4-29 shows the EMC2 results of the fct ($c/a < 1$) lattice model. $\epsilon\text{-ZrH}_2$ was the only predicted ground state which didn't relax to a different space group, and was the only ground state to be simulated with the MC code. Its Gibbs free energies range from -0.54 eV/atom to -0.59 eV/atom for $1.41 \leq \text{H/Zr} \leq 2$. At 300 K the $\epsilon\text{-ZrH}_2$ phase has a lower Gibbs free energy than the δ -phase for the range $1.7 \leq \text{H/Zr} \leq 2$, as shown in Figure 4-30. $\epsilon\text{-ZrH}_2$ is expected to be the most stable phase at $\text{H/Zr}=2$, which is supported by the low energies in the range of $1.9 \leq \text{H/Zr} \leq 2$.

The ATAT package also includes the PHB code [36, 38] which runs two MC simulations simultaneously in order to find the temperature-concentration phase boundary between two different phases. Using the same simulation settings as the EMC2 code, the PHB code was used to find the phase boundaries between the α , γ , δ and ϵ -phases, Figure 4-31. The $\alpha\text{-Zr}$ phase boundary is indicated by a purple line, $\gamma\text{-ZrH}$ by orange, $\delta\text{-ZrH}_x$ by yellow and $\epsilon\text{-ZrH}_2$ by blue. However, these calculations have not been normalized so that the phase boundary formation energies are calculated with respect to the same reference energies. As such, directly comparing the different phases isn't ideal and the following observations are assumed to only serve as approximate. The from 0 K to 210 K the diagram indicates there is a two phase $\alpha\text{-}\gamma$ region for $\text{H/Zr} \leq 1$, and a two phase $\gamma\text{-}\delta$ region for $1 \leq \text{H/Zr} \lesssim 1.67$. $\gamma\text{-ZrH}$ forms a line compound up to 210 K. From 0 K to 340 K there is a two phase $\delta\text{-}\epsilon$ phase for $1.67 \lesssim \text{H/Zr} \lesssim 2$. Above 210 K, $\alpha\text{-Zr}$ forms a two phase region with either $\delta\text{-ZrH}_x$ or $\epsilon\text{-ZrH}_x$.

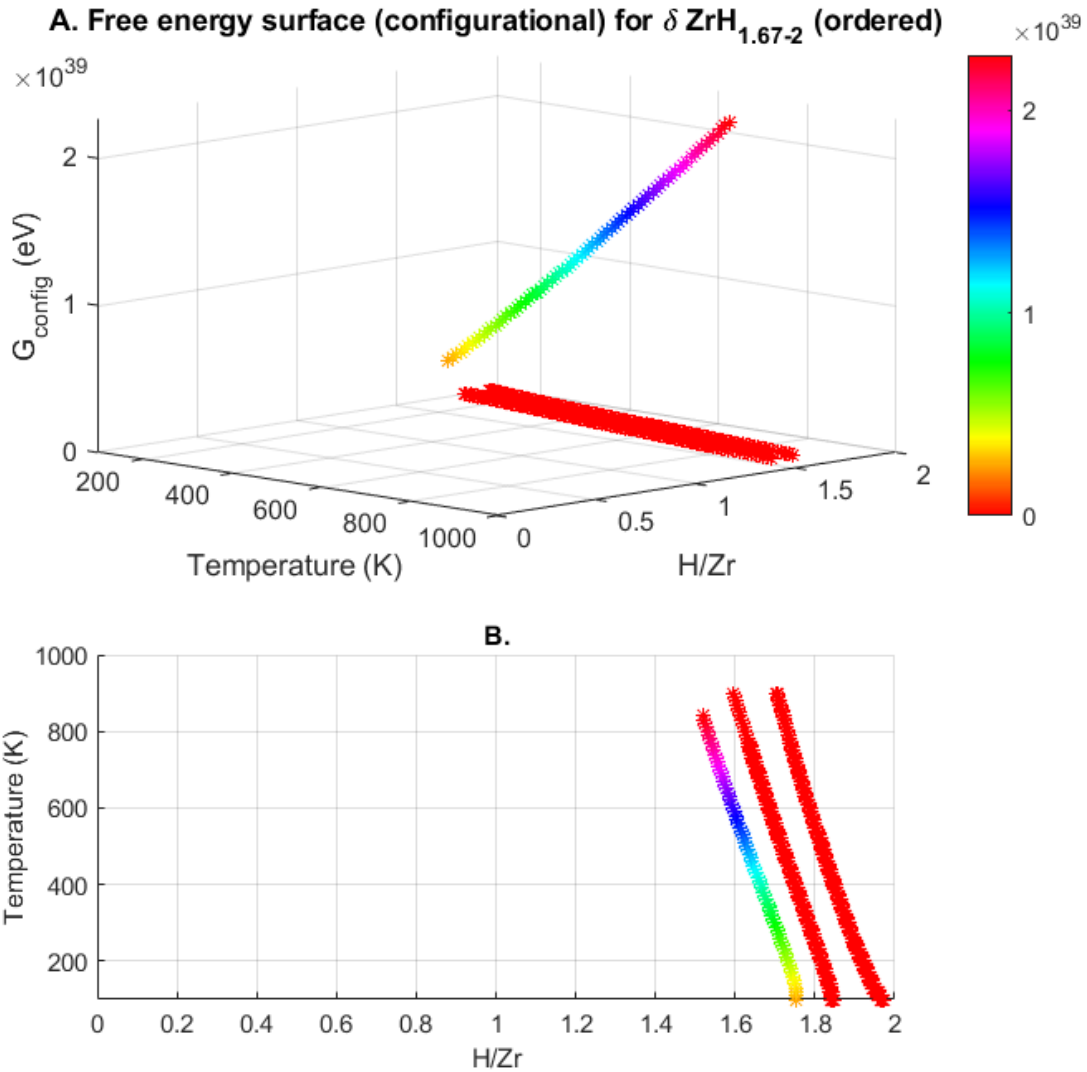


Figure 4-27. Results from MC simulations of the fcc-lattice model. Each point is a stable structure with statistical averages of concentration and temperature calculated by MC methods. A) The configurational Gibbs free energies (eV/atom) of stable structures as a function of temperature (K) and concentration (H/Zr). B) Stable structures as a function of temperature and concentration.

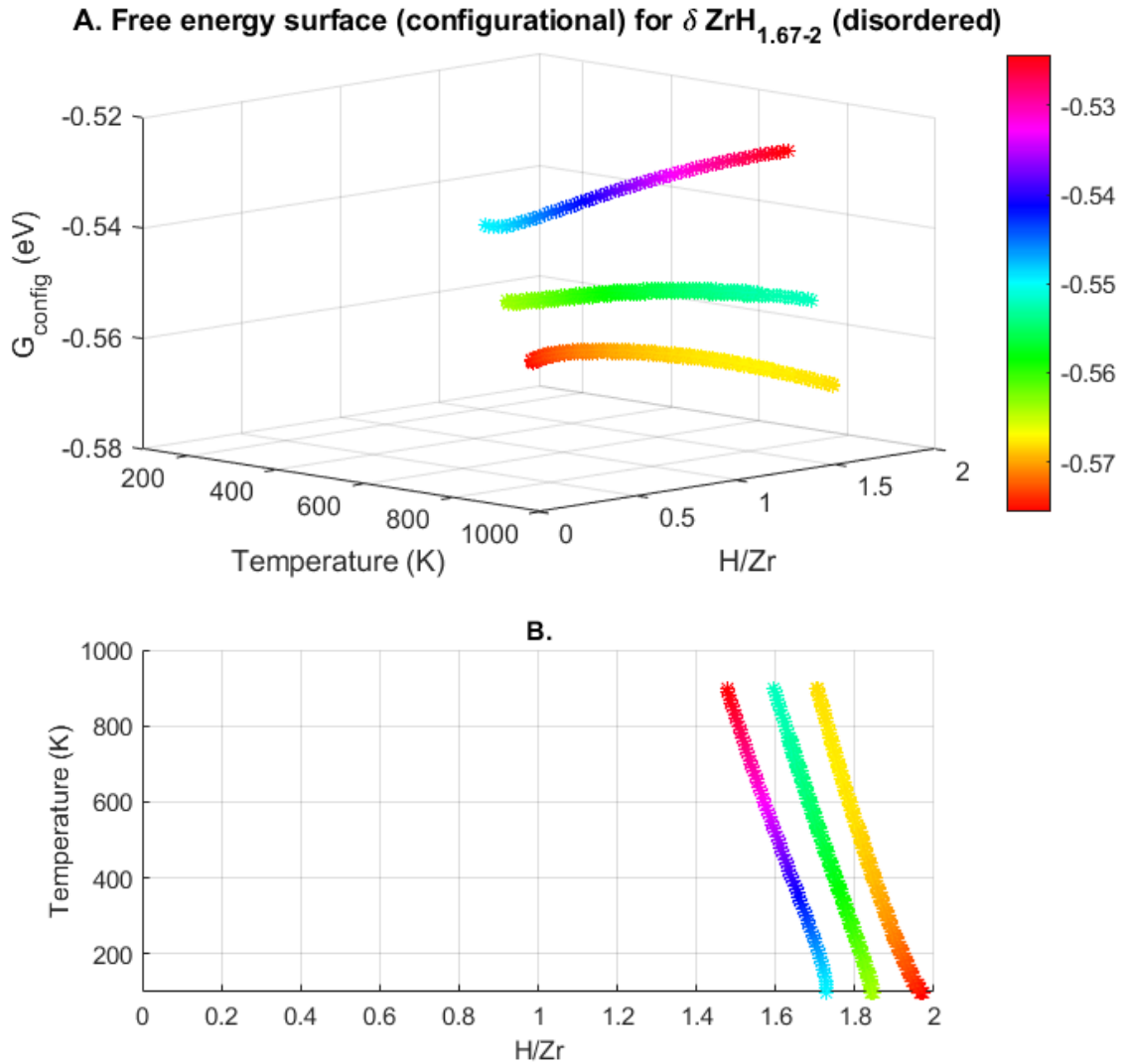


Figure 4-28. Results from MC simulations of the fcc-lattice model. Each point is a stable structure with statistical averages of concentration and temperature calculated by MC methods. A) The configurational Gibbs free energies (eV/atom) of stable structures as a function of temperature (K) and concentration (H/Zr). B) Stable structures as a function of temperature and concentration.

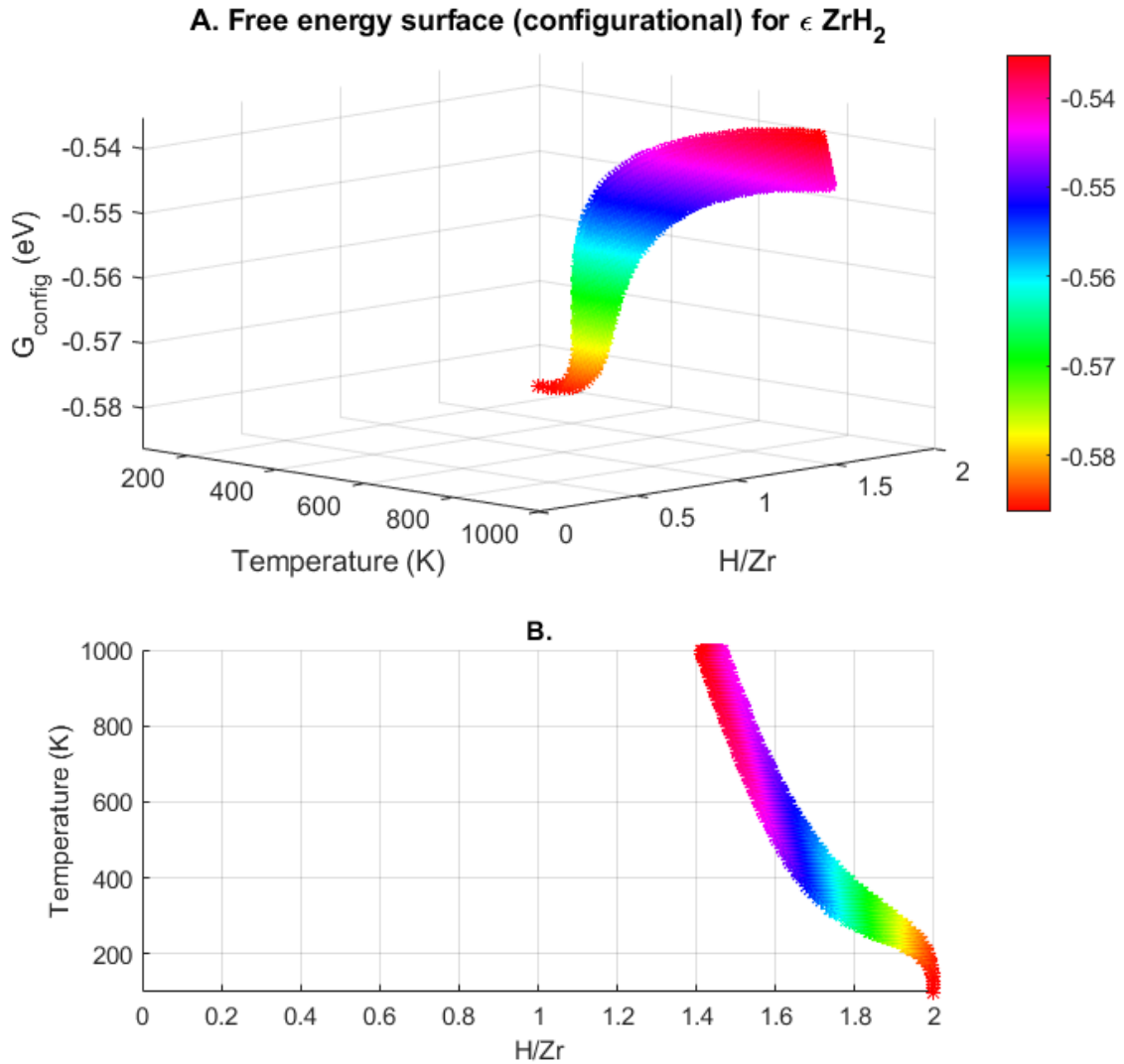


Figure 4-29. Results from MC simulations of the fct ($c/a < 1$)-lattice model. Each point is a stable structure with statistical averages of concentration and temperature calculated by MC methods. A) The configurational Gibbs free energies (eV/atom) of stable structures as a function of temperature (K) and concentration (H/Zr). B) Stable structures as a function of temperature and concentration.

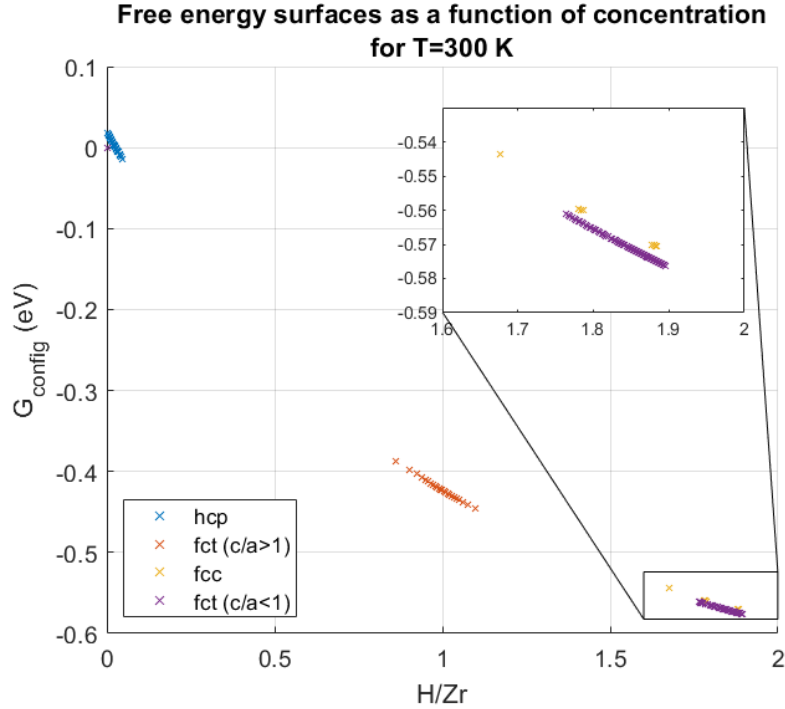


Figure 4-30. Free energy surfaces as a function of concentration for $T = 300$ K. Results from hcp lattice model in blue, fct ($c/a > 1$) in orange, fcc in yellow and fct ($c/a < 1$) in purple.

The two phase region above 210 K cannot distinguished between α - δ or α - ϵ due to the use of different reference energies, as mentioned above.

4.6 Phonon Calculations

Lumley et al. [87] and Besson et al. [93] suggest that phonons play an important role in the phase order of the γ , δ and ϵ Zr-H phases. Lumley concluded that vibrational contributions may be a factor in increasing the stability of the δ -phase while Besson proposed that the inclusion of phonon effects may decrease the γ -phase stability. To investigate the effect of adding phonons in the Zr-H system, the vibrational free energy was calculated using first principles phonon calculations under the harmonic approximation. The harmonic approximation assumes that the energy is a function of atomic displacement only [39]. It cannot accurately describe volume-dependent effects, such as thermal expansion and heat capacity [62], which can instead be calculated with quasi-harmonic approximation (QHA). It is envisioned that this work can be expanded on in the future to include volume-dependent effects.

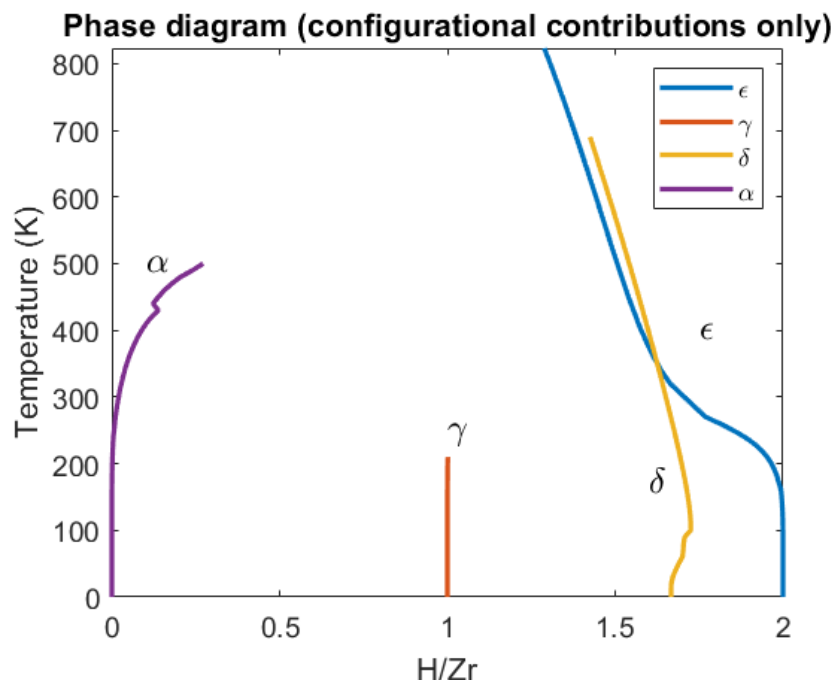


Figure 4-31. Phase diagram calculated by the PHB code. Note, data used to generate this phase diagram only includes configurational contributions. The α -Zr phase boundary is indicated by a purple line, γ -ZrH by orange, δ -ZrH_x by yellow and ϵ -ZrH₂ by blue.

Phonopy [39] is the code used in this work to calculate the phonon energies by the finite displacement method (FDM). Each ground state for each lattice model was used to generate roughly cubic supercells with symmetry-nonequivalent atomic distortions. Each supercell was then used to calculate the force constants with fixed-ion VASP calculations. Once all the fixed-ion calculations finished, Phonopy was used to generate force sets to calculate the force constants and thermal properties of each ground state.

An example of the phonon free energy for the ϵ -ZrH₂ structure calculated by Phonopy is shown in Figure 4-32 from 0 to 800 K. The free energy curve is in good agreement with work by Chattaraj et al. [103], who found the the free energy of ϵ -ZrH₂ to be approximately 0.47 eV at T = 0 K, and 0.11 eV at T = 800 K. This work found F = 0.46 eV at T = 0 K, and 0.11 eV at T = 800 K. Similar curves to Figure 4-32 were calculated for each ground state and used to fit a phonon free energy surface for each lattice model. Figure 4-33A shows the fitted phonon free energy surface for the hcp lattice model and the calculated phonon free energies

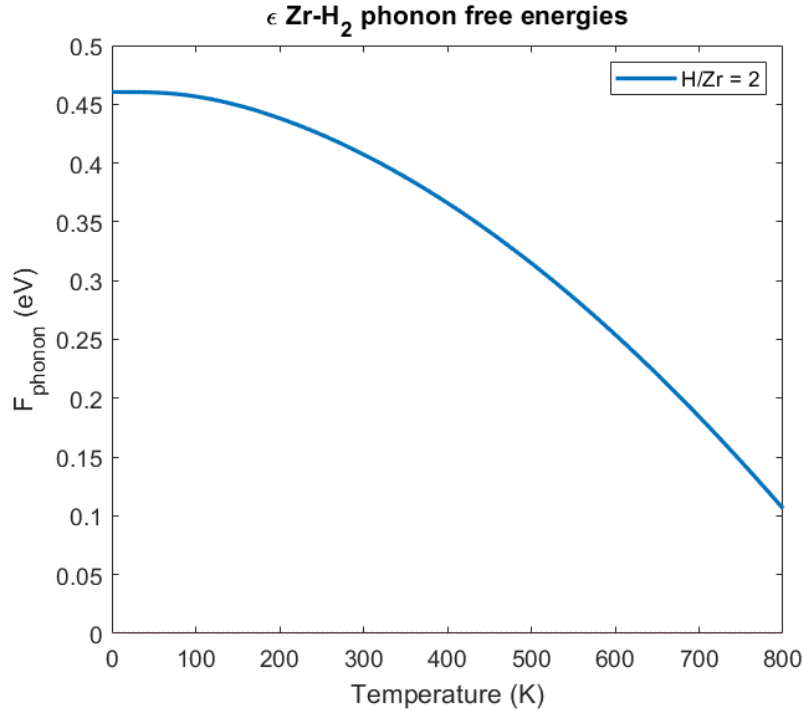


Figure 4-32. Calculated phonon free energies for ϵ -ZrH₂ (eV).

(blue circles) of each of the ground states. The phonon energy surfaces fitted with polynomial functions for each lattice model. These polynomials can be used to estimate the phonon free energy for a structure given its temperature and H concentration. To generate the total Gibbs free energy surfaces with both configurational and vibrational effects the estimated phonon free energy is added to the configurational free energies from Section 4.5.

The surface in Figure 4-33A is a polynomial surface, Equation 4-2, of degree 3 in both T and X, where T is the temperature in K, X is the concentration, H/Zr, and E_{vib} is the phonon free energy per atom. Details of the error values for this fit are reported in Table 4-8 and the residuals of the fit are shown in Figure 4-33B. The phonon free energies for the α -Zr become negative around 185 K, hcp-ZrH at 610 K, hcp-ZrH_{1.5} at 760 K, hcp-ZrH_{1.67} at 810 K and hcp-ZrH₂ at 875 K. The phonon free energy decreases as temperature increases, but increases as H content increases. These trends are observed in all lattice models, Figures 4-34, 4-35 and

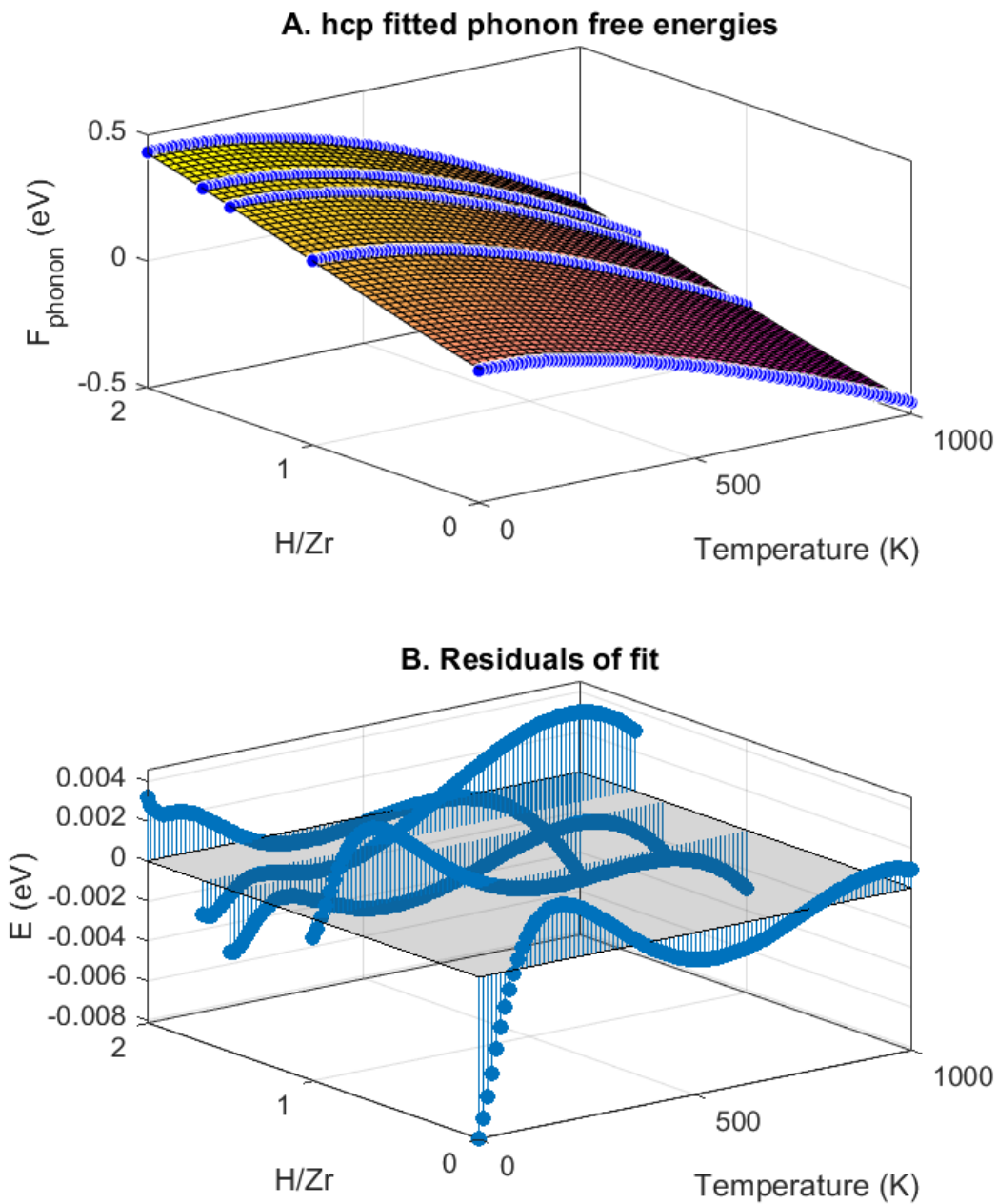


Figure 4-33. Phonon free energy surface for the hcp lattice model ground states. A) Blue circles indicate the phonon free energies calculated by Phonopy, the surface is the fit from Equation 4-2. B) Shows the residuals of the fit.

Table 4-8. Degree of fitted polynomial variables and error values for phonon energies of Zr-H structures. Errors include coefficients of determination (R^2) and root mean squared (RMS) values.

Structure	Degree of polynomial variable		R^2	RMS
	T	X		
hcp	3	3	0.9999	0.002
fct ($c/a > 1$)	3	2	1.0	0.0016
fcc (fluorite)	3	2	0.9993	0.0066
fct ($c/a < 1$)	3	2	1.0	0.0015

4-36.

$$E_{vib}^{hcp}(T, X) = 0.1193 + (-0.1677)T + 0.155X + (-0.03665)T^2 + (-0.004639)TX + (-0.0007193)X^2 + 0.004325T^3 + -0.006038T^2X + 0.001739TX^2 + (-0.004218)X^3 \quad (4-2)$$

Figure 4-34A shows the calculated phonon free energies of the ground states from the fct ($c/a > 1$) lattice model. The surface is fitted with Equation 4-3, with the degrees of the polynomial variables and error values reported in Table 4-8. The residuals of the fit are shown in Figure 4-34B. The phonon free energies for fct ($c/a > 1$)-Zr become negative around 160 K, γ -ZrH at 660 K, and fct ($c/a > 1$)-ZrH₂ at 920 K. The change to negative phonon energies occur at higher temperatures for H/Zr=1 and 2 than that of the same concentrations in the hcp lattice model.

$$E_{vib}^{fct(c/a > 1)}(T, X) = 0.09745 + (-0.1629)T + 0.1906X + (-0.03352)T^2 + (-0.001477)TX + (-0.0103)X^2 + 0.00459T^3 + (-0.006023)T^2X + (-0.001868)TX^2 \quad (4-3)$$

Figure 4-35A shows the calculated phonon free energies of the ground states from the fcc (fluorite) lattice model. The surface is fitted with Equation 4-4, with the degrees of the polynomial variables and error values reported in Table 4-8. The residuals of the fit are shown in Figure 4-35B. The phonon free energies for fcc-Zr become negative around 150 K, fcc-ZrH_{1.67} at 830 K, δ -ZrH_{1.88} at 870 K, and fcc-ZrH₂ at 930 K. The change to negative phonon energies occurs at higher temperatures for H/Zr=2 than the hcp and fct ($c/a > 1$)

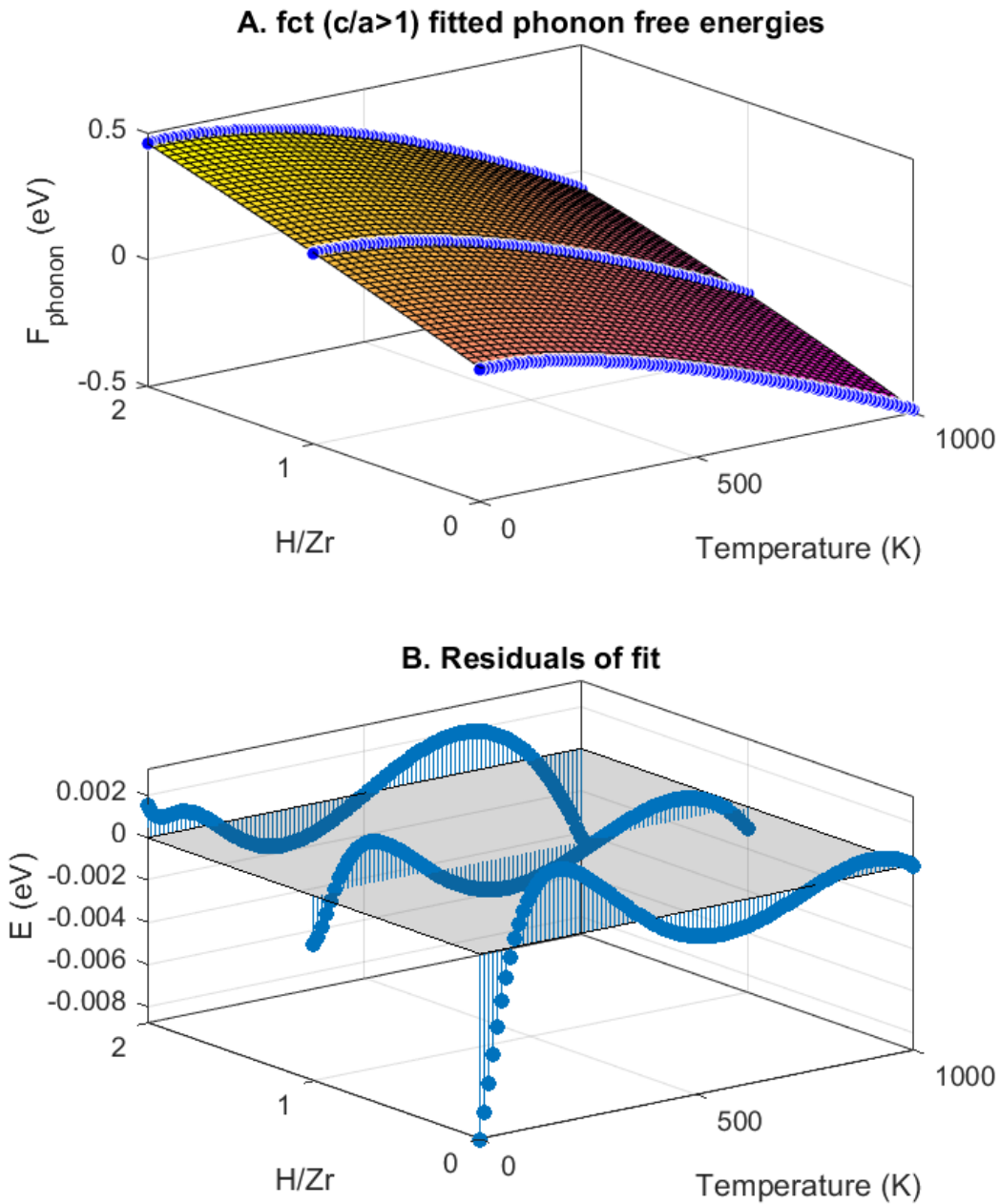


Figure 4-34. Phonon free energy surface for the fct ($c/a > 1$) lattice model ground states. A) Blue circles indicate the phonon free energies calculated by Phonopy, the surface is the fit from Equation 4-3. B) Shows the residuals of the fit.

lattice models.

$$E_{vib}^{fcc}(T, X) = 0.1597 + (-0.1698)T + 0.2015X + (-0.03653)T^2 + (0.004924)TX + (0.01008)X^2 + 0.00395T^3 + (-0.005903)T^2X + (0.004384)TX^2 \quad (4-4)$$

Figure 4-36A shows the calculated phonon free energies of the ground states from the fct (c/a<1) lattice model. The surface is fitted with Equation 4-5, with the degrees of the polynomial variables and error values reported in Table 4-8. The residuals of the fit are shown in Figure 4-36B. The phonon free energies for fct (c/a<1)-Zr become negative around 160 K, fct (c/a<1)-ZrH_{1.5} at 810 K, and ε-ZrH₂ at 920 K. The change to negative phonon energies occurs at the same temperature for H/Zr=2 as the fct (c/a>1) lattice model, but is 10 K lower than the fcc lattice model.

$$E_{vib}^{fct(c/a<1)}(T, X) = 0.1345 + (-0.1621)T + 0.1946X + (-0.03482)T^2 + (-0.002431)TX + (-0.01038)X^2 + 0.004298T^3 + (-0.006245)T^2X + (-0.002641)TX^2 \quad (4-5)$$

4.7 Free Energy Surfaces

The total Gibbs free energy is calculated by adding the configurational, electronic and vibrational Gibbs free energies;

$$G_{total} = G_{config} + G_{ele} + G_{vib} \quad (4-6)$$

In this work the electronic contribution is assumed to be small and has not been calculated.

The configurational contribution was calculated in Section 4.5. With Equations 4-2, 4-3, 4-4 and 4-5 for estimating the phonon free energies per atom at specific temperatures and concentrations, the phonon Gibbs free energies are calculated for all stable structures from the MC simulations as the vibrational contribution.

The total Gibbs free energies in Figures 4-37, 4-38, 4-39 and 4-40 were generated with α-Zr and H₂ (gas) as reference states. . These can be used to create $G - X$ curves from which

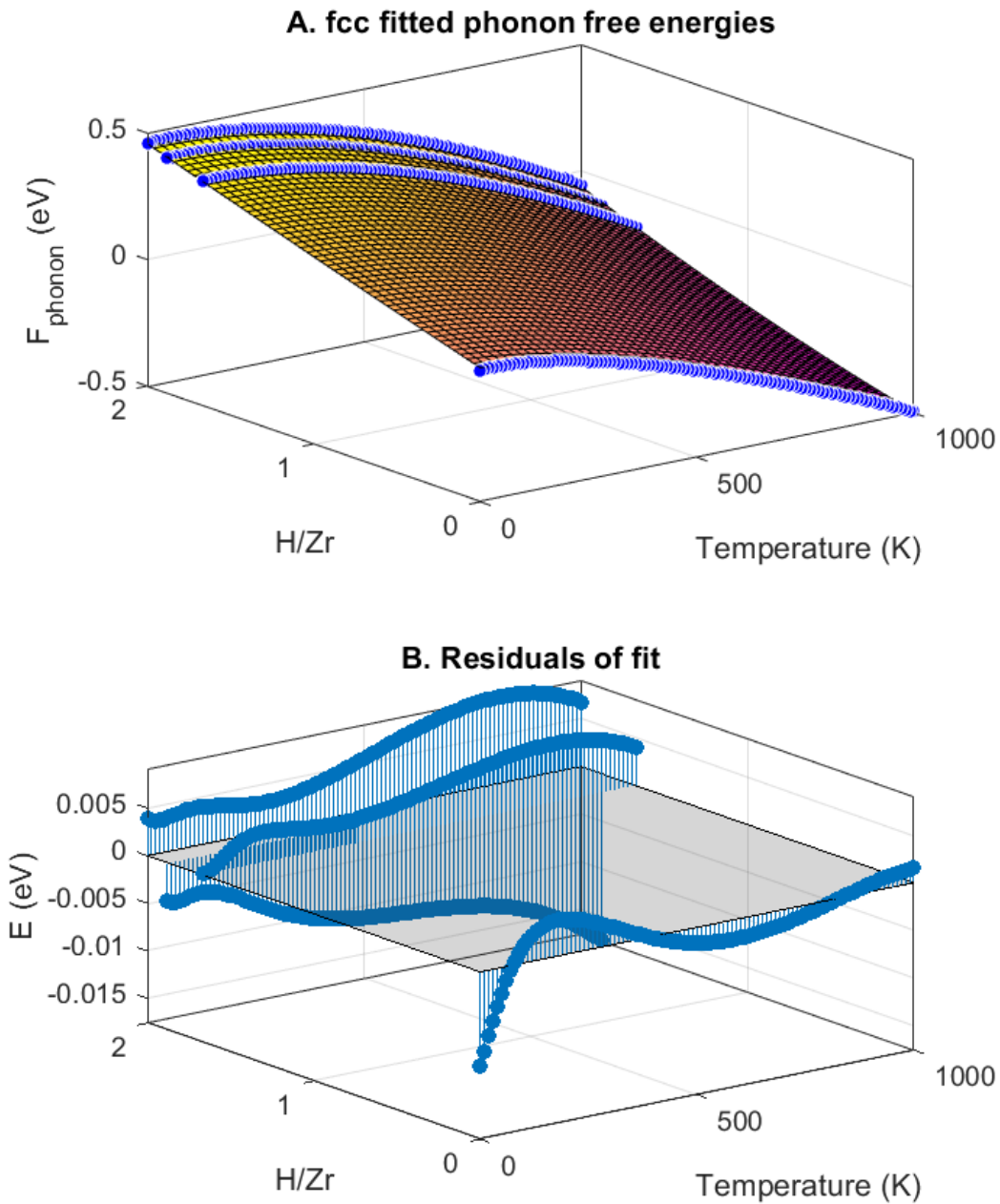


Figure 4-35. Phonon free energy surface for the fcc (fluorite) lattice model ground states. A) Blue circles indicate the phonon free energies calculated by Phonopy, the surface is the fit from Equation 4-5. B) Shows the residuals of the fit.

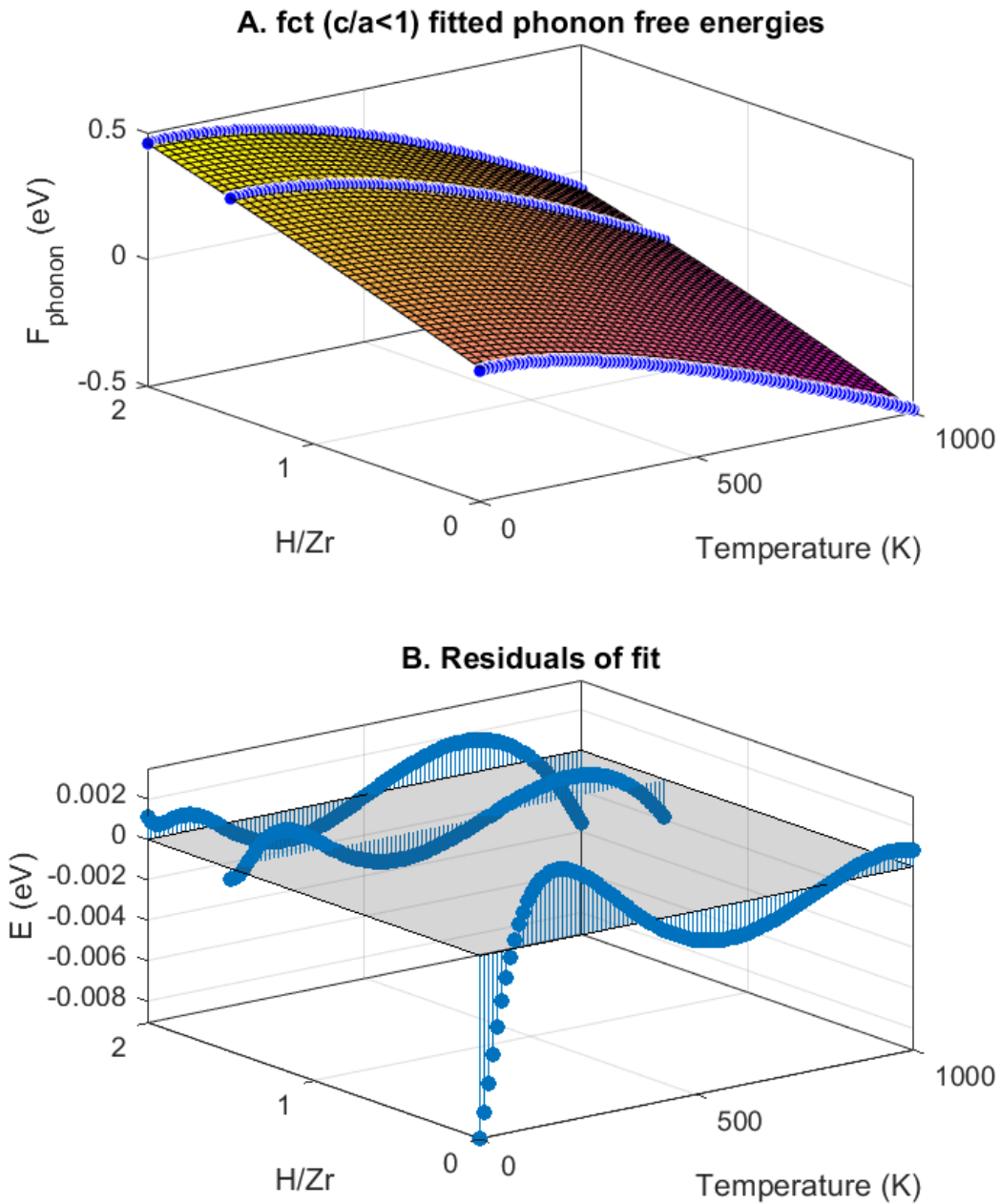


Figure 4-36. Phonon free energy surface for the fct ($c/a < 1$) lattice model ground states. A) Blue circles indicate the phonon free energies calculated by Phonopy, the surface is the fit from Equation 4-5. B) Shows the residuals of the fit.

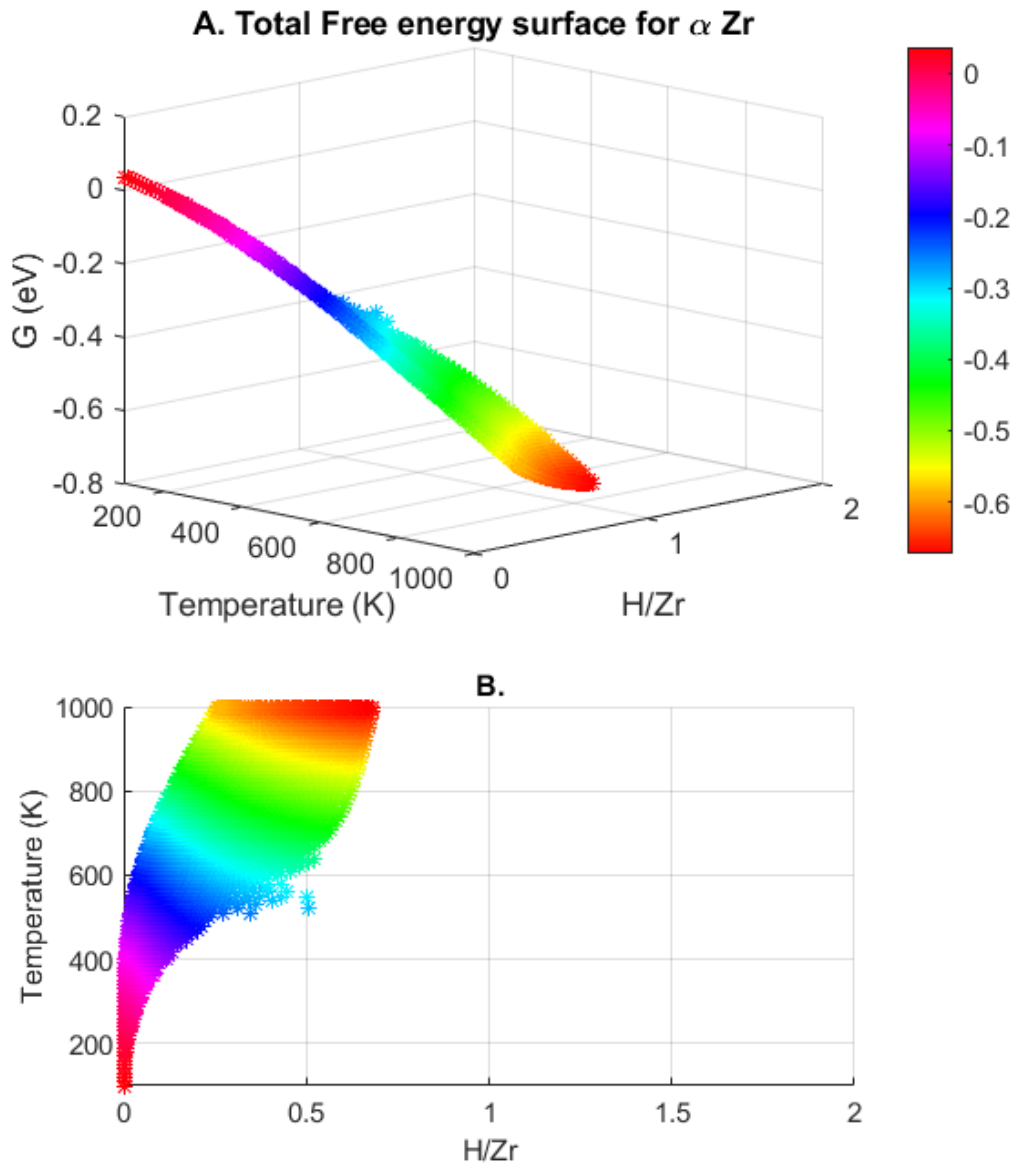


Figure 4-37. Total free energies for α -Zr. Reference states are α -Zr and H_2 (gas).

a phase diagram can be generated using the common tangent method. An example of the $G - X$ curves for temperatures ranging from 100 K to 900K are shown in Figure 4-41 and an example of common tangent construction in Figure 4-42.

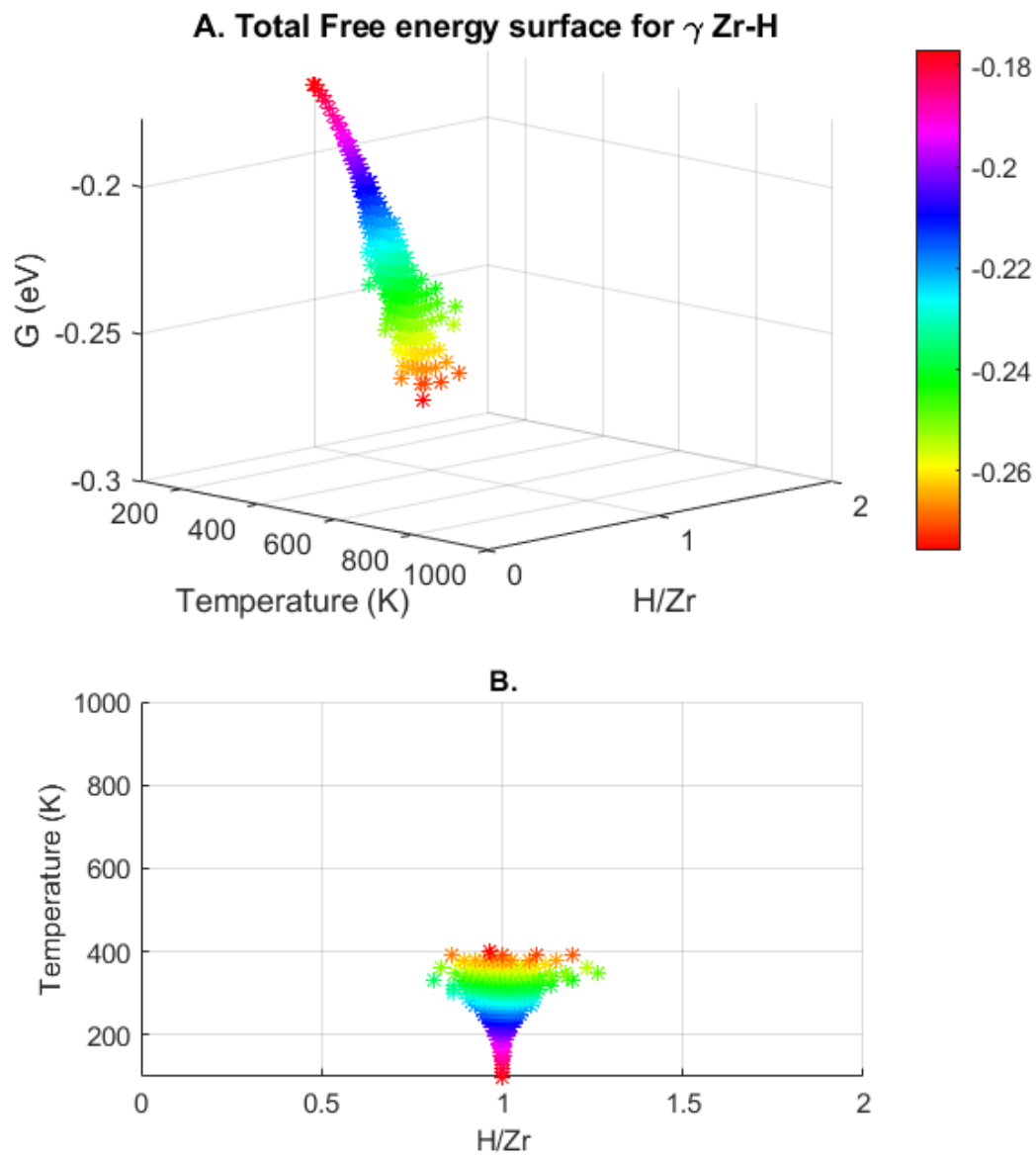


Figure 4-38. Total free energies for γ -ZrH. Reference states are α -Zr and H_2 (gas).

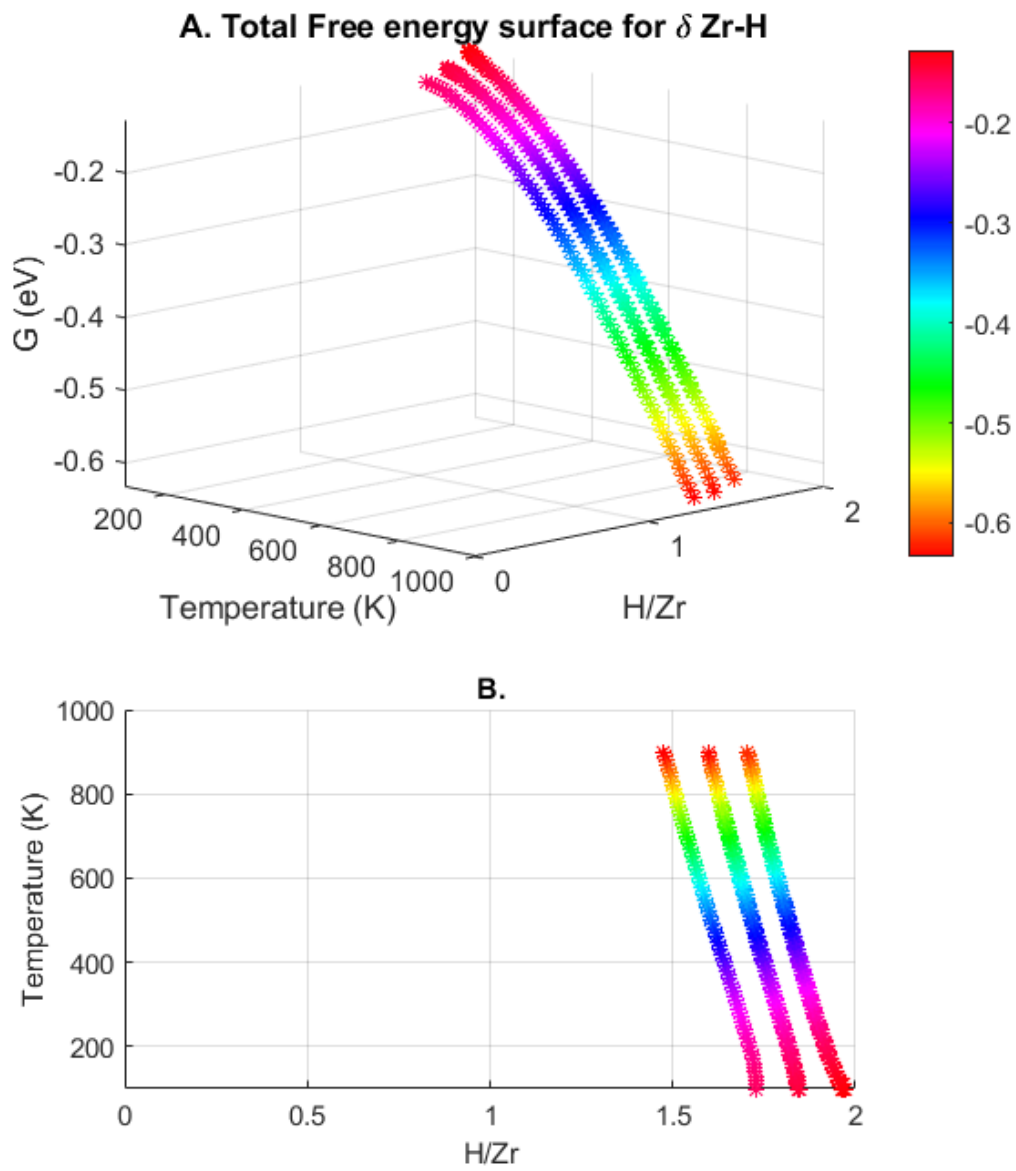


Figure 4-39. Total free energies for δ -ZrH_x. Reference states are α -Zr and H₂ (gas).

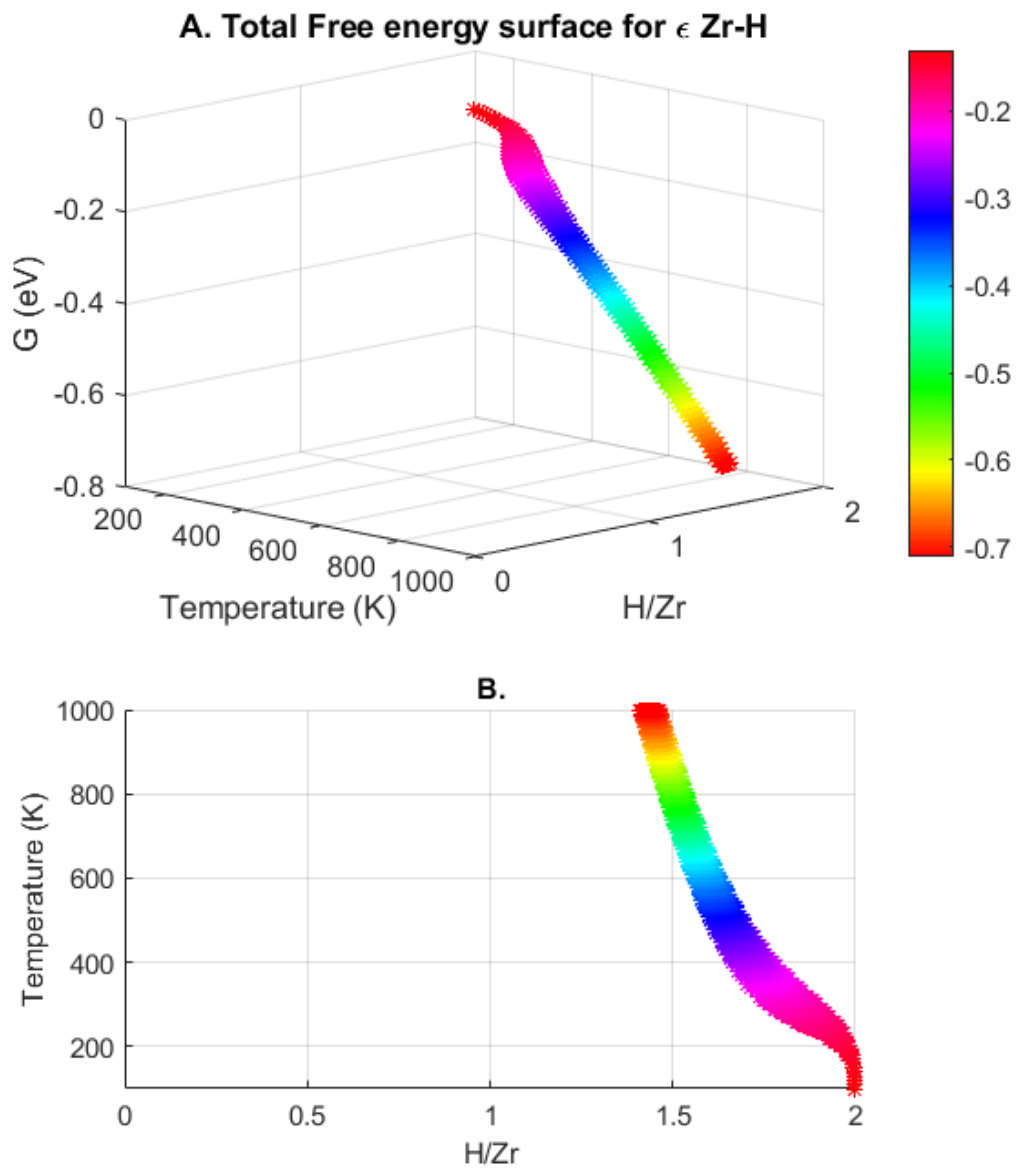


Figure 4-40. Total free energies for ϵ -ZrH₂. Reference states are α -Zr and H₂ (gas).

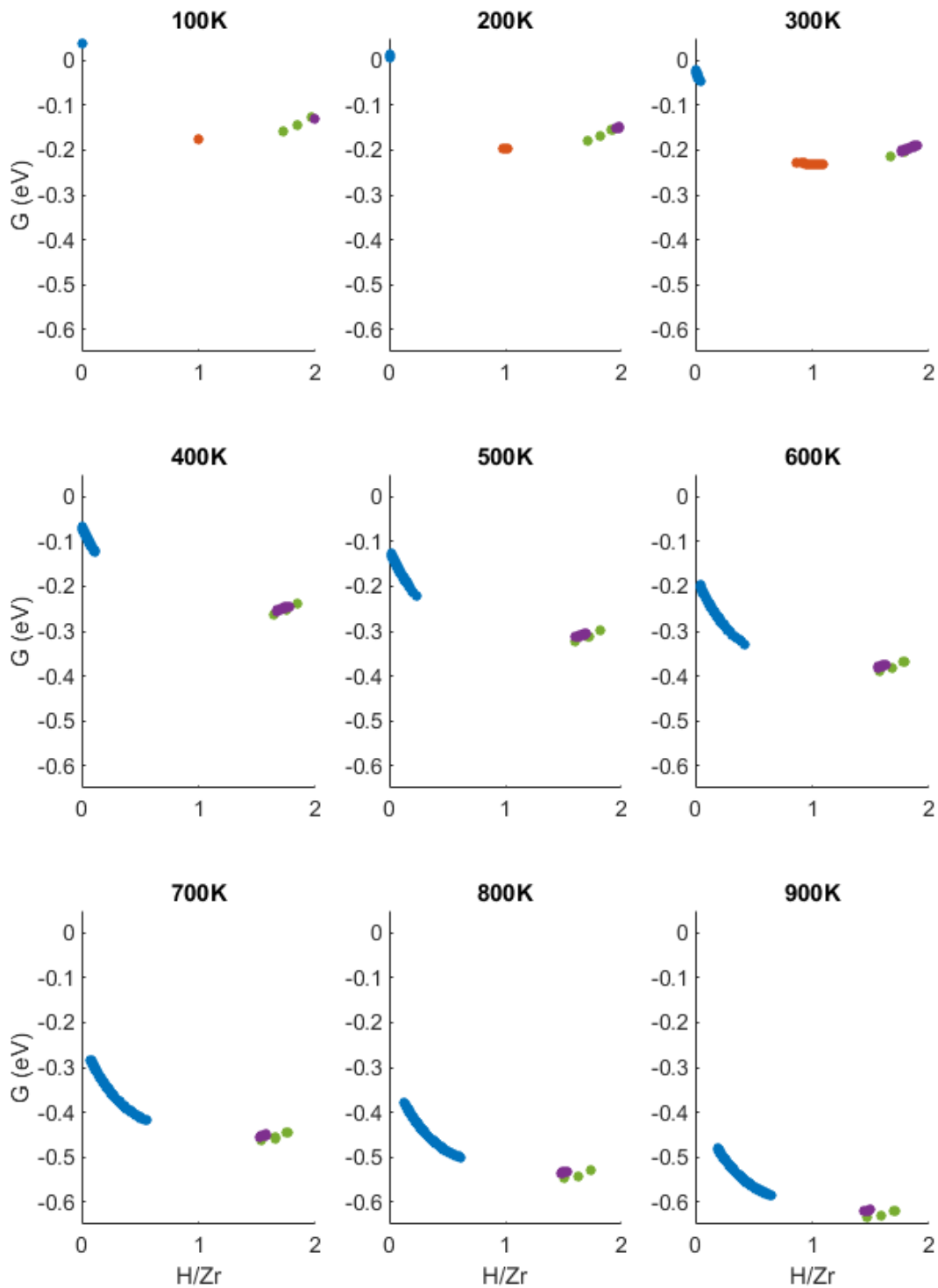


Figure 4-41. Temperature sequence of G-X curves for Zr-H system. α -phase indicated by blue, γ by orange, δ by green and ϵ by purple.

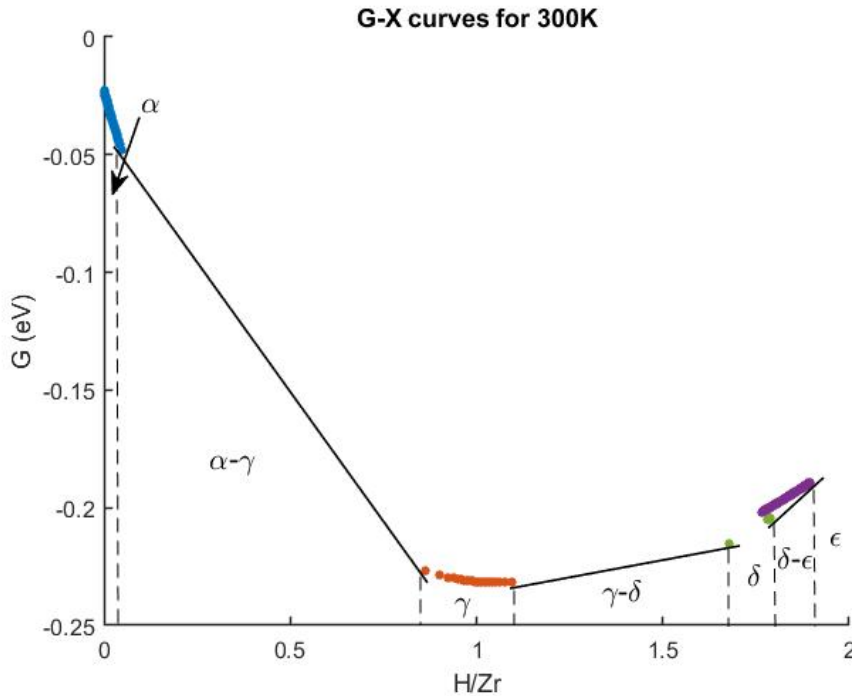


Figure 4-42. Example of common tangent construction for the G-X curves at 300K. Common tangent lines are drawn between the α -phase (blue) and γ -phase (orange), the γ -phase and the δ -phase (green), and the δ -phase and the ϵ -phase (purple).

4.8 Conclusions

Although a phase diagram has not been constructed at this point in time, the example of common tangent construction in Figure 4-42 shows how the range of stability for each phase can be estimated. In comparison to experimental phase diagrams, Figures 1-4, 4-43 and 4-44, in this work the α -phase has a wider region of stability at high temperatures, showing stability to approximately 0.65 wt.% H, or 40 atomic % H. The γ -phase is found to be stable below 400 K, forming a line compound below 200 K at 1 wt.% H. This suggests the γ -phase is low temperature phase, and corresponds to the phase diagrams of Figures 4-43 and 4-44. It may form as the temperature of the cladding increases after insertion into a reactor, but is unlikely to form at operating temperatures as they are generally higher than 400 K. The δ -phase forms from 0 to approximately 300 K, with a over a range extending from 1.71-1.85 wt.% H at 100 K to 1.67-1.78 wt.% H at 300 K, which similar to some experimental phase diagrams, Figures 4-44 and 1-4 (1999DUP). Interestingly, above 300 K the range of stability for the δ -phase

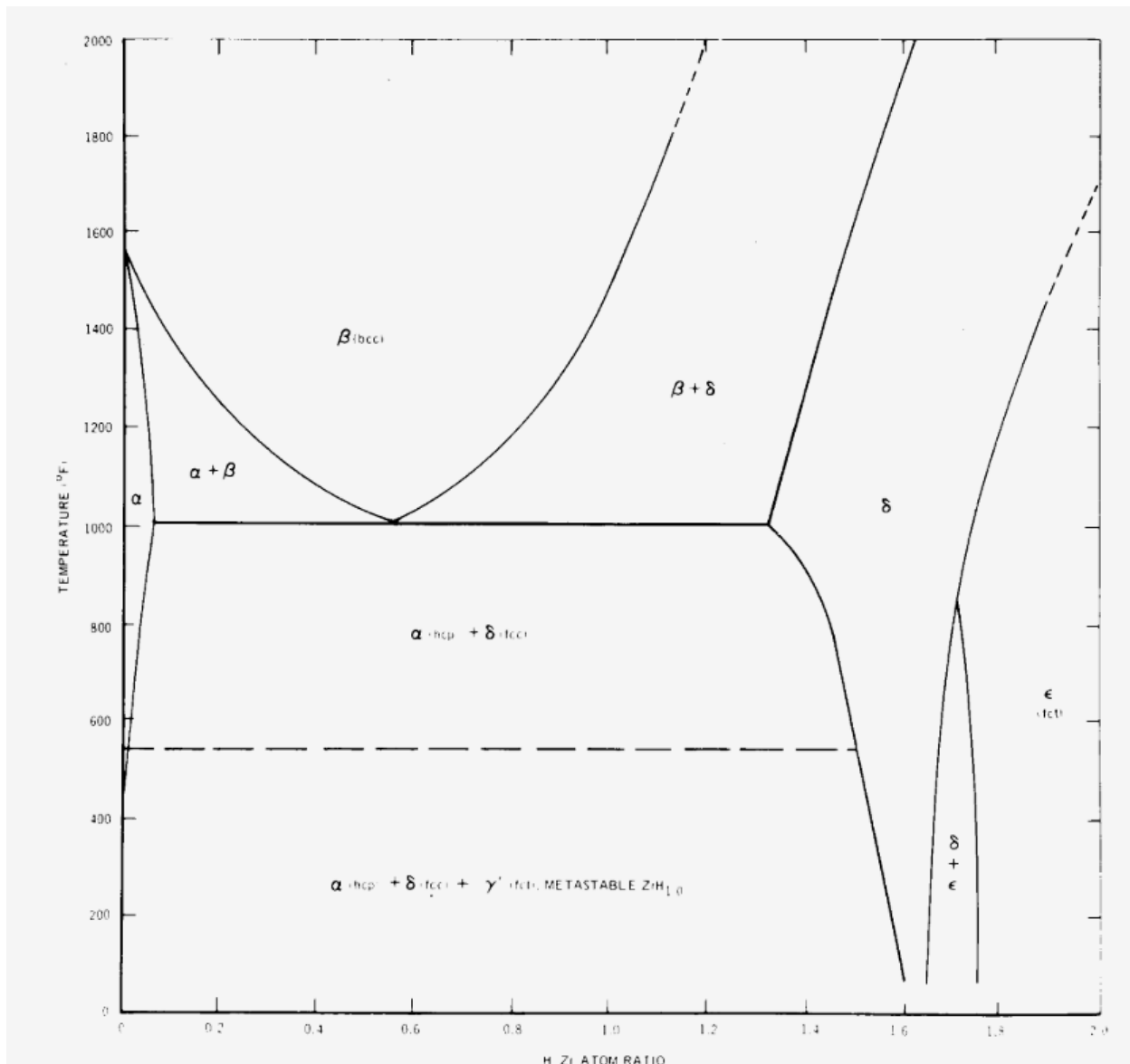


Figure 4-43. Zirconium-Hydride phase diagram published by Simnad et al.[7]. [Used with permission from Simnad et al.[7]]

widens to 1.47 to 2 wt.% H at 900 K, which has also been experimentally observed but at higher temperatures, Figures 4-43 and 1-4 (1990Zuz). Finally, the ϵ -phase is stable at 1.9-2 wt.% H from 0 K to 300 K.

These free energy surfaces are intended for use by mesoscale modeling techniques. In future work it is intended that the surfaces will be fit with a Gibbs free energy functional, as a function of temperature and concentration. Once a functional is fitted, code can be developed

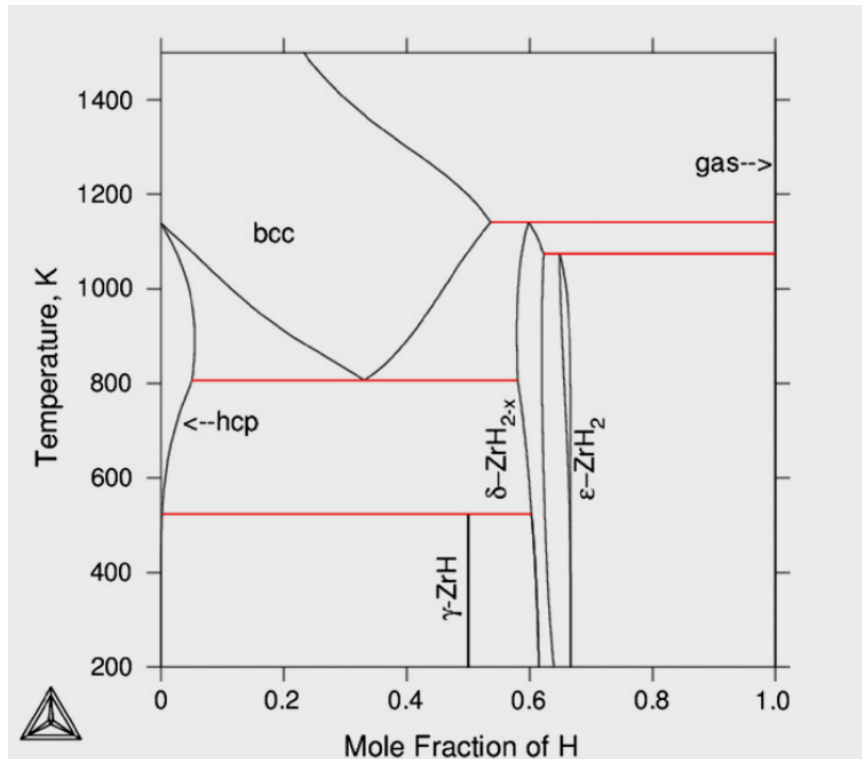


Figure 4-44. Zirconium-Hydride phase diagram published by Zhong et al.[8]. [Used with permission from Zhong et al.[8]]

to calculate the phase diagram. However, the differences in this work to some experimental results suggest that the sensitivity of the calculated free energies are significant. The energy differences between the phases is often on the order of 50 meV or less, and a small uncertainty in the energies of two phases may lead to a large uncertainty in a calculated phase diagram. It is recommended that these results be combined with experimental work before fitting to create more physically accurate functionals and phase diagrams. Additionally, as only the harmonic approximation was used for calculating phonon energies, work studying the quasi-harmonic vibrational contributions should also be undertaken.

CHAPTER 5 SUMMARY AND CONCLUSION

This dissertation has addressed two important problems. First, density functional theory has been used to investigate the formation of charged defect structures in Tellurium doped Gallium Arsenic semiconductors in an effort to increase the understanding of the mechanisms causing electrical deactivation in the material. Second, the thermodynamic properties of the Zirconium-Hydride system were modeled in order to calculate the Gibbs free energy surfaces from first principles methods for use with mesoscale modeling techniques. From the free energy surfaces free energy functionals can be fitted and phase diagrams can be generated.

5.1 Tellurium Doped Gallium Arsenide

In Chapter 3, the formation of charged defects in Tellurium (Te)-doped Gallium Arsenide (GaAs) was studied to gain insight in to the mechanisms behind electrical deactivation. In addition to the defect energetics of the system, a workflow for simulating charged intrinsic and extrinsic point defects and defect complexes was developed. From observations of the defect energetics, the estimation of the formation energy of the defects at 'infinite' distances is suggested in order to minimize the total number of calculations required in future studies of a similar nature. Finally, the suitability of the Freysoldt, Neugebauer and Van de Walle (FNV) method of calculating correction energies accounting for periodic image interactions was assessed.

The most likely defects to form, from lowest formation energies (E_{form}) up, are; the Ga vacancy with $E_{form} = -0.64$ eV for charge $q = -3$ (V_{Ga}^{-3}), as the Fermi level (μ_e) approaches the conduction band (CB), a Ga vacancy and Te substituted with an As atom with $E_{form} = -0.64$ eV for charge $q = -2$ on the system ($[V_{Ga}+Te_{As}]^{-2}$), as μ_e approaches the CB, a Ga vacancy and two Te atoms substituted with As atoms with $E_{form} = -0.62$ eV for charge $q = -1$ on the system ($[V_{Ga}+2Te_{As}]^{-1}$), as μ_e approaches the CB, two Te atoms substituted with As atoms with $E_{form} = -0.34$ eV for charge $q = +2$ ($[2Te_{As}]^{+2}$), as μ_e approaches the valence band (VB), and a Te substituted with an As with $E_{form} = -0.27$ eV

for charge $q = +1$ on the system ($\text{Te}_{\text{As}}^{+1}$), as μ_e approaches the VB. This is in agreement with experimental observations that found the V_{Ga}^{-3} , Te_{As} and $V_{\text{Ga}}+\text{Te}_{\text{As}}$ defects [12, 73].

This work also showed that the charge states of defects varied as the Fermi level shifts either towards the VB or CB. Te-doped GaAs is an n -type semiconductor, indicating the presence of electrons in levels just below the CB and a μ_e also near the CB. Defects predicted to be more stable as μ_e approaches the CB are V_{Ga}^{-3} , $\text{Te}_{\text{As}}^{-1}$, $[V_{\text{Ga}}+\text{Te}_{\text{As}}]^{-2}$, $[2\text{Te}_{\text{As}}]^{-1}$ and $[V_{\text{Ga}}+2\text{Te}_{\text{As}}]^{-2}$.

The defect concentration of V_{Ga} expected to increase as μ_e approaches the CB. Conversely, concentration of Te_{As} and 2Te_{As} are predicted to decrease as μ_e approaches the CB. As the number of Te atoms in the material remains constant, but the concentrations of Te_{As} and 2Te_{As} are predicted to decrease, it is theorized that the Te substitutional defects react with V_{Ga} to form defect complexes. Supporting this theory, the concentrations of the two complexes, $V_{\text{Ga}}+\text{Te}_{\text{As}}$ and $V_{\text{Ga}}+2\text{Te}_{\text{As}}$, are expected to increase as μ_e approaches the CB. The formation of Te-Ga vacancy complexes also leads to the charges across the system becoming less negative, as the most favorable complexes have a charge $q = -2$. This supports the conclusion of Kennon et al. [55] that the formation of group III vacancies-Te defect complexes result in electrical deactivation.

More work can be done to further support and refine the conclusion that group III vacancies-Te point defect reactions are the likely mechanism behind electrical deactivation in Te-doped GaAs. As mentioned in Chapter 3, it is well known that the LDA exchange correlation underestimates the band gaps. Now that the lowest formation energy states have been identified, this could be overcome by simulating them with hybrid functionals. This would also allow for the band structures to be studied in more detail and the Fermi level, conduction band maximum (CBM) and valence band minimum (VBM) to be determined with more accuracy. The VBM and CBM, in conjunction with the the law of mass action and vibrational contributions can be used to refine the defect concentrations as a function of temperature. Finally, the energy barriers to diffusion of the constituent atoms and vacancies, as well as the

binding energies of the defects can be calculated to further understand the kinetics of defects in the system.

The work by Kennon et al. [55] pertains to electrical deactivation observed in Te-doped Indium Gallium Arsenide (InGaAs) after post-growth heat treatments. To extend this work to the InGaAs system in the future, it is recommended that a similar study for Te-doped InAs is performed. Although defect formation energetics are likely to be very similar to the work herein as both Ga and In are group III ions, the differences in atomic radii and occupied electron shells is expected to influence the defect formation energies. The atomic radius of In is larger than Ga, 155 pm in comparison to 130 pm, and has a fully filled fourth shell and electrons occupying $4s^24p^1$ subshells. Te-doped InGaAs is also expected to have defect energetic values somewhere between that of GaAs and InAs. Directly studying the energetics of InGaAs would require simulations of large supercells to ensure periodic images of defects do not interact. The number of bonding environments for defects will also double, increasing the number of simulations required. It is recommended that the Te-doped InGaAs energetics are studied last so that trends observed in defect energetics in Te-doped GaAs and InAs can be used to limit the number of simulations required.

The workflow developed in this work can be employed in future efforts to model similar systems. It was found that favorable defect complexes were combinations of the favorable point defects, and so point defects should be simulated first and used to determine likely defect complexes. The addition of the minimum formation energies of the constituent defects for any μ_e will allow the formation energies for the defects at infinite distances to be estimated. This will help in determining if the defects prefer to be closer or further apart. The combination of these steps will allow for modelling of similar systems with a minimum number of simulations. It was also determined that the FNV method is suitable for calculating the periodic energy correction for defect complexes if a plateau is observable in the short-range potential, between the periodic images of the defect. This indicates the short and long-range effects have been separated.

5.2 Zirconium Hydride

In Chapter 4, the Gibbs free energy surfaces for the Zr-H system, including configuration and vibrational contributions, were generated from first principles calculations, statistical mechanical techniques and finite displacement methods. The cluster expansion (CE) method coupled with density functional theory (DFT) was used to find the ground states in the range of 0 to 2 wt.% H for the four different lattice models which have been experimentally observed in the Zr-H system. The cluster information and effective cluster interactions generated by the CEs was inputted into a semi-grand canonical Monte-Carlo (MC) simulation to generate finite temperature effects due to configurational disorder. Phonon free energies were calculated for the ground states found by the CEs by the finite displacement method under the harmonic approximation. The resulting energies were fitted as a function of temperature and concentration so that the vibrational free energy could be calculated and added to the configurational free energies of the stable structures found by the MC simulations. From the total configurational and vibrational energies the Gibbs free energy surfaces were constructed and trends in phase stability could be garnered.

The CE for the hcp Zr-H phases found five ground states, of which only the α -Zr and hcp ZrH_2 phases did not relax to different structures. The CE also found three of the proposed $\zeta\text{Zr}_2\text{H}$ structures, suggested by Zhao et al. [6] to be a new ground state in the Zr-H system. However, as they had formation energies higher than the convex hull it was concluded that they are not ground states. The CE for the fct ($c/a > 1$) lattice model was used to determine that including octahedral interstitial H sites in the lattice models is not required, and correctly found the γ -ZrH ground state. The fcc (fluorite-like) CE required a tighter constraint on lattice strain (4% as opposed to 10%) to find the δ - $\text{ZrH}_{1.67}$ ground state without relaxing to another structure. The ability of the CE to predict more ground states beyond structures with 30 atoms or more indicated that the δ - $\text{ZrH}_{1.67}$ may be disordered in the H sublattice. The fcc CE also found δ - $\text{ZrH}_{1.86}$ to be a ground state. The fct ($c/a < 1$) CE only found the ϵ - ZrH_2 phase to be stable, with the other ground states relaxing to different structures.

MC simulations of the finite temperature effects for the ground states from the CEs which did not relax into different structures were calculated. The α -Zr phase was found to have a wide range of stability for high temperatures, approximately ranging 0 to 0.66 wt.% H at 900 K. The γ -ZrH phase was found to be stable only below 400 K, suggesting it is a metastable low temperature phase. The δ -ZrH_{1.67} phase initially produced unrealistically high energies. The structure was simulated with a disordered H sublattice, which resulted in energies similar to that of the δ -ZrH_{1.86} phase. Both phases appeared to be line compounds. The ϵ -ZrH₂ phase was found to be stable at 0 K; however, as the temperature increased its range of stability expanded slightly and shifted towards 1.4 wt.% H at 1000 K.

Phonon free energies were calculated and added to the configurational free energy contributions calculated by the MC simulations. This energy can be used to construct Gibbs free energy surfaces and estimates of the range of stability of the phases were made. Similar to the estimates made using just the configurational entropy from the MC simulations, the α -Zr shows a wide range of stability for high temperatures, which is not seen experimentally. The γ -ZrH phase continues to be predicted as a metastable phase, existing as a line compound below 200 K. This is in agreement with some experimental works. The δ -ZrH_{1.67} phase is predicted to be a form below 300 K in the 1.67 to 1.85 wt.% H range. As its temperature increases above 300 K its range of stability widens to 1.47 to 2 wt.% H. Finally, the ϵ -ZrH₂ phase is only predicted to be stable below 300 K and with high H concentrations, 1.9 to 2 wt.% H. Experimental phase diagrams show different ranges of stability for both the δ and ϵ phases, of which some support the results from this work.

Due to the differences between this work and experimental works, it is suggested that these results are combined with experimental works in order to create a more accurate phase diagram for the Zr-H system. Once experimental results are included it will be possible to fit Gibbs free energy functionals which should accurately capture the physics of the system for use in mesoscale modelling techniques. Finally, to increase the accuracy of the simulated data, the

inclusion of volume-dependent effects should be added as vibrational contributions calculated with quasi-harmonic approximation.

APPENDIX A
TE DOPED GAAS SUPPLEMENTAL DATA

Data in Table A-1 calculated with Equation 2-1, below, for stoichiometric conditions using chemical potentials listed in Table 3-2, below.

$$E_{form}[X^q] = E_{tot}[X^q] - E_{tot}[bulk^0] - \sum_i n_i \mu_i + qE_F + E_{corr} \quad (2-1)$$

Data in Table A-3 calculated with Equation 2-22, also below.

Table 3-2. Calculated chemical potentials and energies of bulk Ga, As, Te and GaAs. Chemical potentials in the bulk, $\mu_{(bulk)}$, for Ga, As and Te are in eV per atom and energy per pair of bulk GaAs, $E_{GaAs(bulk)}$ is in eV per formula unit.

System	Energy (eV per atom or formula unit)
μ_{Ga}	-3.93
μ_{As}	-5.71
$\mu_{Te(bulk)}$	-3.80
$E_{GaAs(bulk)}$	-9.64

$$\epsilon(q_a/q_b) = \frac{E_{form}(X^{q_a}; E_F = 0) - E_{form}(X^{q_b}; E_F = 0)}{q_b - q_a} \quad (2-26)$$

Table A-1. Defect formation energies (E_{form}) in eV for Te doped GaAs defects. Calculated with Equation 2-1 and chemical potentials of the bulk elements.

Defect	Distance	Charge (q)						
		-3	-2	-1	0	+1	+2	+3
V_{Ga}	-	3.842	3.175	2.856	2.884	3.244	3.949	5.002
V_{As}	-	5.275	4.237	3.526	3.070	2.810	3.214	3.451
Ga_I	-	8.426	6.364	4.583	3.124	2.104	2.497	3.218
As_I	-	8.765	6.821	5.250	4.239	3.382	3.854	3.998
$Te_{I[Te-Ga]}$	-	10.799	8.873	7.434	6.360	5.621	5.242	5.242
$Te_{I[Te-As]}$	-	9.253	7.271	5.576	4.255	3.960	4.246	4.915
Te_{As}	-	6.039	4.008	2.246	0.789	-0.265	0.165	0.957
Te_{Ga}	-	7.278	5.294	4.552	3.232	2.318	2.419	3.033
$V_{Ga} + Te_{As}$	2.5 Å	4.113	2.348	1.879	1.768	1.992	2.597	3.534
	4.7 Å	4.700	2.929	2.422	2.283	2.475	3.023	3.914
	6.1 Å	4.839	3.049	2.537	2.371	2.543	3.074	3.960
	7.3 Å	4.796	3.044	2.584	2.454	2.621	3.228	4.181
$V_{Ga} + Te_{I[Te-X]}$	2.5 Å	7.244	5.289	3.726	2.882	2.611	2.443	3.058
	2.8 Å	6.736	5.358	4.123	3.166	2.318	2.417	3.028
	4.7 Å	7.037	5.109	4.207	2.844	1.850	1.927	2.465
	4.9 Å	7.137	6.462	6.461	6.348	6.590	7.141	7.824
	6.1 Å	7.923	6.740	5.750	5.571	5.753	6.235	4.062
	6.3 Å	7.535	6.865	6.104	5.945	6.144	6.666	7.505
$Te_{As} + Ga_I$	2.5 Å	9.821	7.789	6.000	4.449	3.201	2.316	2.597
	4.7 Å	9.727	7.956	6.043	4.410	3.087	2.143	2.363
	6.1 Å	9.951	7.839	5.979	4.395	3.124	2.235	2.438
	7.3 Å	10.064	7.904	5.990	4.356	3.030	2.084	2.278
$Te_{As} + As_I$	3.2 Å	9.925	7.978	6.314	5.014	3.985	3.196	3.744
$Te_{As} + Te_I$	2.7 Å	9.821	7.859	6.247	4.881	3.848	3.947	4.458
$V_{As} + Te_{Ga}$	2.5 Å	4.001	2.182	1.812	1.764	2.104	2.851	3.908
	4.7 Å	7.673	6.527	5.841	5.441	5.246	5.316	5.437
	6.1 Å	6.845	6.244	5.355	4.765	4.849	4.432	4.970
	7.3 Å	7.701	6.530	5.837	5.441	5.237	5.265	5.425
$2Te_{As}$	4.7 Å	7.260	5.174	3.354	1.808	0.572	-0.268	0.371
	5.6 Å	7.208	5.133	3.311	1.773	0.544	-0.291	0.340
	6.8 Å	7.184	5.090	3.274	1.730	0.492	-0.348	0.312
	7.9 Å	7.173	5.097	3.273	1.740	0.517	-0.314	0.327
$V_{Ga} + 2Te_{As}$	-	4.311	2.398	0.871	0.698	0.904	1.451	2.343
$2V_{Ga} + Te_{As}$	-	8.454	7.857	7.339	7.643	7.990	8.122	9.046
$V_{Ga} + 2Te_{I[Te-Ga]}$	-	9.680	7.658	6.027	5.427	4.569	4.539	4.871
$V_{Ga} + Te_{As} + Te_{I[Te-Ga]}$	2.6 Å	6.569	5.854	4.235	2.998	2.656	2.346	2.968
	4.4 Å	7.746	5.697	3.971	2.648	2.124	2.095	2.804
	5.9 Å	7.185	5.504	4.493	3.363	2.706	1.825	2.277

Table A-2. Correction energies (E_{corr}) in eV for Te doped GaAs defects.

Defect	Distance	Charge (q)						
		-3	-2	-1	0	+1	+2	+3
V_{Ga}	-	1.389	0.705	0.229	0.000	-0.017	0.193	0.651
V_{As}	-	1.215	0.565	0.199	0.000	-0.012	0.135	0.495
Ga_I	-	0.783	0.303	0.043	0.000	0.178	0.585	1.221
As_I	-	0.873	0.377	0.045	0.000	0.233	0.731	1.485
$Te_{I[Te-Ga]}$	-	0.873	0.377	0.045	0.000	0.233	0.731	1.485
$Te_{I[Te-As]}$	-	0.609	0.191	-0.017	0.000	0.254	0.743	1.443
Te_{As}	-	0.678	0.239	0.013	0.000	0.201	0.595	1.182
Te_{Ga}	-	0.855	0.345	0.072	0.000	0.211	0.705	1.464
$V_{Ga} + Te_{As}$	2.5 Å	1.239	0.633	0.211	0.000	0.024	0.297	0.792
	4.7 Å	1.290	0.667	0.222	0.000	0.010	0.255	0.726
	6.1 Å	1.311	0.671	0.231	0.000	0.006	0.251	0.729
	7.3 Å	1.197	0.585	0.196	0.000	0.006	0.333	0.891
$V_{Ga} + Te_{I[Te-X]}$	2.5 Å	0.846	0.345	0.062	0.000	0.226	0.721	1.485
	2.8 Å	0.936	0.387	0.062	0.000	0.205	0.701	1.449
	4.7 Å	0.570	0.143	-0.001	0.000	0.233	0.753	1.551
	4.9 Å	0.594	0.145	-0.024	0.000	0.248	0.719	1.386
	6.1 Å	0.987	0.397	0.030	0.000	0.201	0.621	1.602
	6.3 Å	0.954	0.297	0.001	0.000	0.228	0.681	1.350
$Te_{As} + Ga_I$	2.5 Å	0.657	0.187	-0.014	0.000	0.239	0.687	1.323
	4.7 Å	0.783	0.315	0.041	0.000	0.184	0.587	1.224
	6.1 Å	0.636	0.195	-0.016	0.000	0.245	0.711	1.347
	7.3 Å	0.765	0.291	0.030	0.000	0.192	0.603	1.242
$Te_{As} + As_I$	3.2 Å	0.843	0.329	0.043	0.000	0.201	0.619	1.275
$Te_{As} + Te_I$	2.7 Å	0.534	0.153	-0.038	0.000	0.308	0.859	1.608
$V_{As} + Te_{Ga}$	2.5 Å	0.837	0.319	0.051	0.000	0.188	0.615	0.250
	4.7 Å	0.978	0.425	0.095	0.000	0.122	0.429	0.825
	6.1 Å	1.140	0.357	0.086	0.000	-0.167	0.299	0.045
	7.3 Å	1.002	0.439	0.096	0.000	0.115	0.401	0.813
$2Te_{As}$	4.7 Å	0.444	0.077	-0.070	0.000	0.293	0.793	1.476
	5.6 Å	0.432	0.077	-0.069	0.000	0.290	0.793	1.467
	6.8 Å	0.435	0.063	-0.077	0.000	0.294	0.799	1.500
	7.9 Å	0.429	0.073	-0.073	0.000	0.295	0.797	1.479
$V_{Ga} + 2Te_{As}$	-	0.819	0.339	0.067	0.000	0.160	0.543	1.149
$2V_{Ga} + Te_{As}$	-	1.080	0.507	0.174	0.000	0.053	0.171	0.681
$V_{Ga} + 2Te_{I[Te-Ga]}$	-	0.444	0.073	-0.075	0.000	0.316	0.901	1.773
$V_{Ga} + Te_{As} + Te_{I[Te-Ga]}$	2.6 Å	0.465	0.081	-0.080	0.000	0.312	0.929	1.755
	4.4 Å	0.531	0.111	-0.056	0.000	0.306	0.901	1.647
	5.9 Å	0.528	0.149	-0.080	0.000	0.291	0.813	1.632

Table A-3. Transition levels ($\epsilon(q_a/q_b)$) in eV for Te doped GaAs defects. Calculated with Equation 2-22.

Defect	Distance	Charge (q)					
		(+3/+2)	(+2/+1)	(+1/0)	(0/-1)	(-1/-2)	(-2/-3)
V_{Ga}	-	-1.05	-0.71	-0.36	-0.03	0.32	0.67
V_{As}	-	-0.24	-0.40	0.26	0.46	0.71	1.04
Ga_I	-	-0.72	-0.39	1.02	1.46	1.78	2.06
As_I	-	-0.14	-0.47	0.86	1.01	1.57	1.94
$Te_{I[Te-Ga]}$	-	0.00	0.38	0.74	1.07	1.44	1.92
$Te_{I[Te-As]}$	-	-0.67	-0.29	0.29	1.32	1.70	1.98
Te_{As}	-	-0.79	-0.43	1.05	1.46	1.76	2.03
Te_{Ga}	-	-0.61	-0.10	0.91	1.32	0.74	1.98
$V_{Ga} + Te_{As}$	2.5 Å	-0.94	-0.61	-0.22	0.11	0.47	1.76
	4.7 Å	-0.89	-0.55	-0.19	0.14	0.51	1.77
	6.1 Å	-0.89	-0.53	-0.17	0.17	0.51	1.79
	7.3 Å	-0.95	-0.61	-0.17	0.13	0.46	1.75
$V_{Ga} + Te_{I[Te-X]}$	2.5 Å	-0.62	0.17	0.27	0.84	1.56	1.96
	2.8 Å	-0.61	-0.10	0.85	0.96	1.23	1.38
	4.7 Å	-0.54	-0.08	0.99	1.36	0.90	1.93
	4.9 Å	-0.68	-0.55	-0.24	0.11	0.00	0.67
	6.1 Å	2.17	-0.48	-0.18	0.18	0.99	1.18
	6.3 Å	-0.84	-0.52	-0.20	0.16	0.76	0.67
$Te_{As} + Ga_I$	2.5 Å	-0.28	0.89	1.25	1.55	1.79	2.03
	4.7 Å	-0.22	0.94	1.32	1.63	1.91	1.77
	6.1 Å	-0.20	0.89	1.27	1.58	1.86	2.11
	7.3 Å	-0.19	0.94	1.33	1.63	1.91	2.16
$Te_{As} + As_I$	3.2 Å	-0.55	0.79	1.03	1.30	1.66	1.95
$Te_{As} + Te_I$	2.7 Å	-0.51	-0.10	1.03	1.37	1.61	1.96
$V_{As} + Te_{Ga}$	2.5 Å	-1.06	-0.75	-0.34	0.05	0.37	1.82
	4.7 Å	-0.12	-0.07	0.19	0.40	0.69	1.14
	6.1 Å	-0.54	0.42	-0.09	0.59	0.89	0.60
	7.3 Å	-0.16	-0.03	0.20	0.40	0.69	1.17
$2Te_{As}$	4.7 Å	-0.64	0.84	1.24	1.55	1.82	2.08
	5.6 Å	-0.63	0.83	1.23	1.54	1.82	2.07
	6.8 Å	-0.66	0.84	1.24	1.54	1.82	2.09
	7.9 Å	-0.64	0.83	1.22	1.53	1.82	2.08
$V_{Ga} + 2Te_{As}$	-	-0.89	-0.55	-0.21	0.17	1.53	1.91
$2V_{Ga} + Te_{As}$	-	-0.92	-0.13	-0.35	-0.30	0.52	0.60
$V_{Ga} + 2Te_{I[Te-Ga]}$	-	-0.33	0.03	0.86	0.60	1.63	2.02
$V_{Ga} + Te_{As} + Te_{I[Te-Ga]}$	2.6 Å	-0.62	0.31	0.34	1.24	1.62	0.71
	4.4 Å	-0.71	0.03	0.52	1.32	1.73	2.05
	5.9 Å	-0.45	0.88	0.66	1.13	1.01	1.68

APPENDIX B
ZR-H SUPPLEMENTAL DATA

Table B-1. Characteristics of calculated Cluster Expansions.

Characteristic	hcp	fct (c/a>1)		fcc		fct (c/a<1)
		tet only	oct + tet	10% strain	4% strain	
No. of structures	181	37	107	137	78	49
No. point clusters	1	1	2	1	1	1
No. pairs	11	4	8	34	18	12
No. triplets	-	-	11	16	16	1
No. quadruplets	-	-	3	17	17	1
CV score (meV/atom)	6.3	17.2	23.3	4	4.2	9.4

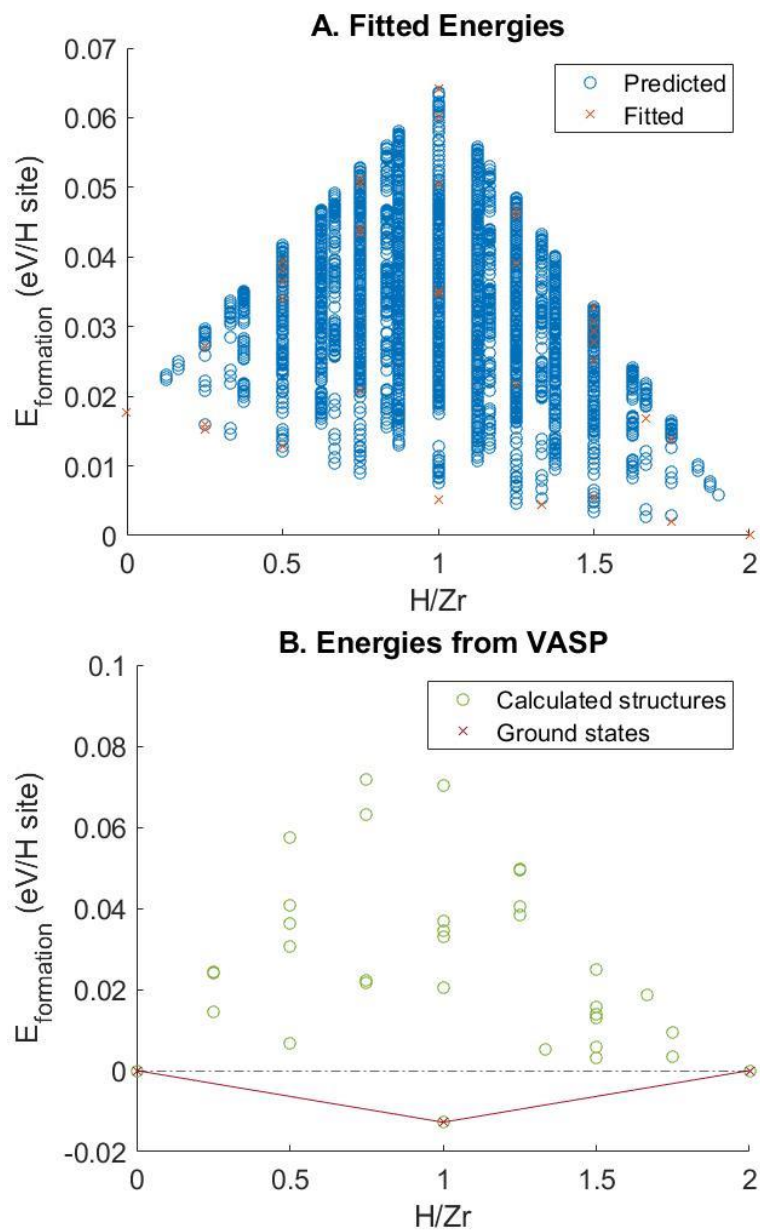


Figure B-1. Predicted, and fitted formation energies (eV/H site), referenced to fct ($c/a > 1$)-Zr and fct ($c/a > 1$)-ZrH₂, from the fct ($c/a > 1$) tetrahedral interstitials only lattice model fitted CE. A) Shows the energies predicted by the CE, blue circles, and energies fitted by the CE, orange crosses. B) Shows the formation energies calculated by VASP, green circles, and the final ground states, red crosses.

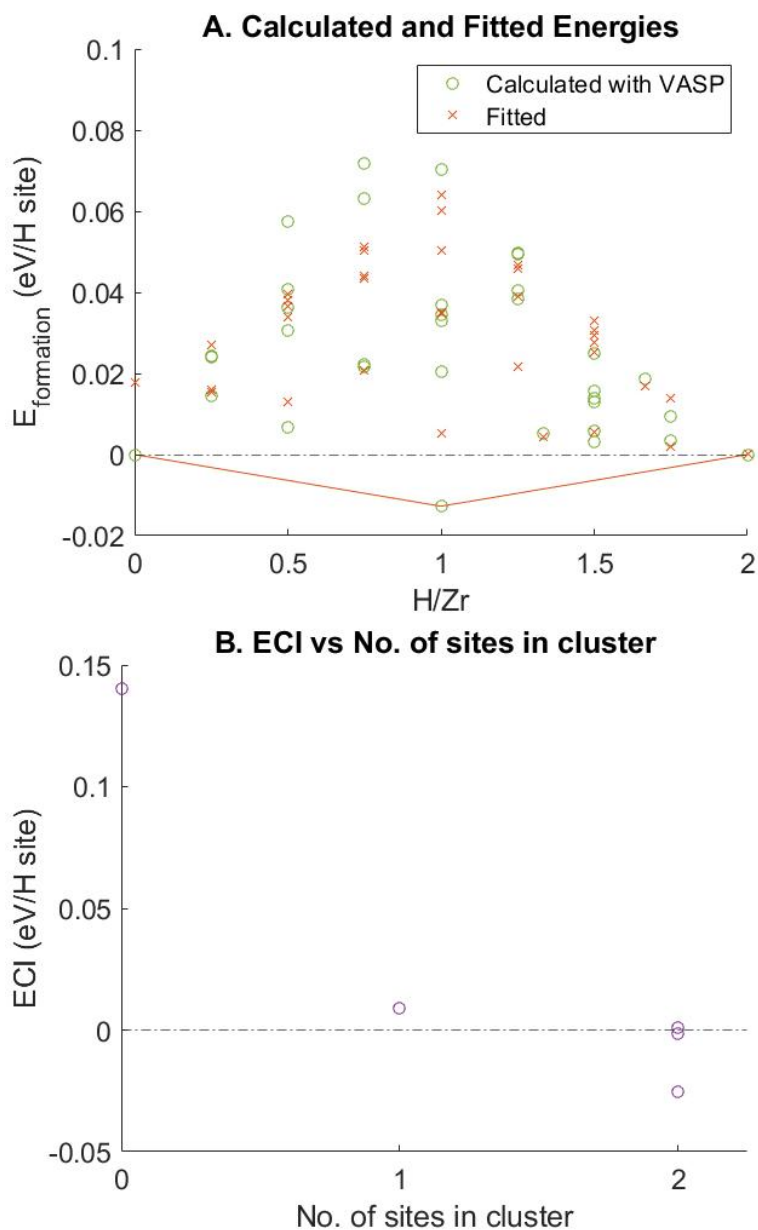


Figure B-2. Formation energies calculated with VASP and residuals of the fit of the fct ($c/a > 1$) tetrahedral interstitials only lattice model CE. A) Compares the VASP formation energies, green circles, with the CE fitted energies, orange crosses. B) Shows the ECI decreases as the number of sites in the clusters increases.

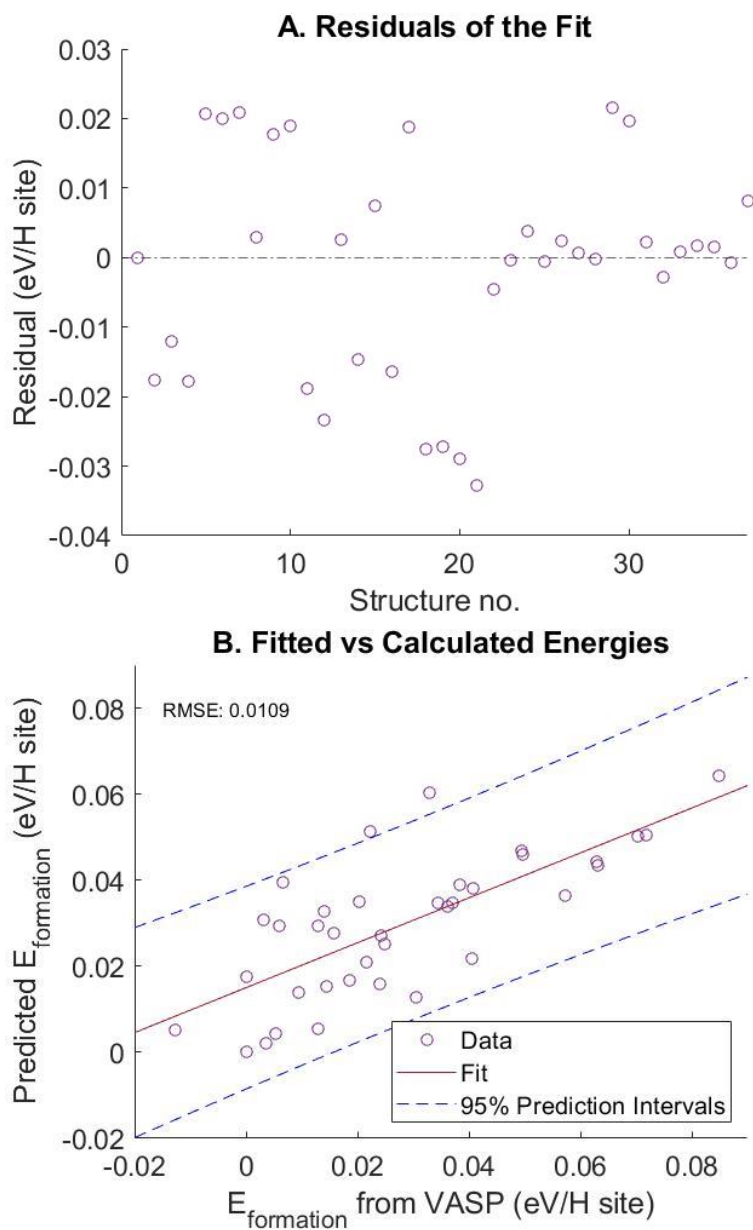


Figure B-3. Residuals of the fit and fitted vs calculated formation energies of the fct ($c/a > 1$) tetrahedral interstitials only lattice model CE. A) Shows the spread of the residuals of the fit range over 0.07 eV/H site. B) Compares the fitted formation energies (eV/H sites) to the formation energies (eV/H site) calculated by VASP.

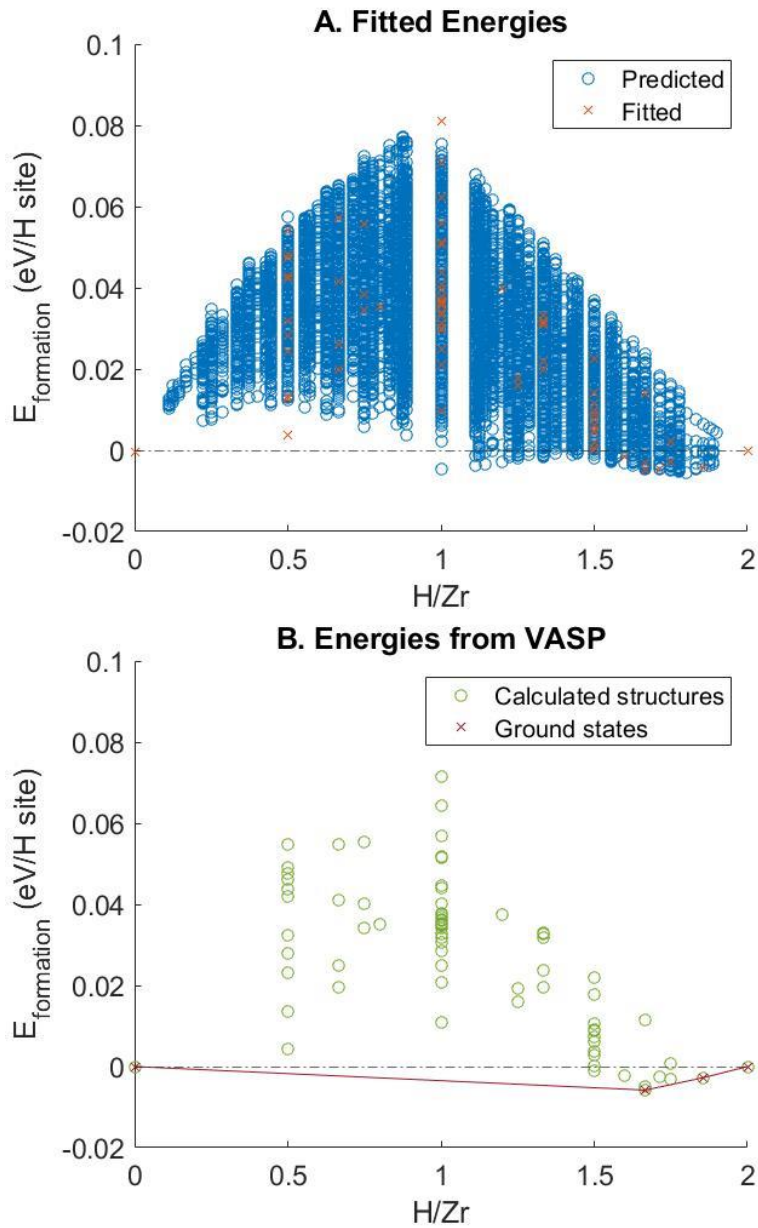


Figure B-4. Predicted, and fitted formation energies (eV/H site), referenced to fcc-Zr and fcc-ZrH₂, from the fcc-lattice model fitted CE limited to 4% strain. A) Shows the energies predicted by the CE, blue circles, and energies fitted by the CE, orange crosses. B) Shows the formation energies calculated by VASP, green circles, and the final ground states, red crosses.

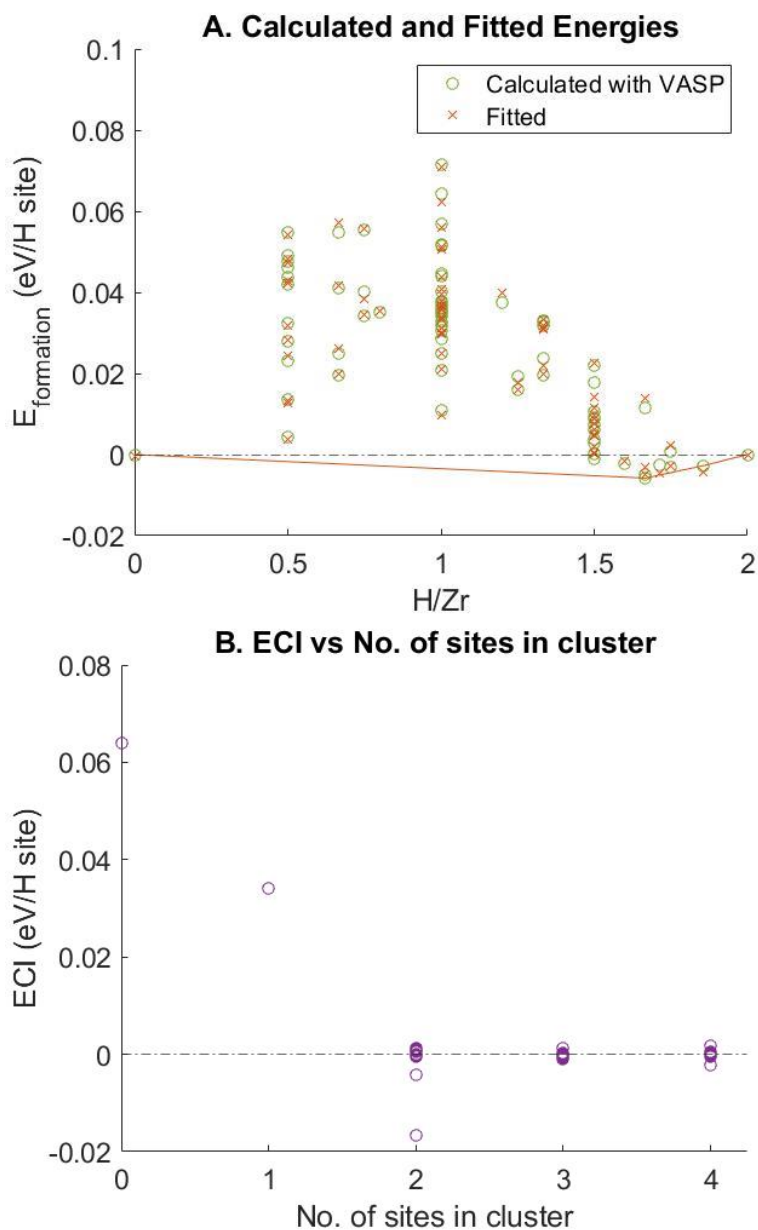


Figure B-5. Formation energies calculated with VASP and residuals of the fit of the fcc-lattice model fitted CE limited to 4% strain. A) Compares the VASP formation energies, green circles, with the CE fitted energies, orange crosses. B) Shows the ECI decreases as the number of sites in the clusters increases.

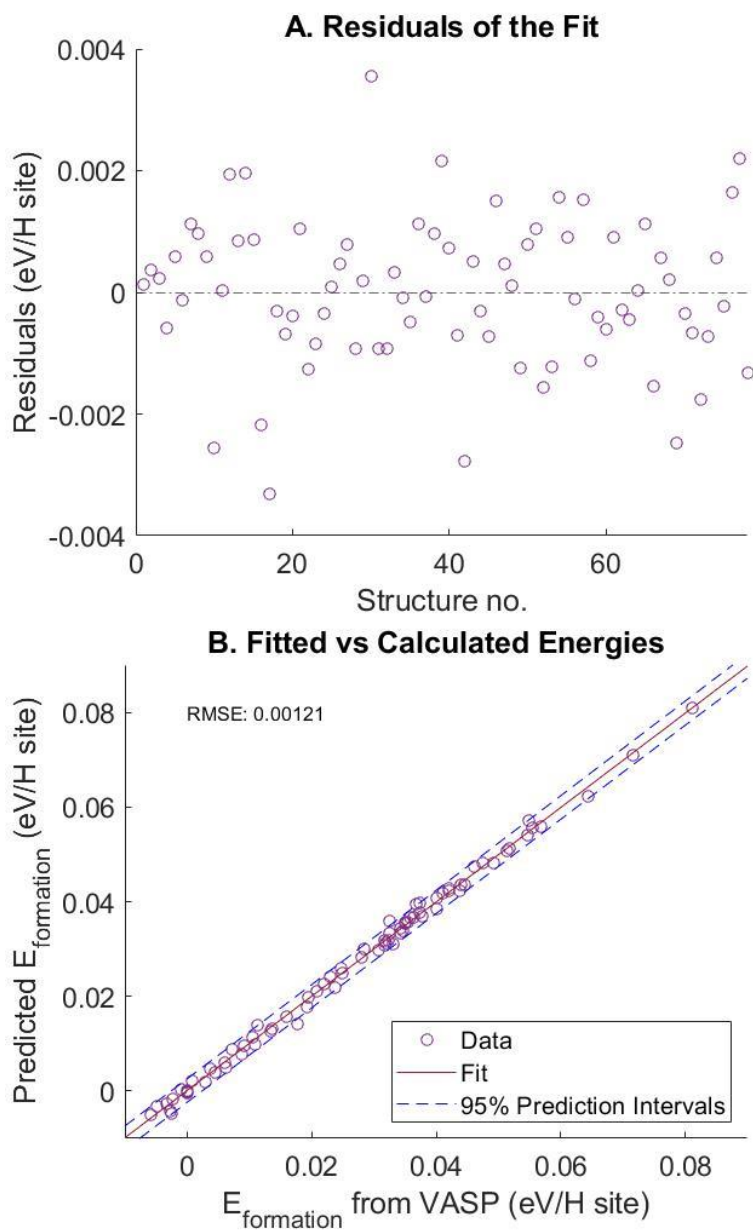


Figure B-6. Residuals of the fit and fitted vs calculated formation energies of the fcc-lattice model fitted CE limited to 4% strain. A) Shows the spread of the residuals of the fit range over 0.008 eV/H site. B) Compares the fitted formation energies (eV/H sites) to the formation energies (eV/H site) calculated by VASP.

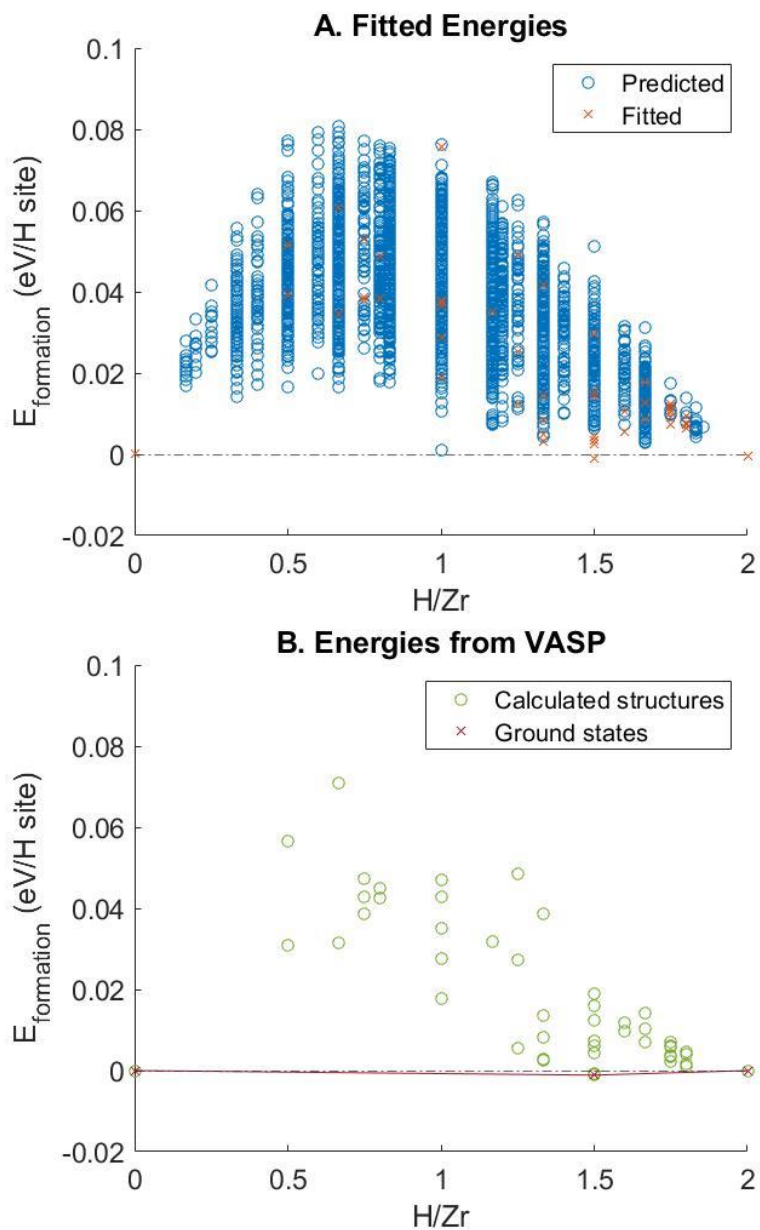


Figure B-7. Predicted, and fitted formation energies (eV/H site), referenced to fct ($c/a < 1$)-Zr and fct ($c/a < 1$)-ZrH₂, from the fct ($c/a < 1$)-lattice model fitted CE. A) Shows the energies predicted by the CE, blue circles, and energies fitted by the CE, orange crosses. B) Shows the formation energies calculated by VASP, green circles, and the final ground states, red crosses.

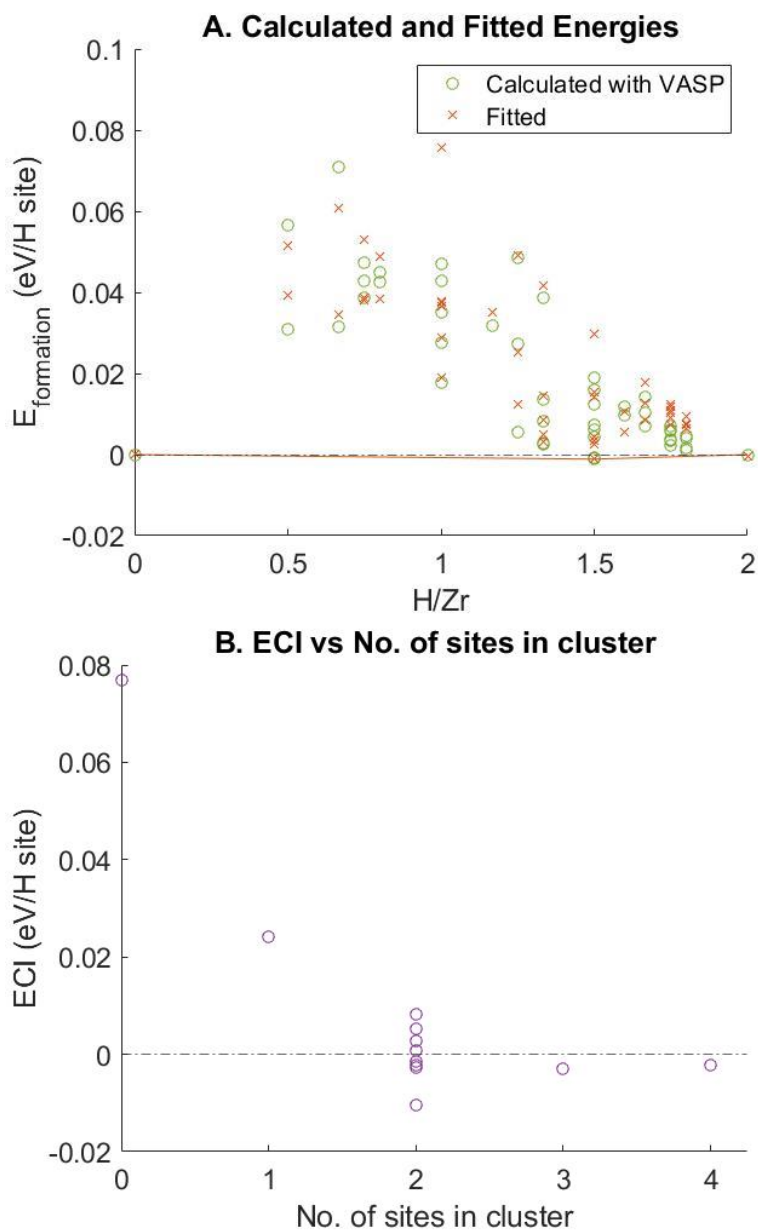


Figure B-8. Formation energies calculated with VASP and residuals of the fit of the fct ($c/a < 1$)-lattice model CE. A) Compares the VASP formation energies, green circles, with the CE fitted energies, orange crosses. B) Shows the ECI decreases as the number of sites in the clusters increases.

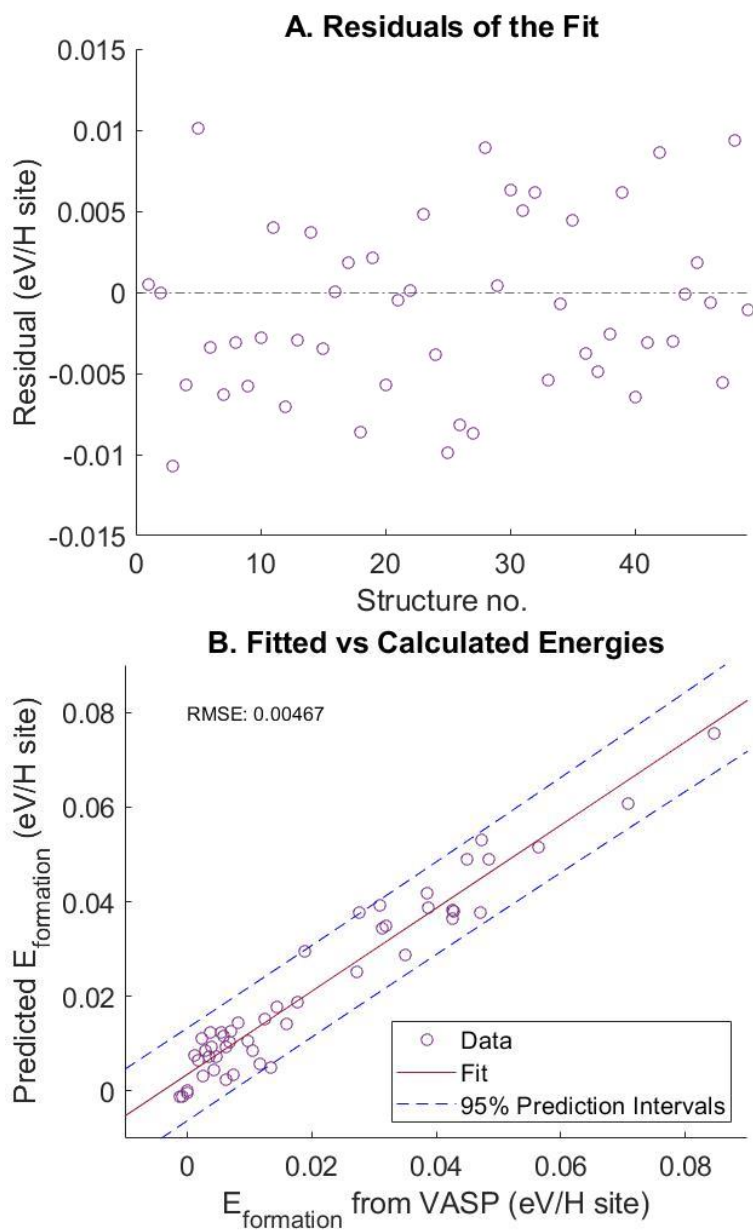


Figure B-9. Residuals of the fit and fitted vs calculated formation energies of the fct ($c/a < 1$)-lattice model CE. A) Shows the spread of the residuals of the fit range over 0.03 eV/H site. B) Compares the fitted formation energies (eV/H sites) to the formation energies (eV/H site) calculated by VASP.

Table B-2. Cluster and ECI information for hcp-lattice model.

Number of atoms in cluster	Diameter of cluster (Å)	No. of equivalent configurations	ECI
0	0.000000	1	0.095310
1	0.000000	4	0.009733
2	1.328847	2	0.054111
2	2.301632	6	-0.001488
2	3.254999	12	0.000317
2	3.255004	12	-0.000895
2	3.515805	12	-0.002528
2	3.986542	2	-0.018184
2	3.986548	6	-0.008044
2	4.407288	6	-0.003289
2	4.603267	12	-0.001434
2	5.146607	12	0.000217
2	5.146611	12	-0.003207

Table B-3. Cluster and ECI information for fct ($c/a > 1$) tetrahedral interstitials only-lattice model.

Number of atoms in cluster	Diameter of cluster (Å)	No. of equivalent configurations	ECI
0	0.000000	1	0.140211
1	0.000000	4	0.008801
2	2.289581	8	-0.001264
2	2.503157	4	-0.025128
2	3.237956	8	-0.001464
2	3.392341	16	0.001099

Table B-4. Cluster and ECI information for fct ($c/a > 1$) tetrahedral and octrahedral interstitials lattice model.

Number of atoms in cluster	Diameter of cluster (Å)	No. of equivalent configurations	ECI
0	0.000000	1	-0.876448
1	0.000000	2	0.050869
1	0.000000	4	0.124727
2	2.046348	16	0.039290
2	2.289581	8	-0.002104
2	2.503157	4	0.012310
2	3.237956	8	0.010684
2	3.237956	4	0.007885
2	3.392341	8	0.002547
2	3.392341	16	0.009042
2	3.830391	32	-0.002640
3	2.289581	16	0.001640
3	2.503157	8	-0.017599
3	3.237956	8	-0.015600
3	3.237956	16	-0.005859
3	3.237956	8	-0.000480
3	3.392341	16	-0.001645
3	3.392341	16	-0.004034
3	3.392341	16	-0.007796
3	3.392341	32	-0.000489
3	3.392341	16	-0.003174
3	3.392341	16	0.000000
4	3.237956	16	0.006955
4	3.237956	4	0.000549
4	3.237956	4	0.001224

Table B-5. Cluster and ECI information for fcc-lattice model limited to 10% strain.

Number of atoms in cluster	Diameter of cluster (Å)	No. of equivalent configurations	ECI
0	0.000000	1	0.065134
1	0.000000	2	0.032384
2	2.301633	6	0.000724
2	3.255000	12	0.000899
2	3.986544	4	-0.011100
2	3.986544	4	-0.004764
2	4.603265	6	-0.002590
2	5.146607	24	-0.000510
2	5.637825	24	-0.000507
2	6.510000	12	-0.001784
2	6.904898	12	0.001528
2	6.904898	12	-0.000490
2	6.904898	6	-0.000171
2	7.278401	24	-0.000711
2	7.633651	12	-0.000094
2	7.633651	12	0.000293
2	7.973089	8	-0.000357
2	8.298654	24	-0.000111
2	8.611920	48	-0.000718
2	9.206530	6	-0.000369
2	9.489874	12	-0.000416
2	9.489874	24	-0.000500
2	9.489874	12	0.000240
2	9.765000	24	-0.000423
2	9.765000	12	0.000019
2	10.032583	12	-0.002135
2	10.032583	12	0.000509
2	10.293213	24	0.000550
2	10.547405	24	0.000296
2	10.547405	24	-0.001337
2	10.795613	24	0.001409
2	11.275650	24	0.001073
2	11.508163	24	0.000321
2	11.508163	6	0.001992
2	11.736069	48	-0.000028
2	11.736069	24	0.001332
3	3.255000	24	-0.000258
3	3.255000	8	0.000169
3	3.255000	8	0.000000
3	3.986544	24	-0.000193

Continued on next page

Table B-5. Continued

Number of atoms in cluster	Diameter of cluster (Å)	No. of equivalent configurations	ECI
3	3.986544	24	-0.000155
3	4.603265	6	0.000677
3	4.603265	24	-0.000176
3	4.603265	24	0.000407
3	5.146607	48	0.000204
3	5.146607	48	0.000012
3	5.146607	48	-0.001004
3	5.146607	24	-0.000631
3	5.146607	48	-0.000131
3	5.146607	24	0.000140
3	5.146607	24	0.000208
3	5.146607	24	-0.000218
4	3.255000	6	-0.001207
4	3.255000	8	-0.000112
4	3.255000	2	-0.002589
4	3.255000	8	-0.000056
4	3.255000	2	0.000000
4	3.986544	24	0.000326
4	3.986544	24	0.000009
4	3.986544	6	0.001374
4	3.986544	24	-0.000153
4	3.986544	24	-0.000025
4	3.986544	6	0.000359
4	4.603265	24	-0.000219
4	4.603265	24	0.000586
4	4.603265	6	-0.000429
4	4.603265	24	0.000267
4	4.603265	48	0.000407
4	4.603265	12	-0.000016

Table B-6. Cluster and ECI information for fcc-lattice model limited to 4% strain.

Number of atoms in cluster	Diameter of cluster (Å)	No. of equivalent configurations	ECI
0	0.000000	1	0.064003
1	0.000000	2	0.034054
2	2.301633	6	0.001302
2	3.255000	12	0.001139
2	3.986544	4	-0.016544
2	3.986544	4	-0.004328
2	4.603265	6	-0.000107
2	5.146607	24	-0.000502
2	5.637825	24	0.000029
2	6.510000	12	0.000644
2	6.904898	12	0.000790
2	6.904898	12	-0.000365
2	6.904898	6	-0.000487
2	7.278401	24	-0.000096
2	7.633651	12	0.000112
2	7.633651	12	0.000454
2	7.973089	8	-0.000484
2	8.298654	24	-0.000557
2	8.611920	48	-0.000211
2	9.206530	6	-0.000084
3	3.255000	24	-0.000017
3	3.255000	8	-0.000693
3	3.255000	8	0.000000
3	3.986544	24	-0.000703
3	3.986544	24	-0.000524
3	4.603265	6	0.001163
3	4.603265	24	-0.000095
3	4.603265	24	0.000192
3	5.146607	48	0.000135
3	5.146607	48	0.000040
3	5.146607	48	-0.000933
3	5.146607	24	-0.000487
3	5.146607	48	0.000059
3	5.146607	24	-0.000015
3	5.146607	24	0.000314
3	5.146607	24	-0.000175
4	3.255000	6	-0.000553
4	3.255000	8	0.000472
4	3.255000	2	-0.002256
4	3.255000	8	-0.000177

Continued on next page

Table B-6. Continued

Number of atoms in cluster	Diameter of cluster (Å)	No. of equivalent configurations	ECI
4	3.255000	2	0.000000
4	3.986544	24	0.000001
4	3.986544	24	-0.000167
4	3.986544	6	0.001665
4	3.986544	24	-0.000225
4	3.986544	24	-0.000019
4	3.986544	6	0.000490
4	4.603265	24	0.000096
4	4.603265	24	0.000336
4	4.603265	6	-0.000511
4	4.603265	24	0.000328
4	4.603265	48	0.000243
4	4.603265	12	-0.000123

Table B-7. Cluster and ECI information for fct ($c/a < 1$) lattice model.

Number of atoms in cluster	Diameter of cluster (Å)	No. of equivalent configurations	ECI
0	0.000000	1	0.076877
1	0.000000	2	0.024145
2	2.226356	2	0.008221
2	2.504477	4	-0.002833
2	3.350980	8	-0.001483
2	3.541870	4	0.005364
2	4.183476	4	-0.010424
2	4.183476	4	-0.002759
2	4.452711	2	0.000715
2	5.008955	4	0.002747
2	5.108719	8	-0.001564
2	5.481450	8	0.000760
2	5.600185	8	-0.002179
2	5.689589	8	-0.002324
3	3.350980	16	-0.002981
4	3.350980	4	-0.002314

REFERENCES

- [1] H. Okamoto, "H-Zr (Hydrogen-Zirconium)," *Journal of Phase Equilibria and Diffusion*, vol. 27, no. 5, pp. 548–549, 2006. [Online]. Available: <http://link.springer.com/10.1007/BF02736475>
- [2] E. Zuzek, J. P. Abriata, A. San-Martin, and F. D. Manchester, "The H-Zr (hydrogen-zirconium) system," *Bulletin of Alloy Phase Diagrams*, vol. 11, no. 4, pp. 385–395, 8 1990. [Online]. Available: <http://link.springer.com/10.1007/BF02843318>
- [3] N. Dupin, I. Ansara, C. Servant, C. Toffolon, C. Lemaignan, and J. Brachet, "A thermodynamic database for zirconium alloys," *Journal of Nuclear Materials*, vol. 275, no. 3, pp. 287–295, 11 1999. [Online]. Available: <https://linkinghub.elsevier.com/retrieve/pii/S0022311599001257>
- [4] D. Setoyama and S. Yamanaka, "Phase diagram of Zr–O–H ternary system," *Journal of Alloys and Compounds*, vol. 370, no. 1-2, pp. 144–148, 5 2004. [Online]. Available: <https://linkinghub.elsevier.com/retrieve/pii/S09255838803009198>
- [5] C. Freysoldt, J. Neugebauer, and C. G. Van de Walle, "Electrostatic interactions between charged defects in supercells," *physica status solidi (b)*, vol. 248, no. 5, pp. 1067–1076, 5 2011. [Online]. Available: <http://doi.wiley.com/10.1002/pssb.201046289>
- [6] Z. Zhao, J.-P. Morniroli, A. Legris, A. Ambard, Y. Khin, L. Legras, and M. Blat-yréix, "Identification and characterization of a new zirconium hydride," *Journal of Microscopy*, vol. 232, no. 3, pp. 410–421, 12 2008. [Online]. Available: <http://doi.wiley.com/10.1111/j.1365-2818.2008.02136.x>
- [7] M. Simnad, "The U ZrH_x alloy: Its properties and use in TRIGA fuel," *Nuclear Engineering and Design*, vol. 64, no. 3, pp. 403–422, 4 1981. [Online]. Available: <https://linkinghub.elsevier.com/retrieve/pii/0029549381901357>
- [8] Y. Zhong and D. D. MacDonald, "Thermodynamics of the Zr-H binary system related to nuclear fuel sheathing and pressure tube hydriding," *Journal of Nuclear Materials*, vol. 423, pp. 87–92, 2012. [Online]. Available: <http://dx.doi.org/10.1016/j.jnucmat.2012.01.016>
- [9] J. R. Rumble, Ed., *Handbook of Chemistry and Physics*, 100th ed. Boca Raton: CRC Press, 2019. [Online]. Available: <http://hbcponline.com/faces/contents/ContentsSearch.xhtml>
- [10] J. S. Blakemore, "Semiconducting and other major properties of gallium arsenide," *Journal of Applied Physics*, vol. 53, no. 10, pp. R123–R181, 10 1982. [Online]. Available: <http://aip.scitation.org/doi/10.1063/1.331665>
- [11] K. Alberi and M. A. Scarpulla, "Suppression of compensating native defect formation during semiconductor processing via excess carriers," *Scientific Reports*, vol. 6, no. May, pp. 1–9, 2016.

- [12] J. Gebauer, E. R. Weber, N. D. Jäger, K. Urban, and P. Ebert, "Determination of the charge carrier compensation mechanism in Te-doped GaAs by scanning tunneling microscopy," *Applied Physics Letters*, vol. 82, no. 13, pp. 2059–2061, 3 2003. [Online]. Available: <http://aip.scitation.org/doi/10.1063/1.1563835>
- [13] J. A. Akintunde, "Effect of Heat Treatments on the Electrical Properties of Te-Implanted Laser-Annealed GaAs," *physica status solidi (a)*, vol. 140, pp. 501–508, 1993.
- [14] M. C. Billone, T. A. Burtseva, and R. E. Einziger, "Ductile-to-brittle transition temperature for high-burnup cladding alloys exposed to simulated drying-storage conditions," *Journal of Nuclear Materials*, vol. 433, no. 1-3, pp. 431–448, 2013. [Online]. Available: <http://dx.doi.org/10.1016/j.jnucmat.2012.10.002>
- [15] D. Schwen, L. K. Aagesen, J. W. Peterson, and M. R. Tonks, "Rapid multiphase-field model development using a modular free energy based approach with automatic differentiation in MOOSE/MARMOT," *Computational Materials Science*, vol. 132, pp. 36–45, 2017. [Online]. Available: <http://dx.doi.org/10.1016/j.commatsci.2017.02.017>
- [16] D. R. Olander and M. Ng, "Hydride fuel behavior in LWRs," *Journal of Nuclear Materials*, vol. 346, no. 2-3, pp. 98–108, 11 2005. [Online]. Available: <https://linkinghub.elsevier.com/retrieve/pii/S0022311505002588>
- [17] A. K. Rajagopal and J. Callaway, "Inhomogeneous Electron Gas," *Physical Review B*, vol. 7, no. 5, pp. 1912–1919, 3 1973. [Online]. Available: <https://link.aps.org/doi/10.1103/PhysRevB.7.1912>
- [18] W. Kohn and L. J. Sham, "Self-Consistent Equations Including Exchange and Correlation Effects," *Physical Review*, vol. 140, no. 4A, pp. A1133–A1138, 11 1965. [Online]. Available: <https://link.aps.org/doi/10.1103/PhysRev.140.A1133>
- [19] G. Kresse and J. Hafner, "Ab initio molecular dynamics for liquid metals," *Physical Review B*, vol. 47, no. 1, pp. 558–561, 1 1993. [Online]. Available: <https://link.aps.org/doi/10.1103/PhysRevB.47.558>
- [20] G. Kresse and J. Furthmüller, "Efficiency of ab-initio total energy calculations for metals and semiconductors using a plane-wave basis set," *Computational Materials Science*, vol. 6, no. 1, pp. 15–50, 7 1996. [Online]. Available: <https://linkinghub.elsevier.com/retrieve/pii/0927025696000080>
- [21] G. Kresse and D. Joubert, "From ultrasoft pseudopotentials to the projector augmented-wave method," *Physical Review B*, vol. 59, no. 3, pp. 1758–1775, 1 1999. [Online]. Available: <https://link.aps.org/doi/10.1103/PhysRevB.59.1758>
- [22] C. Freysoldt, B. Grabowski, T. Hickel, J. Neugebauer, G. Kresse, A. Janotti, and C. G. Van de Walle, "First-principles calculations for point defects in solids," *Reviews of Modern Physics*, vol. 86, no. 1, pp. 253–305, 3 2014. [Online]. Available: <https://link.aps.org/doi/10.1103/RevModPhys.86.253>

- [23] S. B. Zhang and J. E. Northrup, "Chemical potential dependence of defect formation energies in GaAs: Application to Ga self-diffusion," *Physical Review Letters*, vol. 67, no. 17, pp. 2339–2342, 1991.
- [24] L. Q. Chen, "Chemical potential and Gibbs free energy," *MRS Bulletin*, vol. 44, no. 7, pp. 520–523, 2019. [Online]. Available: <https://doi.org/10.1557/mrs.2019.162>
- [25] J. W. Gibbs, "On the equilibrium of heterogeneous substances," *American Journal of Science*, vol. s3-16, no. 96, pp. 441–458, 12 1878. [Online]. Available: <http://www.ajsonline.org/cgi/doi/10.2475/ajs.s3-16.96.441>
- [26] T. Mattila and R. Nieminen, "Ab initio study of oxygen point defects in GaAs, GaN, and AlN." *Physical review. B*, vol. 54, no. 23, pp. 16 676–16 682, 1996. [Online]. Available: <http://www.ncbi.nlm.nih.gov/pubmed/9985795>
- [27] S. Pöykkö, M. Puska, and R. Nieminen, "Ab initio study of fully relaxed divacancies in GaAs," *Physical Review B*, vol. 53, no. 7, pp. 3813–3819, 1996.
- [28] J. T. Schick, C. G. Morgan, and P. Papoulias, "First-principles study of As interstitials in GaAs: Convergence, relaxation, and formation energy," *Physical Review B*, vol. 66, no. 19, p. 195302, 11 2002. [Online]. Available: <https://link.aps.org/doi/10.1103/PhysRevB.66.195302>
- [29] F. El-Mellouhi and N. Mousseau, "Self-vacancies in gallium arsenide: An *ab initio* calculation," *Physical Review B*, vol. 71, no. 12, p. 125207, 2005. [Online]. Available: <https://link.aps.org/doi/10.1103/PhysRevB.71.125207>
- [30] P. A. Schultz and O. A. von Lilienfeld, "Simple intrinsic defects in gallium arsenide," *Modelling and Simulation in Materials Science and Engineering*, vol. 17, no. 8, p. 084007, 12 2009. [Online]. Available: <https://iopscience.iop.org/article/10.1088/0965-0393/17/8/084007>
- [31] C. G. Van De Walle, D. B. Laks, G. F. Neumark, and S. T. Pantelides, "First-principles calculations of solubilities and doping limits: Li, Na, and N in ZnSe," *Physical Review B*, vol. 47, no. 15, pp. 9425–9434, 1993.
- [32] C. Freysoldt, J. Neugebauer, and C. G. Van de Walle, "Fully Ab Initio Finite-Size Corrections for Charged-Defect Supercell Calculations," *Physical Review Letters*, vol. 102, no. 1, p. 016402, 1 2009. [Online]. Available: <https://link.aps.org/doi/10.1103/PhysRevLett.102.016402>
- [33] M. Leslie and N. J. Gillan, "The energy and elastic dipole tensor of defects in ionic crystals calculated by the supercell method," *Journal of Physics C: Solid State Physics*, vol. 18, no. 5, pp. 973–982, 2 1985. [Online]. Available: <https://doi.org/10.1088%2F0022-3719%2F18%2F5%2F005>
- [34] A. Pribram-Jones, S. Pittalis, E. K. U. Gross, and K. Burke, "Thermal Density Functional Theory in Context," in *Frontiers and Challenges in Warm Dense Matter. Lecture Notes*

- in Computational Science and Engineering*, F. Graziani, M. Desjarlais, R. Redmer, and S. Trickey, Eds. Cham, Switzerland: Springer, 2014, vol. 96, pp. 25–60. [Online]. Available: http://link.springer.com/10.1007/978-3-319-04912-0_2
- [35] A. van de Walle and G. Ceder, “Automating first-principles phase diagram calculations,” *Journal of Phase Equilibria*, vol. 23, no. 4, pp. 348–359, 2002. [Online]. Available: <https://doi.org/10.1361/105497102770331596>
- [36] A. van de Walle, M. Asta, and G. Ceder, “The alloy theoretic automated toolkit: A user guide,” *Calphad*, vol. 26, no. 4, pp. 539–553, 12 2002. [Online]. Available: <https://linkinghub.elsevier.com/retrieve/pii/S0364591602800062>
- [37] A. van de Walle, “Multicomponent multisublattice alloys, nonconfigurational entropy and other additions to the Alloy Theoretic Automated Toolkit,” *Calphad*, vol. 33, no. 2, pp. 266–278, 6 2009. [Online]. Available: <https://linkinghub.elsevier.com/retrieve/pii/S0364591608001314>
- [38] A. van de Walle and M. Asta, “Self-driven lattice-model Monte Carlo simulations of alloy thermodynamic properties and phase diagrams,” *Modelling and Simulation in Materials Science and Engineering*, vol. 10, no. 5, pp. 521–538, 9 2002. [Online]. Available: <https://iopscience.iop.org/article/10.1088/0965-0393/10/5/304>
- [39] A. Togo and I. Tanaka, “First principles phonon calculations in materials science,” *Scripta Materialia*, vol. 108, pp. 1–5, 2015. [Online]. Available: <http://dx.doi.org/10.1016/j.scriptamat.2015.07.021>
- [40] G. Ceder, “A derivation of the Ising model for the computation of phase diagrams,” *Computational Materials Science*, vol. 1, no. 2, pp. 144–150, 3 1993. [Online]. Available: <https://linkinghub.elsevier.com/retrieve/pii/0927025693900058>
- [41] J. M. Sanchez and D. de Fontaine, “Ising model phase-diagram calculations in the fcc lattice with first- and second-neighbor interactions,” *Physical Review B*, vol. 25, no. 3, pp. 1759–1765, 1982.
- [42] M. Sluitter, P. Turchi, F. Zvezhong, and D. De Fontaine, “Re-examination of BCC based phase diagrams with constant first and second neighbor pair interactions in the cluster variation approximation,” *Physica A: Statistical Mechanics and its Applications*, vol. 148, no. 1-2, pp. 61–73, 2 1988. [Online]. Available: <https://linkinghub.elsevier.com/retrieve/pii/0378437188901343>
- [43] J. W. D. Connolly and A. R. Williams, “Density-functional theory applied to phase transformations in transition-metal alloys,” *Physical Review B*, vol. 27, no. 8, pp. 5169–5172, 4 1983. [Online]. Available: <https://link.aps.org/doi/10.1103/PhysRevB.27.5169>
- [44] M. Stone, “Cross-Validatory Choice and Assessment of Statistical Predictions,” *Journal of the Royal Statistical Society Series B*, vol. 36, no. 2, pp. 111–147, 1974. [Online]. Available: <https://www.jstor.org/stable/2984809>

- [45] A. van de Walle, "The Alloy-Theoretic Automated Toolkit (ATAT): A User Guide," Brown University, Providence, RI, Tech. Rep., 2019. [Online]. Available: <https://www.brown.edu/Departments/Engineering/Labs/avdw/atat/>
- [46] K.-C. Li, "Asymptotic optimality for C_p , CL , cross-validation and generalized cross-validation: discrete index set," *The Annals of Statistics*, vol. 15, no. 3, pp. 958–975, 1987. [Online]. Available: <https://www.jstor.org/stable/2241809>
- [47] A. van de Walle and G. Ceder, "The effect of lattice vibrations on substitutional alloy thermodynamics," *Reviews of Modern Physics*, vol. 74, no. 1, pp. 11–45, 1 2002. [Online]. Available: <https://link.aps.org/doi/10.1103/RevModPhys.74.11>
- [48] D. P. Landau and K. Binder, *A Guide to Monte Carlo Simulations in Statistical Physics*, 2nd ed. New York: Cambridge University Press, 2005.
- [49] A. Kohan, P. Tepeš, G. Ceder, and C. Wolverton, "Computation of alloy phase diagrams at low temperatures," *Computational Materials Science*, vol. 9, no. 3-4, pp. 389–396, 1 1998. [Online]. Available: <https://linkinghub.elsevier.com/retrieve/pii/S0927025697001687>
- [50] G. Kresse, J. Furthmüller, and J. Hafner, "Ab initio force constant approach to phonon dispersion relations of diamond and graphite," *Epl*, vol. 32, no. 9, pp. 729–734, 1995.
- [51] K. Parlinski, Z. Q. Li, and Y. Kawazoe, "First-Principles Determination of the Soft Mode in Cubic ZrO_2 ," *Physical Review Letters*, vol. 78, no. 21, pp. 4063–4066, 5 1997. [Online]. Available: <https://link.aps.org/doi/10.1103/PhysRevLett.78.4063>
- [52] A. Togo, L. Chaput, and I. Tanaka, "Distributions of phonon lifetimes in Brillouin zones," *Physical Review B - Condensed Matter and Materials Physics*, vol. 91, no. 9, 2015.
- [53] A. Togo, "Phonopy Formulations," 2009. [Online]. Available: <https://atztogo.github.io/phonopy/formulation.html>
- [54] C. Elsässer, S. Schweizer, and M. Fähnle, "Hydrogen Vibration in Cubic Dihydrides MH_2 ($M=Ti, Zr$), and Localization in Cubic Laves Phases $ZrM_2H_{1/2}$ ($M=V, Cr, Fe, Co$)," in *MRS Proceedings*, vol. 453, no. 1. Cambridge University Press, 2 1996, p. 221. [Online]. Available: https://www.cambridge.org/core/product/identifier/S1946427400290337/type/journal_article
- [55] E. L. Kennon, T. Orzali, Y. Xin, A. Vert, A. G. Lind, and K. S. Jones, "Deactivation of electrically supersaturated Te-doped InGaAs grown by MOCVD," *Journal of Materials Science*, vol. 52, no. 18, pp. 10879–10885, 9 2017. [Online]. Available: <http://link.springer.com/10.1007/s10853-017-1254-8>
- [56] M.-A. Malouin, F. El-Mellouhi, and N. Mousseau, "Gallium self-interstitial relaxation in GaAs: An ab initio characterization," *Physical Review B*, vol. 76, no. 4, p. 045211, 7 2007. [Online]. Available: <https://link.aps.org/doi/10.1103/PhysRevB.76.045211>

- [57] G. Kresse and J. Furthmüller, “Efficiency of ab-initio total energy calculations for metals and semiconductors using a plane-wave basis set,” *Computational Materials Science*, vol. 6, no. 1, pp. 15–50, 7 1996. [Online]. Available: <https://linkinghub.elsevier.com/retrieve/pii/0927025696000080>
- [58] —, “Efficient iterative schemes for ab initio total-energy calculations using a plane-wave basis set,” *Physical Review B*, vol. 54, no. 16, pp. 11 169–11 186, 10 1996. [Online]. Available: <https://link.aps.org/doi/10.1103/PhysRevB.54.11169>
- [59] P. E. Blöchl, “Projector augmented-wave method,” *Physical Review B*, vol. 50, no. 24, pp. 17 953–17 979, 12 1994. [Online]. Available: <https://link.aps.org/doi/10.1103/PhysRevB.50.17953>
- [60] J. P. Perdew and A. Zunger, “Self-interaction correction to density-functional approximations for many-electron systems,” *Physical Review B*, vol. 23, no. 10, pp. 5048–5079, 1981.
- [61] C. G. Van de Walle and J. Neugebauer, “First-principles calculations for defects and impurities: Applications to III-nitrides,” *Journal of Applied Physics*, vol. 95, no. 8, pp. 3851–3879, 4 2004. [Online]. Available: <http://aip.scitation.org/doi/10.1063/1.1682673>
- [62] C. Kittel, *Introduction to Solid State Physics*, 8th ed. Wiley, 2004.
- [63] S. Jana, A. Patra, and P. Samal, “Assessing the performance of the Tao-Mo semilocal density functional in the projector-augmented-wave method,” *Journal of Chemical Physics*, vol. 149, no. 4, pp. 1–9, 2018.
- [64] D. Mejia-Rodriguez and S. B. Trickey, “Deorbitalized meta-GGA exchange-correlation functionals in solids,” *Physical Review B*, vol. 98, no. 11, pp. 1–9, 2018.
- [65] Z. H. Yang, H. Peng, J. Sun, and J. P. Perdew, “More realistic band gaps from meta-generalized gradient approximations: Only in a generalized Kohn-Sham scheme,” *Physical Review B*, vol. 93, no. 20, pp. 1–9, 2016.
- [66] H.-P. Komsa, E. Arola, J. Pakarinen, C. S. Peng, and T. T. Rantala, “Beryllium doping of GaAs and GaAsN studied from first principles,” *Physical Review B*, vol. 79, no. 11, p. 115208, 3 2009. [Online]. Available: <https://link.aps.org/doi/10.1103/PhysRevB.79.115208>
- [67] A. Fleszar, “LDA, GW, and exact-exchange Kohn-Sham scheme calculations of the electronic structure of sp semiconductors,” *Physical Review B*, vol. 64, no. 24, p. 245204, 2001. [Online]. Available: <http://link.aps.org/doi/10.1103/PhysRevB.64.245204>
- [68] C. Stampfl and C. G. Van de Walle, “Density-functional calculations for III-V nitrides using the local-density approximation and the generalized gradient approximation,” *Physical Review B*, vol. 59, no. 8, pp. 5521–5535, 2 1999. [Online]. Available: <https://link.aps.org/doi/10.1103/PhysRevB.59.5521>

- [69] —, “Theoretical investigation of native defects, impurities, and complexes in aluminum nitride,” *Physical Review B*, vol. 65, no. 15, p. 155212, 4 2002. [Online]. Available: <https://link.aps.org/doi/10.1103/PhysRevB.65.155212>
- [70] J. Sun, A. Ruzsinszky, and J. Perdew, “Strongly Constrained and Appropriately Normed Semilocal Density Functional,” *Physical Review Letters*, vol. 115, no. 3, p. 036402, 7 2015. [Online]. Available: <https://link.aps.org/doi/10.1103/PhysRevLett.115.036402>
- [71] J. Heyd, G. E. Scuseria, and M. Ernzerhof, “Hybrid functionals based on a screened Coulomb potential,” *Journal of Chemical Physics*, vol. 118, no. 18, pp. 8207–8215, 2003.
- [72] S. Boeck, C. Freysoldt, A. Dick, L. Ismer, and J. Neugebauer, “The object-oriented DFT program library S/PHI/nX,” *Computer Physics Communications*, vol. 182, no. 3, pp. 543–554, 2011. [Online]. Available: <http://dx.doi.org/10.1016/j.cpc.2010.09.016>
- [73] J. Gebauer, M. Lausmann, F. Redmann, R. Krause-Rehberg, H. S. Leipner, E. R. Weber, and P. Ebert, “Determination of the Gibbs free energy of formation of Ga vacancies in GaAs by positron annihilation,” *Physical Review B*, vol. 67, no. 23, p. 235207, 6 2003. [Online]. Available: <https://link.aps.org/doi/10.1103/PhysRevB.67.235207>
- [74] P. Erhart and K. Albe, “Modeling the electrical conductivity in BaTiO₃ on the basis of first-principles calculations,” *Journal of Applied Physics*, vol. 104, no. 4, p. 044315, 8 2008. [Online]. Available: <http://aip.scitation.org/doi/10.1063/1.2956327>
- [75] K. Biswas and S. Lany, “Energetics of quaternary III-V alloys described by incorporation and clustering of impurities,” *Physical Review B*, vol. 80, no. 11, p. 115206, 9 2009. [Online]. Available: <https://link.aps.org/doi/10.1103/PhysRevB.80.115206>
- [76] M. Fullarton, R. Voskoboynikov, and S. Middleburgh, “Hydrogen accommodation in alpha-iron and nickel,” *Journal of Alloys and Compounds*, vol. 587, pp. 794–799, 2 2014. [Online]. Available: <http://www.sciencedirect.com/science/article/pii/S0925838813025954>
- [77] A. Goyal, P. Gorai, E. S. Toberer, and V. Stevanović, “First-principles calculation of intrinsic defect chemistry and self-doping in PbTe,” *npj Computational Materials*, vol. 3, no. 1, p. 42, 12 2017. [Online]. Available: <http://www.nature.com/articles/s41524-017-0047-6>
- [78] A. Glensk, B. Grabowski, T. Hickel, and J. Neugebauer, “Breakdown of the Arrhenius Law in Describing Vacancy Formation Energies: The Importance of Local Anharmonicity Revealed by Ab initio Thermodynamics,” *Physical Review X*, vol. 4, no. 1, p. 011018, 2 2014. [Online]. Available: <https://link.aps.org/doi/10.1103/PhysRevX.4.011018>
- [79] K. Barrett, S. Bragg-Sitton, and D. Galicki, “Advanced LWR Nuclear Fuel Cladding System Development Trade-off Study,” Idaho National Laboratory, Idaho Falls, ID, Tech. Rep. September, 2012. [Online]. Available: <https://www.energy.gov/ne/downloads/advanced-lwr-nuclear-fuel-cladding-system-development-trade-study>

- [80] P. P. Narang, G. L. Paul, and K. N. R. Taylor, "Location of hydrogen in α -zirconium," *Journal of the Less-Common Metals*, vol. 56, no. 1, pp. 125–128, 1977. [Online]. Available: http://inis.iaea.org/search/search.aspx?orig_q=RN:09367264
- [81] M. I. Darby, M. N. Read, and K. N. R. Taylor, "The energy of interstitial hydrogen in α -zirconium," *physica status solidi (a)*, vol. 50, no. 1, pp. 203–211, 1978. [Online]. Available: <https://onlinelibrary.wiley.com/doi/abs/10.1002/pssa.2210500124>
- [82] R. Khoda-Bakhsh and D. K. Ross, "Determination of the hydrogen site occupation in the α phase of zirconium hydride and in the α and β phases of titanium hydride by inelastic neutron scattering," *Journal of Physics F: Metal Physics*, vol. 12, pp. 15–24, 1982. [Online]. Available: <https://doi.org/10.1088/0305-4608/12/1/003>
- [83] L. Lanzani and M. Ruch, "Comments on the stability of zirconium hydride phases in Zircaloy," *Journal of Nuclear Materials*, vol. 324, no. 2-3, pp. 165–176, 1 2004. [Online]. Available: <https://linkinghub.elsevier.com/retrieve/pii/S0022311503004409>
- [84] C. Domain, R. Besson, and A. Legris, "Atomic-scale Ab-initio study of the Zr-H system: I. Bulk properties," *Acta Materialia*, vol. 50, pp. 3513–3526, 2002. [Online]. Available: [https://doi.org/10.1016/S1359-6454\(02\)00173-8](https://doi.org/10.1016/S1359-6454(02)00173-8)
- [85] —, "Atomic-scale ab initio study of the Zr–H system: II. Interaction of H with plane defects and mechanical properties," *Acta Materialia*, vol. 52, pp. 1495–1502, 2004. [Online]. Available: <http://linkinghub.elsevier.com/retrieve/pii/S1359645403007304>
- [86] Y. Udagawa, M. Yamaguchi, H. Abe, N. Sekimura, and T. Fuketa, "Ab initio study on plane defects in zirconium-hydrogen solid solution and zirconium hydride," *Acta Materialia*, vol. 58, pp. 3927–3938, 2010. [Online]. Available: <http://dx.doi.org/10.1016/j.actamat.2010.03.034>
- [87] S. Lumley, R. Grimes, S. Murphy, P. Burr, A. Chroneos, P. Chard-Tuckey, and M. Wenman, "The thermodynamics of hydride precipitation: The importance of entropy, enthalpy and disorder," *Acta Materialia*, vol. 79, pp. 351–362, 2014. [Online]. Available: <http://linkinghub.elsevier.com/retrieve/pii/S1359645414005370>
- [88] H. Wang, A. Chroneos, C. Jiang, and U. Schwingenschlögl, "Modelling zirconium hydrides using the special quasirandom structure approach," *Physical Chemistry Chemical Physics*, vol. 15, no. 20, p. 7599, 2013. [Online]. Available: <http://xlink.rsc.org/?DOI=c3cp50624j>
- [89] P. A. T. Olsson, A. R. Massih, J. Blomqvist, A. M. Alvarez Holston, and C. Bjerken, "Ab initio thermodynamics of zirconium hydrides and deuterides," *Computational Materials Science*, vol. 86, pp. 211–222, 2014. [Online]. Available: <http://dx.doi.org/10.1016/j.commatsci.2014.01.043>
- [90] M. Christensen, W. Wolf, C. Freeman, E. Wimmer, R. B. Adamson, L. Hallstadius, P. E. Cantonwine, and E. V. Mader, "H in α -Zr and in zirconium hydrides: Solubility, effect on dimensional changes, and the role of defects," *Journal*

- of Physics Condensed Matter*, vol. 27, p. 025402, 2015. [Online]. Available: <http://dx.doi.org/10.1088/0953-8984/27/2/025402>
- [91] Z. Zhao, M. Blat-Yrieix, J.-P. Morniroli, A. Legris, L. Thuinet, Y. Kihn, A. Ambard, L. Legras, M. Limback, B. Kammenzind, and S. W. Dean, "Characterization of Zirconium Hydrides and Phase Field Approach to a Mesoscopic-Scale Modeling of Their Precipitation," *Journal of ASTM International*, vol. 5, no. 3, p. 101161, 2008. [Online]. Available: <http://www.astm.org/doiLink.cgi?JAI101161>
- [92] J. P. Perdew, K. Burke, and M. Ernzerhof, "Generalized Gradient Approximation Made Simple," *Physical Review Letters*, vol. 77, no. 18, pp. 3865–3868, 10 1996. [Online]. Available: <https://link.aps.org/doi/10.1103/PhysRevLett.77.3865>
- [93] R. Besson and R. Candela, "Ab initio thermodynamics of fcc H-Zr and formation of hydrides," *Computational Materials Science*, vol. 114, pp. 254–263, 2016. [Online]. Available: <http://dx.doi.org/10.1016/j.commatsci.2015.12.043>
- [94] C. Varvenne, O. Mackain, L. Proville, and E. Clouet, "Hydrogen and vacancy clustering in zirconium," *Acta Materialia*, vol. 102, pp. 56–69, 1 2016. [Online]. Available: <https://linkinghub.elsevier.com/retrieve/pii/S1359645415006850>
- [95] M. Christensen, W. Wolf, C. Freeman, E. Wimmer, R. B. Adamson, L. Hallstadius, P. E. Cantonwine, and E. V. Mader, "Diffusion of point defects , nucleation of dislocation loops , and effect of hydrogen in hcp-Zr : Ab initio and classical simulations," *Journal of Nuclear Materials*, vol. 460, pp. 82–96, 2015. [Online]. Available: <http://dx.doi.org/10.1016/j.jnucmat.2015.02.013>
- [96] J. Zheng, X. Zhou, L. Mao, H. Zhang, J. Liang, L. Sheng, and S. Peng, "First-principles study of the relative stability of various zirconium hydrides using the special quasirandom structures approach," *International Journal of Hydrogen Energy*, vol. 40, no. 13, pp. 4597–4604, 2015. [Online]. Available: <http://dx.doi.org/10.1016/j.ijhydene.2015.02.045>
- [97] P. F. Weck, E. Kim, V. Tikare, and J. A. Mitchell, "Mechanical properties of zirconium alloys and zirconium hydrides predicted from density functional perturbation theory," *Dalton Transactions*, vol. 44, pp. 18 769–18 779, 2015. [Online]. Available: <http://dx.doi.org/10.1039/c5dt03403e>
- [98] M. V. Glazoff, A. Tokuhiro, S. N. Rashkeev, and P. Sabharwall, "Oxidation and hydrogen uptake in zirconium, Zircaloy-2 and Zircaloy-4: Computational thermodynamics and ab initio calculations," *Journal of Nuclear Materials*, vol. 444, no. 1-3, pp. 65–75, 2014. [Online]. Available: <http://dx.doi.org/10.1016/j.jnucmat.2013.09.038>
- [99] G. Kresse, M. Marsman, and J. Furthmuller, "The VASP Manual," Vienna, Austria, 2019. [Online]. Available: <https://cms.mpi.univie.ac.at/wiki/index.php/ISMEAR>
- [100] A. van de Walle, "Alloy Theoretic Automated Toolkit User Forum," 2015. [Online]. Available: <https://www.brown.edu/Departments/Engineering/Labs/avdw/forum/viewtopic.php?f=4&t=239&sid=d1fd6ecb9c1e71b76e89d46c70104862>

- [101] S. Pandey, R. J. Koch, G. Li, S. T. Misture, H. Wang, and S. R. Phillpot, "Thermodynamics and kinetics of ordered and disordered Cu/Au alloys from first principles calculations," *Journal of Alloys and Compounds*, vol. 809, p. 151615, 2019. [Online]. Available: <https://doi.org/10.1016/j.jallcom.2019.07.327>
- [102] A. van de Walle, P. Tiwary, M. De Jong, D. L. Olmsted, M. Asta, A. Dick, D. Shin, Y. Wang, L. Q. Chen, and Z. K. Liu, "Efficient stochastic generation of special quasirandom structures," *Calphad: Computer Coupling of Phase Diagrams and Thermochemistry*, vol. 42, pp. 13–18, 2013. [Online]. Available: <http://dx.doi.org/10.1016/j.calphad.2013.06.006>
- [103] D. Chattaraj, S. C. Parida, S. Dash, and C. Majumder, "On the isotope effects of ZrX₂ (X = H, D and T): A First-principles study," *Condensed Matter Materials Science*, 5 2013. [Online]. Available: <http://arxiv.org/abs/1305.6109>

BIOGRAPHICAL SKETCH

Michele Fullarton was born and raised in Brisbane, Australia. She received a Bachelor in Applied Science majoring in physics and Japanese from the Queensland University of Technology (QUT). After graduation, she taught English at both private companies and Junior High School in Japan for several years. On return to Australia, she furthered her education with a Graduate Certificate of Mathematical Science focusing on applied mathematics and modeling from QUT. She was selected to participate in the Australian Nuclear Science and Technology Organization's Graduate Development program where she was introduced to computational materials science. This work led to the opportunity to join the University of Florida's (UF) Department of Materials Science and Engineering under Professor Simon R. Phillpot. In May 2016 she received a Master of Science in materials science and engineering. During her graduate studies, Michele researched topics such as semiconductor materials and nuclear materials from a first-principles computational approach. Additionally, she interned for eight months at Idaho National Laboratory. She was awarded a Doctor of Philosophy in materials science and engineering from UF in 2020.